Enhancing Coverage and Capacity in Massive MIMO Wireless Communications Systems

Mobeen Mahmood

Department of Electrical & Computer Engineering
McGill University
Montréal, Québec, Canada

November 2024

A thesis submitted to McGill University in partial fulfillment of the requirements for the degree of Doctor of Philosophy

”The greatest glory in living lies not in never falling, but in rising every time we fall.”

Nelson Mandela

Abstract

The ITU's 2030 (6G) framework focuses on enhancing terrestrial networks by integrating aerial communications for peak data rate, ubiquitous coverage, and sensing. In this regard, massive multiple-input multiple-output (mMIMO) is considered as a key enabling technology for large-scale deployments in beyond 5G mobile networks. By utilizing a large number of antennas at base station (BS), mMIMO enables state-of-the-art hybrid beamforming (HBF) and MIMO techniques that are powerful tools for improving end-user experience and capacity in both uplink and downlink. The two-stage HBF architecture is considered a promising solution in mMIMO systems to provide high data rates with much-reduced hardware complexity/cost. We aim to address a set of objectives, including antenna array configurations, beamforming optimization, interference suppression, sum-rate maximization, improved energy efficiency, high self-interference suppression (SIS) quality, and unmanned aerial vehicle (UAV) deployment to enhance both coverage and capacity in terrestrials and UAVs-assisted terrestrial networks.

First, we study different two-dimensional (2D) and three-dimensional (3D) array structures, which can be used at BS to support both aerial and ground users. We consider half-duplex communications and investigate how the system performance can vary based on (i) users angular location, and (ii) number of users. In this regard, we design HBF schemes based on users angular locations to reduce multi-user (MU) interference. We also examine the use of low-resolution hardware components (e.g., digital-to-analog converters (DACs), phase shifters) and their impacts on the system performance.

Secondly, we explore full-duplex (FD) communications. We aim to mitigate strong self-interference (SI) and maximize the total achievable rate based on over-the-air (OTA) measurements of the SI channel measured in an anechoic chamber for a sub-6 GHz frequency band. By using perturbation-based HBF for SI suppression and by exploiting spatial degrees-of-freedom (DoF) due to the use of large antenna arrays, our objective is to bring the SI level down to the noise floor, thus avoiding the use of costly/complex analog cancellation circuits commonly used in FD circuitry. We propose different HBF solutions, which can suppress SI up to 80 dB by optimizing (i) variable gain-controllers, (ii) perturbing the directed beams, and (iii) selecting the best Tx/Rx antenna pairs.

Finally, we consider a UAV-assisted terrestrial system to address the coverage and capacity issues by employing the UAVs as a relay between BS and multiple users. The high mobility and easy deployment of a UAV can provide an additional DoF to improve the overall capacity in mMIMO systems by addressing the signal fading, attenuation issues as well as providing coverage to obscured/inaccessible users. However, the optimal deployment of UAV within a given flying span remains a challenging task. To maximize the total achievable rate in dual-hop mMIMO systems, we investigate a joint HBF solution by optimizing both UAV location and power allocation to multiple users, and sequentially designing the HBF stages for BS and UAV. The RF stages are designed based on the slow time-varying angular information, while the BB stages are designed using the reduced-dimension effective channel matrices. Then, we aim to develop a deep learning-based low-complexity joint HBF solution via a fully connected deep neural network, consisting of an offline training phase, and an online prediction of UAV location and optimal power values for maximizing the achievable rate while significantly reducing the runtime by 99%. Later on, we further extend the performance analysis to multiple UAV-assisted terrestrial systems, which can support many users in a dynamic environment, providing greater network coverage and capacity.

Sommaire

Le cadre 2030 (6G) de l'UIT vise à améliorer les réseaux terrestres en intégrant les communications aériennes pour un débit maximal, une couverture omniprésente, et une meilleure détection. La technologie massive MIMO (mMIMO) est considérée comme essentielle pour les déploiements à grande échelle au-delà de la 5G. Grâce à un grand nombre d'antennes à la station de base (BS), le mMIMO permet des techniques avancées de formation de faisceaux hybrides (HBF) et MIMO, améliorant l'expérience utilisateur et la capacité en liaison montante et descendante. L'architecture HBF à deux étages est prometteuse pour fournir des débits élevés tout en réduisant la complexité et les coûts matériels. Nous visons à optimiser les configurations d'antennes, le beamforming, la suppression des interférences, la maximisation du débit, l'efficacité énergétique, la suppression de l'auto-interférence (SIS) et le déploiement de drones pour améliorer la couverture et la capacité dans les réseaux terrestres assistés par UAV.

Nous étudions différentes structures de réseaux 2D et 3D pouvant être utilisées à la station de base pour prendre en charge les utilisateurs aériens et terrestres. Nous considérons les communications semi-duplex et analysons les performances du système selon la position angulaire des utilisateurs et leur nombre. Nous concevons des schémas HBF basés sur ces positions pour réduire les interférences multi-utilisateurs (MU), et examinons l'impact de l'utilisation de composants matériels à faible résolution (convertisseurs numérique-analogique, déphaseurs) sur les performances.

Nous explorons ensuite les communications full-duplex (FD) pour atténuer l'auto-interférence (SI) et maximiser le débit total réalisable. En utilisant le HBF basé sur les perturbations pour la suppression du SI, et en exploitant les degrés de liberté spatiaux grâce aux grandes antennes, nous cherchons à ramener le SI au niveau du bruit de fond, évitant ainsi des circuits d'annulation analogiques coûteux et complexes. Nous proposons des solutions HBF pouvant réduire le SI jusqu'à 80 dB en optimisant les contrôleurs de gain variables, les faisceaux dirigés perturbés, et la sélection des meilleures paires d'antennes Tx/Rx.

Enfin, nous envisageons un système terrestre assisté par UAV pour résoudre les problèmes de couverture et de capacité, en utilisant les UAV comme relais entre la station de base et plusieurs utilisateurs. La mobilité et la facilité de déploiement d'un UAV offrent un degré de liberté supplémentaire pour améliorer la capacité globale des systèmes mMIMO en traitant les problèmes d'évanouissement et d'atténuation du signal, tout en fournissant une couverture aux utilisateurs inaccessibles. Cependant, le déploiement optimal d'un UAV reste un défi. Pour maximiser le débit total réalisable dans ces systèmes mMIMO, nous explorons une solution HBF conjointe en optimisant à la fois l’emplacement du UAV et l’allocation de puissance, et en concevant successivement les étapes HBF pour la station de base et le UAV. Nous développons également une solution HBF conjointe à faible complexité, basée sur l’apprentissage profond, permettant une prédiction en ligne de l’emplacement optimal du UAV et des valeurs de puissance pour maximiser le débit tout en réduisant le temps d’exécution. Nous étendons cette analyse à des systèmes terrestres assistés par plusieurs UAV, capables de supporter de nombreux utilisateurs dans un environnement dynamique, offrant ainsi une couverture et une capacité réseau accrues.

Acknowledgments

First and foremost, I would like to express my deepest appreciation and gratitude to my supervisor, Prof. Tho Le-Ngoc. His endless passion for research, vast technical knowledge, and ability to integrate theoretical understanding with practical engineering have been a constant source of inspiration and motivation. I feel privileged to have had long, invaluable, and insightful technical discussions with him, which have led to the development of new ideas and numerous successful publications during my doctoral study. My heartfelt thanks also go to Dr. Asil Koc, former Ph.D. student, for the productive research collaborations.

I extend my sincere gratitude to my Ph.D. supervisory committee members, Prof. Ioannis Psaromiligkos and Prof. Milica Popovic, for their time and effort in evaluating my doctoral work and providing constructive feedback that helped me think critically and rigorously about my research. I am also grateful to the other examiners for their thorough review and feedback during their busy schedules.

I am deeply grateful for the generous financial support provided by the McGill Engineering Doctoral Award (MEDA), the Fonds de Recherche du Québec-Nature and Technologies (FRQNT), Huawei Technologies Canada, Mitacs Accelerate Internship Program, and the Centre for Systems, Technologies and Applications for Radio frequency and Communications (STARaCom). Also, I would like to thank various members of the technical staff at Huawei Technologies Canada for the technical discussions and collaboration through my doctoral study.

I am also grateful to my colleagues and friends at McGill University. In particular, I would like to thank Asil, Ibrahim, Yuanzhe, Robert, Quang, Hung, Tuong, Farzanullah, Farhan, Harry, Son, Xianyi, Mason, Arish, Geng, Yuanxing, Mohammadmahdi, Jianbin, Richard, Mohammad, Hossein, Yicheng, Tony, Ali, Reza, Aquib, who have made my stay at McGill truly enjoyable and gratifying.

To my family—my parents, Tariq and Abida, and my siblings, Mateen and Zainab—I owe everything. Your love, patience, and belief in me have been my greatest source of strength. A special thanks to my parents, whose unwavering support and encouragement have been instrumental in helping me achieve this milestone. Despite coming from a modest background, where neither of them had the opportunity to attend university, their belief in the value of education and their sacrifices have made my journey possible. I owe this achievement to their dedication and love.

Finally, I dedicate this thesis to all those in Pakistan and beyond who continue to work hard and pursue their dreams despite facing many challenges. Your determination and perseverance are truly inspiring.

Preface and Contributions of the Author

This research was conducted in the Department of Electrical and Computer Engineering at McGill University between September 2019 and August 2024. The original work detailed in this dissertation was developed by Mr. Mobeen Mahmood under the guidance of Prof. Tho Le-Ngoc within the same department. Portions of the contributions made in this dissertation have been previously presented in the following forums:

- **Journal Papers:**

  [J1] M. Mahmood, A. Koc, and T. Le-Ngoc, ”Energy-Efficient MU-Massive MIMO Hybrid Precoder Design: Low-Resolution Phase Shifters and Digital-to-Analog Converters for 2D Antenna Array Structures”, in IEEE Open J. Commun. Soc, vol. 2, pp. 1842-1861, 2021.

  [J2] M. Mahmood, A. Koc, and T. Le-Ngoc, “3-D antenna array structures for millimeter-wave multiuser massive MIMO hybrid precoder design: A performance comparison,” IEEE Commun. Lett. vol. 26, no. 6, pp. 1393–1397, 2022.

  [J3] M. Mahmood, M. Ghadaksaz, A. Koc and T. Le-Ngoc, “Deep learning meets swarm intelligence for UAV-assisted IoT coverage in massive MIMO,” IEEE Internet Things J., vol. 11, no. 5, pp. 7679–7696, 2024.

  [J4] M. Mahmood, A. Koc, R. Morawski, and T. Le-Ngoc, ”Achieving Capacity Gains in Practical Full-Duplex Massive MIMO Systems: A Hybrid Beamforming-Based Multi-Objective Optimization Approach”, in IEEE Open Journal of the Communications Society, vol. 5, pp. 2268-2286, 2024.

  [J5] T. Le-Ngoc, Y. Gong, M. Mahmood, A. Koc, R. Morawski, J. G. Griffiths, P. Guillemette, J. Zaid, and P. Wang, ”Full-Duplex in Massive Multiple-Input Multiple-Output”, in IEEE Open Journal of Vehicular Technology, vol. 5, pp. 560-576, 2024.

  [J6] Y. Gong, M. Mahmood, R. Morawski and T. Le-Ngoc, ”Dual-Layer Metamaterial Rectangular Antenna Arrays for In-Band Full-Duplex Massive MIMO,” in IEEE Access, vol. 11, pp. 135708- 135727, 2023.

- **Conference papers:**

  [C1] M. Mahmood, A. Koc, and T. Le-Ngoc, “2D antenna array structures for hybrid massive MIMO precoding,” in Proc. IEEE Global Commun. Conf. (GLOBECOM), Taipei, Taiwan, Dec. 7-11, 2020.

  [C2] M. Mahmood, A. Koc, and T. Le-Ngoc, “Massive-MIMO hybrid precoder design using Few-Bit DACs for 2D antenna array structures,” in Proc. IEEE Int. Conf. Commun. (ICC), Montreal, Canada, Jun 14-23, 2021.

  [C3] M. Mahmood, A. Koc and T. Le-Ngoc, ”PSO-Based Joint UAV Positioning and Hybrid Precoding in UAV-Assisted Massive MIMO Systems”, in Proc. IEEE VTC2022-Fall, London, United Kingdom, Sept. 26-29, 2022.

  [C4] M. Mahmood, A. Koc, and T. Le-Ngoc, ”Spherical Array-Based Joint Hybrid Beamforming and UAV Positioning in Massive MIMO Systems”, in Proc. IEEE VTC2023-Spring, Florence, Italy, 2023.

  [C5] A. Koc, M. Mahmood, and T. Le-Ngoc, ”Efficient Dual-Hop Massive MIMO IoT Networks with UAV DF Relaying and Hybrid Beamforming”, in Proc. IEEE Global Commun. Conf. (GLOBECOM), Kuala Lumpur, Malaysia, Dec. 4-8, 2023.

  [C6] M. Mahmood, A. Koc, D. T. Nguyen, R. Morawski, and T. Le-Ngoc, ”Sub-Array Selection in Full-Duplex Massive MIMO for Enhanced Self-Interference Cancellation”, in Proc. IEEE Global Commun. Conf. (GLOBECOM), Kuala Lumpur, Malaysia, Dec. 4-8, 2023.

  [C7] M. Mahmood, Y. Zhang, and T. Le-Ngoc, ”Adaptive Modulus RF Beamforming for Enhanced Self-Interference Suppression in Full-Duplex Massive MIMO Systems”, in Proc IEEE Wireless Communications and Networking Conference (WCNC), Dubai, United Arab Emirates, April 21-24, 2024.

  [C8] M. Mahmood, Y. Yuan, and T. Le-Ngoc, ”Multiple UAV-Assisted Cooperative DF Relaying in Multi-User Massive MIMO IoT Systems”, in Proc IEEE International

Conference on Communications (ICC), Denver, USA, June 9-13, 2024.

[C9] M. Mahmood, Y. Zhang, and T. Le-Ngoc, “Null Space Projection-Based Perturbed Beamforming in sub-THz Massive MIMO Systems”, submitted in Proc. IEEE Global Commun. Conf. (GLOBECOM), Cape Town, South Africa, Dec. 8-12, 2024.

In all of these publications, except [J5], [J6] and [C5], Mr. Mobeen Mahmood as the first author developed and proposed the idea, formulated the problem, developed the algorithms, implemented simulations, and prepared the first draft of the manuscripts. Mr. Mohammadmahdi. Ghadaksaz and Mr. Yuanxing Zhang, both MSc students, and Mr. Yicheng Yuan, the undergraduate student in 2023 Summer Undergraduate Research in Engineering program, assisted partially in performing simulations used in [J3], [C7]-[C9]. Dr. Asil Koc collaborated in [J1]-[J5], [C1]-[C6] during his P.hD. time at McGill University to review the works and to assist in editing and writing. Mr. Nguyen Duc Tuong collaborated in [C6] with some preliminary simulation results.

In [J6], the first author, Mr. Yuanzhe Gong, Ph.D. student, developed the antenna design of 8 × 8 FD mMIMO prototype. The second author, Mr. Mobeen Mahmood, designed the perturbed RF-beamformers for uplink and downlink stage and performed the SI suppression analysis. Mr. Mobeen Mahmood assisted in preparation and revising the manuscript together with Mr. Yuanzhe Gong. Mr. Robert Morawski assisted in reviewing, especially the related experiments and measurements. Prof. Tho Le-Ngoc suggested the topics, main ideas, supervised and reviewed the works, and assisted in the editing and writing of the manuscripts at different stages.

Contents

List of Figures

List of Tables

List of Algorithms

List of Acronyms

1D	One-dimensional
2D	Two-dimensional
3D	Three-dimensional
3GPP	Third generation partnership project
5G	Fifth-generation
6G	Sixth-generation
AAoD	Azimuth AoD
ABF	Analog beamforming
ADC	Analog-to-digital converter
AF	Amplify-and-forward relaying
AI	Artificial intelligence
AoA	Angle-of-arrival
AoD	Angle-of-departure
AQNM	Additive quantization noise model
BB	Baseband
bps	Bits per second
BS	Base station
CM	Constant-modulus
CSI	Channel state information
DAC	Digital-to-analog converter
dB	Decibel
dBm	Decibel milliwatts
DL	Downlink
DF	Decode-and-forward relaying
DNN	Deep neural network
EAoD	Elevation AoD
EBF	Eigen-beamforming
EE	Energy efficiency
eMBB	Enhanced mobile broadband
EQ-PA	Equal power allocation
FC-HBF	Fully-connected hybrid beamforming
FD	Full-duplex
FDBF	Fully-digital beamforming

FDD	Frequency-division duplex
GHz	Gigahertz
HBF	Hybrid beamforming
HC	Hybrid combining
HD	Half-duplex
Hz	Hertz
I-CSI	Imperfect CSI
IoT	Internet of things
IUI	Inter-user interference
ITU	International Telecommunication Union
JGP	Joint-group-processing
J-HBF-PSOPA-FL	Joint HBF and optimal PA for fixed UAV location
J-HBF-PSOL-EQPA	Joint HBF and UAV location optimization for equal PA
J-HBF-PSOLPA	Joint HBF, UAV location optimization, and PA
J-HBF-DLLPA	DL-based joint HBF, UAV location optimization and PA
JSDM	Joint spatial division multiplexing
KKT	Karush-Kuhn-Tucker
LoS	Line-of-sight
LTE	Long-Term Evaluation
MAE	Mean absolute error
MBF	Maximum directivity beamforming
MF	Matched filter
MIMO	Multiple-input multiple-output
mMIMO	Massive MIMO
mMTC	Massive machine type communications
MMSE	Minimum mean square error
mmWave	Millimeter-wave
MOOP	Multi-objective optimization problem
MSE	Mean square error
MU	Multi-user
MU-mMIMO	Multi-user mMIMO
NI	Nature-inspired
NOBF	Non-orthogonal beamforming
NOMA	Non-orthogonal multiple access
NP-hard	Non-deterministic polynomial-time hardness

NLoS	Non-line-of-sight
OBF	Orthogonal beamforming
PA	Power allocation
PBF	Perturbed beamforming
PSs	Phase shifters
PSD	Power spectral density
PSO	Particle swarm optimization
PSO-PA	PSO based power allocation
QoS	Quality of service
RAN	Radio access networks
ReLU	Rectified linear unit
RF	Radio frequency
RZF	Regularized zero-forcing
SAS	Sub-array selection
SC-HBF	Sub-connected hybrid beamforming
SE	Spectral efficiency
SNR	Signal-to-noise ratio
SINR	Signal-to-interference-plus-noise ratio
SI	Self-interference
SIC	Self-interference cancellation
SIS	Self-interference suppression
SOOP	Single-objective optimization problem
SVD	Singular value decomposition
UAV	Unmanned aerial vehicle
UE	User equipment
UL	Uplink
UCA	Uniform circular array
ULA	Uniform linear array
URA	Uniform rectangular array
URLLC	Ultra-reliable and low-latency communications
WSN	Wireless sensor network
ZF	Zero-forcing

List of Key Symbols

Symbol	Description
b	# of beams
d_s	Antenna spacing normalized by the wavelength
k, g, l	UE, group, and path index
L	Total number of paths
N_T	# of antennas at BS
$N_{u,t}$	# antennas at UAV transmit
$N_{u,r}$	# of antennas at UAV receive
N_{RF}	# of RF chains
N_{PS}	# of phase-shifters
Z_p	# of search agents in PSO
P_{RF}, P_{PS}	Power consumption per RF chain and phase-shifter
P_T	Transmit power
T	# of iterations
R_{sum}, R_k	Sum-rate and rate of k^{th} UE
S	# of data streams
$\mathbf{d}$	Data signal vector
$\mathbf{e}$	Steering vector
$\mathbf{B}_D$	Digital BB precoder
$\mathbf{B}_{rs}$	Reduced-size digital BB precoder
$\mathbf{F}_D$	Analog RF beamformer
$\mathbf{H}, \mathbf{h}$	Channel matrix and vector
$\boldsymbol{\mathcal{H}}$	Effective channel matrix
$\mathbf{n}$	Noise vector
$\mathbf{P}$	Multi-user PA block
$\mathbf{S}, \mathbf{s}$	Transmitted (i.e., precoded) signal matrix and vector
$\mathbf{T}$	Transfer Block
$\mathbf{Z}, \mathbf{z}$	Path gain matrix and vector
Φ, ϕ	Phase response matrix and vector
δ^e, δ^a	Elevation angular, Azimuth angular spread
θ, ϕ	Mean Azimuth AoD, Mean Elevation AoD
λ^z, λ^y	Quantized angle-pairs
σ_n^2	Noise power

ϵ	Normalization scalar for transmit power
η_o	Path loss exponent
γ	Normalization factor in RZF
α	Regularization parameter in RZF
β	Weighting factor in multi-objective optimization problem
q	Low-resolution ADCs/DACs
b	Low-resolution PSs
κ	Hyper-parameter for nature-inspired algorithms
μ	Distortion factor of finite-bit DAC
ζ	Imperfect CSI controlling parameter
$\mathcal{A}$	Angular support
L_i	Number of neurons at i^{th} hidden layer
S_r, S_t	Dataset size
M_u	Number of UAVs
x, y, z	3D location coordinates

List of Notations

Notation	**Description**
Bold upper/lower case letters	denote matrices/vectors.
$\mathbb{C}$ and $\mathbb{R}$	represent the set of complex and real numbers, respectively.
$(\cdot)^*$, $(\cdot)^T$, $(\cdot)^H$, $\\|\cdot\\|_2$, and $\\|\cdot\\|_F$	represent the complex conjugate, the transpose, the conjugate transpose, the 2-norm, and the Frobenius norm, respectively.
$\mathbf{I}_K$, $\mathbb{E}\{\cdot\}$, $\mathrm{tr}(\cdot)$, and $\angle(\cdot)$	stand for $K \times K$ identity matrix, the expectation operator, the trace operator, and the argument of a complex number, respectively.
$\mathbf{X}[m, n]$	denotes the element at the intersection of mth row and nth column.
$\mathbf{X} \otimes \mathbf{Y}$	is the Kronecker product of two matrices $\mathbf{X}$ and $\mathbf{Y}$.
$\mathbf{X} \circ \mathbf{Y}$	is the Hadamard product of two matrices $\mathbf{X}$ and $\mathbf{Y}$.
$\mathrm{Span}(\mathbf{X})$	denotes the space spanned by the columns of $\mathbf{X}$.
$\mathrm{Null}(\mathbf{X})$	denotes the null space of $\mathbf{X}$ with the set of all vectors $\mathbf{y}$ such that $\mathbf{X}\mathbf{y} = \mathbf{0}$.
$\mathrm{diag}(\mathbf{x})$	creates a diagonal matrix with the elements of a given vector $\mathbf{x}$.
$\mathrm{clip}(\mathbf{x}, [a, b]) = \max(a, \min(\mathbf{x}, b))$	denotes a clipping function with $a \leq b$.
$\mathbf{x} \sim \mathcal{CN}(0, \sigma^2)$	denotes a complex Gaussian random variable with zero-mean and variance σ^2.
$\mathbf{x} \sim \mathrm{Ber}(\sigma)$	represents a Bernoulli random variable, which equals $x = 1$ with the probability of $\sigma \in [0, 1]$, otherwise, $x = 0$.

Chapter 1

Introduction

1.1 Overview of 5G and Beyond

Over the years, the evolution of cellular networks from the first generation (1G) to the fifth generation (5G) had a profound impact on different aspects of our life. Particularly, the world has seen a rapid digital transformation in the last few years that has changed the way people communicate, conduct business and search for information. A critical element of this digital transition is wireless connectivity [1, 2]. It is expected that 5G and beyond (B5G) networks will pave the way towards realizing the individuals technological aspirations including holographic telepresence, e-health, pervasive connectivity in smart environments, massive robotics, three dimensional massive unmanned mobility, augmented reality, virtual reality, and internet of everything [3]. In this regard, the following statistics highlight the significant increase in data traffic in the next few years:

- According to the International Telecommunication Union (ITU), the annual data traffic increase between 2020 and 2030 is estimated to be around 55%, which can reach 606 exabytes (EB) per month in 2025 and 5016 EB per month in 2030 as shown in Fig. 1.1 [4].
- It is expected that the number of smart devices will surpass 38.9 billion by 2029 (an increase of 148 % when compared to 15.7 billion devices in 2023) [5, 6].
- As per ITU, the overall mobile data traffic will reach 5 zettabytes (ZB) per month [7].

The explosive increase of mobile data traffic is real, driven primarily due to the increased use of smart phones, tablets, video streaming services as well as machine-to-machine (M2M) connections. Hence, with billions of low-power consumption devices, such as

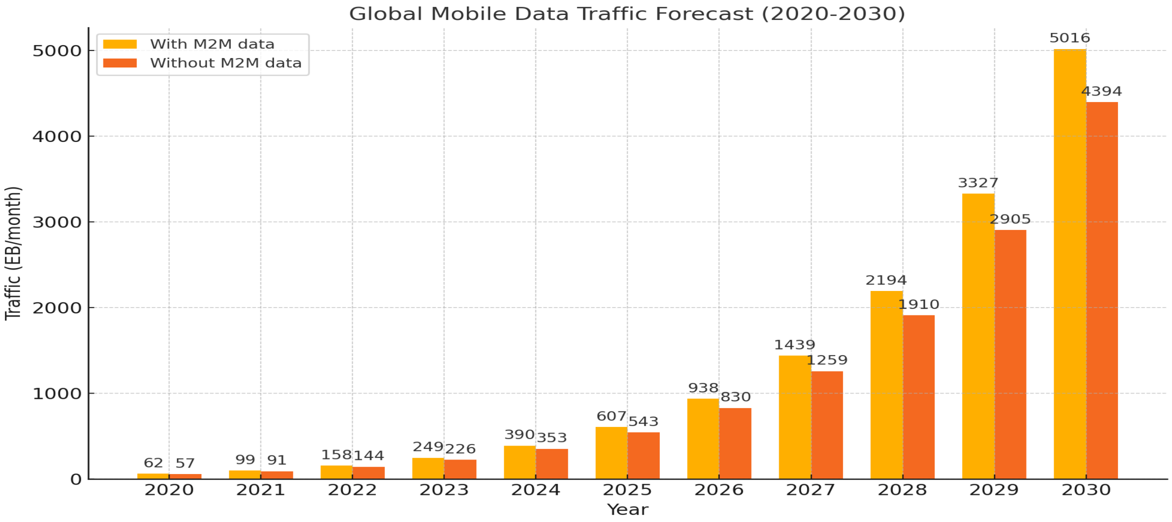

Figure 1.1. Global mobile data traffic forecast by ITU (source Cisco).

wireless sensors, connecting to the internet through the Internet of Things (IoT) framework, there is a significant increase in both energy demand and data traffic. Hence, the need for a new generation of highly scalable cellular networks is inescapable. In particular, this new generation should:

- have a highly scalable and flexible architecture to support various services and applications, such as massive device connectivity in IoT and M2M communications;
- provide larger capacity and improved coverage, while reducing the complexity and cost of ultra dense network deployment;
- be able to make efficient use of different spectrum resources, including both licensed and unlicensed bands as well as high frequency and low frequency bands;
- improve network energy efficiency to adapt to the performance requirements of different applications and services;

To meet the above requirements and to cope with the challenges of ever increasing mobile data traffic as well as demands for much higher data throughput, 5G of cellular networks, also known as 5G new radio or 5G NR, is now becoming a reality. In 2018, the first full set of 5G NR standards were announced by 3rd Generation Partnership Project (3GPP) in release 15 (5G NR phase 1) [8,9], followed by release 16 in 2020, which drove 5G NR phase 2 expansion [10]. Currently, 5G NR networks are being deployed globally, and many 5G-ready smart devices (e.g., cell phones and tablets) are starting to come to market. ITU has defined the following three requirements for 5G NR, each to be fulfilled for one of the three 5G usage scenarios [11].

- peak data rate of 10-20 Gbps (required for the enhanced mobile broadband (eMBB) [12]).
- 1 million connected devices per square kilometer (required for massive machine type communication (mMTC) [4]).
- less than 1 ms latency (required for ultra reliable low latency communications (URLLC) [8, 13]).

The channel capacity is represented by the amount of information bits that can be reliably transmitted to a destination and is given as:

$$\text{Capacity [bps]} = \text{Bandwidth [Hz]} \times \underbrace{\text{Spectral Efficiency [bps/Hz]}}_{\log_2(1+\text{SINR})}, \tag{1.1}$$

which is defined by two factors: (i) operating bandwidth, and (ii) the signal-to-interference-plus-noise ratio (SINR). To fulfill the challenging use cases of future wireless systems for enhanced data rates and coverage, it is essential to consider advanced transmission techniques such as massive multiple-input multiple-output (mMIMO) systems and beamforming. These techniques are particularly effective in improving SINR by focusing signal energy towards the intended receiver and reducing interference. Additionally, exploring new frequency spectrums, such as millimeter-wave (mmWave) communications and sub-terahertz (sub-THz) communications can provide higher bandwidth. The integration of unmanned aerial vehicles (UAVs) as relays can further enhance SINR by providing line-of-sight paths and reducing interference. Moreover, the effective utilization of limited bandwidth resources through techniques like full-duplex (FD) communications can increase capacity by simultaneously transmitting and receiving on the same frequency band, though this also requires sophisticated interference management to maintain a high SINR.

1.2 MIMO to Massive MIMO: A Paradigm Shift in Wireless Technology

Multiple-input multiple-output (MIMO) technology revolutionizes wireless communication by deploying multiple antennas at both the transmitter and receiver ends. This approach significantly enhances capacity and performance by mitigating challenges like path loss and multipath fading that typically degrade wireless signals. Unlike traditional single-antenna systems, MIMO capitalizes on multipath propagation, exploiting the various channel conditions between each antenna pair to provide additional degrees of freedom (DoF). MIMO technology is designed to deliver two key benefits: (i) spatial multiplexing gain, which allows the transmission of parallel data streams without the need for extra bandwidth, thereby boosting spectral efficiency and data rates, and (ii) diversity gain, which leverages distinct channel paths to improve signal quality, reducing errors and enhancing reliability. However, a balance must be struck between these benefits, known as the diversity-multiplexing trade-off. Over the past 15 years, MIMO has become a cornerstone of modern wireless standards, including LTE and WiFi [14–16]. For example, LTE-Advanced supports configurations up to 8x8 MIMO, showcasing its integral role in advancing wireless communication technology [17].

Massive MIMO represents a significant evolution in MIMO technology by addressing the need to serve multiple users simultaneously with enhanced efficiency. Unlike traditional MIMO systems, which primarily focused on point-to-point communication between two devices with multiple antennas, mMIMO is designed for multi-user MIMO scenarios [18]. Here, a base station (BS) equipped with a large array of antennas can simultaneously serve many users, each with a single antenna. This allows for the multiplexing gain to be shared among all users, significantly boosting spectral efficiency and network capacity. The large number of antennas in mMIMO systems also enables the use of simple linear signal processing techniques, to efficiently manage interference and optimize performance across all users, making mMIMO a cornerstone technology for 5G and beyond. The third-generation partnership project (3GPP) has recognized the potential of mMIMO, standardizing deployments of up to 256 antennas at BS in its Release 17 [8].

1.2.1 Benefits

The deployment of large antenna arrays and the capability for 3D beamforming in mMIMO systems offer several key benefits:

- **High Spectral Efficiency:** In multi-user mMIMO (MU-mMIMO) systems, large antenna arrays allow a BS to serve multiple users simultaneously on the same frequency band. Consequently, mMIMO technology enhances both spectral efficiency and overall network capacity.

- **Improved Interference Management:** The narrow beams generated by large antenna arrays in mMIMO systems significantly reduce inter-user interference (IUI). Advanced beamforming techniques not only enhance the desired signal power but also suppress interference power.

- **High Energy Efficiency:** Large antenna arrays in mMIMO systems reduce downlink and uplink transmit powers through advanced beamforming techniques. This enhancement in array gains leads to higher energy efficiency, which is crucial for certain mMTC applications.

- **Scalability:** Massive MIMO systems are highly scalable, making them well-suited for future expansions in wireless networks. This scalability ensures that as the demand for data and connectivity grows, mMIMO systems can be adjusted to meet these increasing needs without substantial changes to the existing infrastructure.

- **Flexibility in Deployment:** The advanced beamforming capabilities of mMIMO systems provide greater flexibility in deployment scenarios. This includes support for both terrestrial and non-terrestrial networks (NTN), making it easier to integrate satellite communications and other emerging technologies.

1.2.2 Challenges

Although mMIMO technology offers substantial benefits, its practical implementation in 5G and beyond wireless networks brings several technical challenges. Key challenges include:

- **High Hardware Costs and Complexity:** One of the most significant obstacles is the high cost and complexity of hardware. Traditional MIMO systems typically rely on fully digital beamforming (FDBF), where each antenna element is associated with its own radio frequency (RF) chain, digital-to-analog converters (DACs) for transmission, analog-to-digital converters (ADCs) for reception, mixers, and other components. In mMIMO systems, the large number of antenna elements dramatically increases hardware costs and power consumption. While substantial beamforming gains can reduce transmit power without compromising spectral efficiency, the high power consumption of these hardware components can significantly impact energy efficiency.

- **Substantial Channel Estimation Overhead:** In mMIMO systems using traditional FDBF techniques, estimating the high-dimensional channel state information (CSI) is crucial for effective beamforming. The increased number of antennas leads to higher channel estimation overhead. Given a fixed coherence time (the period during which the channel remains stable), acquiring extensive CSI requires longer pilot transmission times, which in turn reduces the time available for data transmission. This increased overhead can negatively affect effective spectral efficiency. For example, as the number of antennas approaches infinity, the required pilot transmission length could surpass any finite coherence time, resulting in zero effective spectral efficiency. Therefore, it is essential to develop new beamforming methods that require less CSI overhead for mMIMO systems.

- **High Computational Complexity:** As the size of the antenna array increases, so does the size of the channel matrix. Applying conventional MIMO signal processing algorithms to tasks such as beamforming, channel estimation, and signal detection involves large-scale matrix computations (e.g., matrix inversions, multiplications, singular value decompositions (SVD), and determinants), leading to higher computational complexity.

- **Dynamic and Unpredictable Channel Conditions:** The integration of UAVs introduces highly dynamic and rapidly changing channel conditions due to their mobility and varying altitudes. This makes channel estimation and beamforming in mMIMO systems more challenging, as traditional techniques may not adapt quickly enough to these variations [19].

The advantages of mMIMO technology significantly enhance 5G and future networks, enabling support for emerging services, particularly eMBB and mMTC applications. However, to fully exploit these benefits in both terrestrial and UAV-assisted terrestrial networks, it is vital to address the technical challenges. This necessitates the development of advanced, low-complexity signal processing techniques to reduce hardware costs, complexity, and channel estimation overhead.

Hybrid Beamforming (HBF) has been proposed as a promising solution for mMIMO systems [20]. Unlike the conventional single-stage FDBF, HBF divides the beamforming architecture into two stages: an analog RF stage and a digital baseband (BB) stage, interconnected by a reduced number of RF chains. This HBF architecture helps mitigate the technical challenges of high hardware cost and complexity, large CSI overhead, and increased computational demands. A detailed comparison of beamforming architectures will be presented in Section 2.1.

1.3 UAV-Assisted Terrestrial Communications

With the advent of advanced wireless communications and networking technologies, a new era of innovation has emerged with IoT at its forefront. The potential applications of IoT are vast, ranging from healthcare and urban environments to households [21]. However, deploying IoT effectively and extensively still poses significant challenges, including efficient information transfer between wireless nodes and gateways. To address this issue, various routing schemes have been proposed, including direct transmission or relay structures. Nonetheless, when the distance between the IoT end node and the gateway is substantial, direct transmission may not be feasible or may consume excessive power. In such cases, communication through relay can be a more power-efficient alternative. Moreover, deploying cellular stations in urban areas can be a costly and challenging task, which can further complicate the communications coverage issue in the IoT framework [22]. UAVs, commonly referred to as drones, are viewed as a key component of the next generation of wireless communications networks. UAV as a relay offers several advantages over traditional static relays. Specifically, the ability to deploy on-demand, mobile relaying systems at a relatively low cost and in a timely manner, makes them particularly well-suited for unforeseen or short-term events, such as emergency situations or network offloading [23]. Furthermore, the high mobility of UAVs allows for the dynamic adjustment of their locations to optimize communications conditions, a technique particularly promising for delay-tolerant applications, such as periodic sensing and the transfer of large data [24–26]. UAVs' capability to reach inaccessible locations makes them a viable option for future IoT applications, as they can fly close to IoT devices, sequentially collect sensing data, address coverage issues, and reduce IoT communications networks' overhead [19].

The incorporation of UAVs as relay nodes in wireless sensor networks (WSNs) has the potential to augment communications capacity by connecting remote sensor gateways and addressing the escalating data-rate demands in applications such as virtual reality, device-to-device communications, and smart cities. UAVs can be deployed at high altitudes to increase the likelihood of line-of-sight (LoS) dominated air-to-ground communications channels, thereby supporting high-rate communications. However, the severely congested sub-6 GHz bands can be inadequate to meet the rising data rate requirements. In contrast, millimeter-wave (mmWave) communications, with their abundant spectrum resources, can potentially support the high-throughput and low-latency requirements of various UAV application scenarios [27]. Nonetheless, mmWave signals suffer from high propagation loss, including free-space path loss, atmospheric and molecular absorption, and rain attenuation. This challenge can be surmounted by leveraging mMIMO technology with large array structures to generate high beam gains in UAV-assisted terrestrial systems, which can improve the transmission range and simultaneously suppress interference among IoT nodes by utilizing the advanced capabilities of three-dimensional (3D) beamforming.

1.4 Thesis Contributions and Organization

Massive MIMO refers to utilizing a large number of antennas at BS for improving data rates through spatial multiplexing in single-user mMIMO (SU-mMIMO) and multi-user mMIMO (MU-mMIMO) operation modes. By concentrating signal energy into smaller regions through substantial beamforming gains, mMIMO ensures remarkable advancements in transmission quality in both uplink and downlink directions. The existing studies in mMIMO systems focus on the use of one-dimensional array (i.e., uniform linear array (ULA)), which has been a common array configuration in literature. However, it can not accommodate a very large number of antenna elements, which is important to support a large number of users. Moreover, it creates two important issues: (i) spatial inefficiency, and (ii) restriction to illuminate both azimuth and elevation angles at the same time. Additionally, despite effective precoding/combining solutions, the performance in mMIMO systems can significantly vary due to the following: (i) UE/device angular location, and (ii) UE/device distance from the BS (e.g., users obscured due to buildings, mountains., etc.). Therefore, the antenna configuration can play an important role in serving a large number of users (both ground and aerial) for future IoT applications. In this regard, ITU's IMT-2030 (6G) framework focus on *enhanced capabilities* (refers to the key performance indicators of peak data rate, latency, connection density, mobility, and reliability) as well as *new capabilities* (refers to key parameters of ubiquitous coverage, sensing, sustainability, resilience, and positioning). Thus, to enable these new capabilities, future wireless networks are expected to adopt an integrated terrestrial and NTN architecture. This thesis targets a set of objectives, including 2D/3D array configurations, beamforming optimization, interference suppression, sum-rate maximization, improved energy efficiency, high self-interference suppression (SIS) quality, low channel estimation overhead, and UAV deployment to enhance both coverage and capacity in terrestrials and UAV-assisted terrestrial networks. The remainder of this thesis is organized as follows.

Chapter 2 presents an overview of the beamforming architectures and MU-mMIMO system model. Then, we present a literature review of different relaying schemes in wireless networks. Afterwards, we review different SIS techniques used in FD communications. Finally, we discuss how artificial intelligence (AI) and machine learning (ML) can help solve non-convex optimization problems in wireless communications with less complexity and more reliability.

Chapter 3 investigates different 2D array configurations to be used at BS for enhanced capacity in mMIMO systems. We design three HBF architectures: (i) HBF using full-resolution PSs and DACs, with a baseband transfer block for constant-modulus RF beamformer, (ii) HBF using b-bit PSs and full-resolution DACs, with an orthogonal matching pursuit (OMP) based algorithm that can approach the optimal unconstrained RF beamformer, and (iii) HBF using b-bit PSs and q-bit DACs, taking into account also DAC quantization noise. The proposed HBF schemes not only reduce the hardware cost/complexity by utilizing a limited number of RF chains but also lower the CSI overhead size by designing RF-stage via slow time-varying CSI (i.e., angular information). Therefore, the reduced-size effective CSI is utilized during the BB-stage design. We compare the spatial, spectral and energy efficiencies of HBF designs for different antenna-arrays. In the illustrative results, we show that the proposed HBF schemes achieve higher sum-rate and energy efficiency than other HBF benchmarks.

Chapter 4 compares the performance of various 3D array structures in the design of HBF for mmWave MU mMIMO systems. The proposed HBF scheme involves two stages: (i) RF beamforming based on SVD of the channel matrix, and baseband MU precoding based on the instantaneous effective baseband channel to mitigate MU-interference by a regularized zero-forcing (RZF) technique. The illustrative results show that, in comparison to 2D arrays, 3D array structures can provide high spectral and energy efficiencies as well as non-varying achievable rate independent from the user angular location. Thus, 3D structures can be useful in supporting both terrestrial and non-terrestrial communications.

In Chapter 5, we propose different novel full-duplex hybrid beamforming (FD-HBF) techniques to enhance the overall capacity in mMIMO systems based on over-the-air (OTA) measurements of the SI channel. Our objective is to leverage the spatial DoF in mMIMO systems to enhance FD capacity without the need for expensive analog SI-cancellation circuitry. For a single uplink, single downlink user setup, we develop both constant modulus (CM) and non-constant modulus (NCM) RF-stages via slow time-varying angular information in order to maximize the intended signal power and suppress the strong SI power. Particularly, both CM and NCM RF-stages are constructed for the following schemes: (i) maximizing the directivity towards the intended direction and suppressing the strong SI power via orthogonal beams, (ii) introducing beam perturbations within an allowed directivity degradation to minimize SI power, and (iii) selecting best Tx/Rx sub-array indices jointly with beam perturbation for enhanced SI suppression. Afterwards, the BB-stages are built via the reduced-size effective intended channel. The illustrative results show that FD-HBF significantly suppresses the strong SI power by achieving upto 80 dB SI suppression capability, which remarkably improves the achievable rate capacity and approximately doubles it compared to its HD counterpart.

Chapter 6 introduces a UAV-assisted terrestrial system to enhance both coverage and capacity in SU-mMIMO and MU-mMIMO systems. Due to the limited coverage and fixed deployment of terrestrial networks, the integration of UAVs offer key advantages of rapid deployment especially in emergency situations. Therefore, we consider the UAVs as relaying structures to extend the coverage area of BS. We consider UAV as amplify-and-forward (AF) relay as well as decode-and-forward (DF) relay in both SU-mMIMO and MU-mMIMO systems, where the overall capacity is maximized by optimizing the UAV placement within a deployment area, power allocation (PA) to users jointly with angular-based HBF solutions for both BS and UAV. We introduce two AI/ML-based algorithms for the joint UAV deployment and PA. First, we develop a particle swarm optimization based joint UAV location and PA (PSOLPA) algorithm, which attains almost the optimal sum-rate capacity at the expense of longer runtime for the larger number of users. Second, we introduce a novel deep learning based UAV location and PA (DLLPA) algorithm for faster and more robust prediction of UAV deployment and PA. The proposed DLLPA algorithm has two phases: (i) offline supervised learning via the allocated powers and UAV optimal values calculated by PSOLPA, and (ii) online power and UAV location prediction via the trained deep neural network (DNN). The illustrative results depict that DLLPA closely approaches the optimal sum-rate capacity with remarkably reduced runtime.

Chapter 7 studies the multiple UAVs-assisted terrestrial networks to support a large number of users, enhancing both coverage and capacity, while the proposed HBF techniques in Chapter 6 follows the use of single UAV. We consider multiple UAVs operating as DF relays, which connect the BS to a large number of IoT devices. We utilize structured sequential optimization to address the multi-faceted optimization problem by splitting it into two sub-problems. First,K-means-based user clustering is used for

UAV-users association. Then, the location of each UAV is optimized jointly with PA using swarm intelligence. The RF stages are designed based on the slow time-varying angular information, while BB stages are designed utilizing the reduced-dimension effective channel matrices. Illustrative results show that multiple UAV-assisted cooperative relaying systems outperform a single UAV system in practical user distributions.

Finally, Chapter 8 provides the concluding remarks, summarizes the key findings of this thesis, and discusses the possible future research directions.

Chapter 2

Background

This chapter provides an overview of the beamforming architectures for the mMIMO systems including DBF, ABF, and HBF. We present MU-mMIMO system model. Then, we review the SI suppression (SIS) techniques in FD communications and emphasize the advantages of using DoF provided by large mMIMO array structures to generate narrow beams to enhance the SIS quality. Later on, we discuss different relaying schemes used in UAV-assisted terrestrial communications. Finally, we discuss the AI/ML applications in wireless communications to develop low-complexity and robust solutions for non-convex optimization problems.

2.1 Beamforming Architectures in mMIMO Systems

Beamforming is a fundamental technique in massive MIMO (mMIMO) systems, enhancing communication performance by directing signal energy toward desired directions. This targeted focus is achieved through the use of large antenna arrays that adjust the phase and amplitude of signals. By optimizing the beamforming weights, mMIMO systems can achieve high signal-to-interference-plus-noise ratio (SINR), which is crucial for reliable communication. As the number of antennas increases, the SINR also increases, which is referred to as beamforming gain [28]. This gain allows mMIMO systems to direct the signal energy towards desired regions, reducing interference and improving signal quality. The high beamforming gain in mMIMO systems is particularly effective in overcoming the significant path loss experienced in mmWave communications. Moreover, the spacing between antenna elements also plays a critical role in beamforming performance. Typically, antenna separation is maintained at half the wavelength of the carrier frequency to avoid grating lobes and ensure optimal spatial resolution. This spacing

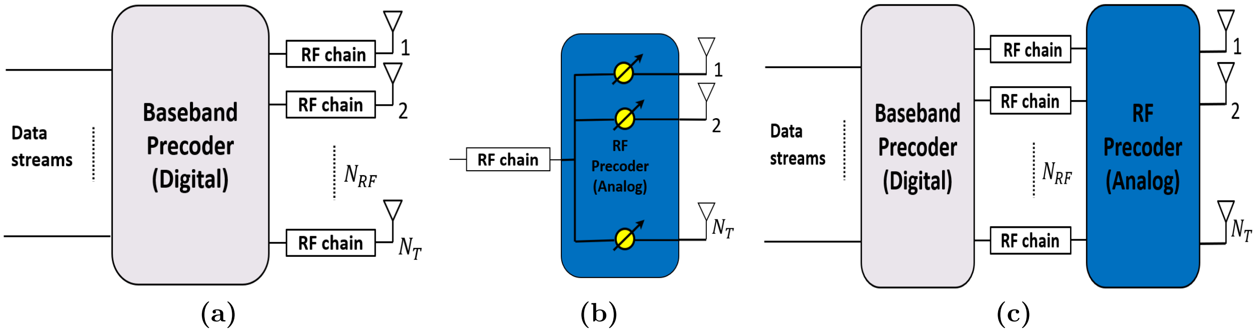

Figure 2.1. Beamforming architectures for the mMIMO systems. (a) FDBF (b) ABF (c) HBF.

is crucial, as it impacts the overall beam pattern, sidelobe levels, and beamforming gain. As shown in Fig. 2.1, the three main architectures for beamforming in mMIMO systems are:

- Single-stage fully digital beamforming (FDBF)
- Single-stage fully analog beamforming (ABF)
- Two-stage hybrid beamforming (HBF)

These architectures have different advantages and limitations. Understanding the strengths and weaknesses of each can help in selecting the appropriate beamforming strategy for specific applications. A brief summary of the advantages and limitation of each beamforming solution is presented in Table 2.1.

2.1.1 Fully Digital Beamforming

In traditional MIMO systems, typically featuring a limited number of antennas, a single-stage FDBF architecture is commonly employed. This approach performs beamforming directly at the baseband level using digital signal processing techniques [29–31]. FDBF offers significant flexibility and a high degree of freedom (DoF), making it possible to implement efficient beamforming algorithms. As illustrated in Fig. 2.1(a), the FDBF architecture supports S data streams using N_T antennas, where $S \leq N_T$. The digital baseband stage for downlink or the digital baseband combiner for uplink is represented by the matrix $\mathbf{B}_{\text{FDBF}} \in \mathbb{C}^{N_T \times S}$. This matrix contains the beamforming weights, which can be adjusted in both magnitude and phase using digital processing techniques. FDBF facilitates the transmission

Table 2.1. Advantages and Limitations of Beamforming Techniques in mMIMO Systems

Aspect	**FDBF**	**ABF**	**HBF**
Advantages	Offers precise control of amplitude and phase per antenna, enabling optimal beamforming and high spectral efficiency	Low-cost and power-efficient as it uses a single RF chain with phase shifters (PSs), making it suitable for large arrays	Balances power consumption and performance; enables multi-stream transmission with fewer RF chains than FDBF
Limitations	High hardware cost and power consumption due to one RF chain per antenna element	Limited flexibility; only controls phase, so performance is lower in multi-user scenarios	Increased complexity compared to ABF; requires optimization of both RF and baseband stages

of multiple data streams simultaneously by effectively mitigating interference, such as inter-symbol interference (ISI) in single-user MIMO (SU-mMIMO) and inter-user interference (IUI) in multi-user MIMO (MU-mMIMO). However, each antenna element in the FDBF architecture requires its own dedicated RF chain, which is both power-intensive and costly. Consequently, in a system with N_T antennas, there are N_T RF chains, leading to significantly increased hardware costs and power consumption as MIMO systems evolve into mMIMO with larger antenna arrays. For example, 3GPP Release 17 specifies the use of 64-256 antennas at BS, making it impractical and costly to deploy 64-256 RF chains using the FDBF approach [32].

Furthermore, as the number of antennas increases, so does the computational complexity associated with beamforming optimization, due to the expanding matrix dimensions of $\mathbf{B}_{\mathrm{FDBF}} \in \mathbb{C}^{N_T \times S}$. Although FDBF can achieve optimal spectral efficiency in mMIMO systems, exploring alternative beamforming architectures is essential to reduce hardware and computational complexity while maintaining near-optimal spectral efficiency. To address the challenges posed by FDBF in mMIMO systems, alternative architectures have been developed. As mMIMO technology continues to advance, these new beamforming architectures will be crucial for enabling scalable and efficient communication systems.

2.1.2 Fully Analog Beamforming

Fig. 2.1(b) depicts the ABF architecture, where a single RF chain supports N_T antennas [33]. In this setup, N_T low-cost PSs connect the RF chain to the antennas. These PSs consume significantly less power compared to RF chains, typically around 1 mW per PS versus 250 mW per RF chain. This substantial reduction in power consumption and hardware costs makes ABF particularly beneficial for mMIMO systems. The use of a single RF chain in the ABF architecture remains constant regardless of the number of antennas, significantly reducing hardware complexity and costs. The analog RF beamforming vector is represented as $\mathbf{f}_{\mathrm{ABF}} \in \mathbb{C}^{N_T}$. Compared to the digital baseband beamforming matrix $\mathbf{B}_{\mathrm{FDBF}} \in \mathbb{C}^{N_T \times S}$, which has $N_T \times S$ elements, $\mathbf{f}_{\mathrm{ABF}}$ with N_T elements exhibits much lower computational complexity [34].

Despite its advantages, the ABF architecture has some significant limitations. The analog RF beamforming vector $\mathbf{f}_{\mathrm{ABF}}$ typically only applies phase shifts to the transmitted and received signals, adhering to the constant-modulus (CM) constraint. This limitation complicates beamforming optimization and reduces the DoF compared to FDBF, which can adjust both the magnitude and phase of signals. As a result, the ABF architecture generally experiences performance degradation compared to FDBF. Moreover, ABF supports only a single data stream, while FDBF, as shown in Fig. 2.1(a), can handle multiple data streams. This limitation reduces spectral efficiency, which is one of the key benefits of mMIMO systems.

Thus, there is a trade-off between digital and analog beamforming architectures. FDBF offers higher spectral efficiency by supporting multiple data streams and providing greater flexibility in signal processing. On the other hand, ABF improves hardware and computational efficiency by reducing power consumption and complexity. The choice between these architectures depends on the specific requirements and constraints of the application, balancing the need for high spectral efficiency with the practical considerations of hardware and power costs.

2.1.3 Hybrid Beamforming

The two-stage HBF architecture has emerged as a promising solution for mMIMO systems, effectively addressing the trade-offs between single-stage FDBF and ABF architectures [20, 35]. As illustrated in Fig. 2.1(c), HBF divides the beamforming process into two stages: an analog transmit (or receive) RF beamformer $\mathbf{F}_{\mathrm{HBF}} \in \mathbb{C}^{N_T \times N_{\mathrm{RF}}}$ and a digital baseband (BB) precoder (or combiner) $\mathbf{B}_{\mathrm{HBF}} \in \mathbb{C}^{N_{\mathrm{RF}} \times S}$ for transmission (or reception). This two-stage approach leverages a reduced number of RF chains, N_{RF}, where $S \leq N_{\mathrm{RF}} \leq N_T$, to minimize hardware cost and complexity in mMIMO systems with large antenna arrays. Additionally, the HBF architecture supports multiple data streams, making it a versatile solution.

In the RF stage, each RF chain connects to every antenna element through PSs, constructing the analog RF beamformer $\mathbf{F}_{\mathrm{HBF}} \in \mathbb{C}^{N_T \times N_{\mathrm{RF}}}$ with $N_T \times N_{\mathrm{RF}}$ PSs. Subsequently, the digital BB precoder/combiner $\mathbf{B}_{\mathrm{HBF}} \in \mathbb{C}^{N_{\mathrm{RF}} \times S}$ is designed in the BB

Table 2.2. Comparison of Fully Digital, Analog, and Hybrid Beamforming in Massive MIMO Systems

Aspect	**DBF**	**ABF**	**HBF**
Hardware Complexity	High: One RF chain per antenna	Low: Single RF chain, phase shifters	Medium: Few RF chains, phase shifters
Power Consumption	High	Low	Medium
Computational Complexity	High	Low	Medium
Flexibility	High: Change magnitude and phase	Low: Change phase only	Medium: Combines DBF and ABF
Spectral Efficiency	High: Optimal	Low: Limited by single stream	High: Near-optimal, multiple streams
Cost	High	Low	Medium
Implementation Feasibility	Difficult for large arrays	Easy, cost-effective	Feasible with trade-offs
CSI Overhead	High	Medium: Slow time varying CSI	Medium: Effective CSI

stage. By employing a reduced number of RF chains, the two-stage HBF architecture significantly cuts down on hardware costs and power consumption. Moreover, HBF techniques optimize both RF and BB stages to enhance system capacity. Numerical studies indicate that HBF can closely match the spectral efficiency of FDBF while significantly outperforming ABF. Thus, HBF achieves high spectral, energy, and hardware efficiency for mMIMO systems, offering more DoF for low-complexity HBF techniques.

Most existing research on FDBF and HBF architectures assumes the availability of full-size instantaneous CSI [36–42]. However, as antenna arrays scale up, the channel dimension and pilot transmission length increase, resulting in substantial channel estimation overhead. The HBF architecture can mitigate this overhead by developing the RF stage using slow time-varying CSI (e.g., channel covariance matrix or angular information), and subsequently designing the BB stage with reduced-size effective instantaneous CSI. This capability further enhances the practicality of HBF by reducing the channel estimation overhead. HBF architectures are categorized into fully-connected (FC) and sub-connected (SC) configurations. In FC HBF architecture, each RF chain connects to all antenna elements, which necessitates $N_T \times N_{\mathrm{RF}}$ PSs. Conversely, SC HBF architecture reduces the number of PSs to N_T by connecting each RF chain to a subset of antennas. In this thesis, we focus on both FC and SC HBF techniques for mMIMO systems. Table 2.2 provides the comparison between ABF, FDBF, and HBF, which shows advanced HBF techniques can achieve high spectral efficiency with low hardware cost/complexity, low CSI overhead size for practical mMIMO systems.

2.2 Multi-User Massive MIMO Communications

One of the key features of mMIMO is to support multi-user communications (i.e., MU-mMIMO), where multiple single-antenna users ($K \leq N_T$) are served simultaneously by employing advanced beamforming techniques. Both downlink and uplink transmissions in MU-mMIMO systems are facilitated by designing appropriate beamforming techniques to enhance the overall sum-rate capacity. The primary goals of beamformer design in MU-mMIMO systems are to maximize the desired signal for each user while effectively mitigating multi-user interference (MUI). MU-mMIMO systems offer significant advantages over SU-mMIMO systems. Firstly, the channel conditions improve due to the spatial diversity provided by users positioned at different locations, leading to a higher channel rank. Secondly, MU-mMIMO systems serve users with fewer antennas, which is more practical for wireless communication systems constrained by hardware limitations and cost considerations.

In the downlink transmission of the FDBF architecture, depicted in Fig. 2.1(a), the signal transmitted from the BS after precoding is represented as $\mathbf{s}_D = \mathbf{B}_D \mathbf{d}_D \in \mathbb{C}^{N_T}$. Here, $\mathbf{B}_D = [\mathbf{b}_{D,1}, \mathbf{b}_{D,2}, \ldots, \mathbf{b}_{D,K}] \in \mathbb{C}^{N_T \times K}$ denotes the digital baseband beamforming matrix, and $\mathbf{d}_D = [d_{D,1}, d_{D,2}, \ldots, d_{D,K}]^T \in \mathbb{C}^K$ is the vector containing the downlink data signals. The received signal at the user side is then expressed as:

$$\mathbf{r}_D = \mathbf{H}_D \mathbf{s}_D + \mathbf{n}_D = \mathbf{H}_D \mathbf{B}_D \mathbf{d}_D + \mathbf{n}_D = \begin{bmatrix} r_{D,1} \\ r_{D,2} \\ \vdots \\ r_{D,K} \end{bmatrix} = \begin{bmatrix} \mathbf{h}_{D,1}^T \mathbf{B}_D \mathbf{d}_D \\ \mathbf{h}_{D,2}^T \mathbf{B}_D \mathbf{d}_D \\ \vdots \\ \mathbf{h}_{D,K}^T \mathbf{B}_D \mathbf{d}_D \end{bmatrix} + \mathbf{n}_D, \tag{2.1}$$

where $\mathbf{H}_D = [\mathbf{h}_{D,1}, \mathbf{h}_{D,2}, \ldots, \mathbf{h}_{D,K}]^T \in \mathbb{C}^{K \times N_T}$ represents the downlink channel matrix, $\mathbf{h}_{D,k} \in \mathbb{C}^M$ corresponds to the channel vector for the k^{th} user, and $\mathbf{n}_D \sim \mathcal{CN}(0, \sigma_n^2 \mathbf{I}_K)$ is the complex Gaussian noise vector. The primary goal of the digital baseband beamforming stage $\mathbf{B}_D$ is to mitigate multi-user interference (MUI) while maximizing the desired signal power. Common linear beamforming methods for designing the digital BB precoder include: (i) matched filter (MF), (ii) zero-forcing (ZF), and (iii) regularized zero-forcing (RZF). The general form of the digital BB precoder is given by:

$$\mathbf{B}_D = \alpha_D \mathbf{X}_D^{-1} \mathbf{H}_D^H \in \mathbb{C}^{N_T \times K}, \tag{2.2}$$

where α_D is a normalization factor ensuring that the transmit power constraint P_T is met, and $\mathbf{X}_D \in \mathbb{C}^{N_T \times N_T}$ varies based on the technique: $\mathbf{X}_D = \mathbf{I}_{N_T}$ for MF, $\mathbf{X}_D = \mathbf{H}_D^H \mathbf{H}_D$ for ZF, and $\mathbf{X}_D = \mathbf{H}_D^H \mathbf{H}_D + \frac{\sigma_n^2}{P_T/K} \mathbf{I}_{N_T}$ for RZF. Similarly, in uplink MU-mMIMO systems, the digital BB combiner $\mathbf{B}_U = [\mathbf{b}_{U,1}, \mathbf{b}_{U,2}, \ldots, \mathbf{b}_{U,K}] \in \mathbb{C}^{K \times N_T}$ is used to combine the signals received at the BS:

$$\tilde{\mathbf{r}}_U = \mathbf{B}_U(\mathbf{H}_U \mathbf{d}_U + \mathbf{n}_U) = \mathbf{B}_U \mathbf{H}_U \mathbf{d}_U + \mathbf{B}_U \mathbf{n}_U = \begin{bmatrix} r_{U,1} \\ r_{U,2} \\ \vdots \\ r_{U,K} \end{bmatrix}, \tag{2.3}$$

where $\mathbf{H}_U \in \mathbb{C}^{N_T \times K}$ is the uplink channel matrix, and $\mathbf{n}_U \sim \mathcal{CN}(0, \sigma_n^2 \mathbf{I}_M)$ is the noise vector. The digital BB combiner's general form is expressed as:

$$\mathbf{B}_U = \mathbf{H}_U^H \mathbf{X}_U^{-1} \in \mathbb{C}^{K \times N_T}, \tag{2.4}$$

where $\mathbf{X}_U = \mathbf{I}_{N_T}$ for MF, $\mathbf{X}_U = \mathbf{H}_U^H \mathbf{H}_U$ for ZF, and $\mathbf{X}_U = \mathbf{H}_U^H \mathbf{H}_U + \frac{\sigma_n^2}{P_U} \mathbf{I}_{N_T}$ for RZF, with P_U being the uplink transmit power. Beyond the conventional single-stage FDBF techniques, the two-stage HBF architecture discussed in Section 2.1.3 can also be utilized in MU-mMIMO systems to enhance spectral efficiency while reducing hardware complexity.

2.3 Self-Interference Suppression (SIS) Techniques for Full-Duplex Communications

Full-duplex (FD) communication systems have the potential to double system capacity by enabling simultaneous transmission and reception on the same frequency bands, thus utilizing time and frequency resources more effectively compared to conventional half-duplex (HD) systems like TDD and FDD. This characteristic makes FD communications especially promising for mMIMO systems. However, FD operation introduces significant self-interference (SI) between co-located transmit and receive antennas, necessitating sophisticated self-interference suppression (SIS) techniques. To maintain performance in FD communications, the strong SI must be reduced to or below the noise floor. For instance, with a noise power spectral density (PSD) of -174 dBm/Hz and a transmission bandwidth of 20 MHz, the noise power is calculated as:

$$\sigma_n^2 = -174 + 10 \log_{10}(20 \times 10^6) \approx -101 \text{ dBm}. \tag{2.5}$$

To facilitate simultaneous downlink and uplink transmission, an FD mMIMO system

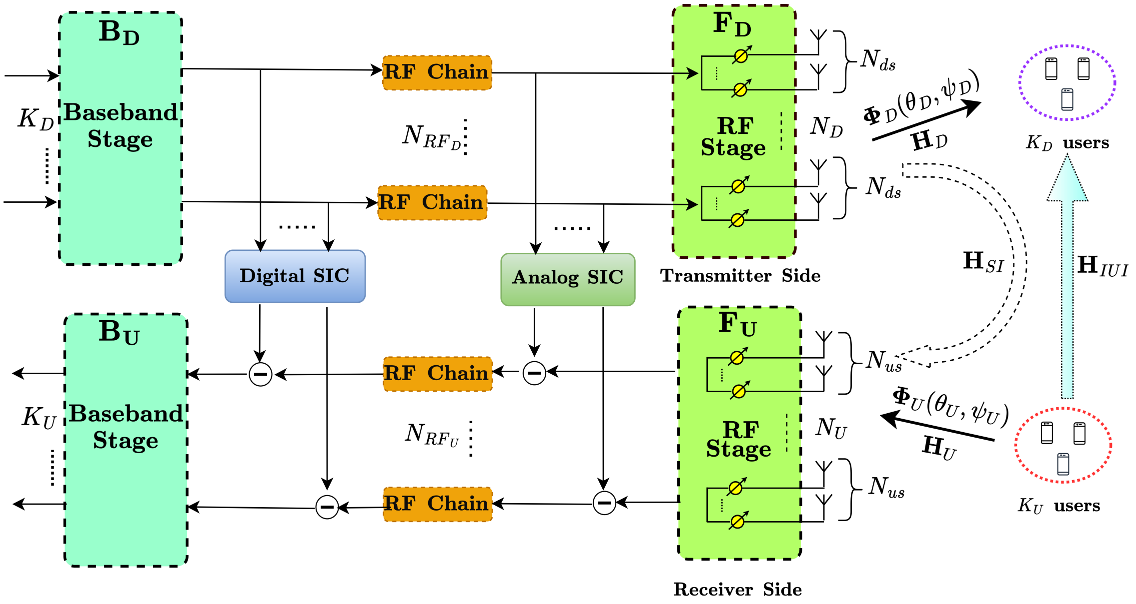

Figure 2.2. Full-duplex mMIMO systems featuring several SIS stages: antenna isolation, analog/digital SIS, RF and BB beamforming stages.

involves five SIS stages: (i) antenna isolation, (ii) analog transmit/receive RF beamforming, (iii) analog SIS, (iv) digital SIS, and (v) digital baseband (BB) precoding/combining. Each stage contributes differently to the overall cancellation/suppression quality. Given a transmit power P_T of 30 dBm, the required SIS must reduce the SI to below -101 dBm, leading to a required SIS of:

$$\text{Required SIS} = P_T - \sigma_n^2 = 30\text{ dBm} - (-101\text{ dBm}) = 131\text{ dB}. \tag{2.6}$$

Achieving such a high level of SIS is challenging, particularly as P_T and the number of antennas increase. Note that an FD mMIMO system might involve various SIS stages to reach the desired SIS quality, as illustrated in Fig. 2.2. Some SIS stages might be omitted due to complexity or inadequate SIS performance. Extensive research has been conducted to enhance SIS quality and maximize the benefits of FD technology [43–45]. One approach involves separating the transmit and receive antenna elements in the passive propagation domain cancellation technique, allowing the signal to be attenuated in the propagation domain before reaching the receive circuitry [46–48]. The goal of passive antenna isolation is to maximize separation between the transmit and receive RF chains. Practical implementations demonstrate SIS levels between 60 and 70 dB based on antenna isolation [49]. Following antenna isolation, the RF stage includes both analog transmit/receive RF beamforming and analog SIC. With large antenna arrays and high beamforming gain in mMIMO systems, the transmit and receive RF beamformers can generate narrow beams for the intended downlink and uplink channels, while keeping them nearly orthogonal to the SI channel [50, 51]. Given the SI channel matrix $\mathbf{H}_{SI} \in \mathbb{C}^{M_U \times M_D}$, the transmit RF beamformer $\mathbf{F}_D \in \mathbb{C}^{M_D \times N_{RF,D}}$ and the receive RF beamformer $\mathbf{F}_U \in \mathbb{C}^{N_{RF,U} \times M_U}$ aim to satisfy:

$$\mathbf{F}_U \mathbf{H}_{SI} \mathbf{F}_D \approx \mathbf{0}, \tag{2.7}$$

which requires joint optimization of $\mathbf{F}_D$ and $\mathbf{F}_U$. The analog SIC stage then generates an accurate replica of the SI signal based on the transmitted signal and estimated SI channel parameters (e.g., delay, attenuation). This replica is subtracted from the received SI signal. However, estimating SI channel parameters becomes more complex with larger array sizes, potentially impacting analog SIC performance. Conversely, larger antenna arrays provide more degrees of freedom for transmit/receive RF beamformers, improving SIS quality and potentially negating the need for analog SIC. Combining antenna isolation, transmit/receive RF beamforming, and analog SIS techniques is critical to prevent overload and saturation in the receive RF chain and ADCs due to high SI power. These methods are vital for advancing SIS in the BB stage and establishing FD communications.

The digital SIC and digital BB precoder/combiner functions at the BB stage. Like analog SIC, digital SIC aims to eliminate the residual SI signal in the digital domain. Digital cancellation techniques, being simpler forms of active cancellation, achieve limited SIS due to hardware imperfections such as transceiver phase noise and non-linearities that restrict the effectiveness of traditional digital cancellation methods [52]. The digital BB precoder $\mathbf{B}_D \in \mathbb{C}^{N_{RF,D} \times K_D}$ and the digital BB combiner $\mathbf{B}_U \in \mathbb{C}^{K_U \times N_{RF,U}}$ further enhance SIS by satisfying:

$$\mathbf{B}_U \mathbf{F}_U \mathbf{H}_{SI} \mathbf{F}_D \mathbf{B}_D \approx \mathbf{0}. \tag{2.8}$$

The objective is to develop innovative HBF techniques to improve SIS quality and reduce SI power below the noise floor. Thus, the proposed HBF techniques for FD mMIMO systems involve the integrated design of four components: (i) analog transmit RF beamformer, (ii) analog receive RF beamformer, (iii) digital BB precoder, (iv) digital BB combiner.

2.4 Massive MIMO Relaying

Relaying techniques in MIMO communications, particularly in the context of HBF, play a vital role in enhancing coverage, reliability, and overall system performance. As discussed earlier, HBF combines the benefits of both analog and digital beamforming, making it an efficient choice for mMIMO systems. This section explores the two primary relaying strategies, amplify-and-forward (AF) and decode-and-forward (DF), in the context of HBF [53–56].

2.4.1 Amplify-and-Forward (AF) Relaying

In AF relaying, the relay node amplifies the received signal and forwards it to the destination. Considering a HBF architecture, the relay utilizes both analog and digital beamforming stages to process the signal efficiently. For a mMIMO communication system with N_T antennas at the transmitter, N_R antennas at the relay, and N_D antennas at the destination, then the received signal at the relay is expressed as:

$$\mathbf{y}_R = \mathbf{H}_{SR}\mathbf{x}_S + \mathbf{n}_R, \tag{2.9}$$

where $\mathbf{H}_{SR} \in \mathbb{C}^{N_R \times N_T}$ is the channel matrix between the source and the relay, $\mathbf{x}_S \in \mathbb{C}^{N_T \times 1}$ is the transmitted signal from the source, and $\mathbf{n}_R \in \mathbb{C}^{N_R \times 1}$ is the noise vector at the relay. Considering a HBF architecture at relay, the received signal is amplified and forwarded to the destination. Then, the signal transmitted from the relay is given by:

$$\mathbf{x}_R = \mathbf{F}\mathbf{B}\mathbf{y}_R, \tag{2.10}$$

where $\mathbf{F} \in \mathbb{C}^{N_R \times N_{RF}}$ is the analog beamforming matrix, and $\mathbf{B} \in \mathbb{C}^{N_{RF} \times N_T}$ is the digital beamforming matrix. The received signal at the destination is:

$$\mathbf{y}_D = \mathbf{H}_{RD}\mathbf{x}_R + \mathbf{n}_D = \mathbf{H}_{RD}\mathbf{F}\mathbf{B}\mathbf{y}_R + \mathbf{n}_D. \tag{2.11}$$

Substituting $\mathbf{y}_R$ into the above equation, we get:

$$\mathbf{y}_D = \mathbf{H}_{RD}\mathbf{F}_{RF}\mathbf{F}_{BB}(\mathbf{H}_{SR}\mathbf{x}_S + \mathbf{n}_R) + \mathbf{n}_D. \tag{2.12}$$

The design of hybrid beamforming stages $\mathbf{F}$ and $\mathbf{B}$ is crucial to balance the trade-off between signal amplification and noise control. The design of HBF matrices can maximize the received

Table 2.3. Comparison of relaying protocols in mMIMO systems.

Criterion	**AF Relaying**	**DF Relaying**
Complexity	Moderate	High
Noise Amplification	Yes	No
Processing Delay	Low	High
Implementation	Moderate	Complex
Reliability	Moderate	High

signal power while minimizing the amplified noise.

2.4.2 Decode-and-Forward (DF) Relaying

In DF relaying, the relay decodes the received signal, re-encodes it, and then forwards it to the destination. The HBF technique can be used at both the relay and the destination to process the signal efficiently. The received signal at the relay in DF relaying is the same as in AF relaying:

$$\mathbf{y}_R = \mathbf{H}_{SR}\mathbf{x}_S + \mathbf{n}_R. \tag{2.13}$$

The relay decodes the received signal to obtain $\hat{\mathbf{x}}_S$, which is an estimate of the transmitted signal $\mathbf{x}_S$. The relay then re-encodes and forwards $\hat{\mathbf{x}}_S$ to the destination using HBF architecture. The transmitted signal from the relay is:

$$\mathbf{x}_R = \mathbf{F}_{RF}\mathbf{F}_{BB}\hat{\mathbf{x}}_S. \tag{2.14}$$

Then, the received signal at the destination is:

$$\mathbf{y}_D = \mathbf{H}_{RD}\mathbf{x}_R + \mathbf{n}_D = \mathbf{H}_{RD}\mathbf{F}_{RF}\mathbf{F}_{BB}\hat{\mathbf{x}}_S + \mathbf{n}_D. \tag{2.15}$$

In practical scenarios, decoding errors at the relay can degrade performance. The joint design of HBF stages at BS, relay, and at destination can maximize the sum-rate capacity by improving SINR.

The choice between AF and DF relaying depends on the specific requirements of the communication system. AF relaying with HBF is simpler and introduces less delay but can amplify noise. DF relaying with HBF provides better performance in terms of noise mitigation but requires more complex processing and introduces decoding delays. A brief comparison of DF versus AF relaying scheme is presented in Table 2.3.

2.5 AI/ML Applications in Wireless Communications

In recent years, the application of artificial intelligence (AI) in wireless communications has garnered significant attention due to its ability to develop low-complexity and robust solutions for non-convex optimization problems. Various terms are used in the literature to refer to AI as it encompasses different branches, including nature-inspired (NI) intelligent algorithms, supervised/unsupervised machine learning (ML), and deep learning (DL). This section briefly introduces NI and DL, followed by a discussion of their potential applications in wireless communications.

2.5.1 NI Intelligent Algorithms

NI algorithms have gained popularity due to their effectiveness in solving complex optimization problems. Unlike traditional deterministic methods, these algorithms employ multiple search agents, which are initially randomly placed in the optimization space and move towards the global optimum through iterative communication, combining deterministic and stochastic movements. Some of the key NI algorithms are: particle swarm optimization (PSO), genetic algorithm (GA), ant colony optimization (ACO)., etc.

Among different NI algorithms, PSO is inspired by the social behavior of animals such as birds flocking or fish schooling. It is used to solve optimization problems by iteratively improving candidate solutions with regard to a given measure of quality. The basic idea of PSO involves a swarm of particles moving through the search space to find the optimal solution. Each particle represents a potential solution and has the following attributes:

- Position: $\mathbf{x}_i \in \mathbb{R}^n$ for particle i.
- Velocity: $\mathbf{v}_i \in \mathbb{R}^n$ for particle i.
- Personal best position: $\mathbf{p}_i \in \mathbb{R}^n$, which is the best position found by particle i so far.
- Global best position: $\mathbf{g} \in \mathbb{R}^n$, which is the best position found by any particle in the swarm.

The velocity and position of each particle are updated iteratively using the following equations:

$$\mathbf{v}_i(t+1) = \omega \mathbf{v}_i(t) + c_1 r_1(\mathbf{p}_i - \mathbf{x}_i(t)) + c_2 r_2(\mathbf{g} - \mathbf{x}_i(t)), \tag{2.16}$$

$$\mathbf{x}_i(t+1) = \mathbf{x}_i(t) + \mathbf{v}_i(t+1), \tag{2.17}$$

where:

- ω is the inertia weight, which controls the impact of the previous velocity.
- c_1 and c_2 are cognitive and social coefficients, respectively, which control the influence of the personal best and global best positions.
- r_1 and r_2 are random numbers uniformly distributed in $[0, 1]$.

The iterative process of PSO can be summarized as follows:

1. Initialize the positions $\mathbf{x}_i(0)$ and velocities $\mathbf{v}_i(0)$ of all particles randomly.
2. Evaluate the fitness of each particle's position.
3. Update each particle's personal best position $\mathbf{p}_i$ if the current position is better.
4. Update the global best position $\mathbf{g}$ if any particle's personal best position is better than the current global best.
5. Update the velocities and positions of all particles using the equations (2.16) and (2.17).
6. Repeat steps 2-5 until a stopping criterion is met (e.g., a maximum number of iterations or a satisfactory fitness level).

2.5.2 Applications of NI-PSO in Wireless Communications

PSO has been effectively applied in various wireless communication problems due to its simplicity and ability to find near-optimal solutions. For example, PSO can be used for:

- **RF Beamformer Design:** Optimizing the phase shifts of RF beamformers to maximize the received signal power or minimize interference.
- **Resource Allocation:** Allocating resources such as power, bandwidth, and time slots to users in a wireless network to optimize overall performance.
- **Antenna Design:** Designing antenna arrays to achieve desired radiation patterns and improve signal quality.

Although NI algorithms promise to achieve almost optimal solutions, they might be computationally expensive and time consuming due to the iterative behavior. On the other hand, when the optimization problem is non-convex, NI algorithms can be also utilized for developing a dataset to train the low-complexity and robust ML techniques.

2.5.3 Deep Learning

Deep learning (DL), a subset of ML, has been pivotal in fields such as computer vision, speech recognition, and natural language processing. Its success has also extended to wireless communications, where it has been used for tasks such as signal detection, resource management, and channel estimation. A single neuron in a neural network performs a weighted sum of the inputs and applies a non-linear activation function. The output y of a single neuron can be expressed as:

$$y = f\left(\sum_{i=1}^{N} w_i x_i + b\right) \tag{2.18}$$

where:

- x_i are the input features.
- w_i are the weights associated with the inputs.
- b is the bias term.
- $f(\cdot)$ is the activation function.

Some common activation functions used in DL are:

- **Sigmoid Function**:

$$f(x) = \frac{1}{1+e^{-x}} \tag{2.19}$$

- **Rectified Linear Unit (ReLU)**:

$$f(x) = \max(0, x) \tag{2.20}$$

- **Hyperbolic Tangent (Tanh)**:

$$f(x) = \tanh(x) = \frac{e^{x} - e^{-x}}{e^{x} + e^{-x}} \tag{2.21}$$

In DL, the loss functions are used to measure the difference between the predicted output and the actual output. Some common loss functions are:

- **Mean Squared Error (MSE)**:

$$\text{MSE} = \frac{1}{N}\sum_{i=1}^{N}(y_i - \hat{y}_i)^2 \tag{2.22}$$

where y_i is the actual value and $\hat{y}_i$ is the predicted value.

- **Mean Absolute Error (MAE)**:

$$\text{MAE} = \frac{1}{N}\sum_{i=1}^{N} |y_i - \hat{y}_i| \tag{2.23}$$

- **Cross-Entropy Loss** (used for classification):

$$L = -\sum_{i=1}^{N} y_i \log(\hat{y}_i) \tag{2.24}$$

In a deep neural network, forward propagation involves calculating the output of each layer from the input layer to the output layer. For a layer l, the operation can be described as:

$$\mathbf{a}^{(l)} = f\left(\mathbf{W}^{(l)}\mathbf{a}^{(l-1)} + \mathbf{b}^{(l)}\right) \tag{2.25}$$

where:

- $\mathbf{a}^{(l-1)}$ is the activation from the previous layer.
- $\mathbf{W}^{(l)}$ is the weight matrix of the current layer.
- $\mathbf{b}^{(l)}$ is the bias vector of the current layer.
- $f(\cdot)$ is the activation function.

On the other hand, backpropagation is used to compute the gradient of the loss function with respect to each weight in the network. It involves:

- **Gradient of the loss with respect to the output of the network**:

$$\frac{\partial L}{\partial \hat{y}} = \hat{y} - y \tag{2.26}$$

- **Gradient of the loss with respect to the weights**:

$$\frac{\partial L}{\partial \mathbf{W}^{(l)}} = \delta^{(l)}\mathbf{a}^{(l-1)^T} \tag{2.27}$$

- **Updating weights using gradient descent**:

  $$\mathbf{W}^{(l)} \leftarrow \mathbf{W}^{(l)} - \eta \frac{\partial L}{\partial \mathbf{W}^{(l)}} \tag{2.28}$$

  where η is the learning rate.

An example DNN architecture includes input, multiple hidden, and output layers, where each hidden layer neuron uses activation functions to learn complex patterns. The depth (number of hidden layers) and the number of neurons per layer directly influence the network's capacity to model intricate relationships.

In summary, both NI algorithms and DL techniques offer significant potential for optimizing and enhancing wireless communication systems, each contributing uniquely to addressing the challenges posed by non-convex optimization problems.

2.6 Concluding Remarks

In this chapter, we have presented an overview of the beamforming architectures for the mMIMO systems and highlighted the benefits of the HBF architecture for high spectral, and energy efficiency with reduced hardware complexity. Afterwards, we discussed MU-mMIMO communications system model. Then, we presented different SIS techniques for the FD communications, including analog RF beamformer and BB precoder/combiner. Also, we have emphasized that the large antenna arrays in the FD mMIMO systems bring a great potential for the improved SIS quality via the HBF design. Then, we discussed different relaying schemes in mMIMO systems, which can extend the coverage area while enhancing the capacity. We also highlighted the use of different AI/ML applications in wireless communications. In the next chapters, we develop novel HBF techniques for various mMIMO systems along with the aforementioned points, which address two key issues: (i) capacity, and (ii) coverage area.

Chapter 3

2D Antenna Array Structures in Hybrid Massive MIMO[1]

3.1 Introduction

As expressed in Chapter 2, the large antenna arrays in mMIMO systems bring two interesting challenges: (i) increased expense and energy consumption due to the use of large number of RF chains, and (ii) the use of significant amount of spectral resources and increased CSI overhead [20]. In order to overcome these problems, HBF has been proposed as a promising solution [20, 31], which is a two-stage precoder consisting of an analog RF beamforming stage and a digital baseband precoding stage, and with much-reduced system complexity/hardware cost, it can achieve the performance close to FDBF which requires full instantaneous CSI. In HBF, large-dimensional processing is carried out by phase shifters (PSs) at the transceiver RF front-end, followed by low-dimensional processing at the baseband level. A few RF chains and digital-to-analog converters/analog-to-digital converters (DACs/ADCs) connect the RF and the baseband stages. Furthermore, at the RF-stage, two commonly used methods of processing input paramters are: (i) using fast time-varying CSI [36–42], and (ii) using slowly time-varying instantaneous CSI [60–68]. The first strategy employs full CSI, whereas, in the second strategy, only the reduced-dimension effective instantaneous CSI seen from the BB-stage is required for the BB precoder design. In other words, the second strategy is capable of reducing both the hardware cost/complexity and the CSI overhead size.

---

[1] Parts of this chapter have been presented at the 2020 IEEE Global Communications Conference (GLOBECOM), Taipei, Taiwan [57], the 2021 IEEE International Conference on Communications (ICC), Montreal, QC, Canada [58], and published in the IEEE Open Journal of the Communications Society [59].

Most of the HBF solutions have assumed the use of full-resolution PSs and DACs to achieve a satisfactory performance close to FDBF structures. However, because of the increased complexity and costs, implementing ∞-bit PSs and DACs/ADCs is impractical. The recent studies show that there has been an increased interest in the use of small, power-efficient, and inexpensive devices for hardware efficient transceivers capable of beamforming. Therefore, the use of low-resolution PSs [69–77] and DACs/ADCs [78–83] allows a more viable HBF solution to be designed. Another important aspect in mMIMO is the number of the antenna elements as well as their arrangement at the transmitter side as the array configurations can be critical in the generation of narrower beams with reduced sidelobes, which can offer small interference to the unintended users. The existing research studies mostly use uniform linear array (ULA) at the BS for the HBF design [36–40, 60–64, 66, 67, 69–74, 78–82]. However, it is not applicable to deploy a large single-dimensional (1D) ULA at the BS because of: (i) spatial inefficiency, and (ii) restriction to illuminate both azimuth and elevation angles at the same time. The antenna elements can be arranged on a two-dimensional (2D) grid to overcome the aforementioned issues. In this chapter, we present the analysis of different 2D array structures (ULA, URA, UCA, and CCA) in mMIMO, where we compare the spatial, spectral and energy efficiencies by designing the HBF using low-resolution PSs and quantized DACs. The proposed HBF schemes include two cascaded stages: (i) the *RF-beamforming stage* is designed via the eigen-decomposition of mMIMO channel second-order correlation matrix, and (ii) the *baseband MU precoding stage* is constructed via the regularized zero-forcing (RZF) technique [84, 85] to mitigate the MU interference in the reduced-dimension effective MU-channel. The main contributions are summarized below:

- **Energy-Efficient HBF Design Using Low-Resolution PSs:** Most of the existing HBF designs (e.g., in [36–40, 60–67, 78–83]) assume the use of full-resolution PSs for the implementation of RF-stage. However, the components required for phase shift with high accuracy can be expensive [86]. Therefore, it is reasonable to use cost-effective PSs in HBF. One possible way to design the HBF with low-resolution PSs is to design the RF beamformer assuming infinite-resolution PSs and then, quantize each PSs value by a finite set [36]. This approach, however, is not suitable for systems with low-resolution phase constraint and requires full CSI. Furthermore, the HBF designs which are presented in [69–71, 73–76] are considered for SU-mMIMO and MU-MISO systems. In this chapter, we design the HBF using low-resolution PSs for MU-mMIMO by taking into account the few-bit phase constraint and formulate the optimization problem which is solved using orthogonal matching pursuit

(OMP) [87, 88]. The algorithmic precoding solution takes the input as the optimal unconstrained (full-resolution) RF beamformer and approximates the constrained (quantized) RF beamformer by exploiting the dominant eigenvectors at the RF. We present the illustrative results of the proposed HBF scheme and show that it is possible to approach the performance limit of the unconstrained RF-stage with as low as 2 bit PSs (i.e., sum-rate degradation ≈ 2-3 bps/Hz).

- **Comparison of 2-D Antenna Array Structures:** In this work, we compare the spatial, spectral and energy efficiencies of different 2D antenna array structures using low-resolution PSs and DACs. The array structure used in [36–40, 60–64, 66, 67, 69–83] is either ULA or URA. However, in this work we compare four different 2D array structures using low-resolution PSs and DACs. The simulation results show that the sum-rate of both CCA and URA can approach the sum-rate of their FDBF counterparts with much-reduced number of RF chains.

- **HBF Design Using Low-Resolution PSs and DACs:** As mentioned above, the HBF is designed using either only low-resolution PSs [69–77] or only low-resolution DACs/ADCs [78–83]. To the best of our knowledge, the design of a MU-mMIMO HBF using both *low-resolution DACs* and *low-resolution PSs* has not been considered yet. Moreover, we also compare the performance of such a reduced-complexity HBF for different 2D array structures i.e., ULA, URA, UCA, and CCA. The simulation results give useful results about the combination of various low-resolution DACs and PSs for near optimal performance. The proposed HBF using 2-bit PSs and 5-bit DACs can achieve almost the same spectral efficiency while offering higher energy efficiency than the HBF using full-resolution PSs and DACs. Therefore, the designed HBF saves power consumption and cost while having negligible impact on the performance.

- **Design of the Quantized Variable Gain RF Beamformer:** In this work, we design the HBF in which the RF beamforming stage is constructed using eigen beamforming based on user's angular location. Eigen beamforming can give sum-rate performance of HBF close to FDBF [60–63], however, the RF beamformer results in having non-constant modulus entities. The quantization of such variable gain RF beamformer is challenging. Also, to the best of our knowledge, the quantization of analog precoder which is designed using eigen beamforming has not been considered yet. Therefore, we solve this problem to modify our system model to have a constant modulus RF beamformer and introduces a transfer block at the baseband stage by formulating an optimization problem. The resulting RF beamformer requires double-PS structure and follows the constant modulus constraint, i.e., the gain of each entity of RF beamformer can vary between 0 and 2. The resulting HBF with constant-modulus gives the same sum-rate performance as the variable gain RF beamformer.

The rest of this chapter is organized as follows. In Section 3.2, we introduce the HBF design using full-resolutions PSs and DACs. Section 3.3 presents the HBF solution when using quantized DACs/ADCs at BS. In Section 3.4, we discuss HBF design using low-resolution PSs followed by the algorithmic HBF solution for few-bit DACs and PSs in Section 3.5. The illustrative results are provided in Section 3.6 to compare the performance of different 2D array structures. Finally, the chapter is concluded in Section 3.7.

3.2 Hybrid Beamforming Design Using Full Resolution PSs and DACs

In this section, we discuss the HBF solution using full-resolution hardware components.

3.2.1 System Model

In the system model shown in Fig. 3.1, we assume that N_T BS antennas at the transmitter are fed by N_{RF} RF chains to serve K single-antenna users. b_T represents the number of orthogonal-beams spanning the degrees of freedom (DoF) provided by the channel, such that $K \leq N_{RF} \leq b_T \ll N_T$. S denotes the independent data streams to be transmitted, which is equal to the number of simultaneously served users in this model (i.e., $S = K$). Furthermore, by selecting $N_{RF} = K$ RF chains, the hybrid precoding matrix $\mathbf{B} = \mathbf{F}_D\mathbf{T}\mathbf{B}_D$ where i) RF-beamforming matrix $\mathbf{F}_D \in \mathbb{C}^{N \times b_T}$ is based on the channel second order statistics and reduces the CSI overhead and the number of RF chains ii) transfer matrix $\mathbf{T} \in \mathbb{C}^{b_T \times N_{RF}}$ exploits the available DoF of the channel, and further reduces the number of RF chains without sacrificing the performance iii) multi-user precoding matrix $\mathbf{B}_D \in \mathbb{C}^{N_{RF} \times S}$ is based on the reduced-dimension effective MU channel, and reduces the MU interference. The received signal at the kth user is expressed as:

$$y_k = \mathbf{h}_k^H \mathbf{B}\mathbf{s} + n_k. \tag{3.1}$$

$\mathbf{s} \in \mathbb{C}^{S \times 1}$ is the transmitted data signal satisfying $\mathbb{E}\left[||\mathbf{s}||_2^2\right] \leq \frac{P_T}{S}\mathbf{I}_s$, where P_T is the transmit power at the BS and n_k denotes the additive circular symmetric Gaussian noise such that

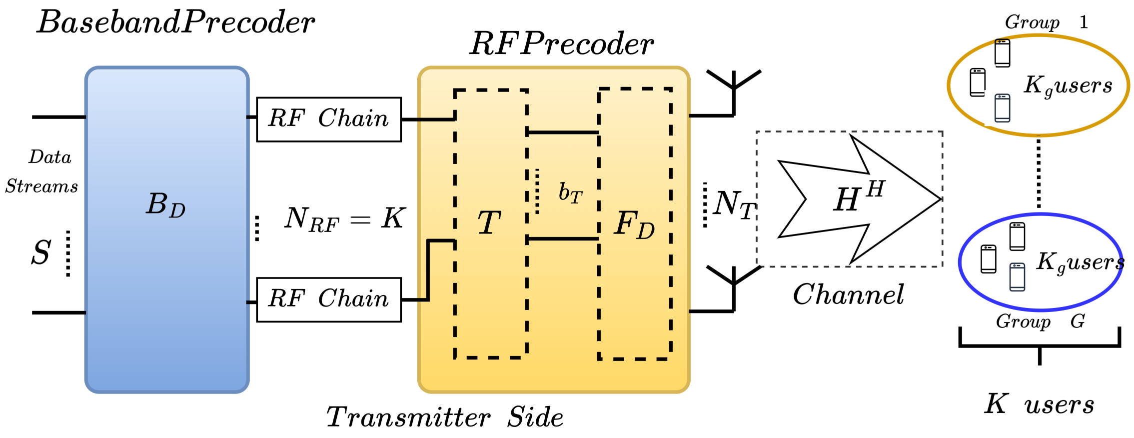

Figure 3.1. System model of the hybrid beamforming architecture.

$n_k \sim \mathcal{CN}(0,1)$. Assuming no line of sight propagation, the channel $\mathbf{h}_k \sim \mathcal{CN}(0,\mathbf{R}_k)$, where $\mathbf{R}_k \in \mathbb{C}^{N\times N}$ is the covariance matrix.

The channel vector $\mathbf{h}_k \in \mathbb{C}^{N\times 1}$ for user k can be expressed by using Karhunen-Loeve decomposition as:

$$\mathbf{h}_k = \mathbf{U}_k \mathbf{\Lambda}_k^{\frac{1}{2}} \mathbf{w}_k, \tag{3.2}$$

where $\mathbf{w}_k \in \mathbb{C}^{r\times\mathbf{1}} \sim \mathcal{CN}(0,\mathbf{I}_r)$ is the complex weight coefficient vector, $\mathbf{\Lambda}_k \in \mathbb{C}^{r\times r}$ is the diagonal matrix containing r eigenvalues of $\mathbf{R}_k$ and $\mathbf{U_k} \in \mathbb{C}^{N\times r}$ is the matrix containing the eigenvectors corresponding to the non-zero eigenvalues. Assuming mutually independent channel vectors $\mathbf{h}_k$, the overall channel model can be expressed as:

$$\mathbf{H} = [\mathbf{h}_1, \mathbf{h}_2, \ldots, \mathbf{h}_K], \tag{3.3}$$

The correlation matrix $\mathbf{R}_k$ is obtained by using the one-ring model [89], where a user is located at some distance r_d and the mean azimuth angle is θ. For the 1D and 2D antenna structures as shown in Fig. 3.2, assuming a uniform distribution of power received from the antennas, the correlations between the channel coefficients of the antennas $1 \leq n,p \leq N$ are respectively given as:

$$\left[\mathbf{R}_{n,p}\right]_{1D} = \frac{1}{2\Delta}\int_{-\Delta+\theta}^{\Delta+\theta} e^{-j2\pi d(n-p)\sin(\beta)}\, d\beta, \tag{3.4}$$

$$\left[\mathbf{R}_{n,p}\right]_{2D} = \frac{1}{2\Delta}\int_{-\Delta}^{\Delta} e^{-j\frac{2\pi}{\lambda}\mathbf{k}(\beta+\theta)(\mathbf{v}_n-\mathbf{v}_p)}\, d\beta, \tag{3.5}$$

where λ is the wavelength. $\Delta \approx \pm \arctan\frac{l}{r_d}$ is the angle spread around the mean azimuth

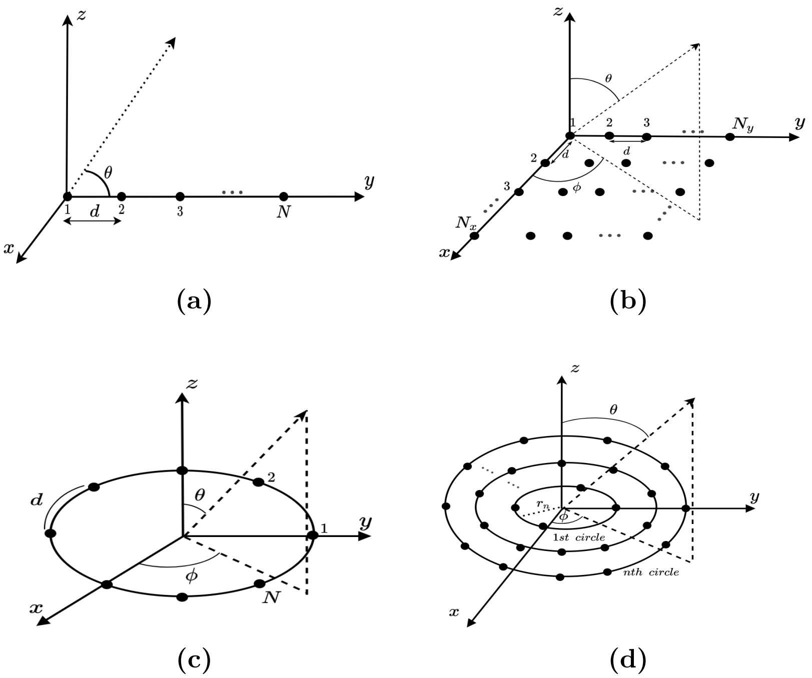

(a) (b) (c) (d)

Figure 3.2. 2D Array structures (a) ULA (b) URA (c) UCA (d) CCA.

angle for a user surrounded by a ring of scatters of radius l , $\mathbf{k}(\beta) = (\cos(\beta), \sin(\beta))^T$ is the wave vector for a planar wave impinging with angle-of-arrival (AoA) β and $\mathbf{v}_n, \mathbf{v}_p$ is $\mathbb{R}^2$. The correlation matrix $\mathbf{R}_{1D}$ for ULA is computed using (3.4) where d is the distance between the *nth* and *pth* antenna. For UCA, URA, and CCA, (3.5) is used to calculate the correlation matrix $\mathbf{R}_{2D}$. Thus, the correlation matrix $\mathbf{R}$ depends on the antenna array configuration employed at the BS, and the corresponding rank of $\mathbf{R} = \mathbf{U\Lambda U}^H$ plays an important role in the sum-rate performance of the array structure. In the eigen-beamforming, the hybrid precoder $\mathbf{B} \in \mathbb{C}^{N_T \times S}$ is constructed by concatenating the RF-beamforming $\mathbf{F}_D \in \mathbb{C}^{N_T \times b_T}$ and reduced-dimensional multi-user precoder (baseband-stage) $\mathbf{B}_D \in \mathbb{C}^{N_{RF} \times S}$ through an intermediate block called transfer block $\mathbf{T} \in \mathbb{C}^{b_T \times N_{RF}}$.

3.2.2 RF-beamforming Stage

Suppose K users are clustered into G groups based on their AoD information, where each group contains K_g number of users such that $K = \sum_{g=1}^{G} K_g$. For simplicity, we assume that the users in the same group have identical covariance matrix $\mathbf{R}_g$, where $g = 1, 2, \ldots, G$. The index $g_k = \sum_{g'=1}^{g-1} K_{g'} + k$ is used to denote the *kth* user in group g. Then, the channel vector for the user k in group g is $\mathbf{h}_{g_k} \sim \mathcal{CN}(0, \mathbf{R}_g)$, where $\mathbf{R}_g = \mathbf{U}_g\mathbf{\Lambda}_g\mathbf{U}_g^H$ is the covariance matrix of the group g. Based on the AoD of the users, the correlation matrix can be written as:

$$\mathbf{R}_g = [\mathbf{U}_g^+, \mathbf{U}_g^-][\mathbf{\Lambda}_g^+, \mathbf{\Lambda}_g^-][\mathbf{U}_g^+, \mathbf{U}_g^-]^H, \tag{3.6}$$

where $\mathbf{U}_g^+ \in \mathbb{C}^{N\times r_g^+}$ is the matrix of eigenvectors corresponding to the dominant eigenvalues for the user group g. Similarly, $\mathbf{\Lambda}_g^+ \in \mathbb{C}^{r_g^+\times r_g^+}$ is the diagonal matrix of the dominant eigenvalues. As a result, the data streams per group is $S_g \in [0,\, \min\{K_g,\, r_g^+\}]$. The maximum number of independent data streams that can be transmitted is limited by the multiplexing gain $\min\{K_g,\, r_g^+\}$. The total data streams can be written as $S = \sum_{g=1}^{G} S_g$. By using Karhunen-Loeve decomposition, we have:

$$\mathbf{h}_{g_k} = \mathbf{U}_g \mathbf{\Lambda}_g^{\frac{1}{2}} \mathbf{w}_{g_k}. \tag{3.7}$$

The overall channel matrix $\mathbf{H}$ can be written as:

$$\mathbf{H} = [\mathbf{H}_1, \mathbf{H}_2, \ldots, \mathbf{H}_G], \tag{3.8}$$

where $\mathbf{H}_g = [\mathbf{h}_{g_1}, \mathbf{h}_{g_2}, \ldots, \mathbf{h}_{g_{K_g}}]$ is the channel matrix for group g. The performance of the hybrid precoder heavily depends on the choice of b_T and N_{RF}. It must be seen that **i)** $N_{RF} \geq S$ to ensure that the minimum number of RF chains used in the precoder is not less than the transmitted signals and **ii)** $N_{RF} = \sum_{g=1}^{G} N_{RF_g}$. The RF-beamforming matrix $\mathbf{F}_D$ depends on the second-order statistics as it relies on the eigenvalues and eigenvectors extracted from the covariance matrix $\mathbf{R}_g$. If $\mathbf{B}_{A,g} = \mathbf{U}_g^+$ is the RF-beamforming matrix of group g and by choosing $b_g = r_g^+$, the complete RF-beamforming matrix can be written as:

$$\mathbf{F}_D = [\mathbf{F}_{D,1}, \mathbf{F}_{D,2}, \ldots, \mathbf{F}_{D,G}]. \tag{3.9}$$

The overall reduced dimensional effective channel matrix is expressed as $\boldsymbol{\mathcal{H}}^H = \mathbf{F}_D^H \mathbf{H}$. Using (3.8) and (3.9), $\boldsymbol{\mathcal{H}}^H$ can be written as:

$$\boldsymbol{\mathcal{H}}^H = \begin{bmatrix} \mathbf{H}_1^H \mathbf{F}_{D,1} & \mathbf{H}_1^H \mathbf{F}_{D,2} & \ldots & \mathbf{H}_1^H \mathbf{F}_{D,G} \\ \mathbf{H}_2^H \mathbf{F}_{D,1} & \mathbf{H}_2^H \mathbf{F}_{D,2} & \ldots & \mathbf{H}_2^H \mathbf{B}_{A,G} \\ \vdots & \vdots & \ddots & \vdots \\ \mathbf{H}_G^H \mathbf{F}_{D,1} & \mathbf{H}_G^H \mathbf{F}_{D,2} & \ldots & \mathbf{H}_G^H \mathbf{F}_{D,G} \end{bmatrix}, \tag{3.10}$$

where the diagonal matrices $\mathbf{H}_g^H \mathbf{F}_{D,g} \in \mathbb{C}^{K_g\times b_g}$ are the effective channel matrix for group g and the off-diagonal matrices $\mathbf{H}_g^H \mathbf{F}_{D,q} \in \mathbb{C}^{K_g\times b_q}$ represent the effective interference channel matrix between groups g and q, $\forall q \neq g$.

3.2.3 Transfer Block and Multiuser Precoder Design

The transfer block $\mathbf{T} \in \mathbb{C}^{b_T \times N_{RF}}$ is designed between the RF-beamforming matrix and the multi-user precoding matrix, reducing the number of RF chains N_{RF} such that $K \leq N_{RF} < b_T$. $\mathbf{T}$ is placed at the RF precoder satisfying $\mathbb{E}\left[||\mathbf{s}||_2^2\right] = \text{tr}(\mathbf{B}_D^H \mathbf{T}^H \mathbf{T} \mathbf{B}_D) \leq P_T$, where P_T is the transmit power. The transfer block $\mathbf{T}$ and the reduced dimensional multi-user precoder $\mathbf{B}_D$ is designed as:

$$\begin{aligned} \min_{\mathbf{T},\mathbf{B}_D} \quad & ||\hat{\mathbf{B}}_D - \mathbf{T}\mathbf{B}_D||_2^2, \\ \text{s.t.} \quad & \mathbf{T} \in \mathbb{T}_o, \\ & \text{tr}(\mathbf{B}_D^H \mathbf{T}^H \mathbf{T} \mathbf{B}_D) \leq P_T, \end{aligned} \tag{3.11}$$

where $\mathbb{T}_o$ represents the set of matrices of size $b_T \times N_{RF}$. $\hat{\mathbf{B}}_D = \gamma \mathbf{X} \boldsymbol{\mathcal{H}}^H$ is the $N_{RF} \times K$ baseband precoder without using the transfer block $\mathbf{T}$. The optimization problem is formulated to design the reduced-size baseband precoder $\mathbf{B}_D$ giving the same performance as $\hat{\mathbf{B}}_D$. $\boldsymbol{\mathcal{H}}^H$ is the reduced dimensional effective channel, $\mathbf{X} = [\boldsymbol{\mathcal{H}}^H \boldsymbol{\mathcal{H}} + \alpha b_T \mathbf{I}_{b_T}]^{-1}$, $\mathbf{I}_{b_T} \in \mathbb{C}^{b_T \times b_T}$, α is the regularization paramter and γ is the normalization factor used to satisfy the power constraint, which can be written as:

$$\gamma = \sqrt{\frac{S}{tr\{\boldsymbol{\mathcal{H}}^H \mathbf{X}^H \mathbf{F}_D^H \mathbf{F}_D \mathbf{X} \boldsymbol{\mathcal{H}}\}}}. \tag{3.12}$$

Since (3.11) is non-convex, so $\mathbf{T}$ is dissolved into $\mathbf{T}_A \in \mathbb{C}^{b_T \times K}$ and $\mathbf{T}_B \in \mathbb{C}^{b_T \times k}$ by using $N_{RF} = K$ RF chains. Then, the optimal solution is given as [90]:

$$\begin{aligned} \mathbf{T}_A(a,b) &= e^{j\left(\angle \hat{\mathbf{B}}_D(a,b) + \cos^{-1}(\frac{\hat{\mathbf{B}}_D(a,b)}{2\mu})\right)}, \\ \mathbf{T}_B(a,b) &= e^{j\left(\angle \hat{\mathbf{B}}_D(a,b) - \cos^{-1}(\frac{\hat{\mathbf{B}}_D(a,b)}{2\mu})\right)}, \\ \mathbf{B}_D &= (\mathbf{T}_A + \mathbf{T}_B)^{\dagger} \hat{\mathbf{B}}_D, \end{aligned} \tag{3.13}$$

where $\mu = \frac{1}{2} \max_{a,b} |\hat{\mathbf{B}}_D(a,b)|$ is the half of the highest modulus element at $\hat{\mathbf{B}}_D$. Then, the joint-group processing (JGP) approach [60] is used for the SINR computation. Therefore,

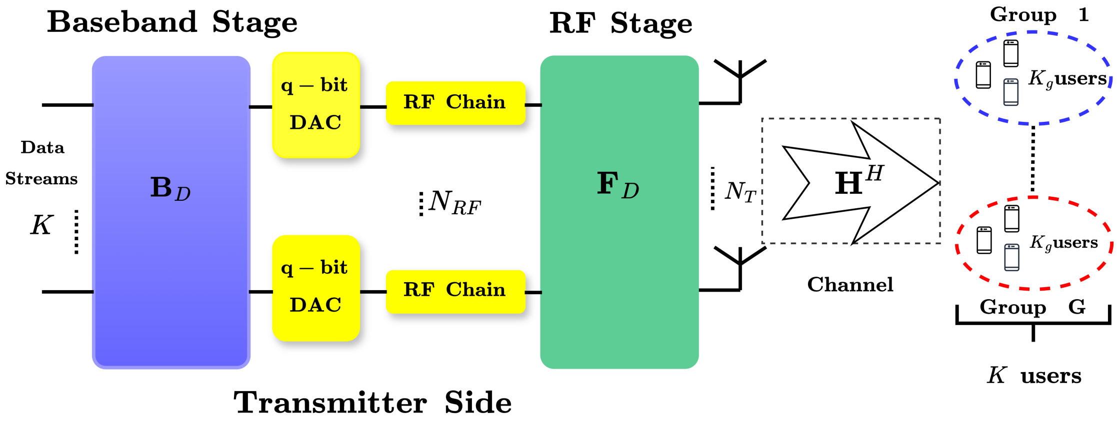

Figure 3.3. Hybrid beamforming architecture using few-bit DACs.

the SINR at the user k in group g can be computed as follows:

$$SINR_{g_k} = \frac{\frac{P_T}{S}|\mathbf{h}_{g_k}^H \mathbf{F}_D \hat{\mathbf{B}}_D \hat{\mathbf{B}}_D^H \mathbf{F}_D^H \mathbf{h}_{g_k}|^2}{1 + \frac{P_T}{S}\sum_{i \neq g_k} |\mathbf{h}_{g_k}^H \mathbf{F}_D \hat{\mathbf{B}}_D \hat{\mathbf{B}}_D^H \mathbf{F}_D^H \mathbf{h}_i|^2}. \tag{3.14}$$

Hence, the corresponding sum-rate performance can be computed as:

$$R = \sum_{K_g=1}^{G} \sum_{g_k=1}^{K_g} \mathbb{E}[\log_2(1 + SINR_{g_k})]. \tag{3.15}$$

3.3 Hybrid Beamforming Design Using Low-Resolution DACs

In this section, we discuss the HBF solution using low-resolution DACs/ADCs in mMIMO systems.

3.3.1 System Model

In the system model shown in Fig. 3.3, we assume that N_T BS antennas at the transmitter are fed by N_{RF} RF chains to serve K single-antenna users, where $K \leq N_{RF} \ll N_T$. The hybrid precoder $\mathbf{B} = \mathbf{F}_D \mathbf{B}_D$ is divided as the RF precoder $\mathbf{F}_D \in \mathbb{C}^{N_T \times N_{RF}}$ and the baseband precoder $\mathbf{B}_D \in \mathbb{C}^{N_{RF} \times K}$. The system model employs low resolution q-bit DACs between the RF and the baseband precoder to reduce the system complexity/cost. To model the

Table 3.1. Distortion factors μ in q-bit DACs ($q \leq 5$).

q	1	2	3	4	5
μ	0.6366	0.8825	0.96546	0.990503	0.997501

precoded signal at the transmitter, we consider the non-uniform quantizer, and adopt the additive quantization noise model (AQNM) as in [91, 92]. Then, the received signal at the kth user is expressed as:

$$\begin{aligned} y_k &= \mathbf{h}_k^H \mathbf{F}_D \mathbb{Q}\{\mathbf{B}_D \mathbf{s}\} + n_k, \\ &= \mathbf{h}_k^H \mathbf{F}_D \{\mu \mathbf{B}_D \mathbf{s} + n_q\} + n_k, \\ &= \underbrace{\mu \mathbf{h}_k^H \mathbf{F}_D \mathbf{B}_D \mathbf{s}}_{\text{Desired Signal}} + \underbrace{\mathbf{h}_k^H \mathbf{F}_D n_q}_{\text{Quantization Noise}} + \underbrace{n_k}_{\text{Noise}}, \end{aligned} \tag{3.16}$$

where $\mathbf{s} \in \mathbb{C}^K$ is the transmitted data signal satisfying the power constraint P_T (i.e., $\mathbb{E}\{\|\mathbf{s}\|_2^2\} \leq P_T$). Here, n_k denotes the additive circular symmetric Gaussian noise such that $n_k \sim \mathcal{CN}(0,1)$, $\mathbb{Q}(.)$ is the quantizer function, μ is the distortion factor of q-bit DAC, and $n_q \sim \mathcal{CN}(0, \mathbf{R}_{n_q})$ is the additive Gaussian quantization noise which is uncorrelated with $\mathbf{s}$. For $q \leq 5$, the exact values of μ is given in Table. 3.1. When quantization bit $q > 5$, then the distortion factor can be approximated as $\mu \approx 1 - \frac{\pi\sqrt{3}}{2} 2^{-2q}$ [92]. Furthermore, the covariance matrix of n_q is given as:

$$\mathbf{R}_{n_q} = \mathbb{E}\left[n_q n_q^H\right] = \mu(1-\mu) \ \mathrm{diag}(\mathbf{B}_D \mathbf{B}_D^H). \tag{3.17}$$

Assuming no line of sight propagation, the channel $\mathbf{h}_k \sim \mathcal{CN}(0, \mathbf{R}_k)$, where $\mathbf{R}_k \in \mathbb{C}^{N_T \times N_T}$ is the covariance matrix. The channel vector $\mathbf{h}_k \in \mathbb{C}^{N_T \times 1}$ for user k can be expressed by using Karhunen-Loeve decomposition as given in (3.2). Similarly, the overall channel model can be expressed as given in (3.4).

3.3.2 RF and BB Stage Design with Low-Resolution DACs

In the eigen-beamforming, the hybrid precoder $\mathbf{B} \in \mathbb{C}^{N_T \times K}$ concatenates the RF-beamforming stage $\mathbf{F}_D \in \mathbb{C}^{N_T \times N_{RF}}$ and the reduced-dimensional baseband MU precoding stage $\mathbf{B}_D \in \mathbb{C}^{N_{RF} \times K}$ through the use of low-resolution DACs. The design of the RF beamforming stage employs full-resolution PSs and the details can be found in Section 3.2.2. After the design of RF beamforming stage $\mathbf{F}_D$, the baseband MU precoder $\mathbf{B}_D$ can be determined by using the joint group processing (JGP) [60]. Using regularized zero forcing, $\mathbf{B}_D$ can be defined as:

$$\mathbf{B}_D = \gamma \mathbf{X} \boldsymbol{\mathcal{H}}^H, \tag{3.18}$$

$\boldsymbol{\mathcal{H}}^H$ is the reduced-dimension effective channel as given in (3.10), $\mathbf{X} = [\boldsymbol{\mathcal{H}}^{\boldsymbol{\mathcal{H}}} \boldsymbol{\mathcal{H}} + \alpha N_{RF} \mathbf{I}_{N_{RF}}]^{-1}$, $\mathbf{I}_{N_{RF}} \in \mathbb{C}^{N_{RF} \times N_{RF}}$, α is the regularization paramter and γ is the normalization factor used to satisfy the power constraint, which can be written as:

$$\gamma = \sqrt{\frac{S}{\mathrm{tr}\{\boldsymbol{\mathcal{H}}^H \mathbf{X}^H \mathbf{F}_D^H \mathbf{F}_D \mathbf{X} \boldsymbol{\mathcal{H}}\}}}. \tag{3.19}$$

Therefore, the signal to quantization, interference and noise ratio (SQINR) at the user k in group g can be computed as follows:

$$\mathrm{SQINR}_{g_k} = \frac{\frac{P_T}{S} |\mathbf{h}_{g_k}^H \mathbf{F}_D \mathbf{X} \mathbf{F}_D^H \mathbf{h}_{g_k}|^2}{1 + \hat{a} + \hat{b}}, \tag{3.20}$$

where $\hat{a} = \frac{P_T}{S} \sum_{i \neq g_k} |\mathbf{h}_{g_k}^H \mathbf{F}_D \mathbf{X} \mathbf{F}_D^H \mathbf{h}_i|^2$ accounts for the multi-user interference and $\hat{b} = \frac{P_T}{S} |\mathbf{h}_{g_k}^H \mathbf{F}_D \mathbf{R}_{n_q} (\mathbf{F}_D^H \mathbf{h}_{g_k})^H|^2$ is the quantization noise. Hence, the corresponding sum-rate performance can be computed as:

$$\mathrm{R} = \sum_{K_g=1}^{G} \sum_{g_k=1}^{K_g} \mathbb{E}[\log_2(1 + \mathrm{SQINR}_{g_k})]. \tag{3.21}$$

3.4 Hybrid beamforming Design Using Low-Resolutions PSs

In this section, we present the HBF design using low-resolution PSs.

3.4.1 System Model

In this section, we introduce the system models of the proposed hybrid MU-mMIMO systems. We consider a MU-mMIMO system with three different HBF structures shown in Figure 3.4. At first, the HBF architecture is depicted in Figure 3.4(a), which considers full-resolution hardware components i.e., ∞-bit DACs and PSs. Then, the HBF using b-bit PSs and ∞-bit DACs is shown in Figure 1(b), which offers an energy efficient structure due

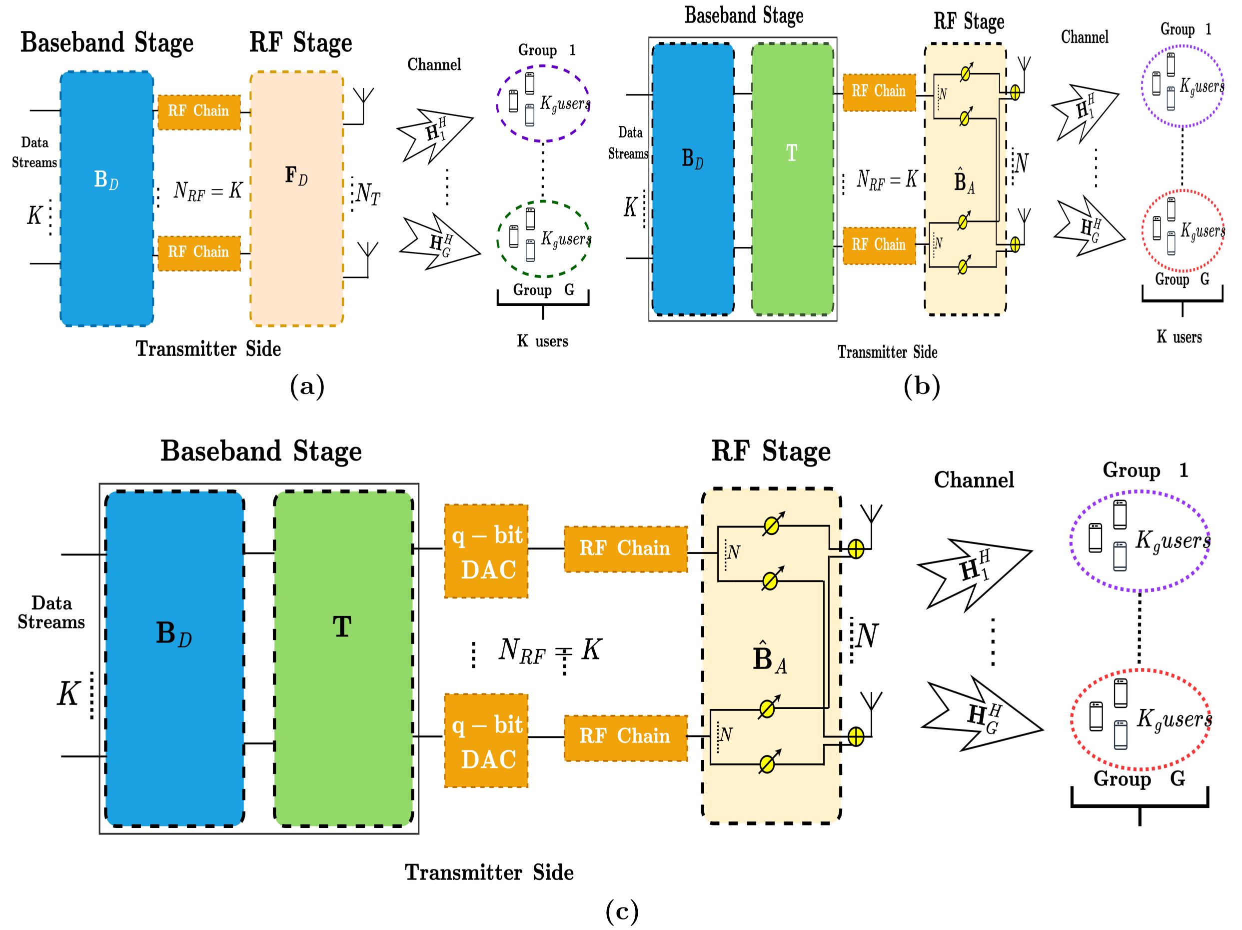

Figure 3.4. MU-mMIMO HBF architectures: (a) HBF with ∞-bits DACs and PSs (b) HBF with b-bit PSs and ∞-bit DACs (c) HBF with q-bit DACs and b-bit PSs.

to less power consumption of finite-bit PSs. Finally, the least power consuming HBF model is presented in Figure 3.4(c), which uses b-bit PSs and q-bit DACs. The BS employs N_T antenna elements at the transmitter, which are fed by N_{RF} RF chains to serve K single-antenna users, where $K \leq N_{RF} \ll N_T$. As shown in Figure 3.4(a), the hybrid precoder $\mathbf{B} = \mathbf{F}_D\mathbf{B}_D$ is divided as the RF beamformer $\mathbf{F}_D \in \mathbb{C}^{N_T \times N_{RF}}$ and the baseband precoder $\mathbf{B}_D \in \mathbb{C}^{N_{RF} \times K}$. The design of HBF helps in reducing the number of RF chains from N_T to N_{RF}. Then, the received signal at the k^{th} user is expressed as:

$$y_k = \mathbf{h}_k^H \mathbf{B}\mathbf{s} + n_k. \tag{3.22}$$

The system model shown in Figure 1(c) employs low resolution q-bit DACs between the RF and the baseband precoders to reduce the system complexity/cost. To model the precoded signal at the transmitter, we consider the non-uniform quantizer, and adopt the additive quantization noise (AQN) model as in [91, 92]. Then, the received signal at the kth user is given as:

$$\begin{aligned} y_k &= \mathbf{h}_k^H \mathbf{F}_D \mathbb{Q}\{\mathbf{T}\mathbf{B}_D\mathbf{s}\} + n_k, \\ &= \mathbf{h}_k^H \mathbf{F}_D \{\mu \mathbf{T}\mathbf{B}_D\mathbf{s} + n_q\} + n_k, \\ &= \underbrace{\mu \mathbf{h}_k^H \mathbf{F}_D \mathbf{T}\mathbf{B}_D\mathbf{s}}_{\text{Desired Signal}} + \underbrace{\mathbf{h}_k^H \mathbf{F}_D n_q}_{\text{Quantization Noise}} + \underbrace{n_k}_{\text{Noise}}, \end{aligned} \tag{3.23}$$

where $\mathbf{s} \in \mathbb{C}^K$ is the transmitted data signal satisfying the power constraint i.e., $\mathbb{E}\{\|\mathbf{s}\|_2^2\} \leq P_T$, where P_T is the transmit power at the BS, n_k denotes the additive circular symmetric Gaussian noise such that $n_k \sim \mathcal{CN}(0,1)$, μ is the distortion factor of q-bit DAC, $n_q \sim \mathcal{CN}(0, \mathbf{R}_{n_q})$ is the additive Gaussian quantization noise which is uncorrelated with $\mathbf{s}$, and $\mathbf{T} \in \mathbb{C}^{N_{RF} \times N_{RF}}$ is the transfer block which is introduced at the baseband stage to have a constant-modulus RF beamformer $\hat{\mathbf{F}}_D \in \mathbb{C}^{N_T \times N_{RF}}$ such that $\hat{\mathbf{F}}_D \mathbf{T} = \mathbf{F}_D$. The covariance matrix of n_q can be written as [83, 93]:

$$\mathbf{R}_{n_q} = \mathbb{E}\left[\mathbf{n}_q \mathbf{n}_q^H\right] = \mu(1-\mu)\ \mathrm{diag}(\mathbf{T}\mathbf{B}_D\mathbf{B}_D^H\mathbf{T}^H). \tag{3.24}$$

For $q = 1, 2, \ldots, 5$, the exact values of μ are 0.6366, 0.8825, 0.96546, 0.990503, and 0.997501, respectively, whereas for $q > 5$, the distortion factor μ can be approximated as $\mu \approx 1 - \frac{\pi\sqrt{3}}{2} 2^{-2q}$ [92].

3.4.2 RF and BB Stage Design with Low-Resolution PSs

In the eigen beamforming, the hybrid precoder $\mathbf{B} \in \mathbb{C}^{N \times K}$ is constructed by concatenating the RF-beamforming stage $\mathbf{F}_D \in \mathbb{C}^{N_T \times N_{RF}}$ and reduced-dimensional MU baseband precoding stage $\mathbf{B}_D \in \mathbb{C}^{N_{RF} \times K}$. The HBF design based on eigen beamforming results in non-constant modulus entities at the RF stage. As discussed earlier, the quantization of this variable gain RF-stage is challenging. To solve this issue, we formulate an optimization problem and introduce a transfer block $\mathbf{T} \in \mathbb{C}^{N_{RF} \times N_{RF}}$ such that $\hat{\mathbf{F}}_D \mathbf{T} = \mathbf{F}_D$, where $\mathbf{F}_D \in \mathbb{C}^{N_T \times N_{RF}}$ is the variable gain RF beamformer, $\mathbf{T} \in \mathbb{C}^{N_{RF} \times N_{RF}}$ is the transfer block placed at the baseband stage and $\hat{\mathbf{F}}_D \in \mathbb{C}^{N_T \times N_{RF}}$ is the RF beamformer with constant-modulus entities. The design of the RF-stage together with the transfer block and the baseband stage is explained in the following sections.

3.4.2.1 Variable-Gain RF Beamformer

We assume K users are clustered into G groups based on their angle-of-departure (AoD) information, where each group contains K_g number of users such that $K = \sum_{g=1}^{G} K_g$. For simplicity, we also assume that the users in the same group have identical covariance matrix $\mathbf{R}_g$, where $g = 1, 2, \ldots, G$. The index $g_k = \sum_{g'=1}^{g-1} K_{g'} + k$ is used to denote the kth user in group g. Then, the channel vector for the user k in group g is $\mathbf{h}_{g_k} \sim \mathcal{CN}(0, \mathbf{R}_g)$, where $\mathbf{R}_g = \mathbf{U}_g \mathbf{\Lambda}_g \mathbf{U}_g^H$ is the covariance matrix of the group g. Based on the AoD of the users, the correlation matrix can be written as:

$$\mathbf{R}_g = [\mathbf{U}_g^{+}, \mathbf{U}_g^{-}][\mathbf{\Lambda}_g^{+}, \mathbf{\Lambda}_g^{-}][\mathbf{U}_g^{+}, \mathbf{U}_g^{-}]^H, \tag{3.25}$$

where $\mathbf{U}_g^{+} \in \mathbb{C}^{N \times r_g^{+}}$ is the matrix of eigenvectors corresponding to the dominant eigenvalues for the user group g. Similarly, $\mathbf{\Lambda}_g^{+} \in \mathbb{C}^{r_g^{+} \times r_g^{+}}$ is the diagonal matrix of the dominant eigenvalues. As a result, the data streams per group is bounded by $S_g \in [0, \min\{K_g, r_g^{+}\}]$. Furthermore, the multiplexing gain limits the maximum number of independent data streams per group that can be transmitted, which is $\min\{K_g, r_g^{+}\}$. Thus, the total data streams can be written as $S = \sum_{g=1}^{G} S_g$. The selection of N_{RF_g} is a design parameter and the performance of HBF heavily depends on its value such that: (i) $N_{RF_g} \geq S_g$ to ensure that the minimum number of RF chains used per group in HBF is not less than the transmitted signals per group, and (ii) the total number of RF chains is determined by the number of groups for K users (i.e., $N_{RF} = \sum_{g=1}^{G} N_{RF_g}$). The RF beamforming matrix $\mathbf{B}_A$ depends on the second-order statistics as it relies on the eigenvalues and eigenvectors extracted from the covariance matrix $\mathbf{R}_g$. If $\mathbf{B}_{A_g} = \mathbf{U}_g^{+}$ is the RF beamforming matrix of group g, then the complete RF beamforming matrix can be written as:

$$\mathbf{F}_D = [\mathbf{F}_{D_1}, \mathbf{F}_{D_2}, \ldots, \mathbf{F}_{D_G}]. \tag{3.26}$$

3.4.2.2 Design of Transfer Block and Constant-Gain RF Beamformer

From (3.26), we can see that $\mathbf{F}_D$ has non-constant modulus entities, which results in a variable-gain RF-stage. To the best of our knowledge, the design of constant-gain analog precoder in mMIMO, which is based on eigen beamforming has not been considered yet. For this challenging issue, we formulate an optimization problem and introduce a transfer block

$\mathbf{T} \in \mathbb{C}^{N_{RF} \times N_{RF}}$ as shown in Figure 1(b) such that $\mathbf{F}_D = \hat{\mathbf{F}}_D \mathbf{T}$, where $\mathbf{F}_D \in \mathbb{C}^{N_T \times N_{RF}}$ is the variable-gain RF beamformer as given in (3.26), $\mathbf{T} \in \mathbb{C}^{N_{RF} \times N_{RF}}$ is the transfer block placed at the baseband stage and $\hat{\mathbf{F}}_D \in \mathbb{C}^{N_T \times N_{RF}}$ is the RF beamformer with constant-gain. The transfer block $\mathbf{T}$ and the RF beamformer with constant-modulus $\hat{\mathbf{F}}_D$ is designed as:

$$\begin{aligned} \underset{\mathbf{T}, \hat{\mathbf{F}}_D}{\arg\min} \quad & \left\| \mathbf{F}_D - \hat{\mathbf{F}}_D \mathbf{T} \right\|_2^2, \\ \text{s.t.} \quad & \hat{\mathbf{F}}_D \in \mathbb{F}_{D_o}, \end{aligned} \tag{3.27}$$

where $\mathbb{F}_{D_o}$ represents the set of matrices of size $N_T \times N_{RF}$ satisfying the unit-modulus property for the constrained RF-beamformer $\hat{\mathbf{F}}_D$, which is constructed using double-PS structure as shown in Fig. 3.4(b). The optimization problem is formulated to design the RF beamformer $\hat{\mathbf{F}}_D$ satisfying the modulus constraint and targeting the same performance as $\mathbf{F}_D$, where $\mathbf{F}_D$ is the RF beamformer whose entities does not satisfy the modulus constraint. Since (3.27) is non-convex because of the unit-modulus constraint, and as proven in [90, Lemma 1], we can dissolve $\hat{\mathbf{F}}_D$ into $\hat{\mathbf{F}}_{D_1} \in \mathbb{C}^{N_T \times N_{RF}}$ and $\hat{\mathbf{F}}_{D_2} \in \mathbb{C}^{N_T \times N_{RF}}$ based on double-PS structure, and can rewrite the equivalent optimization problem as:

$$\begin{aligned} \underset{\mathbf{T}, \hat{\mathbf{F}}_{D_1}, \hat{\mathbf{F}}_{D_2}}{\arg\min} \quad & \left\| \mathbf{F}_D - \left(\hat{\mathbf{F}}_{D_1} + \hat{\mathbf{F}}_{D_2} \right) \mathbf{T} \right\|_2^2, \\ \text{s.t.} \quad & \hat{\mathbf{F}}_{D_1}, \hat{\mathbf{F}}_{D_2} \in \mathbb{F}_{D_o}, \\ & \hat{\mathbf{F}}_D = \hat{\mathbf{F}}_{D_1} + \hat{\mathbf{F}}_{D_2} \end{aligned} \tag{3.28}$$

Then, the optimal solution for the transfer block $\mathbf{T}$ and constant-modulus RF beamformer $\hat{\mathbf{F}}_D$ is given as:

$$\hat{\mathbf{F}}_{D_1}(a,b) = e^{j\left(\angle \mathbf{F}_D(a,b) + \cos^{-1}\left(\frac{\mathbf{F}_D(a,b)}{2\nu} \right) \right)}, \tag{3.29a}$$

$$\hat{\mathbf{F}}_{D_2}(a,b) = e^{j\left(\angle \mathbf{F}_D(a,b) - \cos^{-1}\left(\frac{\mathbf{F}_D(a,b)}{2\nu} \right) \right)}, \tag{3.29b}$$

$$\mathbf{T} = \left(\hat{\mathbf{F}}_{D_1} + \hat{\mathbf{F}}_{D_2} \right)^{\dagger} \mathbf{F}_D, \tag{3.29c}$$

where $\nu = \frac{1}{2} \max_{a,b} |\mathbf{F}_D(a,b)|$ is the half of the highest modulus element at $\mathbf{F}_D$. Each RF chain is connected to the corresponding antenna element through two PSs, which are summed up together to formulate the RF beamforming gain. This summation allows the gain of each RF beamformer entity to vary between 0 and 2, i.e., by relaxing the unit-modulus constraint, the new constraint of the analog stage is $|\hat{\mathbf{F}}_D(a,b)| \leq 2 \ \forall \ a, b$. By implementing the double-PS structure, we can have PS-only RF beamformer without having any impact on the performance of eigen beamforming. In other words, without $\mathbf{T}$ and double-PS structure at RF stage, we would require variable-gain controllers together with PSs, which makes the implementation of HBF using low-resolution PSs challenging.

3.4.2.3 RF Beamformer Quantization

By the introduction of the transfer block in the HBF architecture, each entity of the RF beamformer $\hat{\mathbf{F}}_D$, which is expressed in (3.29), can be converted to a modulus constraint within 0 and 2 (Figure 1(c)). Thus, the analog RF beamformer $\hat{\mathbf{F}}_D$ can have only PSs for the RF processing. Since the phase of each entry of $\hat{\mathbf{F}}_D$ tends to be highly quantized as well as the use of full-resolution PSs is impractical because of the high cost and power consumption, therefore, we need to investigate the performance of our proposed HBF by using low-resolution PSs to be used in a more realistic scenario. For this purpose, we quantize the phase of each entry of $\hat{\mathbf{F}}_D$ i.e., phases of the $(2 \times N_{\scriptscriptstyle RF} N)$ entries of $\hat{\mathbf{F}}_D$ are quantized up to b bits of precision. Each (i, j)th entry is quantized to its nearest neighbor based on the closest Euclidean distance. Thus, we can write as:

$$\hat{l} = \underset{l \,\in\, \mathbb{L}_o}{\arg\min} \left| \vartheta - \frac{2\pi l}{L} \right|, \tag{3.30}$$

where ϑ is the unquantized phase of each entity of RF beamformer obtained from (3.29), $L = 2^b$ and $\mathbb{L}_o$ is the set of all possible quantized phase values i.e., $\mathbb{L}_o = \{0, \ldots, 2^{b-1}\}$. Then the quantized phase of each entry of $\hat{\mathbf{F}}_D$ can be written as:

$$\hat{\vartheta} = \frac{2\pi \hat{l}}{L}.$$

3.4.2.4 RF Beamformer Design for Low-Resolution PSs

As discussed earlier, the straightforward approach for HBF using low-resolution PSs is to design the RF-stage based on full-resolution PSs first, and then quantizing the value of each PSs to a finite set. However, this approach yields a large sum-rate degradation and thus, it is not effective for very low-resolution PSs. To reduce the sum-rate degradation resulting from the constraint of low-resolution PSs, we design the RF beamformer by minimizing the Euclidean distance between the HBF using full-resolution PSs and the HBF using low-resolution PSs. The optimization problem can be formulated as:

$$\begin{aligned} \underset{\mathbf{T}^{(q)},\hat{\mathbf{F}}_D^{(q)}}{\arg\min} \quad & \left\| \hat{\mathbf{F}}_D\mathbf{T} - \hat{\mathbf{F}}_D^{(q)}\mathbf{T}^{(q)} \right\|_F, \\ \text{s.t.} \quad & \hat{\mathbf{F}}_D^{(q)} \in \hat{\mathbb{F}}_D^{(q)}, \\ & \left\| \hat{\mathbf{F}}_D^{(q)}\mathbf{T}^{(q)} \right\|_F^2 = N_{RF}, \end{aligned} \tag{3.31}$$

where $\hat{\mathbb{F}}_D^{(q)}$ represents the set of matrices of size $N_T \times N_{RF}$ under the following constraints: (i) the gain of each entity of the matrix can vary between 0 and 2, and (ii) the phase of each matrix entity is quantized to enable the use of low-resolution PSs at the RF-stage, $\hat{\mathbf{F}}_D\mathbf{T}$ is the optimal unconstrained precoding matrix, $\hat{\mathbf{F}}_D^{(q)}$ and $\mathbf{T}^{(q)}$ are the RF beamformer and the transfer block designed for low-resolution PSs, respectively. The design problem can be defined as finding the projections of the optimal unconstrained precoder $\hat{\mathbf{F}}_D\mathbf{T}$ onto the set of $\hat{\mathbf{F}}_D^{(q)}$ and $\mathbf{T}$. Each entry of $\hat{\mathbf{F}}_D^{(q)}$ follows modulus constraint and can have a distinct phase value as depicted by the constraint $\hat{\mathbf{F}}_D^{(q)} \in \hat{\mathbb{F}}_D^{(q)}$. Furthermore, $\left\| \hat{\mathbf{F}}_D^{(q)}\mathbf{T}^{(q)} \right\|_F^2 = N_{RF}$ represents the normalized transmit power constraint of the RF beamformer. Due to the complex non-convex nature of the feasible set $\hat{\mathbb{F}}_D^{(q)}$, the problem of finding the projections is difficult. However, we can notice that there exits a connection between $\hat{\mathbf{F}}_D$ and $\hat{\mathbf{F}}_D^{(q)}$ by exploiting the structure of the channel $\mathbf{H}$. This can be further explained by the following *remarks*.

1. *Structure of unconstrained RF beamformer*: The design of unconstrained RF beamformer $\hat{\mathbf{F}}_D$ is based on Karhunen-Loeve decomposition of the covariance matrix $\mathbf{R}$. Thus, the eigenvectors (column vectors) for the corresponding dominant eigenvalues form an orthonormal basis.

2. *Relation between $\hat{\mathbf{F}}_D$ and $\hat{\mathbb{F}}_D^{(q)}$*: We notice that there exits an association between $\hat{\mathbf{F}}_D$ and $\hat{\mathbb{F}}_D^{(q)}$ as both are based on the dominant eigenvalues extracted from the covariance matrix. In fact, $\hat{\mathbb{F}}_D^{(q)}$ is the set of quantized matrices of $\mathbf{U}^+$, where $\mathbf{U}^+ = [\mathbf{U}_1^+, \mathbf{U}_2^+, \dots, \mathbf{U}_G^+]$.

3. *Transfer block*: The problem of finding projection of $\hat{\mathbf{F}}_D$ onto $\hat{\mathbf{F}}_D^{(q)}$ alone is challenging. By using the transfer block $\mathbf{T}$, we can find the projection of $\hat{\mathbf{F}}_D\mathbf{T}$ onto the set of $\hat{\mathbf{F}}_D^{(q)}$ and $\mathbf{T}$.

4. *Design of $\hat{\mathbf{F}}_D^{(q)}$*: It must be seen that the feasible quantized RF beamformers in $\hat{\mathbb{F}}_D^{(q)}$ are of size $N_T \times N_{RF}$. Thus, each column of the constrained RF beamformer $\hat{\mathbf{F}}_D^{(q)}$ can be designed by applying N_{RF} vectors, where each vector follows the constant-modulus

Algorithm 3.1 Constrained RF Beamformer Design via Orthogonal Matching Pursuit

```
Given: Optimal unconstrained RF beamformer $\hat{\mathbf{F}}_D = [\hat{\mathbf{F}}_{D_1}, \hat{\mathbf{F}}_{D_2}, \dots, \hat{\mathbf{F}}_{D_G}]$
for $g = 1 : G$ do
    $\hat{\mathbf{F}}_{D_g}^{(q)} = [\ ]$
    $\mathbf{F}_{res_g} = \hat{\mathbf{F}}_{D_g}\mathbf{T}_g$
    for $j \leq N_{RF_g}$ do
        $\Upsilon_g = (\hat{\mathbf{U}}_g^{+})^{*}\mathbf{F}_{res_g}$
        Find the index $l$ which maximizes $(\Upsilon_g \Upsilon_g^{*})$
        $\hat{\mathbf{F}}_{D_g}^{(q)} = \left[\hat{\mathbf{F}}_{D_g}^{(q)} | \hat{\mathbf{U}}_g^{+(l)}\right]$
        Compute $\mathbf{T}_g^{(q)}$ by using least squares
        $\mathbf{T}_g^{(q)} = \left(\hat{\mathbf{F}}_{D_g}^{(q)*}\hat{\mathbf{F}}_{D_g}^{(q)}\right)^{-1}\hat{\mathbf{F}}_{D_g}^{(q)}\hat{\mathbf{F}}_{D_g}$
        $\mathbf{F}_{res_g} = \frac{\hat{\mathbf{F}}_{D_g}\mathbf{T}_g - \hat{\mathbf{F}}_{D_g}^{(q)}\mathbf{T}_g^{(q)}}{\left\|\hat{\mathbf{F}}_{D_g}\mathbf{T}_g - \hat{\mathbf{F}}_{D_g}^{(q)}\mathbf{T}_g^{(q)}\right\|_F}$
    end for
    $\tilde{\mathbf{T}}_g^{(q)} = \frac{N_{RF_g}}{\left\|\hat{\mathbf{F}}_{D_g}^{(q)}\mathbf{T}_g^{(q)}\right\|_F}\mathbf{T}_g^{(q)}$
end for
$\tilde{\mathbf{T}}^{(q)} = [\tilde{\mathbf{T}}_1^{(q)}, \tilde{\mathbf{T}}_2^{(q)}, \dots, \tilde{\mathbf{T}}_G^{(q)}]$
$\hat{\mathbf{F}}_D^{(q)} = [\hat{\mathbf{F}}_{D_1}^{(q)}, \hat{\mathbf{F}}_{D_2}^{(q)}, \dots, \hat{\mathbf{F}}_{D_G}^{(q)}]$
return $\tilde{\mathbf{T}}^{(q)}$, $\hat{\mathbf{F}}_D^{(q)}$
```

and have distinct phase values only. Furthermore, by using the transfer block $\mathbf{T}$, we can form the arbitrary linear combinations of N_{RF} vectors and design the constrained RF beamformer by reducing the Euclidean distance i.e., $\left\|\hat{\mathbf{F}}_D\mathbf{T} - \hat{\mathbf{F}}_D^{(q)}\mathbf{T}^{(q)}\right\|_F$.

Based on remark 2, the optimal constrained RF beamformer can be found by replacing $\hat{\mathbb{F}}_A^{(q)}$ with $\hat{\mathbb{U}}^{+}$, where $\hat{\mathbb{U}}^{+}$ represents the set of matrices of quantized eigenvectors corresponding to the dominant eigenvalues, i.e., $\hat{\mathbf{U}}^{+}$. Subsequently, we can rewrite the optimization problem as follows:

$$\begin{aligned} \underset{\mathbf{T}^{(q)}, \hat{\mathbf{F}}_D^{(q)}}{\arg\min} \quad & \left\|\hat{\mathbf{F}}_D\mathbf{T} - \hat{\mathbf{F}}_D^{(q)}\mathbf{T}^{(q)}\right\|_F, \\ \text{s.t.} \quad & \hat{\mathbf{F}}_D^{(q)} \in \hat{\mathbb{U}}^{+}, \\ & \left\|\hat{\mathbf{F}}_D^{(q)}\mathbf{T}^{(q)}\right\|_F^2 = N_{RF}. \end{aligned} \tag{3.32}$$

We can append the constraint $\hat{\mathbf{F}}_D^{(q)}$ into the optimization objective and formulate the equivalent problem as [88]:

$$\begin{aligned} \underset{\mathbf{T}^{(q)}}{\arg\min} \quad & \left\| \hat{\mathbf{F}}_D \mathbf{T} - \hat{\mathbf{U}}^{+} \mathbf{T}^{(q)} \right\|_F , \\ \text{s.t.} \quad & \left\| \operatorname{diag}(\mathbf{T}^{(q)} \mathbf{T}^{(q)*}) \right\|_0 = N_{RF}, \end{aligned} \tag{3.33}$$

where the constraint $\left\| \operatorname{diag}(\mathbf{T}^{(q)} \mathbf{T}^{(q)*}) \right\|_0 = N_{RF}$ states that the matrix $\mathbf{T}^{(q)}$ acts as an auxilliary variable and can only have a maximum of N_{RF} non-zero rows. As a result, only N_{RF} columns of $\hat{\mathbf{U}}^{+}$ are selected and thus, the transfer block $\mathbf{T}^{(q)}$ can be designed by N_{RF} non-zero rows. The constrained RF beamformer is formulated by projecting the N_{RF} columns of $\hat{\mathbf{U}}^{+}$ onto $\hat{\mathbf{F}}_D$. By employing the OMP technique proposed in [87, 88], we present an algorithmic solution to design the constrained RF beamformer for low-resolution PSs. The pseudo-code is given in Algorithm 3.1, which can be summarized as: (i) the algorithm starts by initializing the constrained precoder $\hat{\mathbf{F}}_{D_g}^{(q)}$ as an empty matrix, (ii) finds the vector along which the unconstrained precoder has the maximum projection, (ii) append the selected column vector to the empty matrix $\hat{\mathbf{F}}_{D_g}^{(q)}$, (iv) using least squares, find the transfer block $\mathbf{T}_g^{(q)}$, (v) remove the contribution of the selected vector, and (vi) finding the column along which the residual precoding matrix $\mathbf{F}_{res_g}$ has the largest projection. The algorithm continues until we find N_{RF_g} precoding vectors. As a result, we get an $N_T \times N_{RF_g}$ RF preoding matrix and $N_{RF_g} \times N_{RF_g}$ transfer matrix. Finally, from Algorithm 3.1, step 11 ensures that the transmit power constraint is satisfied. The process is repeated for all G user groups. Combining the RF and transfer matrix of all groups, we get a large $N_T \times N_{RF}$ RF preoding matrix and $N_{RF} \times N_{RF}$ transfer matrix which minimizes $\left\| \hat{\mathbf{F}}_D \mathbf{T} - \hat{\mathbf{F}}_D^{(q)} \mathbf{T}^{(q)} \right\|_F^2$.

Lemma 3.1. *If the Euclidean distance before normalization is* $\left\| \hat{\mathbf{F}}_{D_g} \mathbf{T}_g - \hat{\mathbf{F}}_{D_g}^{(q)} \mathbf{T}_g^{(q)} \right\|_F \leq \zeta$, *then the Euclidean distance after normalization is* $\left\| \hat{\mathbf{F}}_{D,g} \mathbf{T}_g - \hat{\mathbf{F}}_{D,g}^{(q)} \tilde{\mathbf{T}}_g^{(q)} \right\|_F \leq 2\zeta$.

Proof. See Appendix.

3.4.2.5 Baseband MU Precoder Design

After the design of RF beamformer $\hat{\mathbf{F}}_D^{(q)}$ for b-bit PSs, the baseband MU precoder $\mathbf{B}_D$ can be determined by using the joint group processing (JGP) [60]. The overall reduced dimensional effective channel matrix is expressed as $\boldsymbol{\mathcal{H}} = \tilde{\mathbf{T}}^{(q)} \hat{\mathbf{B}}_A^{(q)H} \mathbf{H}$. Using (3.8) and

(3.26), $\boldsymbol{\mathcal{H}}^H$ can be written as:

$$\boldsymbol{\mathcal{H}}^H = \begin{bmatrix} \mathbf{H}_1^H \hat{\mathbf{F}}_{D_1}^{(q)} \tilde{\mathbf{T}}_1^{(q)} & \mathbf{H}_1^H \hat{\mathbf{F}}_{D_2}^{(q)} \tilde{\mathbf{T}}_2^{(q)} & \dots & \mathbf{H}_1^H \hat{\mathbf{F}}_{D_G}^{(q)} \tilde{\mathbf{T}}_G^{(q)} \\ \mathbf{H}_2^H \hat{\mathbf{F}}_{D_1}^{(q)} \tilde{\mathbf{T}}_1^{(q)} & \mathbf{H}_2^H \hat{\mathbf{F}}_{D_2}^{(q)} \tilde{\mathbf{T}}_2^{(q)} & \dots & \mathbf{H}_2^H \hat{\mathbf{F}}_{D_G}^{(q)} \tilde{\mathbf{T}}_G^{(q)} \\ \vdots & \vdots & \ddots & \vdots \\ \mathbf{H}_G^H \hat{\mathbf{F}}_{D_1}^{(q)} \tilde{\mathbf{T}}_1^{(q)} & \mathbf{H}_G^H \hat{\mathbf{F}}_{D_2}^{(q)} \tilde{\mathbf{T}}_2^{(q)} & \dots & \mathbf{H}_G^H \hat{\mathbf{F}}_{D_G}^{(q)} \tilde{\mathbf{T}}_G^{(q)} \end{bmatrix}, \tag{3.34}$$

where the diagonal matrices $\mathbf{H}_g^H \hat{\mathbf{F}}_{D_g}^{(q)} \tilde{\mathbf{T}}_g \in \mathbb{C}^{K_g \times N_{RF_g}}$ are the effective channel matrix for group g and the off-diagonal matrices $\mathbf{H}_g^H \hat{\mathbf{F}}_{D_{\hat{g}}}^{(q)} \tilde{\mathbf{T}}_{\hat{g}} \in \mathbb{C}^{K_g \times N_{RF_{\hat{g}}}}$ represent the effective interference channel matrix between groups g and $\hat{g}$, $\forall \hat{g} \neq g$. By applying the well-known RZF technique [84, 85], $\mathbf{B}_D$ can be defined as:

$$\mathbf{B}_D = \gamma \mathbf{X} \boldsymbol{\mathcal{H}}^H, \tag{3.35}$$

where $\boldsymbol{\mathcal{H}}^H$ is the reduced-dimension effective channel as given in (3.34), $\mathbf{X} = [\boldsymbol{\mathcal{H}}^H \boldsymbol{\mathcal{H}} + \alpha N_{RF} \mathbf{I}_{N_{RF}}]^{-1}$, $\mathbf{I}_{N_{RF}} \in \mathbb{C}^{N_{RF} \times N_{RF}}$, α is the regularization paramter and γ is the normalization factor used to satisfy the power constraint, which can be written as:

$$\gamma = \sqrt{\frac{S}{\mathrm{tr}\{\boldsymbol{\mathcal{H}}^H \mathbf{X}^H \tilde{\mathbf{T}}^{(q)H} \hat{\mathbf{F}}_D^{(q)H} \hat{\mathbf{F}}_D^{(q)} \tilde{\mathbf{T}}^{(q)} \mathbf{X} \boldsymbol{\mathcal{H}}\}}}. \tag{3.36}$$

Therefore, the signal-to-interference-plus-noise ratio (SINR) at the user k in group g can be computed as follows:

$$\mathrm{SINR}_{g_k} = \frac{\frac{P_T}{S} |\mathbf{h}_{g_k}^H \hat{\mathbf{F}}_D^{(q)} \tilde{\mathbf{T}}^{(q)} \mathbf{X} \tilde{\mathbf{T}}^{(q)H} \hat{\mathbf{F}}_D^{(q)H} \mathbf{h}_{g_k}|^2}{1 + \frac{P_T}{S} \sum\limits_{i \neq g_k} |\mathbf{h}_{g_k}^H \hat{\mathbf{F}}_D^{(q)} \tilde{\mathbf{T}}^{(q)} \mathbf{X} \tilde{\mathbf{T}}^{(q)H} \hat{\mathbf{F}}_D^{(q)H} \mathbf{h}_i|^2}, \tag{3.37}$$

where $\frac{P_T}{S} \sum\limits_{i \neq g_k} |\mathbf{h}_{g_k}^H \hat{\mathbf{F}}_D^{(q)} \tilde{\mathbf{T}}^{(q)} \mathbf{X} \tilde{\mathbf{T}}^{(q)H} \hat{\mathbf{F}}_D^{(q)H} \mathbf{h}_i|^2$ accounts for MU interference. Hence, the corresponding sum-rate performance can be computed as:

$$R_{\mathrm{sum}} = \sum_{g=1}^{G} \sum_{g_k=1}^{K_g} \mathbb{E}[\log_2(1 + \mathrm{SINR}_{g_k})]. \tag{3.38}$$

3.5 Hybrid Beamforming Design Using Low-Resolution PSs and DACs

In this section, we design the HBF using low-resolution hardware components (i.e., q-bit DACs and b-bit PSs). The HBF structure is shown in Fig. 3.4(c). Based on the AoD information of users, we design the RF beamformer and the baseband MU precoder along with a transfer block such that quantization error is minimized.

3.5.1 RF Beamformer and Transfer Block Design

Following the same user distribution as discussed in Section 3.4.2.1, K users are clustered into G groups. Based on the AoD of the users, the correlation matrix of group g is given in (3.25), which consists of the dominant eigenvectors $\mathbf{U}_g^+ \in \mathbb{C}^{N\times r_g^+}$ corresponding to the dominant eigenvalues $\mathbf{\Lambda}_g^+ \in \mathbb{C}^{r_g^+\times r_g^+}$. Moreover, $\min\{K_g,\ r_g^+\}$ limits the maximum number of the independent data streams that can be transmitted. By using Karhunen-Loeve decomposition, we can write the user channel vector $\mathbf{h}_{g_k}$ and the overall channel matrix $\mathbf{H}$ as given in (3.7) and (3.8), respectively. If $\mathbf{F}_{D_g} = \mathbf{U}_g^+$ is the RF beamforming matrix of group g having non-constant modulus, then the complete RF beamforming matrix can be written as given in (3.26). As discussed in Section 3.4.2.2, the variable-gain RF beamforming matrix $\mathbf{F}_{D_g}$ can be converted to a constant-gain beamforming matrix $\hat{\mathbf{F}}_{D_g}$ by using a transfer block $\mathbf{T}_g$ at the baseband. Using this approach, we can rewrite (3.26) as:

$$\mathbf{F}_D = [\hat{\mathbf{F}}_{D_1}\mathbf{T}_1, \hat{\mathbf{F}}_{D_2}\mathbf{T}_2, \ldots, \hat{\mathbf{F}}_{D_G}\mathbf{T}_G]. \tag{3.39}$$

$\hat{\mathbf{F}}_{D_g}$ and $\mathbf{T}_g$ can be found using (3.29), respectively. However, since the RF beamformer employs b-bit PSs for the phase quantization, we can rewrite (3.39) as:

$$\mathbf{F}_D^{(q)} = [\hat{\mathbf{F}}_{D_1}^{(q)}\mathbf{T}_1^{(q)}, \hat{\mathbf{F}}_{D_2}^{(q)}\mathbf{T}_2^{(q)}, \ldots, \hat{\mathbf{F}}_{D_G}^{(q)}\mathbf{T}_G^{(q)}]. \tag{3.40}$$

By using the solution given in Algorithm 3.1, we can find $\hat{\mathbf{F}}_{D_g}^{(q)}$ and $\mathbf{T}_g^{(q)}$ for HBF using b-bit PSs at the RF-stage. The overall RF beamforming matrix and the transfer matrix for low-resolution PSs can be given as:

$$\hat{\mathbf{F}}_D^{(q)} = [\hat{\mathbf{F}}_{D_1}^{(q)}, \hat{\mathbf{F}}_{D_2}^{(q)}, \ldots, \hat{\mathbf{F}}_{D_G}^{(q)}]. \tag{3.41}$$

$$\mathbf{T}^{(q)} = [\mathbf{T}_1^{(q)}, \mathbf{T}_2^{(q)} \ldots, \mathbf{T}_G^{(q)}]. \tag{3.42}$$

3.5.2 Baseband MU Precoder Design With Finite-Resolution DACs

In this section, the design of the baseband MU precoder $\hat{\mathbf{B}}_D^{(q)}$ using q-bit DACs is presented. After designing RF beamformer $\hat{\mathbf{F}}_D^{(q)}$ and the transfer block $\mathbf{T}^{(q)}$ for b-bit PSs as given in (3.41) and (3.42), respectively, the quantized baseband precoder $\hat{\mathbf{B}}_D^{(q)}$ can be designed using RZF as given in (3.35). The use of q-bit DACs introduces the quantization noise. Therefore, the signal to quantization, interference and noise ratio (SQINR) at the user k in group g can be computed as given in (3.43), where $\frac{P_T}{S} \sum_{i \neq g_k} |\mathbf{h}_{g_k}^H \hat{\mathbf{F}}_D^{(q)} \tilde{\mathbf{T}}^{(q)} \mathbf{X} \tilde{\mathbf{T}}^{(q)H} \hat{\mathbf{F}}_D^{(q)H} \mathbf{h}_i|^2$ accounts for the interference experienced by users in group g from the users in group $\hat{g} \neq g$ and $\frac{P_T}{S} |\mathbf{h}_{g_k}^H \hat{\mathbf{F}}_D^{(q)} \tilde{\mathbf{T}}^{(q)} \mathbf{R}_{n_q} (\tilde{\mathbf{T}}^{(q)H} \hat{\mathbf{F}}_D^{(q)H} \mathbf{h}_{g_k})^H|^2$ is the quantization noise when using q-bit DACs. Hence, the corresponding sum-rate performance of HBF with b-bit PSs and q-bit DACs can be computed as:

$$R_{\text{sum}} = \sum_{g=1}^{G} \sum_{g_k=1}^{K_g} \mathbb{E}[\log_2(1 + \text{SQINR}_{g_k})]. \tag{3.44}$$

3.6 Simulation Results

In this section, the Monte-Carlo simulation results are presented based on the hybrid precoding for various array structures. For the presented results, the BS is equipped with 100 isotropic antennas, arranged in 1×100 ULA and 10×10 URA configurations. In UCA, the antennas are equally distributed on a circle of radius $\lambda\nabla$ where $\nabla = \frac{1}{2\sqrt{(1-\cos(\frac{2\pi}{N_T}))^2 + \sin(\frac{2\pi}{N_T})^2}}$, whereas the antennas are distributed on multiple circular rings in CCA. The radius of nth ring is λR_n, where $R_n = nL$ [94]. Then, the corresponding number of antennas on nth ring is $N_n = \frac{2\pi R_n}{d}$, where d is the antenna spacing which is selected as $\frac{\lambda}{2}$ for all array structures. L is the inter-ring spacing which is selected as 0.55λ. Using this configuration of CCA, 100

$$\text{SQINR}_{g_k} = \frac{\frac{P_T}{S} |\mathbf{h}_{g_k}^H \hat{\mathbf{F}}_D^{(q)} \tilde{\mathbf{T}}^{(q)} \mathbf{X} \tilde{\mathbf{T}}^{(q)H} \hat{\mathbf{F}}_D^{(q)H} \mathbf{h}_{g_k}|^2}{1 + \frac{P}{S} \sum_{i \neq g_k} |\mathbf{h}_{g_k}^H \hat{\mathbf{F}}_D^{(q)} \tilde{\mathbf{T}}^{(q)} \mathbf{X} \tilde{\mathbf{T}}^{(q)H} \hat{\mathbf{F}}_D^{(q)H} \mathbf{h}_i|^2 + \frac{P_T}{S} |\mathbf{h}_{g_k}^H \hat{\mathbf{F}}_D^{(q)} \tilde{\mathbf{T}}^{(q)} \mathbf{R}_{n_q} (\tilde{\mathbf{T}}^{(q)H} \hat{\mathbf{F}}_D^{(q)H} \mathbf{h}_{g_k})^H|^2}, \tag{3.43}$$

antennas can be arranged in just 5 rings. The signal-to-noise-ratio (SNR) is defined as $\frac{P}{\sigma^2 K}$ and the regularization parameter $\alpha = \frac{\sigma^2}{P}$ [85]. In the following analysis, the array structures performance is compared based on: i) *spatial efficiency*, ii) *sum-rate versus users AoD*, iii) *sum-rate versus number of the users.*

3.6.1 Spatial Efficiency

To arrange 100 antenna elements with an inter-element spacing d, It can be seen that the 1×100 ULA requires 50λ space in one direction. On the other hand, 10×10 URA requires just 5λ space in horizontal and vertical directions, which is equivalent to a space of $25\lambda^2$. Similarly, UCA with a radius of about 7.96λ (D = 15.92 λ) requires an array size of approximately $199\lambda^2$. It can be seen that URA is more spatially efficient structure compared to both ULA and UCA. In CCA, 100 antennas can be arranged in 5 rings as discussed before. The maximum ring radius in CCA is about 2.75λ, which is more than *three times* smaller in size than UCA having the same number of antennas. In other words, this is equivalent to a space of approximately $24\lambda^2$. To better understand the spatial efficiency, consider the signal frequency is 6 GHz (sub-6 GHz mMIMO frequency). Then, the array sizes of ULA, URA, UCA, and CCA are respectively 2.5 m, 0.0625 m^2, 0.49 m^2, and 0.0592 m^2. Thus, CCA offers the highest spatial efficiency, whereas ULA is the least spatially efficient structure.

3.6.2 Performance Comparison with Full-Resolution Components

In this section, we first compare the performance of different 2D array structures using full-resolution hardware components.

3.6.2.1 Sum-Rate versus User AoD

In this section, the sum-rate of the array structures is compared based on the AoD information of the users around the BS. As discussed, the hybrid precoder is designed using the RF-beamforming stage and the optimized reduced-size baseband stage. The RF-beamforming stage depends on the dominant eigenvalues extracted from the covariance matrix $\mathbf{R}$ [see (3.9)]. Based on the different geometrical configuration of ULA, URA, UCA, and CCA, the rank of the covariance matrix can vary [see (3.4), (3.5)], playing an important role in the sum-rate performance of the array structures. For $N_T = 100$, the rank r is 21 and 17 for UCA and ULA respectively and 13 for CCA and URA. Also, some of the non-zero eigenvalues are too small that can be ignored. So, the dominant eigenvalues r_g^+ of UCA, ULA, CCA, and URA become 10, 9, 4, and 3, respectively. In Table. 3.2, a

Table 3.2. Number of dominant eigenvalues of ULA, URA, UCA, and CCA versus number of antennas.

Number of antennas ($\mathbf{N}_T$)	**URA**	**CCA**	**ULA**	**UCA**
64	3	4	6	8
128	4	6	10	13
256	9	8	19	26
512	14	11	39	49
1024	20	14	71	89

comparison of numbers of the dominant eigenvalues of different array structures is presented. With the increased number of antennas, both ULA and UCA can have a higher value of r_g^+ and can support an increased number of independent data streams. On the other hand, URA and CCA can have a small increase in r_g^+ because of the much-reduced array size. As a result, the correlation between the antennas is increased, resulting in small increment in dominant eigenvalues in URA and CCA. In Fig. 3.5, the sum-rate is calculated for multiple user groups, when $N_T = 100$. We consider three user groups ($G = 3$) are located around the BS at mean azimuth locations $\theta_1 = 30°$, $\theta_2 = 90°$, $\theta_3 = 150°$ with $\Delta = 15°$. The sum-rate performance of hybrid precoding for the array structures is compared with their FDBF counterparts using RZF. Fig. 3.5(a) shows the result of the hybrid precoding without using the transfer block, when $N_{RF_g} = K_g = 3$, $N_{RF} = K = 9$ and $b_g = 3$. As expected, FDBF provides the highest sum-rate. For the hybrid beamforming sum-rates, URA and CCA give the highest sum-rate whereas ULA gives the lowest sum-rate. On the other hand, the sum-rate of UCA is comparable to the sum-rate of URA and CCA. By using the transfer block in the hybrid precoder, when, $N_{RF_g} = K_g = 3$, $N_{RF} = K = 9$ and $b_g = 5$, it can be seen in Fig. 3.5(b) that the sum-rate of the array structures is increased significantly. The sum-rate of URA and CCA approaches to the sum-rate of their FDBF equivalents. Though ULA still provides the lowest sum-rate among the array structures, it shows a sum-rate increase of about 20 bps/Hz after using the transfer block. Thus, we can conclude that for the same number of RF chains, the use of transfer block greatly increases the sum-rate performance of the array structures. Furthermore, both URA and CCA provides the best performance among the array structures by converging to their FDBF sum-rate. Secondly, the sum-rate is compared versus users AoD. For a fixed SNR = 10 dB, the sum-rate using hybrid precoding with a

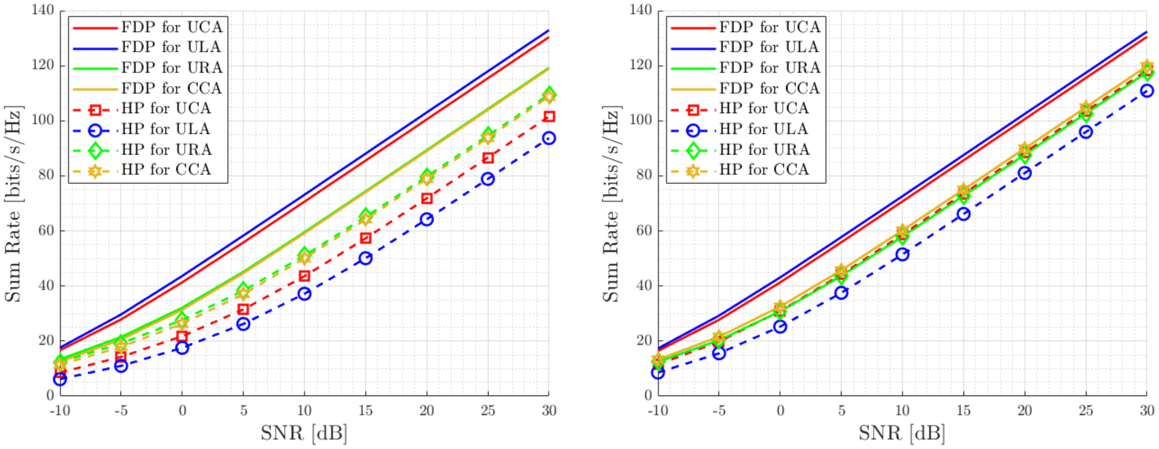

(a) **(b)**

Figure 3.5. Sum-rate comparison of ULA, URA, CCA, and UCA, $N_T = 100$, $G = 3$, $N_{RF_g} = K_g = 3$, $N_{RF} = K = 9$, $\theta_1 = 30°$, $\theta_2 = 90°$, $\theta_3 = 150°$, $\Delta = \pm15°$: (a) $b_g = 3$ without transfer block (b) $b_g = 5$ with transfer block.

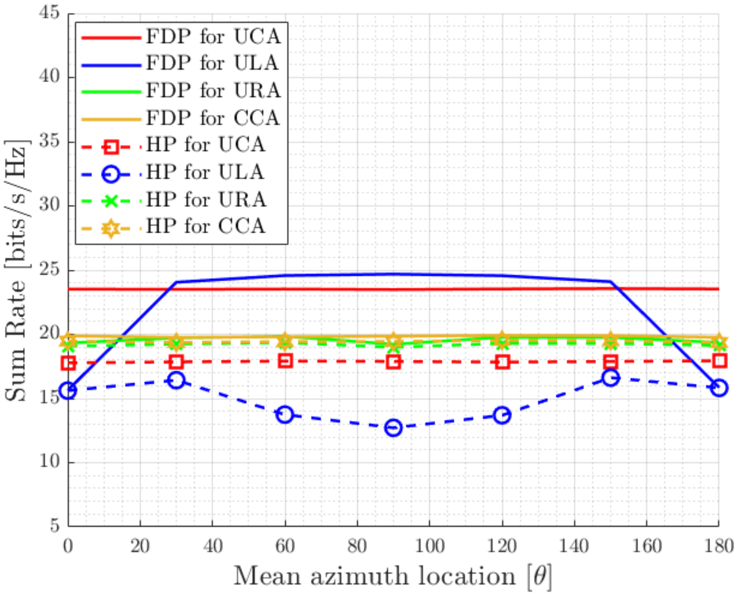

Figure 3.6. Sum-rate comparison of ULA, URA, CCA, and UCA versus mean azimuth user location, $N_T = 100$, $G = 1$, $N_{RF} = K = 3$, $b = 4$, $\Delta = \pm15°$, SNR = 10 dB.

Table 3.3. Performance comparison of ULA, UCA, URA and CCA.

	ULA	**UCA**	**URA**	**CCA**
Spatial efficiency	Low	Low	High	High
Sum-rate versus mean azimuth location $\theta \in [0°,180°]$	Low sum-rate. The sum-rate varies about 5 bps/Hz for fixed K. (see Fig. 3.6)	High sum-rate. The sum-rate remains same for fixed K (see Fig. 3.6)	High sum-rate. The sum-rate varies about 2 bps/Hz for a fixed K (see Fig. 3.6)	High sum-rate. The sum-rate remains same for fixed K (see Fig. 3.6)
Sum-rate versus number of users	Low sum-rate (see Fig. 3.7)	High sum-rate (see Fig. 3.7)	High sum-rate (see Fig. 3.7)	High sum-rate (see Fig. 3.7)

transfer block is compared for the mean azimuth user locations between $\theta = 0°$ to $\theta = 180°$ as shown in Fig. 3.6. URA and CCA give the best sum-rate at all azimuth user locations, when $G = 1$, $N_{RF_g} = K_g = 3$, $N_{RF} = K = 3$, $b_g = b = 4$, $\Delta = \pm 15°$. The sum-rate of ULA is the lowest, whereas UCA gives a reasonably high sum-rate. Furthermore, the sum-rate variation of UCA and CCA is $\ll 1$ bps/Hz, whereas the variation is about 2 bps/Hz for URA. On the other hand, the sum-rate of ULA varies about 5 bps/Hz. Thus, it can be concluded that for a fixed number of users, the hybrid precoding sum-rate can vary w.r.t the *users AoD* depending on the array structure. Both CCA and URA can provide a very high sum-rate at all azimuth user locations.

3.6.2.2 Sum-Rate versus Number of Users

Finally, a comparison of the sum-rate versus the number of users is provided now. In Fig. 3.7, the sum-rate of the array structures using the hybrid precoding is compared for different number of users. The result is shown for a single user group ($G = 1$) at fixed SNR = 10 dB, when $N_{RF_g} = K_g = 3$, $N_{RF} = K = 3$, $b_g = b = 4$, $\theta = 60°$, $\Delta = \pm 15°$. Based on the dominant eigenvalue r_g^+ as discussed previously, the users are gradually increased from 1 to 3, and the corresponding sum-rate of the array structure is plotted. The FDBF sum-rates are compared with the sum-rate of the hybrid precoding with the transfer block. ULA provides the lowest sum-rate performance among the array structures. Also, a large performance gap exists between the FDBF and hybrid precoding results of ULA. UCA provides a reasonably high sum-rate versus K and it can approach its FDBF sum-rate only when $K = 1$. On the other hand, the sum-rate of URA and CCA using the hybrid precoding can approach their respective FDBF sum-rates at all K values as shown in Fig. 3.7. Thus, both URA and CCA can provide the highest sum-rate versus K among the array structures. The overall performance comparison of the array structures is summarized in Table. 3.3.

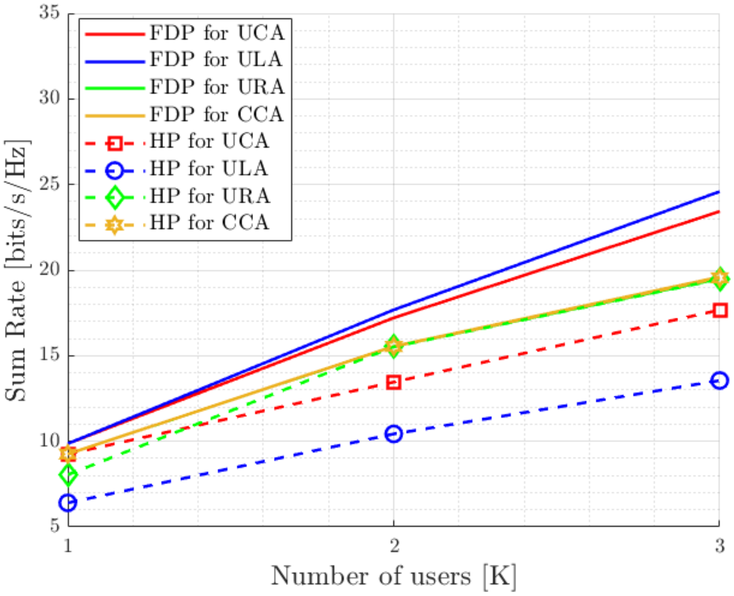

Figure 3.7. Sum-rate comparison of ULA, URA, CCA, and UCA versus number of users, $N_T = 100$, $G = 1$, $N_{RF} = K = 3$, $b = 4$, $\theta = 60°$, $\Delta = \pm 15°$, SNR $= 10$ dB.

3.6.3 Performance Comparison with Low-Resolution DACs

In the following analysis, 2D array structures are compared based on: i) spectral efficiency using q-bit DACs, ii) energy efficiency using q-bit DACs.

3.6.3.1 Spectral Efficiency Using q-Bit DACs:

In this section, we analyze the spectral efficiency of ULA, URA, UCA, and CCA by computing the sum-rate of the HBF using few-bit DACs. At first, we compare the sum-rate of the HBF using q-bit DACs for ULA, URA, UCA, and CCA.

In Fig. 3.8, the sum-rate is calculated for multiple user groups, when $N_T = 100$. We consider three user groups ($G = 3$) are located around the BS at mean elevation angle $\theta = 73°$, mean azimuth locations $(\phi_1, \phi_2, \phi_3) = (30°, 90°, 150°)$ with $\delta_a = 15°$ and $\delta_e = 12.5°$. The sum-rate of HBF for the array structures is compared with their FDBF counterparts using RZF. Figure. 3.8 shows the sum-rate of HBF of different 2D array structures by using different quantization levels of DAC. It can be seen that 1-bit quantization gives the lowest sum-rate for all array structures, though having the advantage of least DAC power consumption. The sum-rate increases with an increase in the number of DAC quantization bits. Moreover, CCA gives the highest sum-rate when compared to ULA, URA, and UCA

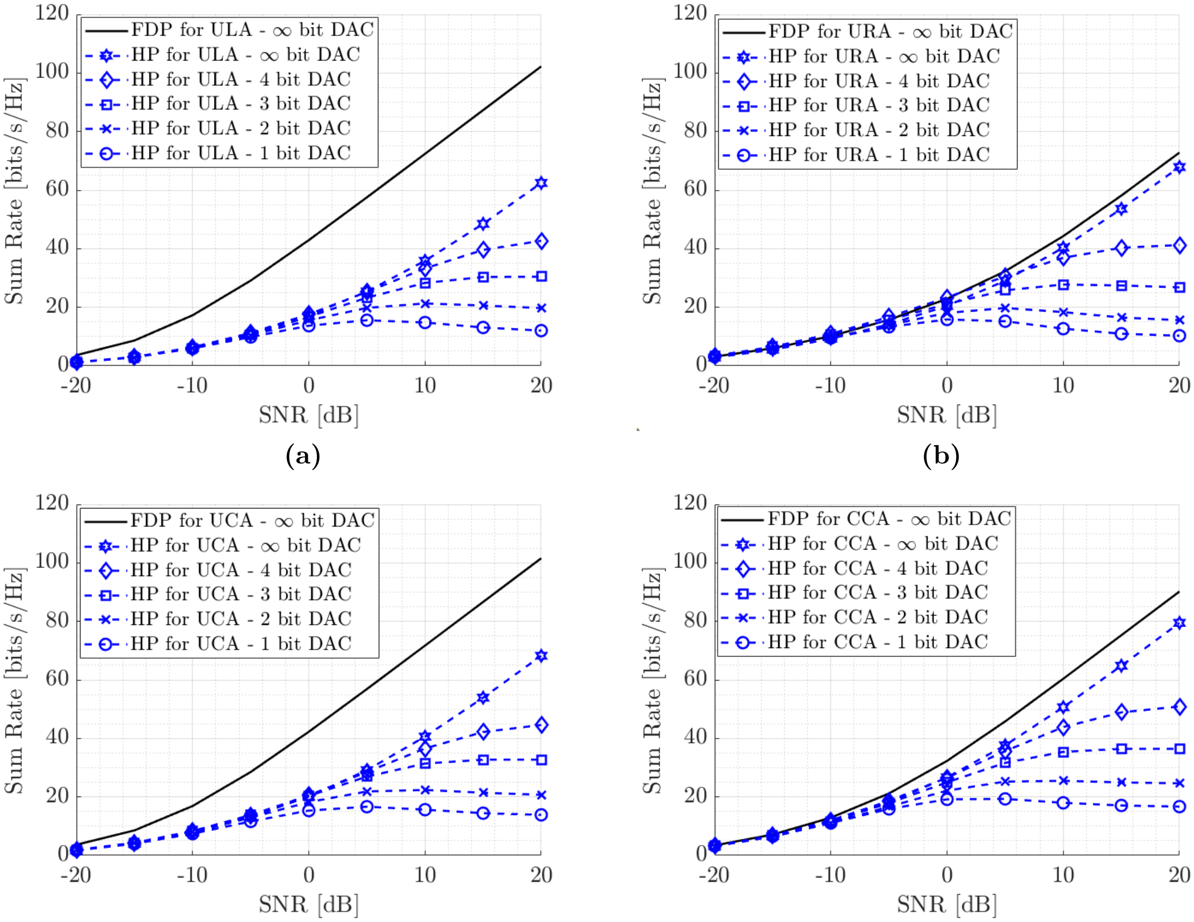

(a) (b)

(c) (d)

Figure 3.8. Sum-rate versus SNR comparison using few-bit DACs, $N_T = 100$, $G = 3$, $N_{RF_g} = K_g = 3$, $N_{RF} = K = 9$, $\theta = 73°$, $(\phi_1, \phi_2, \phi_3) = (30°, 90°, 150°)$, $(\delta_a, \delta_e) = (\pm 15°, \pm 12.5°)$ (a) ULA (b) URA (c) UCA (d) CCA.

for both full and low-resolution DACs.

3.6.3.2 Energy Efficiency Using q-Bit DACs

In this section, the energy efficiency of HBF using q-bit DACs is compared for different 2D array structures. The energy efficiency is defined as the ratio of the sum-rate R_{sum} and the total power consumption P_{total} [95], i.e.,

$$\epsilon = \frac{R_{sum}}{P_{total}} = \frac{R_{sum}}{\mathrm{tr}(\mathbf{B}\mathbf{B}^*) + N_{RF} P_{RF} 2^{2q}}, \tag{3.45}$$

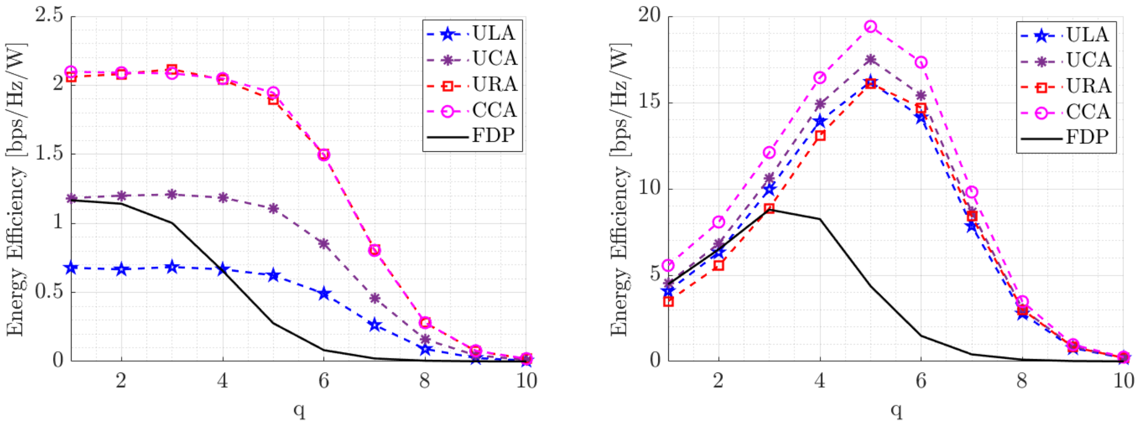

(a) **(b)**

Figure 3.9. Energy efficiency versus q for different array structures, $N_T = 100$, $G = 3$, $N_{RF_g} = K_g = 3$, $N_{RF} = K = 9$, $\delta_a = \pm 15°$, $\delta_e = \pm 12.5°$, $\theta = 73°$, $(\phi_1, \phi_2, \phi_3) = (30°, 90°, 150°)$, (a) SNR = -20 dB (b) 20 dB.

where $\mathrm{tr}(\mathbf{BB}^*)$ represents the total transmission power, P_{RF} is the power consumption per RF chain, N_T is the total number of the antennas, N_{RF} is the number of the RF chains and q is the different number of the bits used for DAC quantization.

The use of few-bit DACs in HBF significantly reduces the power consumption, which increases the overall energy efficiency. However, this increase in energy efficiency comes at the expense of slight decrease in the spectral efficiency. Fig. 3.9 compares the energy efficiency of HBF using ULA, URA, UCA, and CCA with the energy efficiency of FDBF (here we are taking only FDBF of UCA for comparison as it provides the highest FDBF sum-rate among 2D array structures) for different q-bit DACs, where $q = 1, 2, 3, \ldots, 10$. Fig. 3.9(a) shows the energy efficiency at very low SNR at -20 dB, whereas Fig. 3.9(b) shows the energy efficiency at high SNR at 20 dB. CCA and URA, both gives the highest energy efficiency at very low SNR, and this highest value can be achieved even by using 1-bit DAC as shown in Fig. 3.9a. At high SNR, CCA still provides the highest energy efficiency among the compared array structures. The highest efficiency value is achieved by using ($q = 5$)-bit DAC. In comparison, FDBF offers very low energy efficiency due to the use of large number of power-hungry RF chains ($N_{RF} = N_T$).

Finally, we examine the energy efficiency of 2D array structures versus q at different values of SNR. Fig. 3.10 compares the performance of ULA, URA, UCA, and CCA in terms of energy efficiency. For all compared array structures, we can achieve very high energy

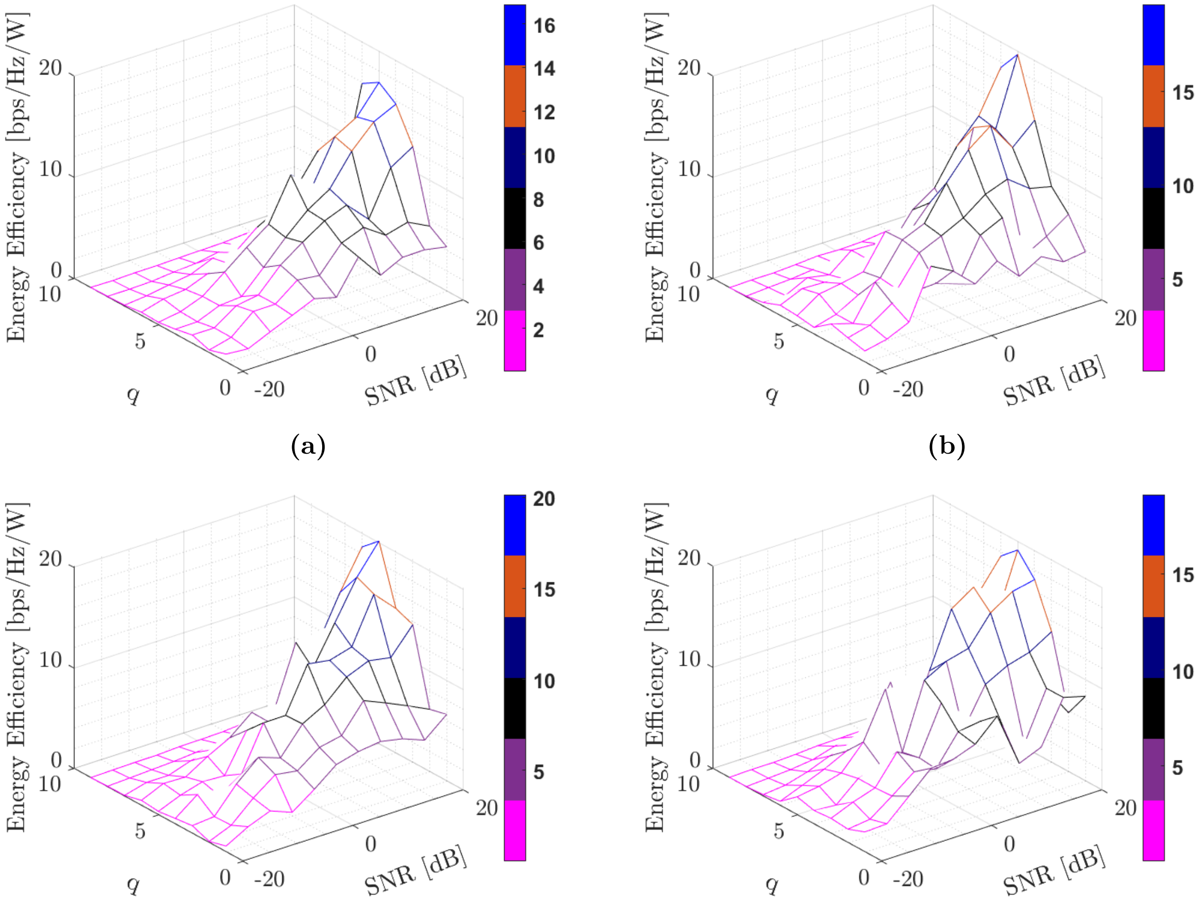

(a) (b)

(c) (d)

Figure 3.10. Energy efficiency versus q and SNR, $N_T = 100$, $G = 3$, $N_{RF_g} = K_g = 3$, $N_{RF} = K = 9$, $\theta = 73°$, $(\phi_1, \phi_2, \phi_3) = (30°, 90°, 150°)$, $\delta_a = \pm 15°$, $\delta_e = \pm 12.5°$ (a) ULA (b) URA (c) UCA (d) CCA.

efficiency by using ($q \leq 5$)-bit DACs in HBF. From Fig. 3.10, it can be seen that: i) 1-bit DACs can contribute the highest energy efficiency only at very low SNR ii) at very high SNR, only (3-5)-bit DACs are sufficient to provide the highest energy efficiency along with very good spectral efficiency. The overall performance comparison of the array structures is summarized in Table. 3.4.

Table 3.4. Performance comparison of ULA, UCA, URA, and CCA with few-bit DACs.

	ULA	**UCA**	**URA**	**CCA**
Sum-rate using few-bit DACs (see Fig. 3.8)	Low sum-rate	Low sum-rate	High sum-rate	High sum-rate
Energy efficiency using few-bit DACs (see Fig. 3.9 - Fig. 3.10)	Low efficiency	Low efficiency	High efficiency	High efficiency

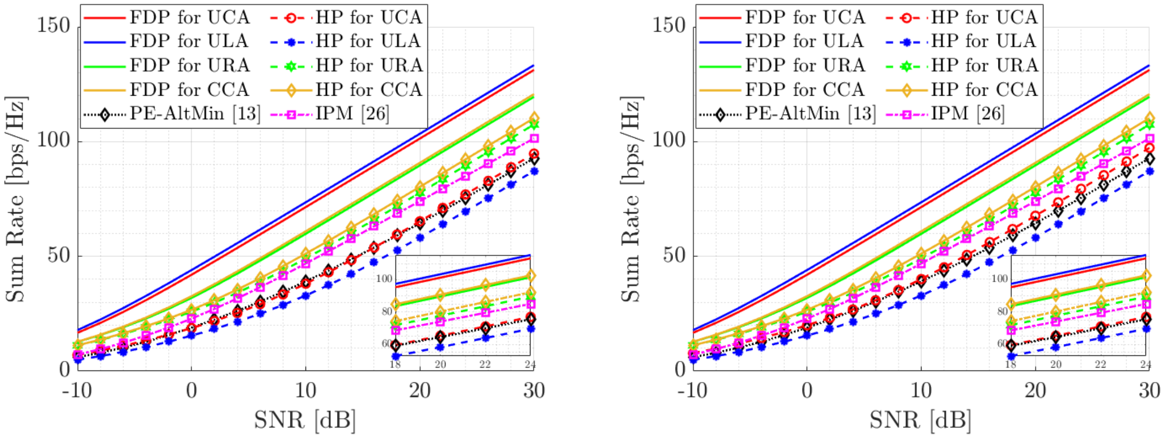

(a) **(b)**

Figure 3.11. Sum-rate comparison of ULA, UCA, URA and CCA using full-resolution PSs and DACs: (a) variable-gain RF beamformer (b) constant-modulus RF beamformer (with transfer block).

3.6.4 Performance Comparison with Low-Resolution PSs and DACs

In this section, we compare the performance of different 2D array structures using low-resolution PSs and DACs. Since the RF beamformer can be designed for constant and variable-gain entities, therefore, we first compare the performance of the HBF for the two cases: (i) HBF with variable-gain RF beamformer, and (ii) HBF with transfer block and constant-gain RF beamformer. To compare the performance of these two HBF schemes, we assume full-resolution hardware components (i.e., DACs and PSs).

In Fig. 3.11(a), the sum-rate of proposed HBF scheme with variable-gain RF beamformer is compared to FDBF as well as different HBF techniques (i.e., phase extraction alternative minimization (PE-AltMin) method in [42] and iterative phase

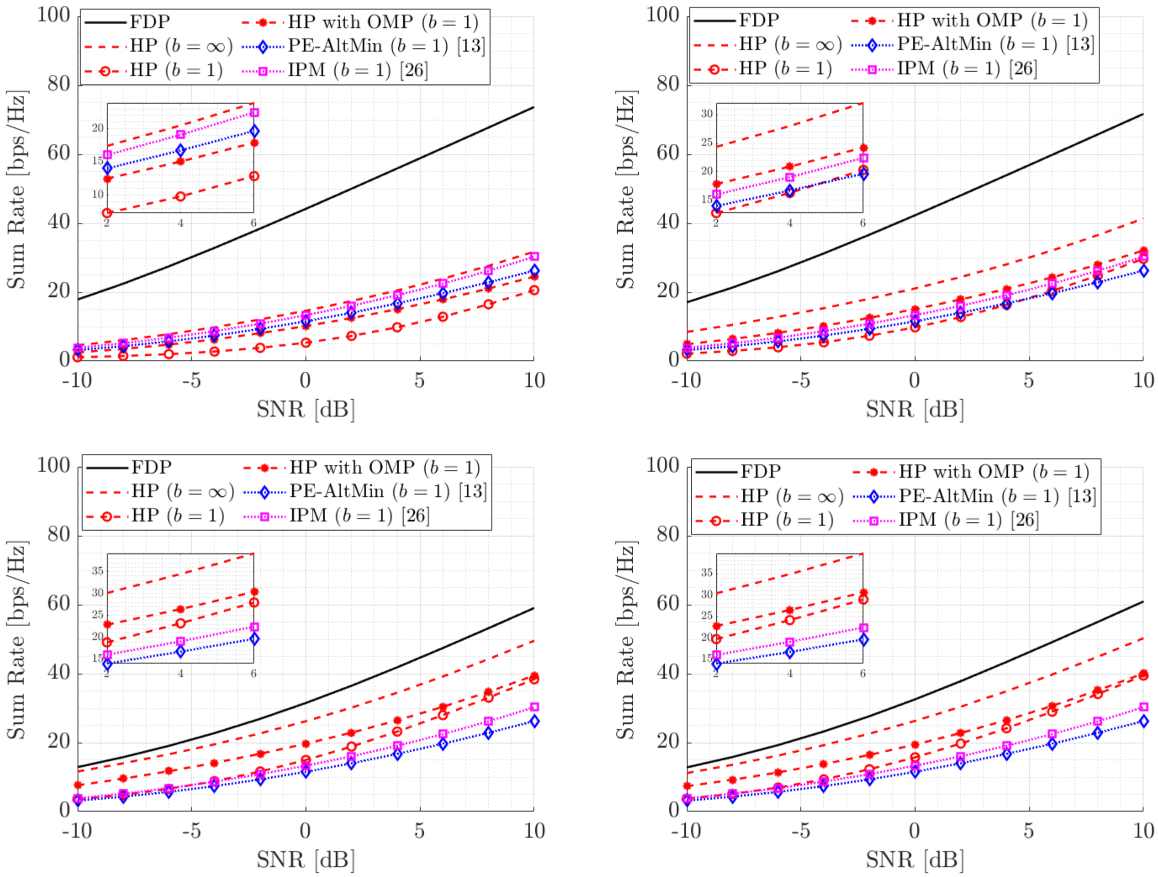

(c) URA **(d)** CCA

Figure 3.12. Sum-rate comparison with 1-bit PSs: (a) ULA (b) UCA (c) URA (d) CCA.

matching (IPM) HBF technique in [72]) for different array structures, whereas in Fig. 3.11(b), the sum-rate of HBF with transfer block and constant-gain RF beamformer is presented. It can be seen that both HBF schemes (i.e., two-stage HBF as in Fig. 3.11(a) and three-stage HBF as in Fig. 3.11(b)) yield similar performance for ULA, URA, UCA, and CCA. Furthermore, FDBF achieves higher sum-rate at the expense of large number of RF chains i.e., $N_{RF} = N_T = 100$, whereas for both proposed HBF schemes, we can approach the sum-rate of FDBF with relatively small number of RF chains, i.e., $N_{RF} = 9$. Also, both CCA and URA can give high sum-rate when compared to ULA and UCA as well as the HBF solutions presented in [42] and [72]. In the following analysis, we provide an extensive comparison of spectral and energy efficiencies of the array structures for the case of: (i) HBF with b-bit PSs and ∞-bit DACs, and (ii) HBF with b-bit PSs and q-bit DACs.

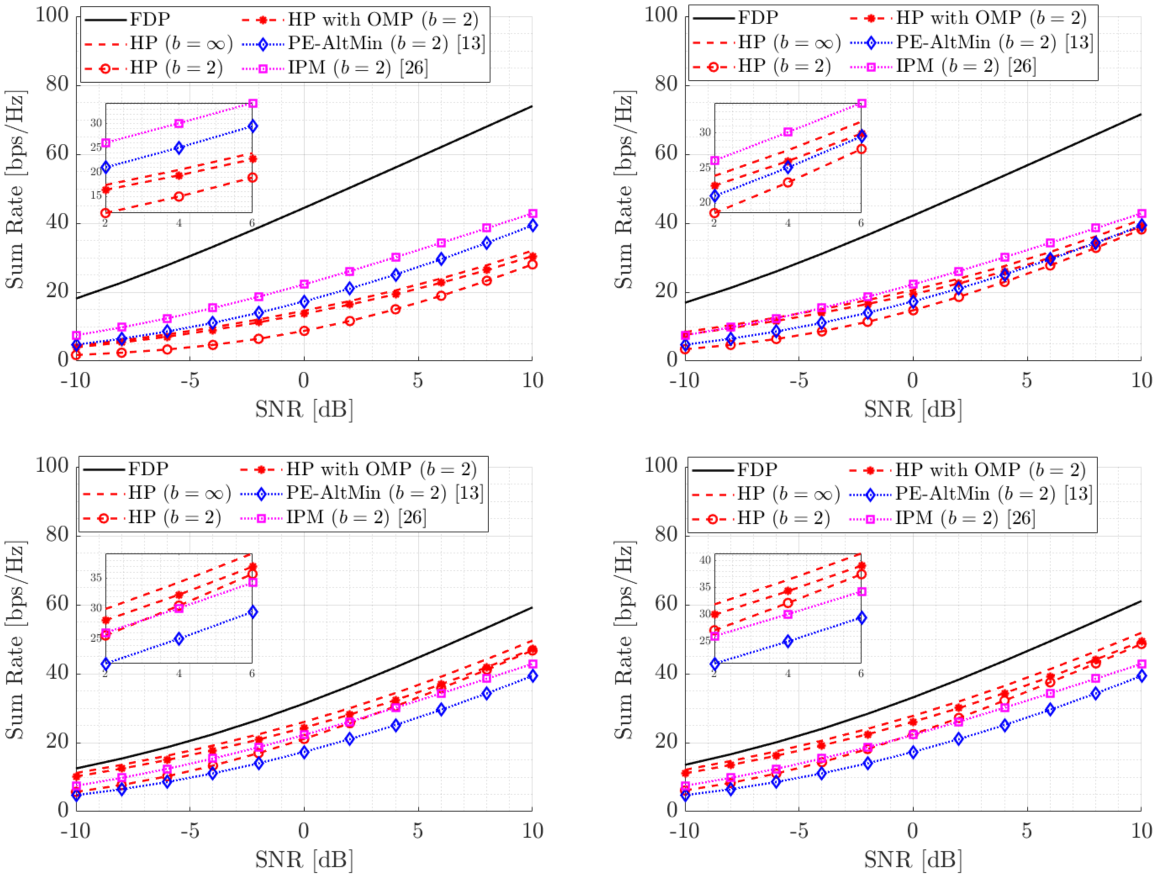

(c) URA **(d)** CCA

Figure 3.13. Sum-rate comparison with 2-bit PSs: (a) ULA (b) UCA (c) URA (d) CCA.

3.6.4.1 *b*-bit PSs AND ∞-bit DACs

In this section, we analyze the performance of ULA, URA, UCA, and CCA by evaluating the proposed HBF schemes when using few-bit PSs only. Fig. 3.12 depicts the sum-rate of different array structures for the following cases: (i) FDBF, (ii) HBF using ∞-bit PSs, (iii) HBF using 1-bit PSs $\big($phase quantization of (ii)$\big)$, (iv) HBF using 1-bit PSs (OMP), (v) HBF using PE-AltMin [42], and (vi) HBF using IPM [72]. By using the same simulation parameters as mentioned earlier, it can be seen that the proposed OMP based HBF design for 1-bit PSs can provide higher sum-rates than the HBF designed with simple phase quantization as well as different HBF solutions (i.e., [42, 72]) for URA and CCA array structures. Also, the sum-rate degradation is reduced to around (3-4) [bps/Hz] at low SNR, whereas at high SNR, the degradation is $\approx$ $(8-10)$ [bps/Hz] due to high quantization error. However, by using only 2-bit PSs, we can approach the sum-rate of

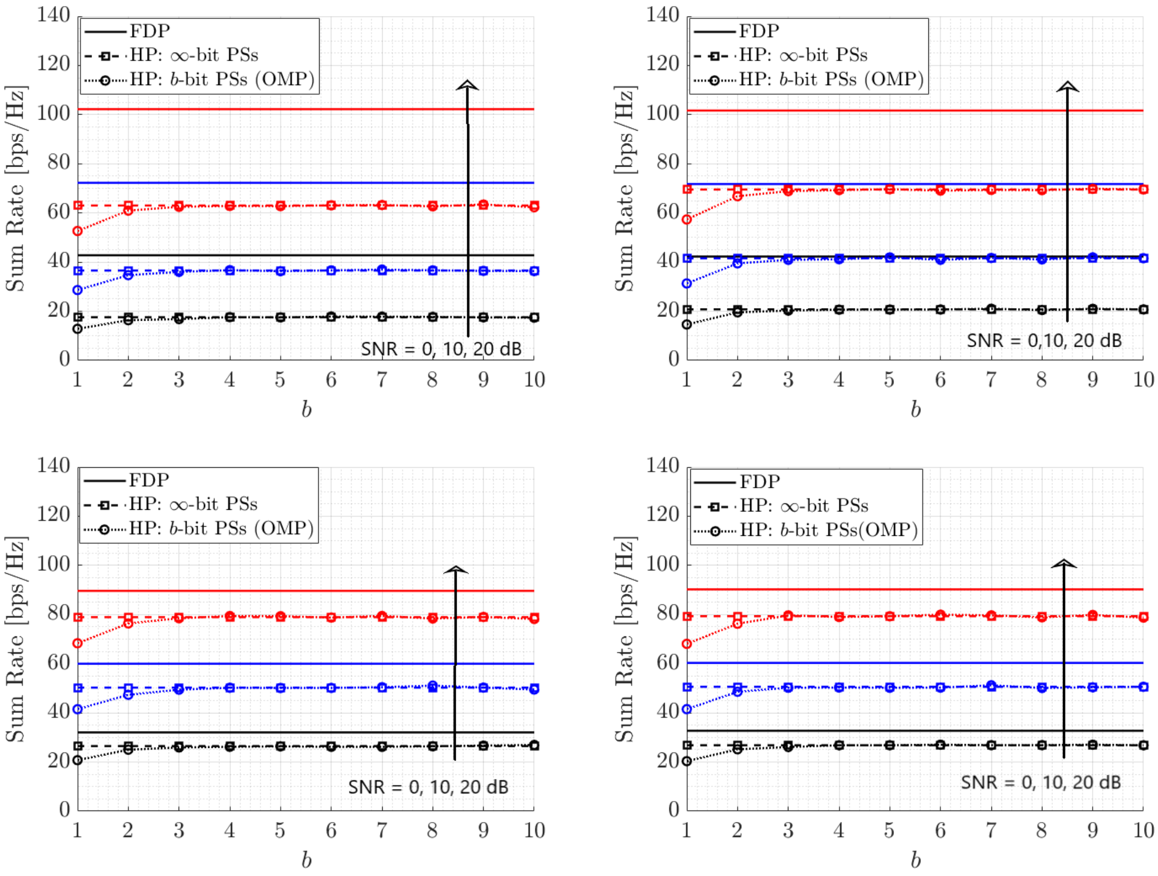

(c) URA (d) CCA

Figure 3.14. Sum-rate vs b at SNR $= (0, 10, 20)$ dB: (a) ULA (b) UCA (c) URA (d) CCA.

∞-bit PSs as shown in Fig. 3.13. In this case, the sum-rate degradation is reduced to $\approx (2-3)$ [bps/Hz] at all SNR values. From Figures 3.12 and 3.13, we can also see that URA and CCA can give higher sum-rate than ULA and UCA for both 1-bit and 2-bit PSs.

Fig. 3.14 plot the sum-rate versus b, where b is the number of the bits of the PSs, and compares the spectral efficiency of ULA, URA, UCA, and CCA. The results are presented at SNR of 0, 10 and 20 dB. Fig. 3.14 indicates that the proposed HBF scheme with 2-bit PSs can approach the performance of HBF with ∞-bit PSs. For a given SNR, the sum-rate performance gap between the FDBF and HBF with ∞-bit PSs in the case of URA and CCA is much smaller than in the case of ULA and UCA. Furthermore, for all array structures, the sum-rate gap increases with increasing SNR. Similarly, for the same SNR values, we investigate the sum-rate versus N_{RF_g} of FDBF, HBF's with ∞-bit and 1-bit PS in different array structures as plotted in Fig. 3.15. The results show that both URA and CCA can

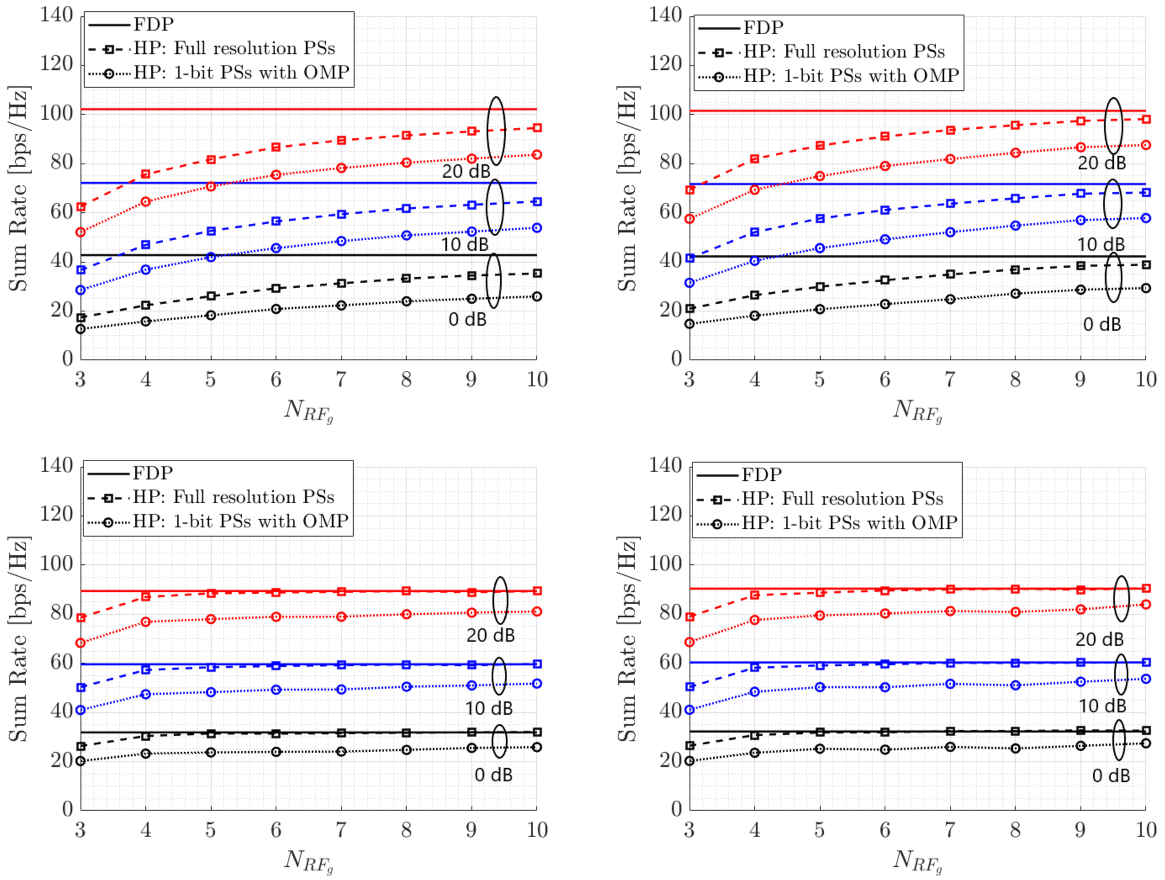

(c) URA **(d)** CCA

Figure 3.15. Sum-rate vs N_{RF_g} with 1-bit PSs at SNR = $(0, 10, 20)$ dB: (a) ULA (b) UCA (c) URA (d) CCA.

give high sum-rate with a slight increase in N_{RF_g}. The sum-rate increases by approximately 20 % for ULA and UCA, and almost 10 % for URA and CCA by increasing N_{RF_g} from 3 to 4. Also, in Fig. 3.16, we plot the sum-rate versus N_{RF_g} of FDBF, HBF's with ∞-bit and 2-bit PS. It can be seen that by increasing N_{RF_g} from 3 to 4, the proposed HBF scheme using either URA or CCA can approach the performance of FDBF with ∞-bit PSs, and offers a slightly lower sum-rate with 2-bit PSs. On the other hand, the propsed HBF scheme using ULA and UCA requires more RF chains to approach the performance of the FDBF.

The use of low-resolution PSs with the proposed HBF scheme not only offers high spectral efficiency but can also provide high energy efficiency compared to FDBF and HBF using full-resolution PSs. The energy efficiency is defined as the ratio of the sum-rate R_{sum} and the

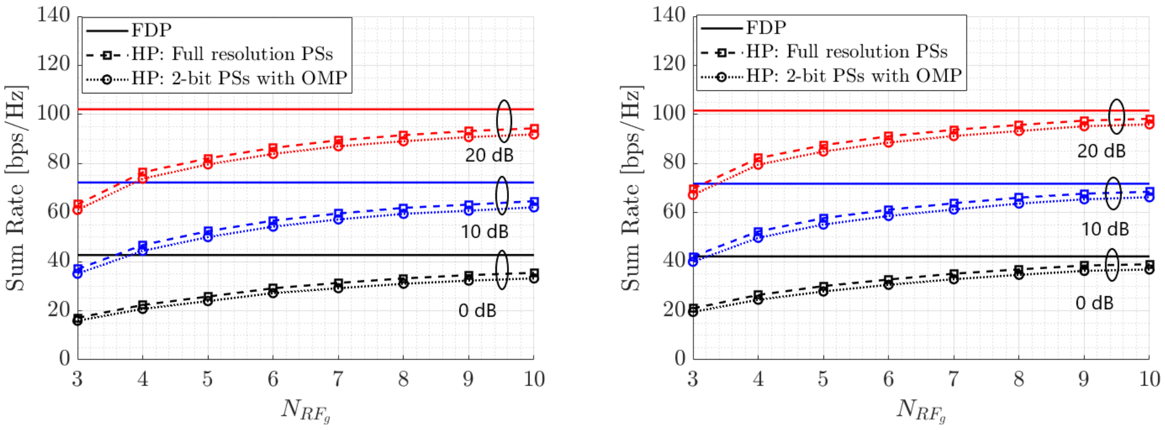

(a) ULA **(b)** UCA

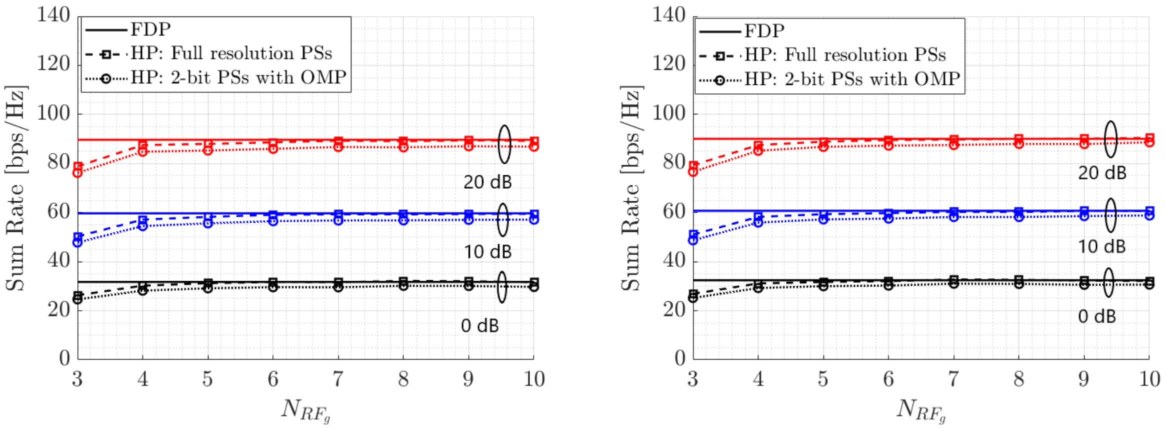

(c) URA **(d)** CCA

Figure 3.16. Sum-rate vs N_{RF_g} with 2-bit PSs at SNR $= (0, 10, 20)$ dB: (a) ULA (b) UCA (c) URA (d) CCA.

total power consumption P_{total}, i.e.,

$$\epsilon = \frac{R_{sum}}{P_{total}} = \frac{R_{sum}}{P_T + N_{RF}P_{RF} + N_{PS}P_{PS_b}}, \tag{3.46}$$

where P_T represents the total transmission power, N_{RF} is the total number of RF chains, P_{RF} is the power consumption of each RF chain, and P_{PS_b} is the power consumption of b-bit PSs. As in [90], we use $P_T = 1$ W and $P_{RF} = 250$ mW. The use of transfer block yields a constant-gain RF beamformer but also doubles the number of PSs per each RF chain due to double-PS structure (as discussed in Section 3.4.2.2). Thus, $N_{PS} = 2 \times N_{RF} \times N$. We use

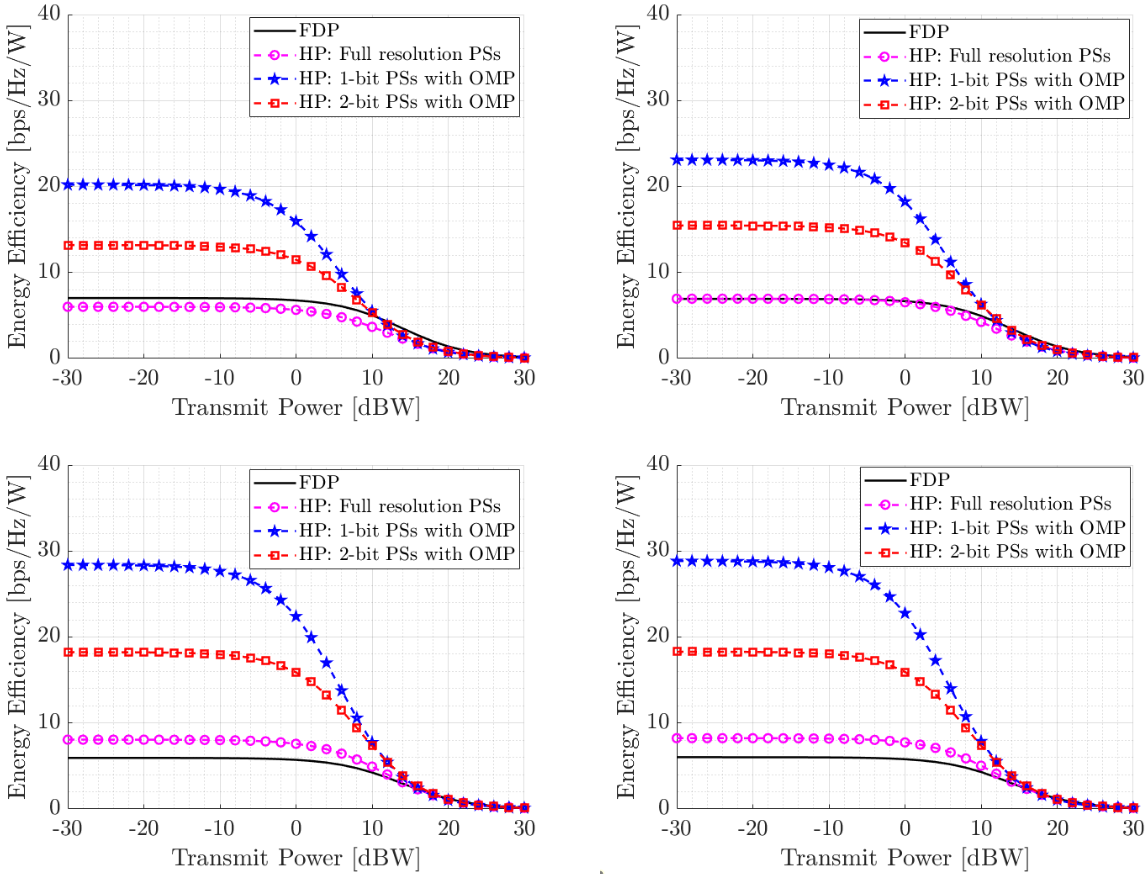

(c) URA **(d)** CCA

Figure 3.17. Energy efficiency comparison versus transmit power at SNR= 15 dB: (a) ULA (b) UCA (c) URA (d) CCA.

5 mW and 10 mW as the power consumption values for 1-bit and 2-bit PSs i.e., ($P_{PS_1} = 5$ mW, $P_{PS_2} = 10$ mW) [96,97]. Fig. 3.17 analyzes the energy efficiency of ULA, UCA, URA, and CCA versus transmit power, which varies from -30 dB to 30 dB and compares ϵ at SNR = 15 dB for four cases which are: (i) FDBF, (ii) HBF using ∞-bit PSs, (iii) HBF using 1-bit PSs, and (iv) HBF using 2-bit PSs. For the full-resolution PSs, we assume 5-bit PSs be a good choice to replicate the performance of ∞-bit PSs.

Fig. 3.17 shows that both 1-bit and 2-bit PSs can offer high energy efficiency compared to FDBF and HBF using ∞-bit PSs. However, the energy efficiency decreases sharply beyond 0 dB for all array structures because of high transmit power. Compared to ULA and UCA, both URA and CCA can offer higher energy efficiency when using only 1 or 2-bit PSs at the RF-stage.

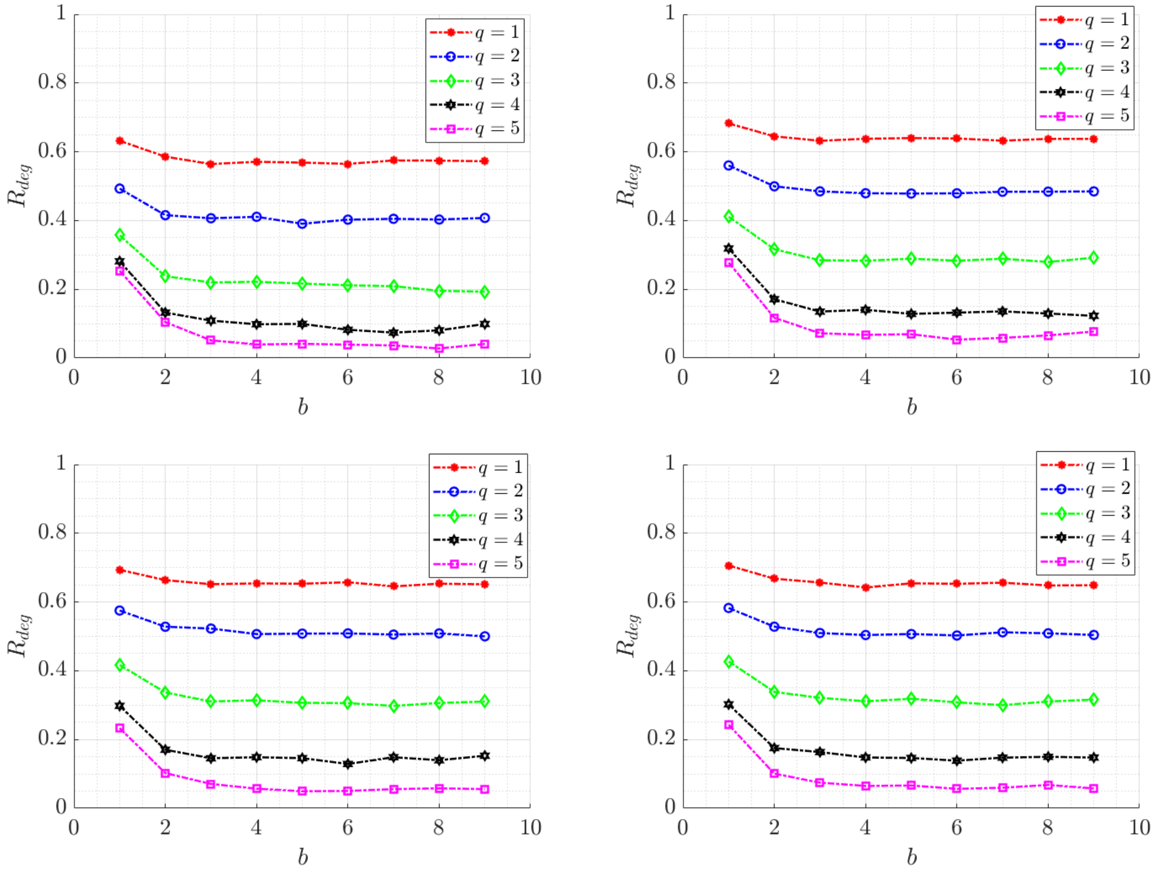

(c) URA

(d) CCA

Figure 3.18. Sum-rate degradation versus b for different DAC resolutions at SNR = 10 dB: (a) ULA (b) UCA (c) URA (d) CCA.

3.6.4.2 b-bit PSs AND q-bit DACs

In this section, we examine the spectral effiency of the proposed HBF scheme with low-resolution DACs and PSs, i.e., the combined effect of q-bit DACs and b-bit PSs on the sum-rate performance for ULA, URA, UCA, and CCA. To better understand the effect of low-resolution PSs and DACs on the sum-rate degradation R_{deg}, we first plot R_{deg} due to each individual hardware component (i.e., DACs or PSs). Fig. 3.18 shows various R_{deg} plots versus b for different values of q. It can be seen that 1-bit DAC can give large sum-rate degradation (≈ 65%). The large quantization noise introduced by the use of only 1-bit DAC impede the performance improvement even by increasing PSs resolution (i.e., b). However, by increasing DAC resolution, we can see that R_{deg} decreases significantly, e.g., R_{deg} reduces to ≈ 25% with 5-bit DACs and 1-bit PSs. In other words, we can approach the performance

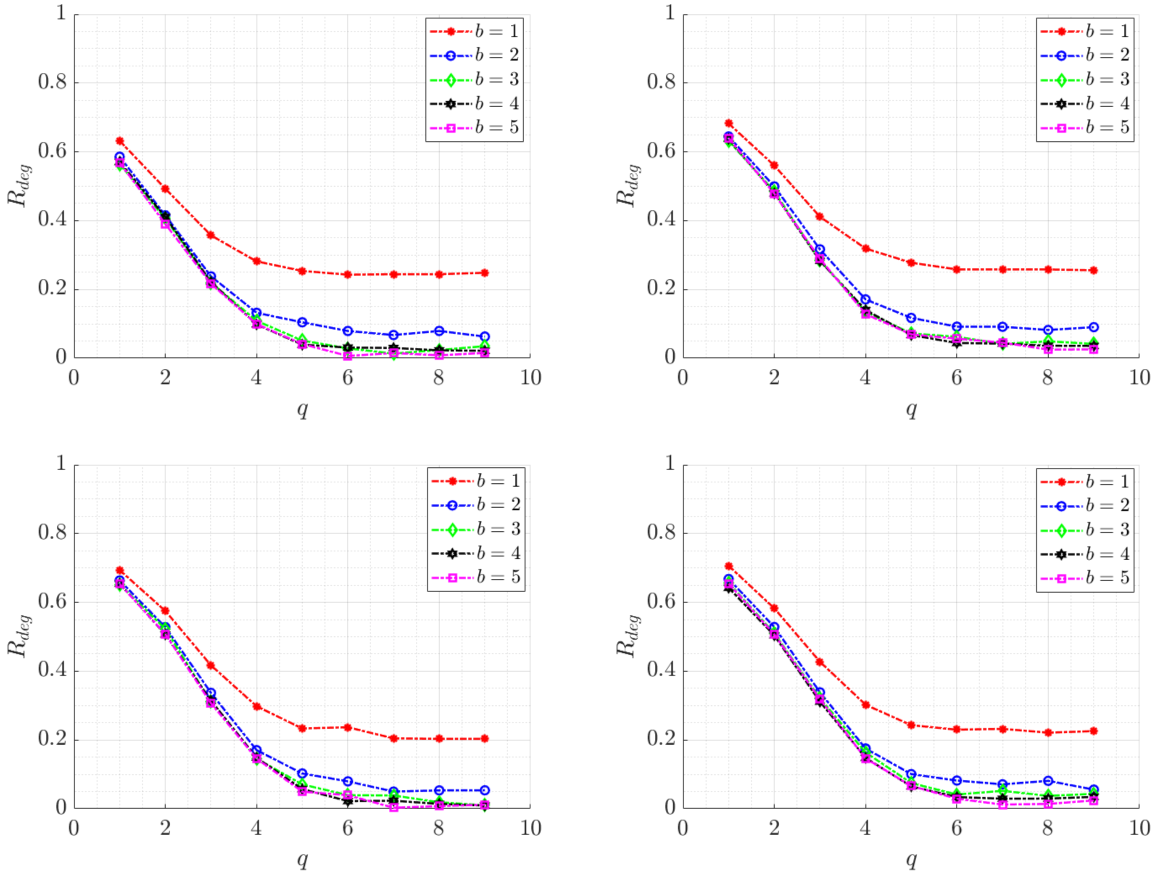

(c) URA **(d)** CCA

Figure 3.19. Sum-rate degradation versus q for different PS resolutions at SNR $= 10$ dB: (a) ULA (b) UCA (c) URA (d) CCA.

of HBF with ∞-bit resolution with just 5-bit DACs, offering significant advantages in power consumption and cost.

Fig. 3.19 plots R_{deg} versus q for different PSs resolution. Similar to the case of 1-bit DACs, HBF using 1-bit PSs can give high R_{deg} ($\approx 70\%$). However, this degradation can be decreased significantly by increasing the resolution of DACs. Thus, HBF with 1-bit PSs can provide higher sum-rate than HBF with 1-bit DACs. Also, for $b \geq 2$, we can see that R_{deg} is almost the same for all resolution levels i.e, $b = 2, 3, 4, 5$, which indicates that the performance of HBF depends more on DAC resolution than on PS resolution. Furthermore, this analysis gives us the least numbers of bits of DACs and PSs required to achieve a satisfactory performance close to FDBF and HBF using ∞-bit components.

Fig. 3.20 plots the sum-rate versus q and b for ULA, UCA, URA, and CCA at SNR $= 10$

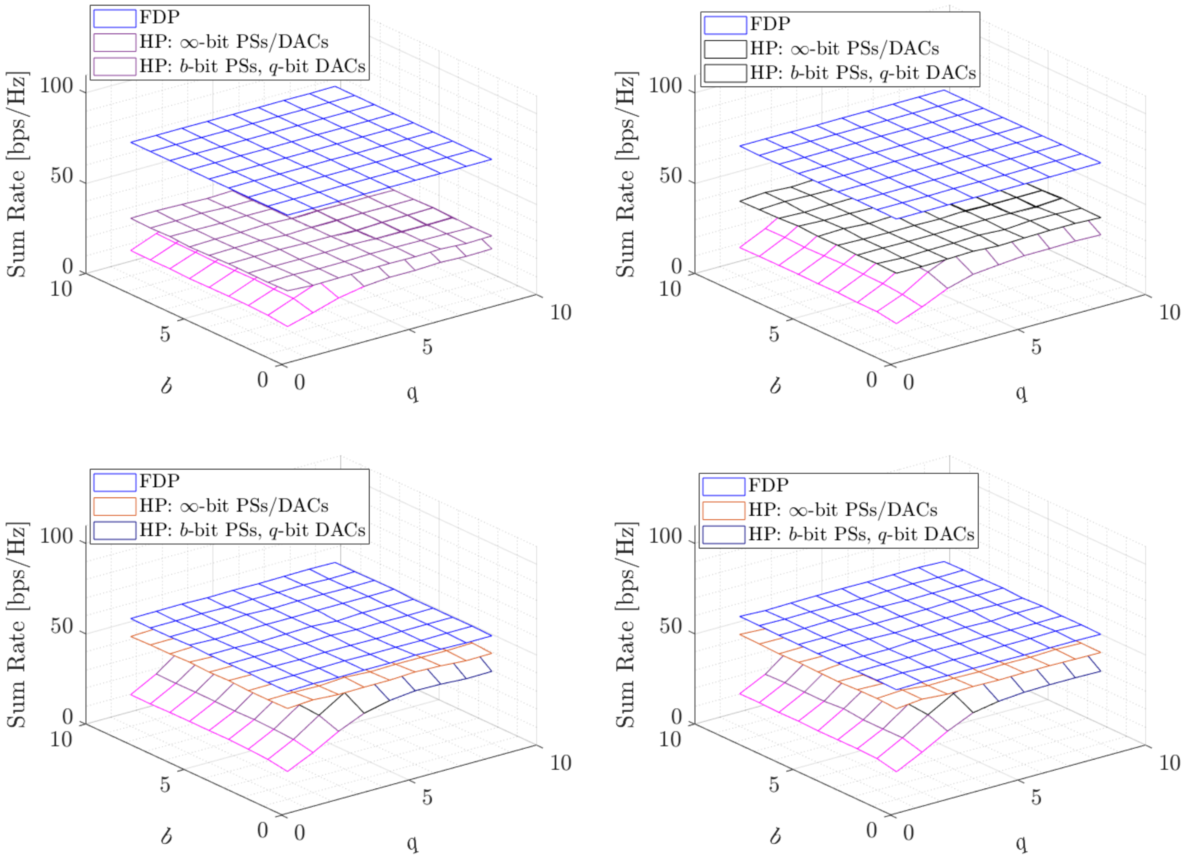

(c) URA **(d)** CCA

Figure 3.20. Sum-rate versus q and b at SNR = 10 dB: (a) ULA (b) UCA (c) URA (d) CCA.

dB and b and q varying from 1 to 10. The sum-rate performance gap between the FDBF and proposed HBF using ULA and UCA is larger than the case using URA and CCA. Moreover, the analysis of the results obtained in Fig. 3.18 and Fig. 3.19 gives some following useful notes: (i) the use of low-resolution DACs significantly degrades the sum-rate performance as compared to the use of low-resolution PSs (e.g., $R_{(q=1,b=10)} \ll R_{(q=10,b=1)}$), (ii) single-layered array structures (i.e., ULA and UCA) give low sum-rate, whereas, the multi-layered array structures (i.e., URA and CCA) can approach the sum-rate of FDBF, and (iii) the optimal sum-rate can be obtained by using different combinations of q and b and thus, offers the choice to use which combination of low-resolution hardware components for increased sum-rate. This can also be better understood by the equal-sum-rate contour plots shown in Fig. 3.21. It can be observed that we can get reasonably high sum-rate by using the proposed

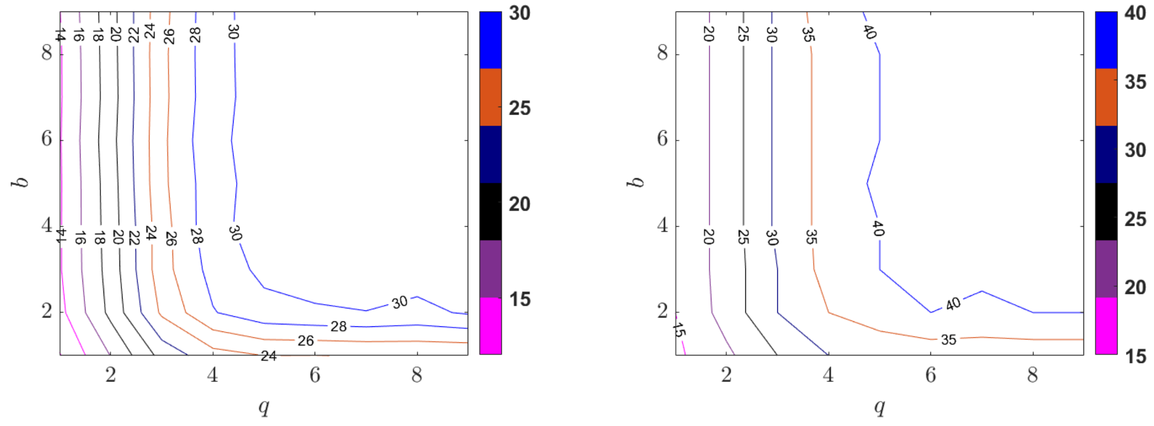

(a) ULA **(b)** UCA

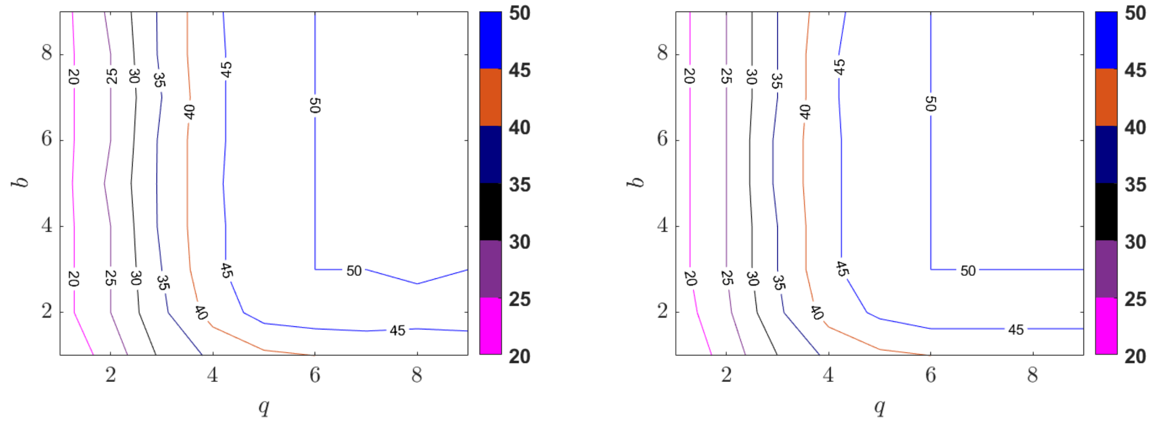

(c) URA **(d)** CCA

Figure 3.21. Equal-sum-rate contour plots at SNR = 10 dB: (a) ULA (b) UCA (c) URA (d) CCA.

HBF with ($q \geq 5, b \geq 2$), which is, in particular, close to that of FDBF for both CCA and URA. Finally, Table 3.5 gives the comprehensive comparison of spatial, spectral and energy efficiencies of ULA, UCA, URA, and CCA when using few-bit DACs and PSs.

3.7 Concluding Remarks

In this chapter, we have presented the MU-mMIMO hybrid beamforming (HBF) design for low-resolution PSs and/or DACs, and investigated its performance using different 2D antenna array structures. In the HBF design, the RF precoder has been developed via the

Table 3.5. Performance comparison of ULA, UCA, URA and CCA using low-resolution PSs and DACs.

	ULA	UCA	URA	CCA
Spatial efficiency	Low	Low	High	High
Sum-rate using b-bit PSs (see Figure 3.12 - Figure 3.12)	Low	High	High	High
Energy efficiency using b-bit PSs (see Figure 3.17)	Low	High	High	High
Sum-rate using q-bit DACs and b-bit PSs (see Figure 3.18 - Figure 3.19)	Low	Low	High	High

slow time-varying AoD information, whereas the reduced-size effective CSI is utilized at the baseband precoder. Considering the hardware complexity, we have considered the following cases in the HBF design: (i) low-resolution PSs only, and (ii) low-resolution PSs and DACs. An optimization problem has been formulated to provide an RF beamformer with uniform gain entities by introducing a transfer block at the baseband stage. Furthermore, we have proposed an algorithmic solution using OMP to reduce the Euclidean distance between the HBF with full-resolution PSs and the HBF with low-resolution PSs. Based on OMP, we have first designed HBF using b-bit PSs and ∞-bit DACs, then constructed the HBF using b-bit PSs and q-bit DACs to significantly reduce hardware complexity and costs in MU-mMIMO HBF systems. The spectral and energy efficiencies of ULA, UCA, URA, and CCA have been compared using Monte Carlo simulations. Illustrative results indicate that the proposed HBF using both URA and CCA can provide high sum-rates, which are comparable to their FDBF counterparts. Also, the use of low-resolution PSs and DACs can provide high energy efficiency. Finally, we have presented different combinations of PS and DAC quantization levels to achieve near-optimal sum-rate. It has been shown that HBF using only 2-bit PSs and 5-bit DACs can provide high performance close to FDBF.

3.8 Appendix: Proof of Lemma 3.1

Let the normalization factor $\frac{N_{RF_g}}{\left\|\hat{\mathbf{F}}_{D_g}^{(q)}\mathbf{T}_g^{(q)}\right\|_F}$ is equal to $\frac{1}{\rho}$. Then, we can write:

$$\left\|\hat{\mathbf{F}}_{D_g}^{(q)}\mathbf{T}_g^{(q)}\right\|_F = \rho N_{RF_g} = \rho \left\|\hat{\mathbf{F}}_{D_g}\mathbf{T}_g\right\|_F . \tag{3.47}$$

Using norm inequality, we have:

$$\begin{aligned}\left\|\hat{\mathbf{F}}_{D_g}\mathbf{T}_g - \hat{\mathbf{F}}_{D_g}^{(q)}\mathbf{T}_g^{(q)}\right\|_F &\geq \left|\left\|\hat{\mathbf{F}}_{D_g}\mathbf{T}_g\right\|_F - \left\|\hat{\mathbf{F}}_{D_g}^{(q)}\mathbf{T}_g^{(q)}\right\|_F\right|, \\ &= |1-\rho|\left\|\hat{\mathbf{F}}_{D_g}\mathbf{T}_g\right\|_F, \end{aligned} \tag{3.48}$$

which is equivalent to $\left\|\hat{\mathbf{F}}_{D_g}\mathbf{T}_g\right\|_F \leq \frac{1}{|\rho-1|}\zeta$. When $\rho \neq 1$, we have $\left\|\hat{\mathbf{F}}_{D_g}\mathbf{T}_g - \hat{\mathbf{F}}_{D_g}^{(q)}\mathbf{T}_g^{(q)}\right\|_F \neq 0$. Then,

$$\begin{aligned}\left\|\hat{\mathbf{F}}_{D_g}\mathbf{T}_g - \hat{\mathbf{F}}_{D_g}^{(q)}\tilde{\mathbf{T}}_g^{(q)}\right\|_F &= \left\|\hat{\mathbf{F}}_{D_g}\mathbf{T}_g - \hat{\mathbf{F}}_{D_g}^{(q)}\mathbf{T}_g^{(q)} + \left(1-\frac{1}{\rho}\hat{\mathbf{F}}_{D_g}^{(q)}\mathbf{T}_g^{(q)}\right)\right\|_F, \\ &\leq \left\|\hat{\mathbf{F}}_{D_g}\mathbf{T}_g - \hat{\mathbf{F}}_{D_g}^{(q)}\mathbf{T}_g^{(q)}\right\|_F + \left|1-\frac{1}{\rho}\right|\left\|\hat{\mathbf{F}}_{D_g}^{(q)}\tilde{\mathbf{T}}_g^{(q)}\right\|_F, \\ &\leq \zeta + |\rho-1|\left\|\hat{\mathbf{F}}_{D_g}\mathbf{T}_g\right\|_F \\ &\leq \zeta + \frac{|\rho-1|}{|\rho-1|}\zeta, \\ &= 2\zeta. \end{aligned} \tag{3.49}$$

From (3.49), we can write as:

$$\left\|\hat{\mathbf{F}}_{D_g}\mathbf{T}_g - \hat{\mathbf{F}}_{D_g}^{(q)}\tilde{\mathbf{T}}_g^{(q)}\right\|_F = 2\zeta. \tag{3.50}$$

Chapter 4

3D Antenna Array Structures in Hybrid Massive MIMO[1]

4.1 Introduction

As discussed in Chapter 3, the antenna elements at the BS can be configured in a number of ways, resulting in narrower beams to reduce MU interference. A comparison of different 2D array structures in MU-mMIMO is presented in [57, 58], showing higher spectral and energy efficiencies of uniform rectangular array (URA) and concentric circular array (CCA) than uniform linear array (ULA) and uniform circular array (UCA). Given the massive wireless connectivity requirements of IoT, mMTC, and future aerial applications involving mobile drones, UAVs, satellites, existing array structures lack the ability to transmit signals in arbitrary location in 3D space. As a result, in future wireless applications, the 3D configuration of antenna elements will be critical. The design of uniform spherical array (USA) is presented in [99], which shows significant advantages in mMIMO. Antenna elements can also be placed in a 3D cylindrical array to increase SE as shown in [100]. The majority of existing research on HBF solutions in mmWave MU-mMIMO systems is focused on ULA or URA (e.g., [42, 62, 88, 90]). Therefore, analyzing the performance of various 3D array topologies remains an unaddressed research problem.

In this chapter, we compare the spectral and energy efficiencies of three different 3D array structures in mmWave MU-mMIMO systems., i.e., cylindrical array (CA), hemi-spherical array (HSA), and spherical array (SA) and analyze the computational complexity as well as

---

[1] Parts of this chapter have been published in the IEEE Communications Letters [98].

robustness of the proposed HBF scheme. The main contributions of this chapter are outlined as follows:

- **SVD-Based HBF Design:** We consider the design of HBF for mmWave MU-mMIMO systems, which involves two stages: (i) RF beamforming based on SVD of channel matrix, and baseband MU precoding based on the instantaneous effective baseband channel to mitigate MU-interference by RZF technique.
- **Comparison of 3D Antenna Array Structures:** We compare the spectral and energy efficiencies of different 3D antenna array structures in mmWave MU-mMIMO systems. Particularly, we consider three different 3D array configuration, namely, SA, HSA, and CA, and compare their performance versus URA (2D array configuration). We show that in comparison to 2D arrays, 3D array structures can provide high spectral and energy efficiencies as well as non-varying achievable rate independent from the user angular location.
- **Robustness of HBF to CSI Errors:** We compare the effect of channel estimation error on the sum-rate performance for different array structures and show that the proposed HBF scheme is not sensitive to the accuracy of CSI.

The rest of this chapter is organized as follows. In Section 4.2, we discuss the system and channel model for mmWave MU-mMIMO systems. Section 4.3 presents the SVD-based HBF solution to maximize the total achievable rate. The illustrative results are provided in Section 4.4 to compare the performance of different 3D array structures. Finally, the chapter is concluded in Section 4.5.

4.2 System and Channel Model

In this section, we introduce the system and channel models of the proposed hybrid mmWave MU-mMIMO systems.

4.2.1 System Model

We consider the downlink of a mmWave MU-mMIMO system with HBF structure, as depicted in Fig. 4.1. The BS employs N antenna elements at the transmitter, which are fed by N_{RF} RF chains simultaneously communicating with K single-antenna users. At the BS, the hybrid precoder $\mathbf{B} = \mathbf{F}_D\mathbf{B}_D$ consists of the digital baseband precoder $\mathbf{B}_D \in \mathbb{C}^{N_{RF}\times K}$

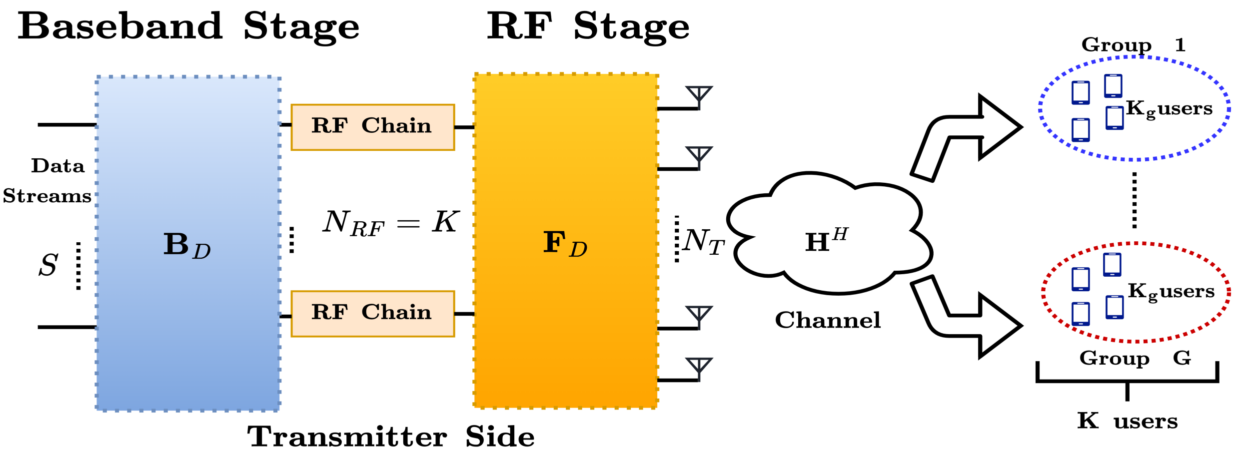

Figure 4.1. System model for the proposed mmWave MU-mMIMO hybrid precoding.

and the analog RF beamformer $\mathbf{F}_D \in \mathbb{C}^{N_T \times N_{RF}}$ that is implemented using phase shifters and thus, imposes a constant-modulus contraint., i.e., $|\mathbf{F}_D(i,j)| = \frac{1}{\sqrt{N_T}}$ $\forall i, j$. The design of HBF reduces the number of RF chains from N_T to N_{RF}, while satisfying $K \leq N_{RF} \ll N_T$. Assuming the number of data streams S equal to the number of the users K., i.e., $S = K$, the precoded signal at the transmitter is given by:

$$\mathbf{s} = \mathbf{F}_D \mathbf{B}_D \mathbf{d}, \tag{4.1}$$

where $\mathbf{d} \in \mathbb{C}^K$ is the data signal with $\mathbb{E}\{\mathbf{d}\mathbf{d}^H\} = \mathbf{I}_K$. The transmitted signal satisfies the power constraint., i.e., $\mathbb{E}\{\|\mathbf{s}\|_2^2\} \leq P_T$, where P_T is the transmit power at the BS. Then, the received signal at k^{th} user is given by:

$$\begin{aligned} y_k &= \mathbf{h}_k^H \mathbf{B}\mathbf{s} + n_k, \\ &= \underbrace{\mathbf{h}_k^H \mathbf{F}_D \mathbf{b}_{d_k} d_k}_{\text{Desired Signal}} + \underbrace{\sum_{\hat{k} \neq k}^{K} \mathbf{h}_k^H \mathbf{F}_D \mathbf{b}_{d_{\hat{k}}} d_{\hat{k}}}_{\text{IUI}} + \underbrace{n_k}_{\text{Noise}}, \end{aligned} \tag{4.2}$$

where $\mathbf{h}_k \in \mathbb{C}^{N_T}$ and $\mathbf{s}_k$ are the narrowband flat-fading channel vector and data signal for k^{th} user, respectively, $\mathbf{b}_{d_k}$ is the k^{th} column of $\mathbf{B}_D$, and n_k denotes the additive circular symmetric Gaussian noise such that $n_k \sim \mathcal{CN}(0, \sigma^2)$.

By using (4.1) and (4.2), the instantaneous signal-to-interference-plus-noise ratio (SINR) expression at k^{th} user is derived as follows:

$$\mathrm{SINR}_k = \frac{|\mathbf{h}_k^H \mathbf{F}_D \mathbf{b}_{d_k}|^2}{\sum_{\hat{k}\neq k}^{K} |\mathbf{h}_k^H \mathbf{F}_D \mathbf{b}_{d_{\hat{k}}}|^2 + \sigma^2}. \tag{4.3}$$

By using the instantaneous SINR, the ergodic sum-rate capacity R_{sum} for the MU-mMIMO systems is given by:

$$R_{\text{sum}} = \sum_{k=1}^{K} \mathbb{E}[\log_2(1 + \mathrm{SINR}_k)]. \tag{4.4}$$

The design of $\mathbf{F}_D, \mathbf{B}_D$ aims at maximizing the SE of mmWave MU-mMIMO systems. Then, the optimization problem can be formulated as follows:

$$\max_{\mathbf{F}_D, \mathbf{B}_D} \quad R_{\text{sum}}\Big(\mathbf{F}_D, \mathbf{B}_D\Big) \tag{4.5a}$$

$$\text{s.t.} \quad |\mathbf{F}_D(i,j)| = \frac{1}{\sqrt{N_T}}, \tag{4.5b}$$

$$\mathbb{E}\{\|\mathbf{s}\|_2^2\} \leq P_T. \tag{4.5c}$$

4.2.2 Channel Model

We consider a narrowband clustered channel model, based on the extended Saleh-Valenzuela model to characterize the sparse scattering of the mmWave communication channel [88]. We assume the channel matrix $\mathbf{H} \in \mathbb{C}^{N_T \times K}$ be the sum of $N_{\scriptscriptstyle C}$ scattering clusters, where each cluster contributes $N_{\scriptscriptstyle P}$ propagation paths. Then, the narrowband channel vector $\mathbf{h}_k$ for k^{th} user can be written as:

$$\mathbf{h}_k = \sqrt{\frac{N_T}{N_{\scriptscriptstyle C} L}} \sum_{m=0}^{N_C - 1} \sum_{l=0}^{L-1} \alpha_k^{m,l} \mathbf{a}_k(\phi_k^{m,l}, \theta_k^{m,l}), \tag{4.6}$$

where $\alpha_k^{m,l}$ corresponds to the complex gain of the lth multipath ray in the mth cluster, $\mathbf{a}_k(\phi_k^{m,l}, \theta_k^{m,l})$ is the transmit array response vector, where $\phi_k^{m,l} \in [\phi_k - \delta_e, \phi_k + \delta_e]$ represents the mean elevation angle of the corresponding path with angle spread δ_e and $\theta_k^{m,l} \in [\theta_k - \delta_a, \theta_k + \delta_a]$ represents the azimuth angle of departure (AoD) with azimuth angle spread δ_a. We assume complex weights $\alpha^{m,l}$ are i.i.d $\mathcal{CN}(0, \sigma_{\alpha,m}^2)$, where $\sigma_{\alpha,m}^2$ is the average power of the mth

cluster such that $\sum_{m=0}^{N_C-1}\sigma^2_{\alpha,m}=\sqrt{\frac{N_T}{N_C L}}$. The array steering vector is given as [90, 99, 100]:

$$\mathbf{a}(\phi,\theta)=\frac{1}{\sqrt{N_T}}[a_1(\phi,\theta),a_2(\phi,\theta),\ldots,a_N(\phi,\theta)]^T, \tag{4.7}$$

where $a_n(\phi,\theta)=e^{j\frac{2\pi}{\lambda}\mathbf{r}_n^T\mathbf{u}(\phi,\theta)}$, N_T is the number of the antenna elements at BS, $\mathbf{r}_n=[x_n,y_n,z_n]^T$ is the position of the n^{th} antenna element and $\mathbf{u}(\phi,\theta)=[\cos\theta\sin\phi,\sin\theta\sin\phi,\cos\theta]^T$. Different from the conventional array structures, we assume the antenna elements arranged in 3D space namely, CA, HSA, and SA, and compare their performance with that of 2D array i.e., URA, as shown in Fig. 4.2.

4.3 Hybrid Beamforming Design

In this section, we present the design of proposed hybrid precoder $\mathbf{B}\in\mathbb{C}^{N_T\times K}$, which maximizes the spectral and energy efficiencies of mmWave MU-mMIMO systems. The HBF is constructed by concatenating the RF beamformer $\mathbf{F}_D\in\mathbb{C}^{N_T\times N_{RF}}$ and reduced-dimensional MU baseband precoder $\mathbf{B}_D\in\mathbb{C}^{N_{RF}\times K}$. The HBF solutions presented in literature (e.g., [42,62,88]) can achieve a high sum-rate performance but depends on finding the optimal fully digital precoder $\mathbf{F}_{opt}$, which increases the computational complexity. Eigen beamforming (EBF), on the other hand, can give high performance with reduced complexity. However, the RF beamformer in this case constitutes variable-gain entities and thus, does not meet the constraint given in (4.5b). To design the constant-modulus RF beamformer while using EBF is a challenging problem. The simple solution is to formulate the correlation matrix $\mathbf{R}$ based on the array response vector $\mathbf{a}_k$ [101]. Then, the correlation matrix for k^{th} user can be written as:

$$\mathbf{R}_k=\mathbf{a}_k\mathbf{a}_k^T. \tag{4.8}$$

By using Karhunen-Loeve decomposition, we let $\mathbf{R}_k=\mathbf{U}_k\mathbf{\Lambda}_k\mathbf{U}_k^H$. Then, the RF beamformer can be designed using the dominant eigenvalues., i.e., $\mathbf{U}_k^*$. However, this approach gives low performance. In [59], a three-stage HBF is designed using EBF but it requires the use of doubling phase shifter structure. In the proposed HBF design, we introduce a low-complexity solution, which uses ordered SVD of the mmWave MU-mMIMO channel and achieves high performance without requiring $\mathbf{F}_{opt}$ [102].

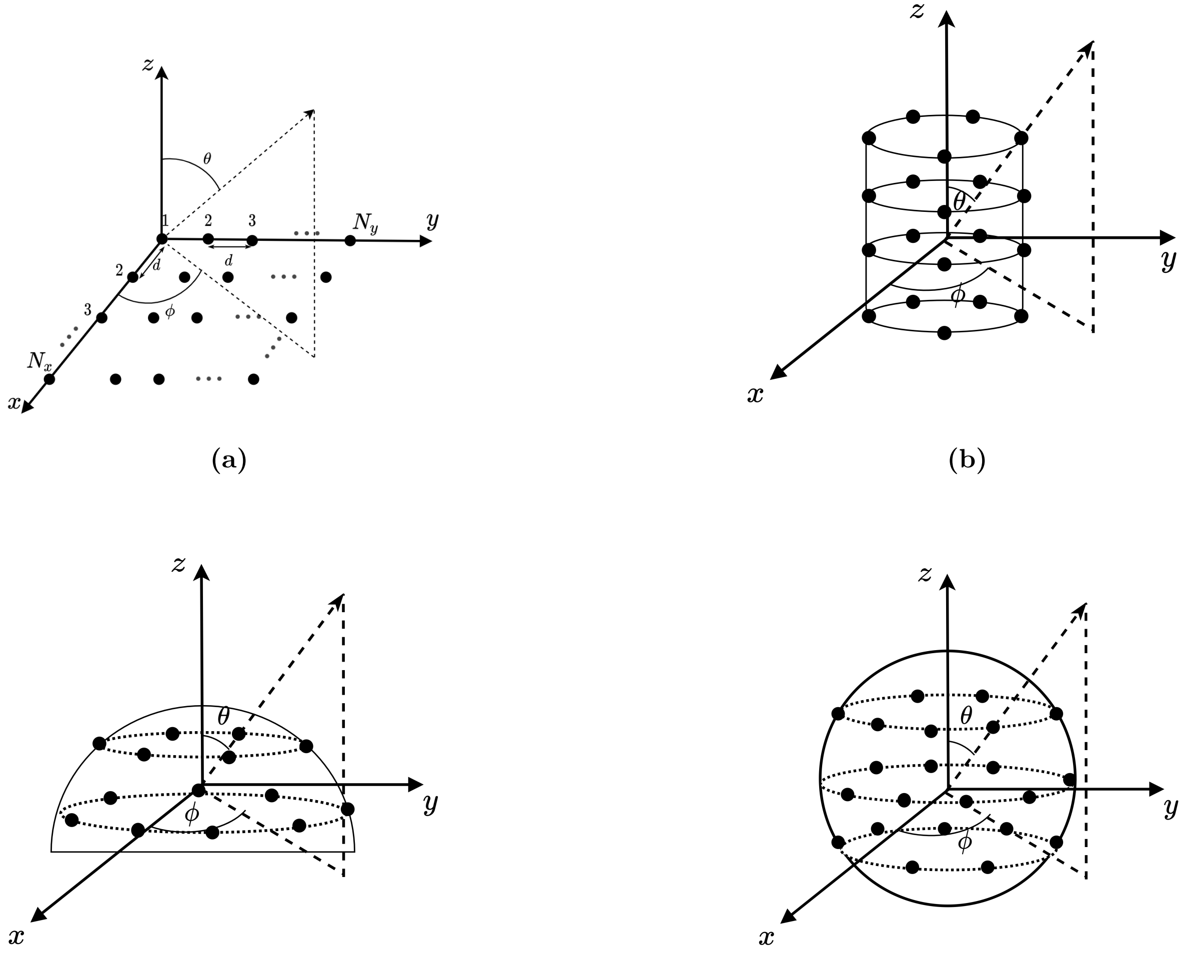

(a) (b)

(c) (d)

Figure 4.2. mmWave MU-mMIMO array structures: (a) URA (b) CA (c) HSA (d) SA.

4.3.1 RF Beamformer Design

We assume K users are clustered into G groups based on their AoD information, where each group contains K_g number of users such that $K = \sum_{g=1}^{G} K_g$. The index $g_k = \sum_{g'=1}^{g-1} K_{g'} + k$ is used to denote the k^{th} user in group g. Then, the channel matrix $\mathbf{H}^{(g)}$ for gth group can be written as:

$$\mathbf{H}^{(g)} = \mathbf{Q}^{(g)} \mathbf{\Sigma}^{(g)} \mathbf{V}^{H(g)}, \tag{4.9}$$

where $\mathbf{Q}^{(g)}$ and $\mathbf{V}^{(g)}$ are $K_g \times K_g$ and $N_T \times N_T$ unitary matrices, respectively. $\mathbf{\Sigma}^{(g)}$ is a $K_g \times N_T$ rectangular diagonal matrix with non-negative real numbers on the diagonal, and

Algorithm 4.1 SVD Based RF Beamformer Design

```
Input: $[\theta_k^{(g)}, \phi_k^{(g)}]$ for $k = 1, \ldots, K$
for $g = 1 : G$ do
    Compute channel matrix $\mathbf{h}_k^{(g)}$ via (4.6)
    Using (4.9), form the unitary matrices $\mathbf{Q}^{(g)}$ and $\mathbf{V}^{(g)}$
    for $n = 1 : N_T$ do
        Calculate the phase of each entity of $\mathbf{V}(:, n)^{(g)}$, i.e., $\psi(:, n)^{(g)}$
        Construct the phase vector $\gamma_n^{(g)}$
    end for
    Formulate $\mathbf{\Gamma}^{(g)}$ via (4.10)
    Compute $\mathbf{W}^{(g)}$ using $N_{RF}^{(g)}$ via (4.11)
end for
$\mathbf{F}_D = [\mathbf{W}^{(1)}, \mathbf{W}^{(2)}, \ldots, \mathbf{W}^{(G)}]$
```

the elements are arranged in decreasing order. Let $\mathbf{\Gamma}^{(g)}$ be the matrix containing N_T column vectors. Then, we can write as:

$$\mathbf{\Gamma}^{(g)} = [\upsilon_1^{(g)}, \upsilon_2^{(g)}, \ldots, \upsilon_{N_T}^{(g)}], \tag{4.10}$$

where $\upsilon_n^{(g)} = [e^{j\psi_{1,n}^{(g)}}, e^{j\psi_{2,n}^{(g)}}, \ldots, e^{j\psi_{N,n}^{(g)}}]^T \in \mathbb{C}^N$ is the phase vector of group g, and $\psi_{m,n}^{(g)}$ is the phase angle of the $(m, n) - th$ entry of $\mathbf{V}$. Comparing (4.9) and (4.10), we can see that each entry of $\upsilon_n^{(g)}$ and $\mathbf{V}_g(n)$ have the same phase angle., i.e., ψ. Let $\mathbf{W}^{(g)}$ be the set containing $N_{RF}^{(g)}$ columns where each *nth* column represents the *nth* largest singular value of channel matrix $\mathbf{H}^{(g)}$. We can write $\mathbf{W}^{(g)}$ as:

$$\mathbf{W}^{(g)} = [\upsilon_1^{(g)}, \upsilon_2^{(g)}, \ldots, \upsilon_{N_{RF}}^{(g)}] \tag{4.11}$$

The pseudo-code for RF beamformer design is given in Algorithm 4.1.

4.3.2 Baseband MU Precoder Design

After the design of RF beamformer $\mathbf{F}_D$, the baseband MU precoder $\mathbf{B}_D$ can be determined by using the joint group processing (JGP) [90]. The overall reduced dimensional effective channel matrix is expressed as $\boldsymbol{\mathcal{H}}^{H} = \mathbf{F}_D^{H}\mathbf{H}$. The effective channel $\boldsymbol{\mathcal{H}}$ can be written as:

$$\boldsymbol{\mathcal{H}} = \begin{bmatrix} \mathbf{H}^{H(1)}\mathbf{F}_D^{(1)} & \mathbf{H}^{H(1)}\mathbf{F}_D^{(2)} & \dots & \mathbf{H}^{H(1)}\mathbf{F}_D^{(G)} \\ \mathbf{H}^{H(2)}\mathbf{F}_D^{(1)} & \mathbf{H}^{H(2)}\mathbf{F}_D^{(2)} & \dots & \mathbf{H}^{H(2)}\mathbf{F}_D^{(G)} \\ \vdots & \vdots & \ddots & \vdots \\ \mathbf{H}^{H(G)}\mathbf{F}_D^{(1)} & \mathbf{H}^{H(G)}\mathbf{F}_D^{(2)} & \dots & \mathbf{H}^{H(G)}\mathbf{F}_D^{(G)} \end{bmatrix}, \tag{4.12}$$

where the diagonal matrices $\mathbf{H}^{H(g)}\mathbf{F}_D^{(g)} \in \mathbb{C}^{K(g)\times N_{RF(g)}}$ are the effective channel matrix for group g and the off-diagonal matrices $\mathbf{H}^{H(g)}\mathbf{F}_D^{(\hat{g})} \in \mathbb{C}^{K(g)\times N_{RF\hat{g}}}$ represent the effective interference channel matrix between groups g and $\hat{g}$, $\forall \hat{g} \neq g$. By applying the well-known RZF technique, $\mathbf{B}_D$ is defined as:

$$\mathbf{B}_D = \gamma \mathbf{T}\boldsymbol{\mathcal{H}}, \tag{4.13}$$

where $\boldsymbol{\mathcal{H}}$ is the reduced-dimension effective channel as provided in (4.12), $\mathbf{T} = [\boldsymbol{\mathcal{H}}\boldsymbol{\mathcal{H}}^H + \alpha N_{RF}\mathbf{I}_{N_{RF}}]^{-1}$, $\mathbf{I}_{N_{RF}} \in \mathbb{C}^{N_{RF}\times N_{RF}}$, α is the regularization parameter and γ is the normalization factor used to satisfy the power constraint, which can be written as:

$$\gamma = \sqrt{\frac{S}{\mathrm{tr}\{\boldsymbol{\mathcal{H}}^{H}\mathbf{T}^{H}\mathbf{F}_D^{H}\mathbf{F}_D\mathbf{T}\boldsymbol{\mathcal{H}}\}}}. \tag{4.14}$$

4.4 Illustrative Results

In this section, the Monte-Carlo simulation results are presented based on the proposed hybrid precoding for various array structures. For the presented results, we assume the BS is equipped different array configurations as depicted in Fig. 4.2. For URA(CA), we arrange the antenna elements in 20 rows(rings), where each row(ring) having 10 elements with a spacing of $d_s = \frac{\lambda}{2}$ [90, 100]. For HSA and SA, the antenna elements are arranged having uniform angle spacing [99]. The signal-to-noise-ratio (SNR) is defined as $\frac{P_T}{\sigma^2 K}$ and the regularization parameter $\alpha = \frac{\sigma^2}{P_T}$ [59].

4.4.1 Spectral Efficiency (SE) Comparison

In this section, we compare the spectral efficiency of different 3D array structures in mmWave MU-mMIMO systems both with 2D array structure (i.e., URA) and HBF solutions presented in [42,88,101]. In Fig. 4.3, we compare the sum-rate performance of different array structures, when $N = 200$. We consider $K = 12$ users are equally distributed into $G = 3$

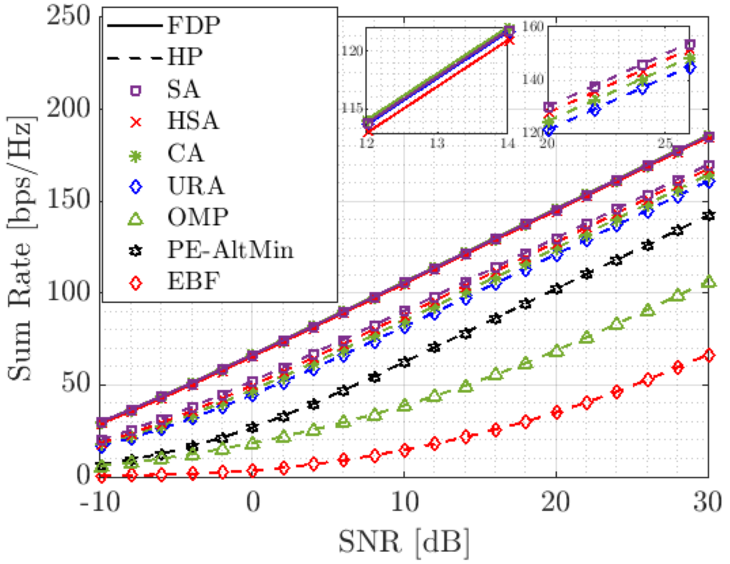

Figure 4.3. Sum-rate versus SNR comparison for URA, CA, HSA and SA.

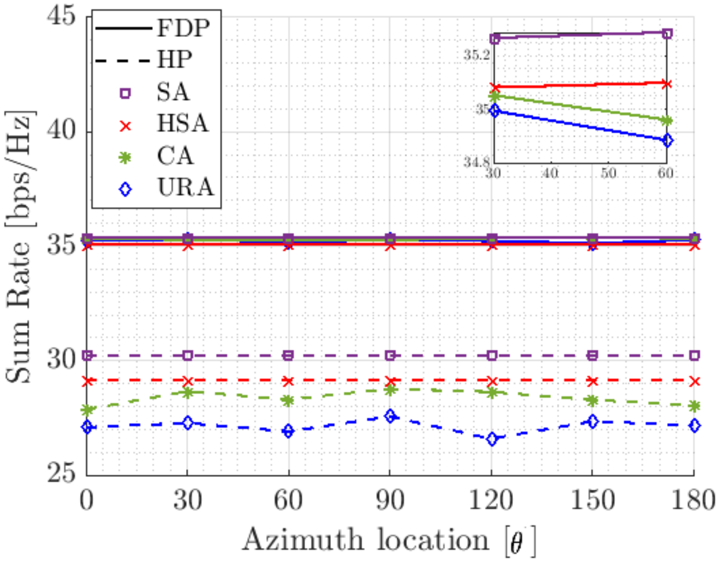

Figure 4.4. Sum-rate versus azimuth location θ, $\phi = 73°$, SNR = 10 dB.

groups (i.e., $K_g = 4$, $\forall g$), which are located around the BS at mean elevation angle $\phi = 73°$, mean azimuth locations $(\theta_1, \theta_2, \theta_3) = (30°, 90°, 150°)$ with $\delta_a = 15°$ and $\delta_e = 12.5°$. Each user having minimum number of RF chains (i.e., $N_{RF_g} = K_g = 4$). For SNR varying from -10 dB to 30 dB, we plot the sum-rate of URA, CA, HSA and SA in Fig. 4.3. FDBF achieves higher sum-rate but it requires the utilization of 200 RF chains. On the other hand,

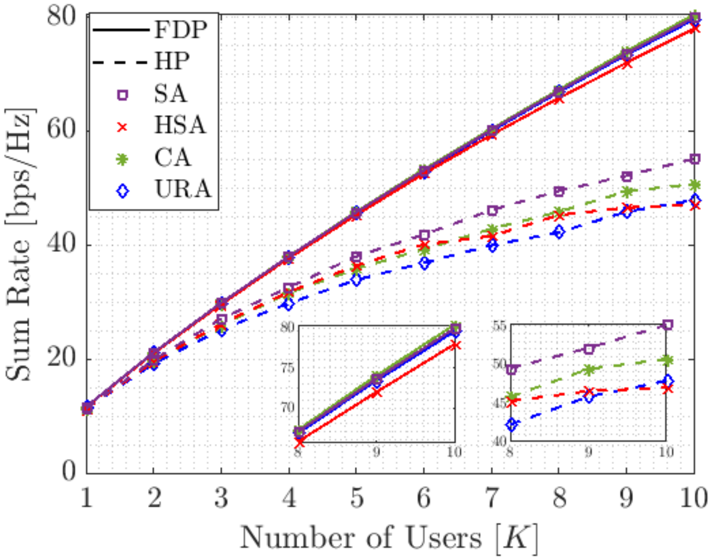

Figure 4.5. Sum-rate versus number of users K, $N = 200$, $G = 1$, $N_{RF} = K$, $\phi = 73°$, $\theta = 90°$, $(\delta_a, \delta_e) = (\pm 15°, \pm 12.5°)$, SNR $= 20$ dB.

by using the proposed HBF, the sum-rate capacity of FDBF can be closely achieved with HBF by only using 12 RF chains., i.e., a 94% reduction of RF chains. Also, the use of 3D array structure can provide a higher sum-rate when compared to URA (e.g., the sum-rate increases by approximately 10 bps/Hz via CA, HSA or SA) as well as the HBF schemes in [42, 88, 101]. In Fig. 4.4, we investigate the variation of sum-rate for different array structures when the user changes its angular location. We consider single user group., i.e., $G = 1$ having $N_{RF_g} = K_g = 4$. Fig. 4.4 shows the sum-rate versus the mean azimuth location of a user group θ, where θ varies between [0°:30°:180°] and $\phi = 73°$ at SNR $=$ 10 dB. It can be seen that both HSA and SA can provide a non-varying/uniform sum-rate irrespective of the angular location θ because of a more symmetrical configuration, whereas the sum-rate can vary slightly for URA and CA. Also, both SA and HSA provide a higher sum-rate.

Fig. 4.5 plot the sum-rate versus number of users K for single user group ($G = 1$) located at $\theta = 90°$ and evaluated at SNR $=$ 20 dB. 3D array structures can provide a higher sum-rate, where in particular SA can offer the highest sum-rate among all the array structures. Considering the future massive wireless connectivity requirements of IoT and for different aerial applications (e.g., in UAVs), different 3D array structures can be considered, which can provide a high sum-rate while supporting more number of users/devices.

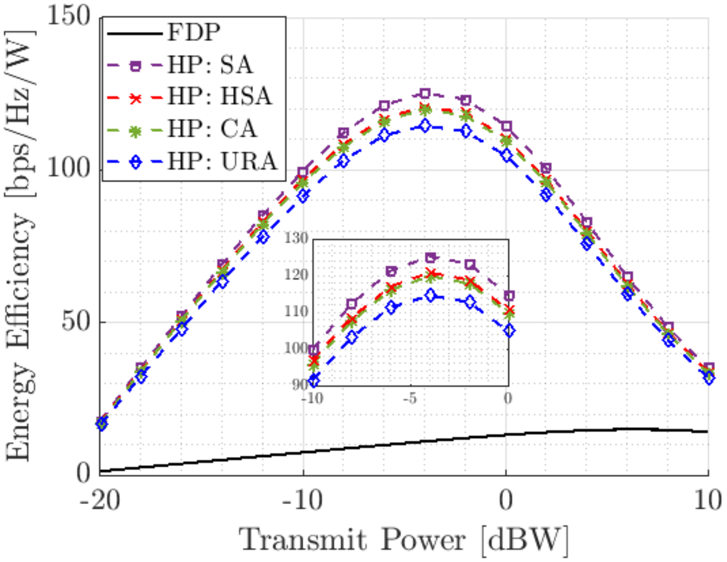

Figure 4.6. Energy efficiency versus transmit power P_T.

4.4.2 Energy Efficiency Comparison

In this section, we compare the energy efficiency of the proposed HBF in mmWave MU-mMIMO systems using different 3D array structures. The energy efficiency ϵ is defined as the ratio of the sum-rate R_{sum} and the total power consumption P_{total}, i.e.,

$$\epsilon = \frac{R_{sum}}{P_{total}} = \frac{R_{sum}}{P_T + N_{RF}P_{RF} + N_{PS}P_{PS}}, \tag{4.15}$$

where P_T represents the total transmission power, N_{RF} is the total number of RF chains, P_{RF} and P_{PS} are the power consumptions of each RF chain and PS, respectively. $N_{PS} = N_{RF} \times N_T$ is the total number of PSs used at the RF front end. As in [90], we use $P_T = 1$ W, $P_{RF} = 250$ mW and $P_{PS} = 1$ mW. In Fig. 4.6, we plot energy efficiency versus transmit power for single user group (i.e., $G = 1$) located at $\phi = 73°$, $\theta = 30°$. We analyze the performance of different 3D array structures at SNR $= 10$ dB. FDBF provides very low performance due to use of large number of RF chains. On the other hand, the proposed HBF can provide a higher energy efficiency as it uses only a few number of RF chains (in this case, $N_{RF} = K = 4$). Furthermore, 3D array structures can give a more energy-efficient HBF design in mmWave MU-mMIMO systems when compared to 2D array structures.

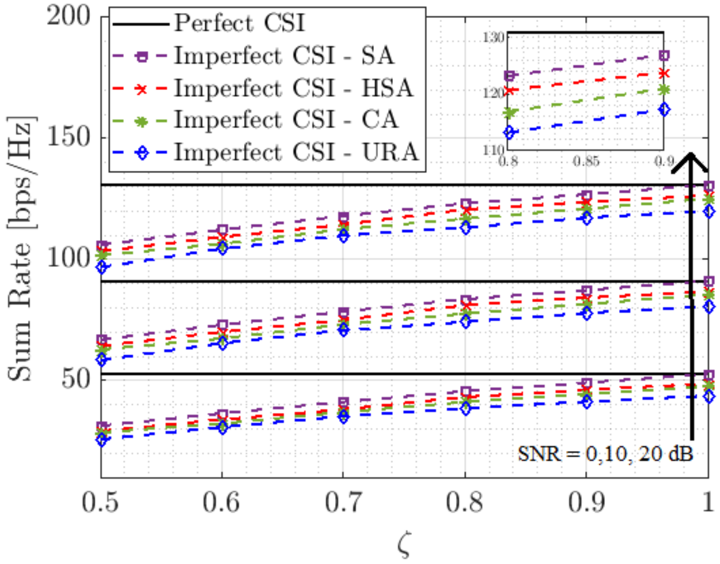

Figure 4.7. Sum-rate versus imperfect CSI ζ at SNR = 0, 10, 20 dB.

4.4.3 Complexity Analysis

The design of FDBF requires $\mathcal{O}(N^3 + KN^2)$ operations, where $\mathcal{O}(KN^2)$ is required for computation of $\mathbf{H}\mathbf{H}^H$ and matrix inversion requires $\mathcal{O}(N^3)$. For the proposed HBF, to obtain RF beamformer $\mathbf{F}_D$ as given in Algorithm 4.1, the complexity is $\mathcal{O}(GN)$, where N_T is the total number of antennas and G is the total number of user groups. Then, the design of baseband precoder (as given in (4.13)) $\mathbf{B}_D$ requires $\mathcal{O}(N_{RF}^3 + KN_{RF}^2)$ operations, which makes the computational complexity of the proposed HBF solution as $\mathcal{O}(GN_T + N_{RF}^3 + KN_{RF}^2)$. For the HBF solution in [88] and [42], the computational complexity of $\mathbf{F}_{opt}$ requires $\mathcal{O}(K^2 N_T)$ operations. Thus, the overall complexity becomes $\mathcal{O}\Big(K^2 N_T + N_T^2 K N_{RF}\Big)$ and $\mathcal{O}\Big(K^2 N_T + k N_T N_{RF}^2\Big)$, respectively, where k is the number of iterations. As an example, consider $N_T = 100$, $G = 3$, $K = 3$ and $N_{RF} = 3$, the complexity of the proposed HBF solution is only about 1 percent of the complexity of the HBF methods in [42, 88].

4.4.4 Imperfect CSI

In practical systems, CSI is contaminated by estimation error, therefore, we evaluate the impact of imperfect CSI on the performance of the proposed HBF solution. The estimated channel matrix $\hat{\boldsymbol{\mathcal{H}}}$ is given as [90]:

$$\hat{\boldsymbol{\mathcal{H}}} = \zeta \boldsymbol{\mathcal{H}} + \sqrt{1 - \zeta^2}\mathbf{E}, \tag{4.16}$$

where $\boldsymbol{\mathcal{H}}$ is the reduced-dimensional effective channel matrix at the baseband, $\zeta \in [0, 1]$ is the parameter that controls CSI accuracy and $\mathbf{E}$ is the error matrix with entities following the standard complex Gaussian distribution. In Fig. 4.7, we compare the effect of channel estimation error on the sum-rate for different array structures and observe that the proposed HBF scheme is not sensitive to the accuracy of CSI. In particular, SA can provide a higher sum-rate when compared to HSA, CA and URA with imperfect CSI (e.g., $\zeta = 0.7$).

4.5 Concluding Remarks

In this chapter, we have presented the mmWave MU-mMIMO HBF design and investigated the performance comparison of different 3D antenna array structures. In the low-complexity HBF design, the RF beamformer has been developed by using the ordered SVD of the channel matrix, whereas the baseband precoder is designed using the reduced-dimensional effective channel matrix via RZF. The simulation results show the high spectral and energy efficiencies of 3D antenna arrays when compared to URA for the proposed HBF solution as well as the robustness to the channel imperfections. Among different 3D configurations introduced in this letter, both HSA and SA can provide high uniform performance irrespective of the users' angular location around the BS.

Chapter 5

Enhancing Capacity in Full-Duplex Massive MIMO: Hybrid Beamforming Approach[1]

5.1 Introduction

In the previous chapters, the HBF techniques have been proposed for the half-duplex (HD) mMIMO systems. Full-duplex (FD) communications can further extend the expected impacts of the mMIMO systems since it theoretically doubles the capacity via simultaneous transmission and reception over the same frequency band. Although FD is severely affected by the strong self-interference (SI), the recent developments in SI suppression (SIS) techniques make it more practical [43–45]. For instance, the Tx and Rx antenna sub-systems can be designed in such a way to isolate the transmit and receive RF chains as much as possible [46–48]. The practical demonstrations show SI suppression between -60 and -70 dB based on antenna isolation [49]. On the other hand, active SI cancellation refers to mitigating SI by subtracting a processed copy of the transmitted signal from the received signal. Then, based on the signal domain, where the SI signal is subtracted, active cancellation is divided into digital and analog SI cancellations. Analog SI cancellation requires the use of specially designed circuitry to reconstruct the SI counterpart and substract it from the received signal at the analog front-end of the local

---

[1] Parts of this chapter have been presented at the 2023 IEEE Global Communications Conference (GLOBECOM), KualaLumpur, Malaysia [103], the 2024 IEEE Wireless Communications and Networking Conference (WCNC), Dubai, UAE [104], and published in the IEEE Open Journal of the Communications Society [105].

Rx [106–108]. Digital SI cancellation techniques are considered to be the simplest forms of active cancellation techniques. However, the amount of SI cancellation achieved through digital techniques is quite limited due to hardware imperfections, particularly transceiver phase noise and non-linearities that restrict the performance of traditional digital cancellation techniques [52]. Therefore, antenna isolation, analog and digital SI cancellation (suppression), and their combinations have been used to suppress the strong SI signal below the Rx noise floor in FD communications [109–111].

In 5G and beyond systems, there is a growing trend towards utilizing an increased number of antennas at BS. For instance, 3GPP has been considering configurations with 64-256 antennas [32]. However, the increased number of antennas introduces additional challenges for analog SI cancellation in FD mMIMO systems. This results in high analog complexity, which is not affordable. An alternative approach relies exclusively on transmit beamforming to suppress SI, thereby completely obviating the need for analog cancelers [112]. The use of large array structures both at the transmitter and receiver in FD communications can provide additional spatial DoF, which can help to suppress strong SI and can double the capacity. The existing research studies, for instance [113–120], consider HBF in FD mMIMO systems to mitigate the strong SI from Tx to Rx. However, the SI suppression evaluation in these studies relies exclusively on the theoretical SI channel models. In other words, the studies in [113–120] do not consider the experimental evaluations to validate the theoretical doubling of capacity/throughput. Instead, the studies assume both residual near-field SI channel via LoS paths and the far-field SI channel via the reflected non-line-of-sight (NLoS) paths in a simulated manner. In practical implementations, real-world platforms inevitably experience SINR loss due to the impact of strong SI. Therefore, it is important to develop a robust understanding of beamforming-based SI suppression capabilities by utilizing the experimentally measured SI channels. Therefore, investigating the effectiveness of beamforming-based SI suppression in the real-time implementation of FD mMIMO systems becomes essential to bridge this gap between theory and practical performance.

Additionally, most existing FD studies primarily consider FC-HBF architectures. In the FC-HBF scheme, each RF chain is connected to all antenna elements, which allows the RF chain to exploit the full beamforming capability of the antenna array. However, this leads to increased cost and complexity. On the other hand, SC-HBF architectures require the connection of each RF chain to a subset of antennas, significantly reducing the connectivity and implementation cost/complexity. Thus, SC-HBF utilizes fewer RF PSs circuits compared to FC-HBF, and its use can reduce power consumption at the expense of some performance degradation. However, SC-HBF can provide a better spectral-energy efficiency tradeoff [104,121]. Thus, it is more suitable to deploy SC-HBF structure for future key enabling technologies, for instance, mmWave and sub-Terahertz (THz) communications [122–124]. It is worth noting that the SC-HBF architecture is mainly considered in HD transmission studies, while most research in FD communications has focused on the use of FC-HBF [113–120]. Therefore, it is important to explore SC-HBF architecture's potential in FD mMIMO systems to reveal its advantages and enable its deployment in emerging technologies.

The main contributions of this chapter are outlined as follows:

- We formulate a multi-objective optimization framework that focuses on maximizing the total achievable-rate and SI minimization in FD mMIMO systems. To solve this challenging non-convex MOOP, we propose swarm intelligence-based SI suppression scheme that optimizes the beam perturbations in the UL and DL UE directions and find the best Tx and Rx sub-arrays while satisfying the directivity degradation constraints.

- We propose two different SI suppression schemes for the design of UL/DL RF beamformers, namely maximum-directivity beamforming (MBF) and perturbed beamforming (PBF) incorporating SAS for MOOP[1]. The MBF scheme optimizes the RF beamformers by maximizing the intended signal power and suppressing SI leakage power using maximum-directivity beams. In the joint PBF with SAS scheme, we introduce perturbations to the MBF beams to enhance SI suppression. Compared to the PBF scheme in [117], which uses phase-range constraints, the proposed PBF scheme uses directivity-loss constraints, which offer greater flexibility in perturbing the MBF beams while maintaining low directivity loss. Additionally, we jointly select the best Tx and Rx sub-arrays, optimizing the UL and DL beam directions to further enhance SI suppression by leveraging the spatial DoF.

- For the practical application purpose, we implement a testbed in an anechoic chamber to measure the SI channel in the sub-6GHz band. The experimental setup considers 64 Tx and 64 Rx antenna elements as per 3GPP [32] and the measurements are done without external surrounding reflections (i.e., SI channel is mainly due to "internal" coupling between Tx and Rx antenna arrays) for a frequency band between 3 GHz and 4 GHz. We formulate RF beamforming stages using the proposed perturbation-based

---

[1] It must be noted that the MBF and PBF RF beamformers design in [103] reduces SI only, whereas, in this work, the MBF and PBF RF beamformers formulation is based on a multi-objective design criteria i.e., reducing SI and maximizing the total rate.

PBF schemes using the measured SI channel for 20 MHz bandwidth (BW). Moreover, we employ a SC-HBF architecture for both Tx and Rx arrays, and investigate SI suppression for the measured SI channel. The illustrative results show the significant SI suppression achieved using the proposed joint PBF with SAS scheme compared to the MBF scheme. We also demonstrate that using only 4 (1×4) or 8 (1×8) antenna elements, SI value can be brought down to -78 dB, which shows the spatial suppression abilities of FD mMIMO systems.

- We provide a realistic capacity gain in FD communications compared to HD transmissions in mMIMO systems. Specifically, we consider the extreme case when both UL and DL users are at same angular locations. Our results show that FD performance degrades significantly when using MBF scheme due to inter-user interference (IUI). However, using the proposed joint PBF with SAS scheme can achieve approximately 1.85 times more capacity than HD communications in real-time implementations.

The rest of this chapter is organized as follows. In Section 5.2, we discuss the channel model for the FD mMIMO systems. Section 5.3 presents CM HBF design jointly with sub-array selection scheme., whereas in Section 5.4, we discuss the non-constant modulus (NCM) HBF design. The illustrative results are provided in Section 5.5 to compare the performance of the proposed HBF schemes. Finally, the chapter is concluded in Section 5.6.

5.2 Channel Model

In this subsection, we present the intended channel, IUI channel, and the measured SI channel in an acnechoic chamber.

5.2.1 Intended Channel

Based on the geometry-based 3D channel model [125], the channel vector between the BS and UE is given by:

$$\mathbf{h}_i^T = \sum_{l=1}^{L} \tau_{i_l}^{-\eta} z_{i_l} \boldsymbol{\phi}_i(\theta_{i_l}, \phi_{i_l}) = \mathbf{z}_i^T \boldsymbol{\Phi}_i \in \mathbb{C}^{M_i}, \tag{5.1}$$

where $\tau_{i_l}^{-n}$ and $z_{i_l} \sim \mathcal{CN}\left(0, \frac{1}{L}\right)$ are the distance and complex path gain of the l^{th} path, η is the path loss exponent and $\boldsymbol{\phi}_i(.\,.)$ is the array steering vector with $i = \{D, U\}$ is the DL phase response vector for $i = D$ or the UL phase response vector for $i = U$. Here, the angles $\theta_{i_l} \in \left[\theta_i - \delta_i^\theta, \theta_i + \delta_i^\theta\right]$ and $\phi_{i_l} \in \left[\phi_i - \delta_i^\phi, \phi_i + \delta_i^\phi\right]$ are the azimuth AoD (AAoD) and elevation AoD (EAoD) for l^{th} path in i^{th} channel, respectively. $\theta_i(\phi_i)$ is the mean AAoD(EAoD) with angular spread $\delta_i^\theta(\delta_i^\phi)$. Then, the i^{th} instantaneous channel vector for the user is represented via the fast time-varying path gain vector $\mathbf{z}_i = \left[\tau_{i_1}^{-\eta} z_{i_1}, \cdots, \tau_{i_L}^{-\eta} z_{i_L}\right]^T \in \mathbb{C}^L$ and the slow time-varying phase response matrix as:

$$\mathbf{\Phi}_i = \begin{bmatrix} \boldsymbol{\phi}_i^T\left(\theta_{i_1}, \phi_{i_1}\right) \\ \vdots \\ \boldsymbol{\phi}_i^T\left(\theta_{i_L}, \phi_{i_L}\right) \end{bmatrix} \in \mathbb{C}^{L \times M_i}, \tag{5.2}$$

where $M_i \in \{M_{ds}, M_{us}\}$ is the Tx/Rx antenna elements.

5.2.2 IUI Channel

Based on the array phase response vectors $\boldsymbol{\phi}_D$ and $\boldsymbol{\phi}_U$ (as given in (5.2)), the IUI channel for single antenna u^{th} UL UE and d^{th} DL UE can be written as [117]:

$$\mathbf{H}_{\text{IUI}}(u,d) = \tau_{\text{IUI}_{u,d}}^{-\eta} z_{\text{IUI}_{u,d}}, \tag{5.3}$$

where $\tau_{\text{IUI}_{u,d}}$ and $z_{\text{IUI}_{u,d}} \sim \mathcal{CN}(0,1)$ are the distance and path gain for the UL and DL UEs, respectively.

5.2.3 Measured SI Channel

We consider a measured SI channel based on the measurement setup designed in an anechoic chamber (i.e., without external surrounding reflections) as shown in Fig. 5.1. The OTA FD lab setup has following internal dimensions: 1) length = 20 ft (6.096 m); 2) width = 8 ft (2.438 m); and 3) height = 8 ft (2.438 m). This non-reflective space was large enough to place our antenna array under test (measuring 84 cm × 32 cm, W×H) on a positioner, approximately 4 ft away from each of C-RAM SFC-48 absorber covered five walls (reflection < -45 dB at 3.5 GHz). We did not observe significant changes to the measured SI channel when slightly rotating the antenna under test. The antenna arrays consisted of 64 right-hand circular polarization Tx elements and 64 left-hand circular polarization Rx elements. These elements were designed to minimize cross-polarization, and all antenna elements shared a common ground plane. Both the Tx and Rx antenna arrays were arranged in an 8×8 URA configuration, with a spacing of 20 cm between these two arrays, enhancing passive

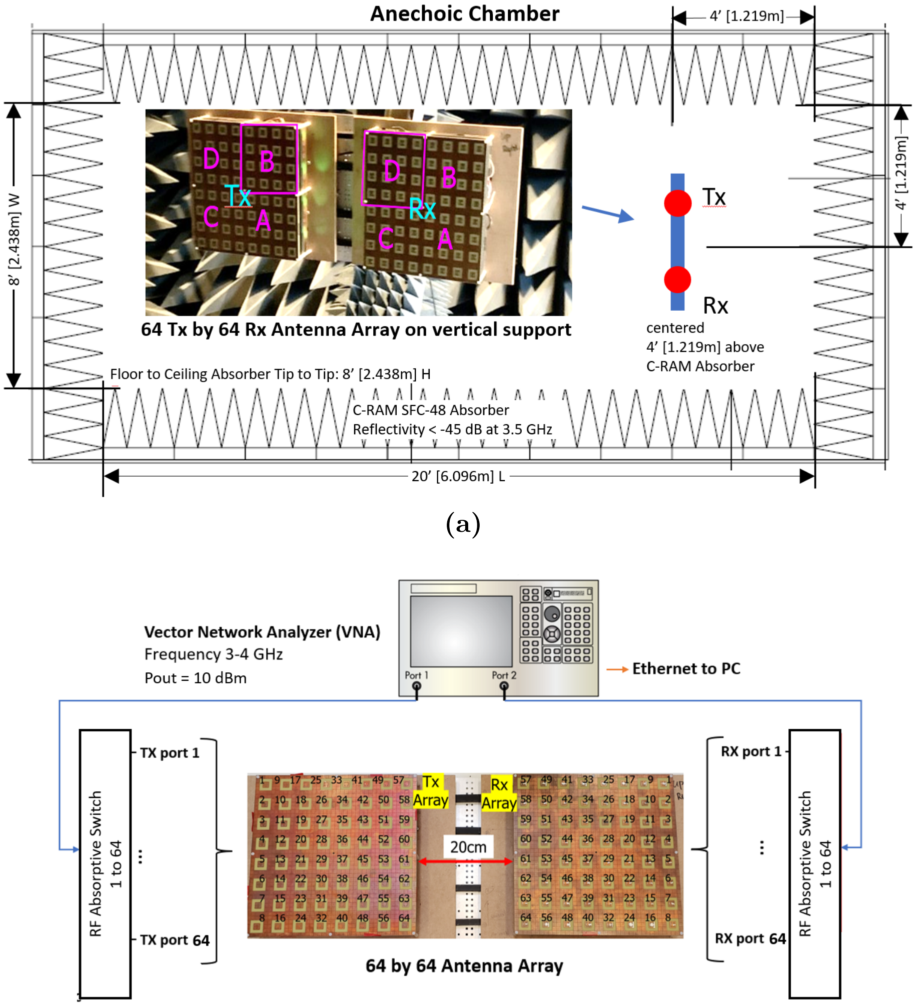

(a)

(b)

Figure 5.1. OTA FD mMIMO lab setup for SI measurement. (a) Anechoic chamber. (b) Tx and Rx setup.

isolation. Fig. 5.1 illustrates the mapping of the 64 Tx and 64 Rx antenna arrays. The S-parameters were measured with vector network analyzer (VNA) Keysight PNA N5247A, configured with an output power of 10 dBm. To reduce the effect of noise on the expected high isolation measurements, intermediate frequency (IF) BW should be set 300 Hz (resulting in an integrated thermal noise power of -149 dBm), and trace smoothing function was set to 1%, the averaging was turned off. The measurement bandwidth was 1 GHz, from 3 GHz to 4 GHz, with a step size of 625 kHz (resulting in 1601 measurement points). The sweep time for each antenna elements pair was $\sim$10 sec, thus total measurement time for $64 \times 64 = 4096$ combinations, was expected to be 11.5 hrs.

The Tx and Rx antennas were connected to the VNA via 5m long coaxial cables, and MCL USB-1SP16T-83H RF absorptive switches, with approximate total insertion loss of 12.5 dB, on both the Tx and Rx sides. To construct the full 64×64 s-parameters matrix, the measurements were done using two SP16T RF switches (one for Tx and one for Rx) connected to each 4×4 sub-section at a time. The obtained s-parameters were transmitted to a PC via Ethernet and post-processed in MATLAB, to de-embed all insertion losses of the test setup, and to construct 64 Tx by 64 Rx SI channel matrix for further use in analysis and simulations of the FD mMIMO testbed system. The detailed results of the measured 64 Tx by 64 Rx SI channel, such as magnitude, phase, and delay are discussed in detail in [126]. The individual isolation between each Tx and Rx element ranged from approximately 37 dB to 80 dB, thus the resulting minimum SNR, in front of the VNA receiver, was expected to be approximately 54 dB (10dBm – 12.5dB – 80dB – 12.5 dB + 149dBm). The observed trace variations over frequency, for fixed RF attenuator of 100dB at VNA ports, were approximately ±0.75 dB, ±3°, and ±100ps for group delay. This setup is used for SI channel measurement.

The resulting parameters in the form of .S2P file are used to get a 64x64 SI channel matrix, which is mainly due to *internal* coupling between Tx and Rx antenna elements (i.e., consisting of only LoS path components). Then, the complete SI channel matrix $\mathbf{H}_{\text{SI, ALL}}$ has dimensions of $64 \times 64 \times 1601$ for a total of 1601 different frequency points. As mentioned earlier, we consider a ULA sub-array configurations of 4 and 8 antenna elements for both Tx and Rx. Hence, the corresponding SI channels for 1×4 and 1×8 sub-array configurations can be represented as $\mathbf{H}_{\text{SI}} \in \mathbb{C}^{4\times4\times1601}$ and $\mathbf{H}_{\text{SI}} \in \mathbb{C}^{8\times8\times1601}$, respectively. As per 3GPP specification, the UL and DL channel BW can vary from 5 MHz to 100 MHz [127], then the corresponding SI channel for the given BW can be written as: $\mathbf{H}_{\text{SI},B} = \mathbf{H}_{\text{SI}}(:,:,n) \in \mathbb{C}^{i\times i\times n}$, where $i = \{4, 8\}$, B is the given BW, and $n = 1, 2, \ldots, N$ is the sample frequency point for a total of N frequency points in a given BW. For instance, for a BW of 20 MHz, $n = 1, 2, \ldots, 33$ for the frequency range from 3.49 GHz to 3.51 GHz. Similarly, for a BW of 100 MHz, $n = 1, 2, \ldots, 161$ for the frequency range from 3.45 GHz to 3.55 GHz.

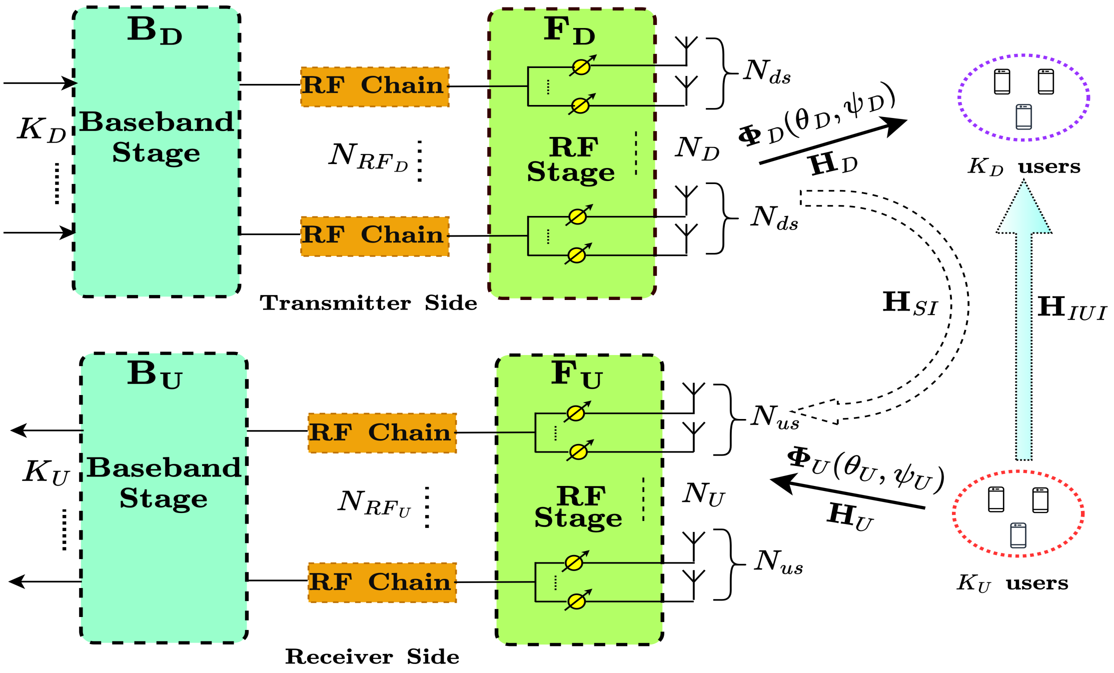

Figure 5.2. FD mMIMO system using SC-HBF architecture.

5.3 Constat-Modulus Hybrid Beamforming Design: Joint Beam-Perturbation and Sub-Array Selection

5.3.1 System Model

We consider a single-cell FD mMIMO systems for joint DL and UL transmission as shown in Fig. 5.2. Here, the BS is equipped with transmit/receive uniform rectangular arrays (URAs), and operates in FD mode to simultaneously serve K_D DL and K_U UL single-antenna users over the same frequency band, while the users operate in HD mode due to the hardware/software constraints (e.g., low power consumption, limited signal processing and active/passive SI suppression capability). Specifically, the transmit (receive) URA has $N_D = N_D^{(x)} \times N_D^{(y)}(N_U = N_U^{(x)} \times N_U^{(y)})$ antennas, where $N_D^{(x)}(N_U^{(x)})$ and $N_D^{(y)}(N_U^{(y)})$ denote the number of transmit (receive) antennas along x-axis and y-axis, respectively.

For the proposed FD mMIMO systems, we consider the DL signal is processed through DL BB stage $\mathbf{B}_D = [\mathbf{b}_{D,1}, \mathbf{b}_{D,2}, \dots, \mathbf{b}_{D,K_D}] \in \mathbb{C}^{N_{RF_D} \times K_D}$ and DL RF beamformer $\mathbf{F}_D \in \mathbb{C}^{N_D \times N_{RF_D}}$, where N_{RF_D} is the number of RF chains such that $K_D \leq N_{RF_D} \ll N_D$ and

$\mathbf{b}_{D,k} \in N_{RF_D}$ is the BB stage vector for k^{th} DL UE. Similarly, the received UL signal at BS is processed through UL RF beamformer $\mathbf{F}_U \in \mathbb{C}^{N_{RF_U} \times N_U}$ and UL BB combiner $\mathbf{B}_U = [\mathbf{b}_{U,1}, \mathbf{b}_{U,2}, \ldots, \mathbf{b}_{U,K_U}]^T \in \mathbb{C}^{K_U \times N_{RF_U}}$ by utilizing $K_U \leq N_{RF_U} \ll N_U$ RF chains. To further reduce the complexity and cost, we consider a SC-HBF architecture as shown in Fig. 5.2, where the Tx (Rx) URA is divided into $M_D(M_U)$ different sub-arrays in the form of uniform linear array (ULA). Hence, compared to $N_D \times N_{RF_D}$ PSs for Tx ($N_U \times N_{RF_U}$ PSs for Rx), only $N_{ds} \times N_{RF_D}(N_{us} \times N_{RF_U})$ PSs are required as RF chain s is connected to a specific sub-array, comprising a distinct set of antenna elements. Here, $M_{ds}(M_{us})$ represents the number of Tx (Rx) antenna elements for RF chain s, where $\sum_{s=1}^{M_D} N_{ds} = N_D$ and $\sum_{s=1}^{M_U} N_{us} = N_U$. The m_D^{th} Tx sub-array, for instance, consists of N_{ds} antenna elements numbered from 1 to N_{ds}, ensuring a sequential distribution of elements within each sub-array. Similarly, the m_U^{th} Rx sub-array comprises antenna elements numbered from 1 to N_{us}. This approach ensures an orderly arrangement of antenna elements within each sub-array. We assume that $N_{ds}(N_{us})$ is an integer value such that each Tx (Rx) sub-array has the same number of antennas. It must be noted that each sub-array is independent of each other. Thus, we can write the DL and UL RF beamformers as follows:

$$\mathbf{F}_D = \begin{bmatrix} \mathbf{f}_D^{(1)} & \mathbf{0} & \ldots & \mathbf{0} \\ \mathbf{0} & \mathbf{f}_D^{(2)} & \ldots & \mathbf{0} \\ \vdots & \vdots & \ddots & \vdots \\ \mathbf{0} & \mathbf{0} & \ldots & \mathbf{f}_D^{(L_D)} \end{bmatrix} \in \mathbb{C}^{N_D \times N_{RF_D}}, \tag{5.4}$$

$$\mathbf{F}_U = \begin{bmatrix} \mathbf{f}_U^{(1)} & \mathbf{0} & \ldots & \mathbf{0} \\ \mathbf{0} & \mathbf{f}_U^{(2)} & \ldots & \mathbf{0} \\ \vdots & \vdots & \ddots & \vdots \\ \mathbf{0} & \mathbf{0} & \ldots & \mathbf{f}_U^{(L_U)} \end{bmatrix}^H \in \mathbb{C}^{N_{RF_U} \times N_U}, \tag{5.5}$$

where $\mathbf{f}_D^{(l_D)} \in \mathbb{C}^{N_{ds}}$ is the DL RF beamformer associated with m_D^{th} Tx sub-array. Similarly, $\mathbf{f}_U^{(m_U)} \in \mathbb{C}^{N_{us}}$ is the UL RF beamformer associated with m_U^{th} Rx sub-array. Here, the UL and DL RF beamforming stages (i.e., $\mathbf{F}_U$ and $\mathbf{F}_D$) are built using low-cost PSs, which brings the constant-modulus (CM) constraint due to the use of PSs. Then, the DL channel matrix is denoted as $\mathbf{H}_D = [\mathbf{h}_{D,1}, \mathbf{h}_{D,2}, \ldots, \mathbf{h}_{D,K_D}]^T \in \mathbb{C}^{K_D \times N_D}$ with $\mathbf{h}_{D,d} \in \mathbb{C}^{N_D}$ as the d^{th} DL UE channel vector. Similarly, $\mathbf{H}_U = [\mathbf{h}_{U,1}, \mathbf{h}_{U,2}, \ldots, \mathbf{h}_{U,K_U}] \in \mathbb{C}^{N_U \times K_U}$ is the UL channel matrix with $\mathbf{h}_{U,u} \in \mathbb{C}^{N_U}$ as the u^{th} UL UE channel vector. Due to the FD transmission, the SI channel matrix $\mathbf{H}_{\text{SI}} \in \mathbb{C}^{N_U \times N_D}$ is present between Tx and Rx antennas at the BS. For the DL transmission, the transmitted signal vector at the BS is defined as $\mathbf{s}_D = \mathbf{F}_D \mathbf{B}_D \mathbf{d}_D \in \mathbb{C}^{N_D}$, where $\mathbf{d}_D = [d_{D,1}, \ldots, d_{D,K_D}]^T \in \mathbb{C}^{K_D}$ is the DL data signal vector such that $\mathbb{E}\{\mathbf{d}_D\mathbf{d}_D^H\} = \mathbf{I}_{K_D}$. The transmitted signal vector satisfies the maximum DL transmit power constraint, which is $\mathbb{E}\{||\mathbf{s}_D||^2\} = \mathrm{tr}(\mathbf{F}_D\mathbf{B}_D\mathbf{B}_D^H\mathbf{F}_D^H) \leq P_D$, where P_D is the total DL transmit power. The IUI channel $\mathbf{H}_{\mathrm{IUI}} = [\mathbf{h}_{\mathrm{IUI},1}, \ldots, \mathbf{h}_{\mathrm{IUI},K_D}]^T \in \mathbb{C}^{K_D \times K_U}$ exists between DL and UL UEs, where $\mathbf{h}_{\mathrm{IUI},d}$ denotes the channel vector from all UL UEs to the d^{th} DL UE. For the practical FD implementation, we consider the scenario of a single UL UE and a single DL UE (i.e., $K_D = K_U = 1$) to understand how close the FD systems can achieve in terms of theoretical doubling of the sum-rate capacity by suppressing strong measured SI based on beamforming capability of mMIMO systems [2]. Then, the received signal at the DL UE is given as follows:

$$r_D = \underbrace{\mathbf{h}_D^T\mathbf{f}_D\mathbf{b}_D d_D}_{\text{Desired Signal}} + \underbrace{\mathbf{h}_{\mathrm{IUI}}^T d_U}_{\text{IUI by UL UE}} + \underbrace{n_D}_{\text{Noise}}, \tag{5.6}$$

where d_U is the UL data signal, $\mathbf{f}_D \in \mathbb{C}^{N_{ds} \times N_{RF_D}}$ is the DL RF beamformer, and $n_D \sim \mathcal{CN}(0, \sigma_n^2)$ is the additive circular symmetric Gaussian noise. The received signal includes the desired DL signal, IUI generated by UL UE as well as the noise. Thus, the DL UE is exposed to IUI from UL UE due to the FD transmission. After some mathematical manipulations, we derive the instantaneous SINR at the DL UE as follows:

$$\mathrm{SINR_D} = \frac{|\mathbf{h}_D^T\mathbf{f}_D\mathbf{b}_D|^2}{P_U||\mathbf{h}_{\mathrm{IUI}}||^2 + \sigma_{\mathrm{n}}^2}. \tag{5.7}$$

Here, P_U is defined as the transmit power of UL UE. Similar to the DL data signal, the UL received signal at BS can be written as follows:

$$\tilde{r}_U = \underbrace{\mathbf{b}_U^T\mathbf{f}_U\mathbf{h}_U d_U}_{\text{Desired Signal}} + \underbrace{\mathbf{b}_U^T\mathbf{f}_U\mathbf{H}_{\mathrm{SI}}\mathbf{f}_D\mathbf{b}_D\mathbf{d}_D}_{\text{SI}} + \underbrace{\tilde{\mathbf{n}}_U}_{\text{Modified Noise}}, \tag{5.8}$$

where $\tilde{\mathbf{n}}_U = \mathbf{b}_U\mathbf{f}_U\mathbf{n}_U$, $\mathbf{n}_U \sim \mathcal{CN}(0, \sigma_n^2\mathbf{I}_{N_{us}})$ is the complex circularly symmetric Gaussian noise vector and $\mathbf{f}_U \in \mathbb{C}^{N_{RF_U} \times N_{us}}$ is the UL RF beamformer. If $\boldsymbol{\mathcal{H}}_{\mathrm{SI}} = \mathbf{f}_U\mathbf{H}_{\mathrm{SI}}\mathbf{f}_D \in \mathbb{C}^{N_{RF_U} \times N_{RF_D}}$ is the effective SI channel seen from the BB-stage after applying DL and UL RF beamformers,

---

[2] In this real-time FD implementation, we consider the scenario of single UL and a single DL UE to understand how effective SI suppression can be achieved solely based on beamforming capability with SAS based on a measured SI channel. The proposed perturbation-based PBF scheme can be applied to the case of multiple UL and DL UEs in real-time systems.

then the instantaneous SINR for the UL UE can be given as:

$$\mathrm{SINR_U} = \frac{\frac{P_U|\mathbf{b}_U^T\mathbf{f}_U\mathbf{h}_U|^2}{||\mathbf{b}_U^T\mathbf{f}_U||^2}}{\frac{||\mathbf{b}_U^T\boldsymbol{\mathcal{H}}_{\mathrm{SI}}\mathbf{b}_D||^2}{||\mathbf{b}_U^T\mathbf{f}_U||^2}+\sigma_n^2}. \tag{5.9}$$

5.3.2 Sub-Array Mapping and Problem Formulation

In this section, we discuss the Tx and Rx sub-array mapping for the measured SI channel as well as the problem formulation using multiple optimization objectives.

5.3.2.1 Sub-Array Mapping

In Fig. 5.3(a), the antenna mapping is shown for both Tx and Rx of BS, which consists of 8×8 = 64 elements at BS and separated by an antenna isolation block. We present the sub-array mapping for our FD mMIMO setup in an anechoic chamber by using the following two different sub-array configurations for Tx and Rx: 1) 1×4 sub-array; and 2) 1×8 sub-array. Given 64 Tx and 64 Rx antenna elements, we can have 16 distinct Tx sub-arrays and similarly 16 Rx sub-arrays, each of 1×4 elements, which are arranged in the form of ULA. The mapping of the 1×4 sub-arrays for Tx and Rx ends can be represented mathematically as: Let $Tx(i,j)$ represent the (i,j)th element of the 8×8 Tx antenna array, where i denotes the row index and j denotes the column index. The mapping of the p^{th} 1×4 Tx sub-array, denoted as $Tx_{\mathrm{sub},4}(p)$, can be expressed as follows:

$$Tx_{\mathrm{sub},4}(p) = [Tx(i,j); \quad (i,j) \in S_{p_4}], \tag{5.10}$$

where S_{p_4} represents the set of indices corresponding to the elements in the p^{th} 1×4 Tx sub-array. Similarly, let $Rx(i,j)$ represent the (i,j)th element of the 8×8 Rx antenna array. The mapping of the q^{th} 1×4 Rx sub-array, denoted as $Rx_{\mathrm{sub},4}(q)$, can be expressed as follows:

$$Rx_{\mathrm{sub},4}(q) = [Rx(i,j); \quad (i,j) \in S_{q_4}], \tag{5.11}$$

where S_{q_4} represents the set of indices corresponding to the elements in the q^{th} 1×4 Rx sub-array. Fig. 5.3(b) depicts the mapping of 16 distinct 1×4 sub-arrays for both Tx and Rx. For instance, sub-array 1 for Tx and Rx constitutes antenna elements with index values 1,9,17,25. It can be seen that using 1×4 sub-arrays at Tx and Rx can give rise to $16 \times 16 = 256$ possible combinations for the Tx and Rx sub-array pair selection. Thus, the use of a particular or a fixed Tx and Rx sub-array in FD mMIMO can not suppress the strong SI effectively

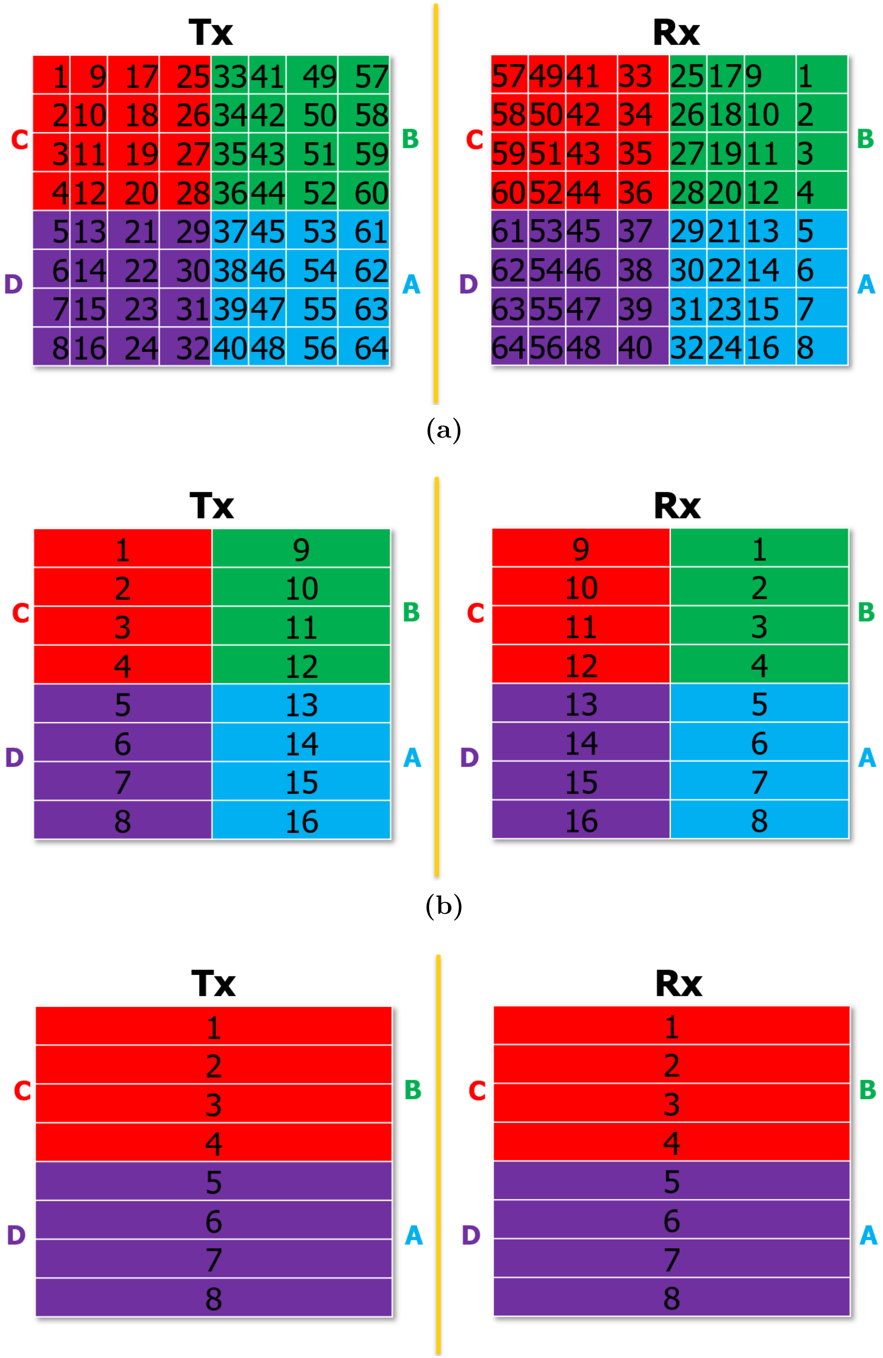

Tx

1	9	17	25	33	41	49	57
2	10	18	26	34	42	50	58
3	11	19	27	35	43	51	59
4	12	20	28	36	44	52	60
5	13	21	29	37	45	53	61
6	14	22	30	38	46	54	62
7	15	23	31	39	47	55	63
8	16	24	32	40	48	56	64

Rx

57	49	41	33	25	17	9	1
58	50	42	34	26	18	10	2
59	51	43	35	27	19	11	3
60	52	44	36	28	20	12	4
61	53	45	37	29	21	13	5
62	54	46	38	30	22	14	6
63	55	47	39	31	23	15	7
64	56	48	40	32	24	16	8

(a)

Tx

1	9
2	10
3	11
4	12
5	13
6	14
7	15
8	16

Rx

9	1
10	2
11	3
12	4
13	5
14	6
15	7
16	8

(b)

Tx

1
2
3
4
5
6
7
8

Rx

1
2
3
4
5
6
7
8

(c)

Figure 5.3. Antenna mapping. (a) 64 Tx and 64 Rx antennas index. (b) 1×4 Tx and Rx sub-array mapping. (c) 1×8 Tx and Rx sub-array mapping.

and limits the potential of utilizing the spatial DoF provided due to the use of large array structures in mMIMO. Hence, finding the optimal Tx and Rx sub-array combination can result in enhanced SI suppression, which can lead to significant performance gains in FD communications.

To further explore the realm of sub-array configurations, we consider the use of 1×8 Tx and Rx sub-arrays. The mapping of the p^{th} 1×8 Tx sub-array, denoted as $Tx_{sub,8}(p)$, can be expressed as follows:

$$Tx_{\text{sub},8}(p) = [Tx(i,j); \quad (i,j) \in S_{p_8}], \tag{5.12}$$

where S_{p_8} represents the set of indices corresponding to the elements in the p^{th} 1×8 Tx sub-array. Similarly, for the q^{th} 1×8 Rx sub-array, we can write as follows:

$$Rx_{\text{sub},8}(q) = [Rx(i,j); \quad (i,j) \in S_{q_8}], \tag{5.13}$$

where S_{q_8} represents the set of indices corresponding to the elements in the q^{th} 1×8 sub-array. Fig. 5.3(c) depicts the mapping for different 1×8 sub-arrays for both Tx and Rx. For instance, sub-array 1 for Tx and Rx now constitutes antennas with indices 1,9,17,25,33,41,49,57. The selection of 1×8 Tx and 1×8 Rx sub-array gives rise to $8 \times 8 = 64$ possible combinations for SAS.

5.3.2.2 Problem Formulation

We aim to address a multi-objective optimization framework that involves two primary design objectives: 1) minimizing self-interference; and 2) maximizing achievable rate in FD mMIMO systems. To achieve this, we present a formulation that balances these objectives within a MOOP framework.

Objective 1 - Minimizing Self-Interference:
We consider minimizing the strong SI caused by simultaneous transmission and reception in the FD system. We quantify SI by considering the average power of the interference signal between UL and DL channels. Based on the DL and UL RF beamforming stages, we can express the total achieved SI for FD mMIMO system as follows:

$$\mathrm{A}_{\text{SI}} = -10\log_{10}\left(\frac{1}{N}\sum\nolimits_n \left|\mathbf{f}_U^T(\hat{\theta}_U)\mathbf{H}_{\text{SI}}(:,:,n)\mathbf{f}_D(\hat{\theta}_D)\right|^2\right). \tag{5.14}$$

Lemma 5.1. *If* $\mathbf{F}_D$ *and* $\mathbf{F}_U$ *are the DL and UL beamforming stages, respectively. Then, for* *a given* $(i,j)^{th}$ *DL-UL pair* $\{\theta_{D_i}, \theta_{U_j}\}$ *in large array structures, the following holds:*

$$\mathbf{F}_U \mathbf{H}_{\mathrm{SI}} \mathbf{F}_D \approx \mathbf{0}. \tag{5.15}$$

Proof. See Appendix.

By steering the UL and DL beams to the desirable directions (i.e. $\hat{\theta}_U = \theta_U$, $\hat{\theta}_D = \theta_D$), we can get maximum directivity in DL and UL directions, which can be given as:

$$|\boldsymbol{\Phi}_D^T(\theta_D)\mathbf{f}_D(\hat{\theta}_D)|^2 = N_{ds}, |\mathbf{f}_U^T(\hat{\theta}_U)\boldsymbol{\Phi}_U(\theta_U)|^2 = N_{us}. \tag{5.16}$$

For a FD mMIMO system consisting of DL and UL RF beamformers $\mathbf{f}_D$ and $\mathbf{f}_U$, and using sub-array structures at Tx and Rx of BS, the total achieved SI can be minimized by the optimization of UL and DL perturbation angles $\hat{\theta}_U$, $\hat{\theta}_D$ jointly with finding best combination of Tx and Rx sub-arrays. Let p and q represents the sub-array index for Tx and Rx, respectively, then, we can formulate the optimization problem for achieved SI as follows:

$$\begin{aligned} \min_{\{\hat{\theta}_D, \hat{\theta}_U, p, q\}} \quad & \frac{1}{N} \sum\nolimits_n \left| \mathbf{f}_U^T(\hat{\theta}_U) \mathbf{H}_{\mathrm{SI},p,q}(:,:,n) \mathbf{f}_D(\hat{\theta}_D) \right|^2 \\ \text{s.t.} \quad & C_1: \; N_D - |\boldsymbol{\Phi}_D^T(\theta_D)\mathbf{f}_D(\hat{\theta}_D)|^2 \leq \eta, \\ & C_2: \; N_U - |\mathbf{f}_U^T(\hat{\theta}_U)\boldsymbol{\Phi}_U(\theta_U)|^2 \leq \eta, \\ & C_3: \; \sum_q x_{pq} = 1 \; \forall p, \\ & C_4: \; \sum_p x_{pq} = 1 \; \forall q, \end{aligned} \tag{5.17}$$

where C_1 and C_2 refers to the directivity degradation constraints in DL and UL directions, respectively. In other words, the constraints mean that we limit the degradation of directivities from the main beam directions θ_D and θ_U to a small value η. The constraints C_3 and C_4 ensure that exactly one Tx sub-array is selected for each Rx sub-array and vice versa, resulting in a one-to-one mapping between the Tx and Rx sub-arrays. The optimization problem defined in (5.17) is non-convex and intractable due to the non-linearity constraints.

Objective 2 - Maximizing Total Achievable Rate:

The second objective is to maximize the total achievable data rate in FD system. Using the SINR expressions for both DL and UL (as given in (5.7) and (5.9)), we can write the achievable rate for the DL and UL UE as follows:

$$\begin{aligned} \mathrm{R}_D &= \log_2(1+\mathrm{SINR}_D) \\ \mathrm{R}_U &= \log_2(1+\mathrm{SINR}_U) \\ \mathrm{R}_\mathrm{T} &= \mathrm{R}_D + \mathrm{R}_U, \end{aligned} \tag{5.18}$$

where R_D and R_U are the achievable rates for DL and UL UE, respectively. Then, the optimization problem can be expressed as follows:

$$\begin{aligned} \max_{\{\hat{\theta}_D, \hat{\theta}_U, p, q\}} \quad & \mathrm{R}_\mathrm{T}(\hat{\theta}_D, \hat{\theta}_U, p, q) \\ \text{s.t.} \quad & C_1 - C_4. \end{aligned} \tag{5.19}$$

Multi-Objective Optimization Problem:
To balance the conflicting objectives of minimizing self-interference and maximizing achievable rate, we formulate a multi-objective optimization problem. We introduce a weighting factor, β, to adjust the trade-off between the objectives. Then, the problem can be expressed as follows:

$$\begin{aligned} \min_{\{\hat{\theta}_D, \hat{\theta}_U, p, q\}} \; & \frac{1}{N} \sum\nolimits_n \left| \mathbf{f}_U^T(\hat{\theta}_U) \mathbf{H}_{\mathrm{SI},p,q}(:,:,n) \mathbf{f}_D(\hat{\theta}_D) \right|^2 - \beta \mathrm{R}_\mathrm{T} \\ \text{s.t.} \quad & C_1 - C_4. \end{aligned} \tag{5.20}$$

In this formulation, the objective combines the minimized SI term with the weighted negative logarithm of the total achievable rate to balance the objectives. By varying the weighting factor β, we can explore different trade-offs between self-interference and achievable rate[3].

Remark: This problem formulation is tailored to address the objectives of minimizing SI and maximizing total achievable rate in an FD communications system. It accounts for the UL/DL RF beamforming vectors, interference thresholds, and SINR values to guide the optimization process. The multi-objective optimization approach allows for using mMIMO spatial DoF to achieve different trade-offs between the objectives.

Our objective in this research work is to consider the practical FD mMIMO implementation using OTA measured SI channel and to study the capacity gains of FD mMIMO system over HD transmissions using the data-driven analysis. Therefore, the proposed solution can help to understand how close the FD systems can achieve in terms of

---

[3] Here, our objective is to enhance FD capacity while suppressing SI. Therefore, the optimization of β is beyond the scope of this research work.

theoretical doubling of the achievable rate by suppressing strong SI based on beamforming capability of mMIMO systems. Then, the phase response vectors can be written as follows:

$$\boldsymbol{\phi}_D(\theta_D) = [1, e^{-j2\pi d\cos(\theta_D)}, \cdots, e^{-j2\pi d(N_{ds}-1)\cos(\theta_D)}]^T \in \mathbb{C}^{M_{ds}\times 1}, \tag{5.21}$$

$$\boldsymbol{\phi}_U(\theta_U) = [1, e^{j2\pi d\cos(\theta_U)}, \cdots, e^{j2\pi d(M_{us}-1)\cos(\theta_U)}]^T \in \mathbb{C}^{N_{us}\times 1}. \tag{5.22}$$

5.3.3 Hybrid Beamforming With SAS

In this section, our objectives are to suppress strong SI and maximize the total achievable rate solely by utilizing the spatial DoF of the large array structures, which can avoid the use of costly analog SI-cancellation circuits. In particular, we use a swarm intelligence-based algorithmic solution and present the HBF design based on beam perturbations jointly with SAS approach, where the Tx and Rx sub-arrays are selected jointly with perturbed UL and DL RF beam angles to minimize MOOP (as given in (5.20)) while satisfying the directivity degradation constraints in the respective directions.

5.3.3.1 RF Stages Design

In the rest of this section, we discuss the proposed HBF with following two schemes: 1) Maximum-directivity RF beamformer (MBF); and 2) Perturbed RF beamformer with SAS (PBF).

5.3.3.1.1 MBF RF Stages Design In this scheme, our aim is to suppress the strong SI and maximize $\mathrm{R_T}$ via designing the DL RF stage $\mathbf{f}_D$, which steers the beam at DL user jointly with the design of UL RF stage $\mathbf{f}_U$ for UL user. The objective here is to generate the maximum-directivity beams, which are steered at the desired DL and UL user, which are located at θ_D and θ_U, respectively. In particular, we use the measured SI channel $\mathbf{H}_{\mathrm{SI}}$, which consists of LoS path components. Then, the effective reduced-size SI channel matrix as seen from the BB-stages can be written as follows:

$$\boldsymbol{\mathcal{H}}_{\mathrm{SI}}(:,:,n) = \mathbf{f}_U^T \mathbf{H}_{\mathrm{SI}}(:,:,n)\mathbf{f}_D. \tag{5.23}$$

Based on the orthogonality principle, we can generate $N_{ds}(N_{us})$ maximum-directivity DL (UL) beams. Here, the design of DL and UL MBF RF stages, which satisfies the maximum-directivity property, can be given as follows [117]:

$$\begin{aligned}
\mathbf{f}_D^{\mathrm{MBF}}(\theta_D) &= \tfrac{1}{\sqrt{M_{ds}}} \quad [1, e^{j2\pi d\cos(\theta_D)}, \cdots, e^{j2\pi d(N_{ds}-1)\cos(\theta_D)}]^T && (5.24)\\
\mathbf{f}_U^{\mathrm{MBF}}(\theta_U) &= \tfrac{1}{\sqrt{N_{us}}} \quad [1, e^{-j2\pi d\cos(\theta_U)}, \cdots, e^{-j2\pi d(N_{us}-1)\cos(\theta_U)}]^T. && (5.25)
\end{aligned}$$

The use of SC architecture for beamforming simplifies the design of $\mathbf{f}_D^{\mathrm{MBF}}$ and $\mathbf{f}_U^{\mathrm{MBF}}$ as it requires only $\log_2(N_{ds})$ and $\log_2(N_{us})$ PSs at Tx and Rx, respectively when compared to $\log_2(N_D)$ and $\log_2(N_U)$ PSs when using FC antenna array. The MBF RF stages are formulated using the DL/UL angle pair while satisfying CM constraints.

5.3.3.1.2 PBF RF Beamformer With SAS Design The simulation results in [117] show that HBF based on PBF RF beamformer stages can achieve better SI suppression than MBF RF stages, where the latter is formulated using the orthogonal angle pairs. In this proposed HBF scheme using PBF RF stages, our motivation is to suppress the strong SI while maximizing the total achievable rate for a FD mMIMO system using a measured SI channel (i.e., real-time implementation). Particularly, we introduce beam perturbations jointly with Tx-Rx SAS to design the RF beamforming stages.

Remark 1: The maximum-directivity constraint limits the number of UL and DL beam pairs that can be supported in a given system, which can become a bottleneck in scenarios of high user density. As the number of UL and DL users increases, the available orthogonal/non-overlapping resources may be exhausted, leading to reduced system capacity and throughput.

Remark 2: Compared to the PBF scheme in [117], which introduces phase-range constraint scheme, the proposed directivity-loss constraint PBF scheme allows a more freedom to perturb the maximum-directivity beams while keeping the directivity loss to a small value. Moreover, the proposed PBF scheme in [117] is limited by the quantized angle pairs, where the users' AoD and AoA have to be quantized, and then the DL and UL beams are steered within the boundary of the quantized angles. Thus, for a small number of antennas, the quantization process can introduce large errors, which can result in reduced directivity gain. On the other hand, the quantization error can be low for large number of antennas, however, the perturbed beams can only be steered within tight boundaries, so the beamforming-based SI suppression might be limited.

Remark 3: The use of SC Tx and Rx structures enable the creation of a reduced-size SI channel matrix based on the chosen Tx and Rx sub-array configuration. This reduced-size matrix captures the SI channel characteristics specific to the selected antennas. By leveraging the spatial properties of the sub-arrays, the SI channel exhibits improved isolation and reduced coupling, leading to a lower level of SI. By choosing the best subset of antennas, we can increase the spatial separation between the desired signal and the interfering signals, thereby augmenting the system's capability to support multiple independent spatial channels simultaneously. This increased spatial DoF translates into higher capacity, improved system performance, and efficient management of interference in FD mMIMO systems.

As a continuation to the SI suppression scheme in [117], we propose to explore the HBF with PBF RF beamformers jointly with SAS to minimize SI and maximize capacity. Instead of using the quantized angle pairs, we allow the DL and UL beams to be slightly steered away from the AoD and AoA angles to minimize the SI power while maintaining possible degradation in directivity within affordable constraints. In particular, the proposed PBF with SAS approach optimize the UL and DL RF beamformers via new perturbed angles as well as selects the best Tx-Rx sub-array pair for enhanced SI suppression in FD mMIMO systems. For a given maximum-directivity angle pair $\{\theta_D, \theta_U\}$, we introduce a perturbation to make them steered at perturbed angle pair to suppress SI (i.e., the UL and DL RF beamformers steer the non-maximum-directivity beams at $\{\hat{\theta}_D, \hat{\theta}_U\}$).

We propose a swarm intelligence inspired particle swarm optimization (PSO)-based perturbation scheme to solve the challenging non-convex optimization problem (as given in (5.20)), which can find the optimal DL and UL beam directions $\hat{\theta}_D, \hat{\theta}_U$ jointly with Tx and Rx best sub-array pair $\{p, q\}$ to minimize SI and maximize total achievable rate while satisfying the corresponding directivity degradation and SAS constraints $C_1 - C_4$. The algorithm starts with a swarm of Z particles, each with its own position, velocity, and fitness value, which are randomly placed in optimization search space of perturbation coefficients. During a total of T iterations, the particle z communicates with each other, and move for the exploration of the optimization space to find the optimal solution. Let $\mathbf{X}_z^{(t)}$ be the perturbation vector of z^{th} particle during t^{th} iteration, which consists of optimization variables, and can be given as follows:

$$\mathbf{X}_z^{(t)} = [\hat{\theta}_D^z, \hat{\theta}_U^z, p^z, q^z], \tag{5.26}$$

where $z = 1, \ldots, Z$ and $t = 0, 1, \ldots, T$. For each z^{th} particle, by substituting (5.26) in (5.24) and (5.25), the DL and UL PBF RF beamformers $\mathbf{f}_D(\mathbf{X}_z^{(t)})$ and $\mathbf{f}_U(\mathbf{X}_z^{(t)})$ can be obtained as function of perturbation angles $\hat{\theta}_D^z$ and $\hat{\theta}_U^z$, respectively. By using (5.42), MOOP can be written as:

$$\frac{1}{N}\sum\nolimits_{n}\left|\mathbf{f}_{U}^{T}(\mathbf{X}_{z}^{(t)})\mathbf{H}_{\mathrm{SI}}(\mathbf{X}_{z}^{(t)})\mathbf{f}_{D}(\mathbf{X}_{z}^{(t)})\right|^{2}-\beta\mathrm{R}_{\mathrm{T}}(\mathbf{X}_{z}^{(t)}) \tag{5.27}$$

Based on the sub-array mapping as discussed in Section 5.3.2.1, each z^{th} particle finds the best Tx-Rx sub-array indices p^{z}, q^{z}, and uses the corresponding measured SI channel $\mathbf{H}_{\mathrm{SI}}(\mathbf{X}_{z}^{(t)})$ instead of using the complete measured SI channel $\mathbf{H}_{\mathrm{SI,ALL}}$, which greatly reduces SI. Then, the personal best for the z^{th} particle and the current global best among all particles at the t^{th} iteration, are respectively found as follows:

$$\mathbf{X}_{\mathrm{best},z}^{(t)}=\underset{\mathbf{X}_{z}^{(t^{*})},\forall t^{*}=0,1,\cdots,t}{\arg\min}\ \frac{1}{N}\sum\nolimits_{n}\left|\mathbf{f}_{U}^{T}(\mathbf{X}_{z}^{(t)})\mathbf{H}_{\mathrm{SI}}(\mathbf{X}_{z}^{(t)})\mathbf{f}_{D}(\mathbf{X}_{z}^{(t)})\right|^{2}-\beta\mathrm{R}_{\mathrm{T}}(\mathbf{X}_{z}^{(t)}) \tag{5.28}$$

$$\mathbf{X}_{\mathrm{best}}^{(t)}=\underset{\mathbf{X}_{\mathrm{best},z}^{(t)},\forall z=0,1,\cdots,Z}{\arg\min}\ \frac{1}{N}\sum\nolimits_{n}\left|\mathbf{f}_{U}^{T}(\mathbf{X}_{\mathrm{best},z}^{(t)})\mathbf{H}_{\mathrm{SI}}(\mathbf{X}_{\mathrm{best},z}^{(t)})\mathbf{f}_{D}(\mathbf{X}_{\mathrm{best},z}^{(t)})\right|^{2}-\beta\mathrm{R}_{\mathrm{T}}(\mathbf{X}_{\mathrm{best},z}^{(t)}) \tag{5.29}$$

The convergence of the proposed joint PBF scheme with SAS for enhanced SI suppression depends on the velocity vector $\mathbf{v}_{z}$ for both personal best $\mathbf{X}_{\mathrm{best},z}$ and global best $\mathbf{X}_{\mathrm{best}}$ solutions, which is defined as follows:

$$\mathbf{v}_{z}^{(t+1)}=\mathbf{\Omega}_{1}(\mathbf{X}_{\mathrm{best}}^{(t)}-\mathbf{X}_{z}^{(t)})+\mathbf{\Omega}_{2}(\mathbf{X}_{\mathrm{best},z}^{(t)}-\mathbf{X}_{z}^{(t)})+\mathbf{\Omega}_{3}^{(t)}v_{z}^{(t)}, \tag{5.30}$$

where $\mathbf{v}_{z}^{(t)}$ is the velocity of the z^{th} particle at the t^{th} iteration, $\mathbf{\Omega}_{1}, \mathbf{\Omega}_{2}$ are the random diagonal matrices with the uniformly distributed entries over $[0, 2]$ and represent the social relations among the particles, and the tendency of a given particle for moving towards its personal best, respectively. Here, $\mathbf{\Omega}_{3}=\left(\frac{T-1}{T}\right)\mathbf{I}_{\left(2N_{RF_{D}}+2N_{RF_{U}}\right)}$ is the diagonal inertia weight matrix, which finds the balance between exploration and exploitation for optimal solution in search space. By using (6.19), the position of each particle during t^{th} iteration is updated as:

$$\mathbf{X}_{z}^{(t+1)}=\mathrm{clip}\left(\mathbf{X}_{z}^{(t)}+\mathbf{v}_{z}^{(t+1)},\mathbf{X}_{\mathrm{Low}},\mathbf{X}_{\mathrm{Upp}}\right), \tag{5.31}$$

where $\mathbf{X}_{\mathrm{Low}}\in\mathbb{R}^{\left(2N_{RF_{D}}+2N_{RF_{U}}\right)}$ and $\mathbf{X}_{\mathrm{Upp}}\in\mathbb{R}^{\left(2N_{RF_{D}}+2N_{RF_{U}}\right)}$ are the lower-bound and upper-bound vectors for the perturbation coefficients, respectively, and are constructed according to the earlier defined boundaries of each perturbation coefficient given in $C_{1}-C_{4}$. Here, we define $\mathrm{clip}(x, a, b) = \min(\max(x, a), b)$ as the clipping function to avoid exceeding the bounds. Furthermore, different from the sub-optimal approach, we here consider each perturbation coefficient as a continuous variable inside its boundary. Then, we can design the PBF RF

Algorithm 5.1 Proposed Swarm Intelligence-based PBF RF Stages With SAS

```
Input: $Z, T, N_{ds}, N_{us}, \mathbf{H}_{SI}, (\theta_D, \phi_D), (\theta_U, \phi_U)$.
Output: $\hat{\theta}_D, \hat{\theta}_U$.
for $t = 0 : T$ do
    for $z = 1 : Z$ do
        if $t = 0$ then
            Initialize the velocity as $\mathbf{v}_z^{(0)} = \mathbf{0}$.
            Initialize $\mathbf{X}_z^{(t)}$ uniformly distributed in $[\mathbf{X}_{\text{Low}}, \mathbf{X}_{\text{Upp}}]$.
        else
            Update the velocity $\mathbf{v}_z^{(t)}$ via (5.30).
            Update the perturbation $\mathbf{X}_z^{(t)}$ via (5.31).
        end if
        Find the personal best $\mathbf{X}_{\text{best},z}^{(t)}$ via (5.28).
    end for
    Find the global best $\mathbf{X}_{\text{best}}^{(t)}$ as in (5.29).
    Design RF stages $\mathbf{f}_D$, $\mathbf{f}_U$ via (5.32), (5.33).
end for
```

stages with SAS as follows:

$$\mathbf{f}_D^{\text{PBF}}(\hat{\theta}_D, p) = \frac{1}{\sqrt{N_{ds}^{(p)}}} \left[1, e^{j2\pi d\cos(\hat{\theta}_D)}, \cdots, e^{j2\pi d(N_{ds}^{(p)}-1)\cos(\hat{\theta}_D)}\right]^T \tag{5.32}$$

$$\mathbf{f}_U^{\text{PBF}}(\hat{\theta}_U, q) = \frac{1}{\sqrt{N_{us}^{(q)}}} \left[1, e^{-j2\pi d\cos(\hat{\theta}_U)}, \cdots, e^{-j2\pi d(N_{us}^{(q)}-1)\cos(\hat{\theta}_U)}\right]^T. \tag{5.33}$$

The design of proposed swarm intelligence-based PBF RF stages utilizing beam perturbations jointly with SAS is summarized in Algorithm 5.1.

5.3.3.2 BB Stages Design

After designing the RF beamformers $\mathbf{f}_D$ and $\mathbf{f}_U$, the BB precoder stages $\mathbf{B}_D$ and $\mathbf{B}_U$ only employ the reduced-size effective downlink channel matrix $\boldsymbol{\mathcal{H}}_D = \mathbf{H}_D\mathbf{f}_D \in \mathbb{C}^{K_D \times N_{RF_D}}$ and uplink channel matrix $\boldsymbol{\mathcal{H}}_U = \mathbf{f}_U\mathbf{H}_U \in \mathbb{C}^{N_{RF_U} \times K_U}$, respectively. Therefore, it remarkably reduces the channel estimation overhead size in the FD mMIMO systems with large antenna arrays. Considering that the number of RF chains in the proposed FD SC-HBF scheme is significantly smaller than the number of antennas (i.e., $N_{RF_D} \ll N_{ds}$ and $N_{RF_U} \ll N_{us}$), the utilization of effective DL/UL channel matrices reduces the total CSI overhead size from $N_{ds} \times K_D + N_{us} \times K_U$ to $N_{RF_D} \times K_D + N_{RF_U} \times K_U$. It is important to highlight that the instantaneous SI channel matrix $\mathbf{H}_{\text{SI}}$ is not required in the proposed BB precoder/combiner design. We here develop BB precoder/combiner via applying regularized zero-forcing (RZF).

Here, the primary objective is maximizing the intended DL and UL signal power while suppressing the IUI power. According to the well-known RZF technique, we first define the BB DL stage as follows:

$$\mathbf{B}_D = \gamma_D \mathbf{X}_D^{-1} \boldsymbol{\mathcal{H}}_D^H \in \mathbb{C}^{N_{RF_D} \times K_D} \tag{5.34}$$

where $\gamma_D = \sqrt{P_D / \operatorname{tr}\left(\boldsymbol{\mathcal{H}}_D \mathbf{X}_D^{-1} \mathbf{f}_D^H \mathbf{f}_D \mathbf{X}_D^{-1} \boldsymbol{\mathcal{H}}_D^H\right)}$ is the normalization scalar satisfying the maximum DL transmit power constraint of P_D. According to the RZF technique, we here define $\mathbf{X}_D = \boldsymbol{\mathcal{H}}_D^H \boldsymbol{\mathcal{H}}_D + \frac{\sigma_w^2}{P_D/K_D} \mathbf{I}_{N_{RF_D}} \in \mathbb{C}^{N_{RF_D} \times N_{RF_D}}$, which aims to eliminate IUI by taking noise power σ_w^2 into account for the regularization. Similarly, the UL BB stage $\mathbf{B}_U$ is also designed as:

$$\mathbf{B}_U = \boldsymbol{\mathcal{H}}_U^H \mathbf{X}_U^{-1} \in \mathbb{C}^{K_U \times N_{RF_U}}, \tag{5.35}$$

where $\mathbf{X}_U = \boldsymbol{\mathcal{H}}_U \boldsymbol{\mathcal{H}}_U^H + \frac{\sigma_w^2}{P_U} \mathbf{I}_{N_{RF_U}} \in \mathbb{C}^{N_{RF_U} \times N_{RF_U}}$ according to the RZF technique.

5.4 Non Constant-Modulus RF Beamforming Design

In this section, we propose a novel SI suppression scheme in FD mMIMO systems using a URA SC-HBF architecture. Particularly, the proposed non-constant modulus RF beamforming-based SI suppression (NCM-BF-SIS) scheme optimizes the uplink and downlink beam directions jointly with Tx/Rx variable gain controllers while adhering to the directivity degradation constraints. Our objectives here are twofold: first, to show that the beam perturbation combined with tuned Tx/Rx gain controllers in RF beamformers design can significantly improve SI suppression and can bring the SI level close to the noise floor; and second, to show that the use of URA SC-HBF architecture can provide better performance than ULA SC-HBF.

5.4.1 System Model

We consider a single-cell FD mMIMO system for joint uplink and downlink transmission as shown in Fig. 5.4. The BS operates in FD mode to simultaneously serve K_D (K_U) downlink (uplink) single-antenna UEs over the same frequency band, while the UEs operate in HD mode due to the hardware/software constraints on UEs (e.g., low power consumption, limited signal processing and active/passive SI suppression capability). The BS is equipped with Tx and Rx URAs. Specifically, the Tx (Rx) URA has $N_D = N_D^{(x)} \times N_D^{(y)} (N_U = N_U^{(x)} \times N_U^{(y)})$ antennas, where $N_D^{(x)} (N_U^{(x)})$ and $N_D^{(y)} (N_U^{(y)})$ denote the numbers of Tx (Rx) antennas along x-axis and y-axis, respectively.

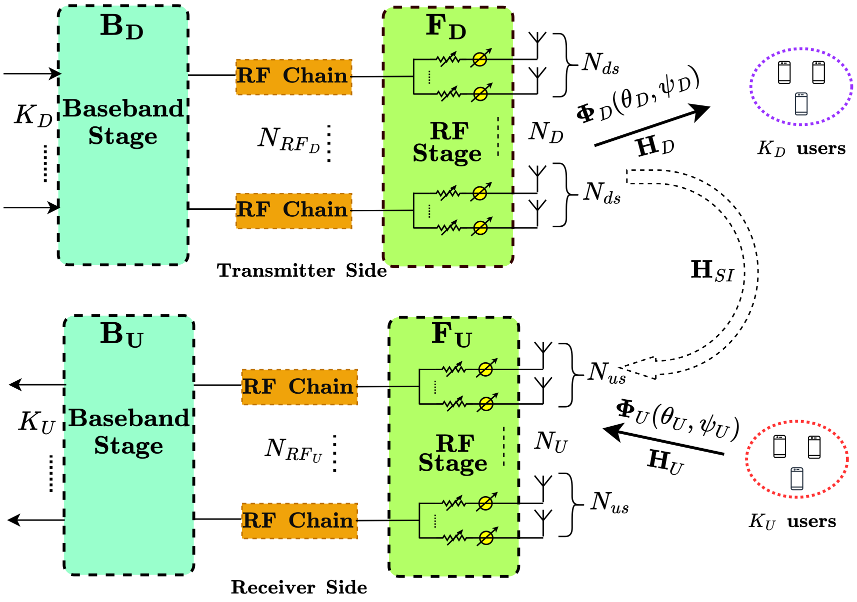

Figure 5.4. FD mMIMO system using NCM SC-HBF architecture.

For the proposed FD mMIMO system, we consider the downlink signal processed through BB stage $\mathbf{B}_D \in \mathbb{C}^{N_{RF_D} \times K_D}$ and RF beamformer $\mathbf{F}_D \in \mathbb{C}^{N_D \times N_{RF_D}}$, where N_{RF_D} is the number of RF chains such that $K_D \leq N_{RF_D} \ll N_D$. Similarly, the received uplink signal at BS is processed through RF combiner $\mathbf{F}_U \in \mathbb{C}^{N_{RF_U} \times N_U}$ and BB combiner $\mathbf{B}_U \in \mathbb{C}^{K_U \times N_{RF_U}}$ by utilizing $K_U \leq N_{RF_U} \ll N_U$ RF chains. Here, the RF beamforming stages (i.e., $\mathbf{F}_U$ and $\mathbf{F}_D$) are built using low-cost PSs and variable gain controllers. The downlink channel matrix is denoted as $\mathbf{H}_D \in \mathbb{C}^{K_D \times N_D}$ with $\mathbf{h}_{D,k} \in \mathbb{C}^{N_D}$ as the k^{th} DL UE channel vector. Similarly, $\mathbf{H}_U \in \mathbb{C}^{N_U \times K_U}$ is the uplink channel matrix with $\mathbf{h}_{U,k} \in \mathbb{C}^{N_U}$ as the k^{th} uplink UE channel vector. Due to the FD transmission, the SI channel matrix $\mathbf{H}_{SI} \in \mathbb{C}^{N_U \times N_D}$ is present between Tx and Rx antennas at the BS. Then, the transmitted signal vector at the BS is defined as $\mathbf{s}_D = \mathbf{F}_D \mathbf{B}_D \mathbf{d}_D \in \mathbb{C}^{N_D}$, where $\mathbf{d}_D = [d_{D,1}, \cdots, d_{D,K_D}]^T \in \mathbb{C}^{K_D}$ is the downlink data signal vector such that $\mathbb{E}\{\mathbf{d}_D \mathbf{d}_D^H\} = \mathbf{I}_{K_D}$. The transmitted signal vector satisfies the maximum downlink transmit power constraint, which is $\mathbb{E}\{||\mathbf{s}_D||^2\} = \mathrm{tr}(\mathbf{F}_D \mathbf{B}_D \mathbf{B}_D^H \mathbf{F}_D^H) \leq P_D$, where P_D is the total downlink transmit power. Then, the received downlink signal vector is given as follows:

$$\mathbf{r}_D = \underbrace{\mathbf{H}_D \mathbf{F}_D \mathbf{B}_D \mathbf{d}_D}_{\text{Desired Signal}} + \underbrace{\mathbf{H}_U \mathbf{d}_U}_{\text{IUI by uplink UE}} + \underbrace{\mathbf{n}_D}_{\text{Noise}}, \tag{5.36}$$

where $\mathbf{H}_U \in \mathbb{C}^{K_D \times K_U}$ is the inter-user interference (IUI) between the downlink and uplink UE, and $\mathbf{n}_D = [n_{D,1}, \cdots, n_{D,K_D}]^T \sim \mathcal{CN}(0, \sigma_n^2 \mathbf{I}_{K_D})$ is the complex circularly symmetric Gaussian noise vector. Here, we define P_U as the transmit power of each uplink UE. Similar to the downlink data signal vector, the uplink received signal at BS can be written as:

$$\tilde{\mathbf{r}}_U = \underbrace{\mathbf{B}_U\mathbf{F}_U\mathbf{H}_U\mathbf{d}_U}_{\text{Desired Signal}} + \underbrace{\mathbf{B}_U\mathbf{F}_U\mathbf{H}_{SI}\mathbf{F}_D\mathbf{B}_D\mathbf{d}_D}_{\text{SI}} + \underbrace{\tilde{\mathbf{n}_U}}_{\text{Modified Noise}}, \tag{5.37}$$

where $\mathbf{d}_U = [d_{U,1}, \cdots, d_{U,K_U}]^T \in \mathbb{C}^{K_U}$ is the uplink data signal vector such that $\mathrm{E}\left\{\mathbf{d}_U\mathbf{d}_U^H\right\} = \mathbf{I}_{K_U}$ and $\tilde{\mathbf{n}_U} = \mathbf{B}_U\mathbf{F}_U\mathbf{w}_U$, where $\mathbf{n}_U = [n_{u,1}, \cdots, n_{U,K_U}]^T \sim \mathcal{CN}(0, \sigma_n^2\mathbf{I}_{K_U})$ is the complex circularly symmetric Gaussian noise vector. The desirable downlink (uplink) beam direction has elevation and azimuth angles $\phi_D(\phi_U)$ and $\theta_D(\theta_U)$, respectively. We define the phase-response vector as:

$$\begin{aligned}\mathbf{\Phi}(\theta, \phi, N^{(x)}, N^{(y)}) = &\left[1, e^{j2\pi d\sin(\theta)\cos(\phi)}, \ldots, e^{j2\pi d(N^{(x)}-1)\sin(\theta)\cos(\phi)}\right]^T \\ &\otimes \left[1, e^{j2\pi d\sin(\theta)\sin(\phi)}, \ldots, e^{j2\pi(N^{(y)}-1)\sin(\theta)\sin(\phi)}\right]^T,\end{aligned} \tag{5.38}$$

where θ (ϕ) represents the azimuth (elevation) angle, $N^{(x)}$, ($N^{(y)}$) denote the number of antennas along the x (y)-axis, d_s is the antenna spacing, and $\otimes$ is the Kronecker product.

Based on the number of antenna elements in both Tx and Rx sub-arrays, the corresponding SI channels can be represented as $\mathbf{H}_{SI}^{(sub)} \in \mathbb{C}^{N_{us}\times N_{ds}\times 1601}$, where, $N_{ds}(N_{us}) = \frac{N_D}{L_D}\left(\frac{N_U}{L_U}\right)$ represents the number of Tx (Rx) antenna elements in $m_d^{th}(m_u^{th})$ sub-array for $m_d = 1, \cdots, M_D(m_u = 1, \cdots, M_U)$. As per 3GPP specification, the uplink and downlink channel bandwidth can vary from 5 MHz to 100 MHz [127], then the corresponding SI channel for the given BW can be written as: $\mathbf{H}_{SI,B}^{(sub)} = \mathbf{H}_{SI}^{(sub)}(:,:,n) \in \mathbb{C}^{i\times i\times n}$, where $i = \{N_{ds}, N_{us}\}$, B is the given bandwidth, and $n = 1, 2, \ldots, N$ is the sample frequency point selected from a total of N frequency points for a given bandwidth. For instance, the 20 MHz band constitutes $n = 1, 2, \ldots, 33$ points for the frequency range from 3.49 GHz to 3.51 GHz. Similarly, for the band of 100 MHz, $n = 1, 2, \ldots, 161$ points in the frequency range from 3.45 GHz to 3.55 GHz are considered.

5.4.2 URA SC-HBF Architecture and Problem Formulation for SI Suppression

5.4.2.1 URA SC-HBF Architecture

We consider a URA SC-HBF architecture, where the Tx (Rx) URA is divided into $M_D(M_U)$ different sub-arrays in the form of URA. Hence, compared to $N_D \times N_{RF_D}$ PSs for Tx ($N_U \times N_{RF_U}$ PSs for Rx), only $N_{ds} \times N_{RF_D}(N_{us} \times N_{RF_U})$ PSs are required as each Tx

(Rx) RF chain is connected to $\left\lfloor \frac{N_D}{M_D} \right\rfloor \left(\left\lfloor \frac{N_U}{M_U} \right\rfloor \right)$ Tx (Rx) antennas, where $\lfloor . \rfloor$ represents the largest integer less than or equal to a real number. Then, the downlink and uplink phase response vectors are given as:

$$\begin{aligned} \mathbf{\Phi}_D(\theta_D, \phi_D, N_{\text{ds}}^{(x)}, N_{\text{ds}}^{(y)}) &= \mathbf{\Phi}(\theta_D, \phi_D, N_{\text{ds}}^{(x)}, N_{\text{ds}}^{(y)}), \\ \mathbf{\Phi}_U(\theta_U, \phi_U, N_{\text{us}}^{(x)}, N_{\text{us}}^{(y)}) &= \mathbf{\Phi}^H(\theta_U, \phi_U, N_{\text{us}}^{(x)}, N_{\text{us}}^{(y)}), \end{aligned} \tag{5.39}$$

where $\mathbf{\Phi}_D(\mathbf{\Phi}_U)$ is the Tx(Rx) phase response vector as given in (5.38). By controlling the phase of the signals transmitted or received by the array elements, we can effectively steer the beam in the desired uplink/downlink UE direction, and maximize the radiated energy while minimizing interference from other directions. We consider the MU scenario using a single uplink and a single downlink UE (i.e., $K_D = N_D = 1$, $K_U = N_U = 1$)[4]. Moreover, the Tx (Rx) RF beamformer constitutes gain controllers, which scales the amplitudes of the signals transmitted (received) from the antennas as shown in Fig. 5.4. Then, the RF beamformer $\mathbf{f}_D$ for the single downlink UE can be written as:

$$\mathbf{f}_D = \frac{1}{\sqrt{N_{ds}^{(x)} N_{ds}^{(y)}}} \mathbf{\Phi}_D\Big(\theta_D, \phi_D, N_{ds}^{(x)}, N_{ds}^{(y)}\Big) \odot \mathbf{G}_D \in \mathbb{C}^{N_{ds} \times 1}, \tag{5.40}$$

where $\mathbf{G}_D = [g_1^{(x)}, \ldots, g_{M_{ds}}^{(x)}, g_1^{(y)}, \ldots, g_{N_{ds}}^{(y)}]^T$ is the vector containing the gain values for Tx URA with $g_i^{(x)}$ $(g_j^{(y)})$ representing the gain value of $i^{th}(j^{th})$ antenna for $i = 1, \cdots, N_{ds}^{(x)}\Big(j = 1, \cdots, N_{ds}^{(y)}\Big)$. Similarly, the uplink RF beamformer $\mathbf{f}_U$ can be expressed as follows:

$$\mathbf{f}_U = \frac{1}{\sqrt{N_{us}^{(x)} N_{us}^{(y)}}} \mathbf{\Phi}_U\Big(\theta_U, \phi_U, N_{us}^{(x)}, N_{us}^{(y)}\Big) \odot \mathbf{G}_U \in \mathbb{C}^{1 \times N_{us}}, \tag{5.41}$$

where $\mathbf{G}_U = [g_1^{(x)}, \ldots, g_{N_{us}}^{(x)}, g_1^{(y)}, \ldots, g_{N_{us}}^{(y)}]$ is the vector containing the gain values for Rx URA with $g_p^{(x)}$ $(g_q^{(y)})$ is the gain value of $p^{th}(q^{th})$ antenna for $p = 1, \cdots, N_{us}^{(x)}\Big(q = 1, \cdots, N_{us}^{(y)}\Big)$.

5.4.2.2 Problem Formulation

Based on the downlink and uplink RF beamforming stages, we can write the total achieved SI as:

$$\mathrm{A}_{\text{SI}} = -10 \log_{10} \left(\frac{1}{N} \sum_n \left| \mathbf{f}_U^T \mathbf{H}_{SI}^{(sub)}(:, :, n) \mathbf{f}_D \right|^2 \right). \tag{5.42}$$

---

[4] Here, we consider a simple scenario with a single uplink and downlink UE to investigate the SI suppression in FD mMIMO systems. However, the proposed scheme can be applied to multiple uplink and multiple downlink UEs, which is left as our future work.

By steering the uplink and downlink beams to the desirable directions (i.e. $\hat{\theta}_U = \theta_U$, $\hat{\theta}_D = \theta_D$, $\hat{\phi}_U = \phi_U$, $\hat{\phi}_D = \phi_D$), the Tx and Rx directivities reach their maxima as follows:

$$\begin{aligned}
|\mathbf{\Phi}_D^T(\theta_D, \phi_D, N_{ds}^{(x)}, N_{ds}^{(y)})\mathbf{f}_D(\theta_D, \phi_D, N_{ds}^{(x)}, N_{ds}^{(y)})|^2 = N_{ds},\\
|\mathbf{f}_U^T(\theta_U, \phi_U, N_{us}^{(x)}, N_{us}^{(y)})\mathbf{\Phi}_U(\theta_U, \phi_U, N_{us}^{(x)}, N_{us}^{(y)})|^2 = N_{us}.
\end{aligned} \tag{5.43}$$

For a FD mMIMO system consisting of RF beamformers $\mathbf{f}_D$ and $\mathbf{f}_U$ with variable gain controllers, and using URA SC-HBF architecture at Tx and Rx of BS, the SI can be minimized by finding the uplink and downlink perturbation angles $\{(\hat{\theta}_U, \hat{\theta}_D), (\hat{\phi}_U, \hat{\phi}_D)\}$ jointly with Tx/Rx variable gain controller coefficient optimization. Then, we can formulate the joint optimization problem for SI suppression as:

$$\begin{aligned}
\min_{\left\{\substack{\hat{\theta}_D, \hat{\theta}_U, \hat{\phi}_D, \hat{\phi}_U\\ g_1, \cdots, g_{M_{ds}}\\ g_1, \cdots, g_{M_{us}}}\right\}} \quad & \frac{1}{N}\sum_n \left|\mathbf{f}_U^T(\hat{\phi}_U, \hat{\theta}_U, \mathbf{G}_U)\mathbf{H}_{SI}^{(sub)}(:,:,n)\mathbf{f}_D(\hat{\phi}_D, \hat{\theta}_D, \mathbf{G}_D)\right|^2\\
\text{s.t. } & C_1 : N_{ds} - |\mathbf{\Phi}_D^T(\theta_D, \phi_D, N_{ds})\mathbf{f}_D(\hat{\phi}_D, \hat{\theta}_D, \mathbf{G}_D, N_{ds})|^2 \leq \eta,\\
& C_2 : N_{us} - |\mathbf{f}_U^T(\hat{\phi}_U, \hat{\theta}_U, \mathbf{G}_U, N_{us})\mathbf{\Phi}_U(\theta_U, \phi_U, N_{us})|^2 \leq \eta,\\
& C_3 : \ \hat{\phi}_D, \hat{\phi}_U, \hat{\theta}_D, \hat{\theta}_U \in [0, 2\pi],\\
& C_4 : \ g_1, \cdots, g_{N_{ds}} \in [0, 1],\\
& C_5 : \ g_1, \cdots, g_{N_{us}} \in [0, 1],
\end{aligned} \tag{5.44}$$

where C_1 and C_2 refer to the directivity degradation constraints in downlink and uplink UE directions, respectively, i.e., to limit the directivity degradation from the main beam directions $\{(\theta_U, \theta_D), (\phi_U, \phi_D)\}$ to a small value η. The constraint C_3 limits the perturbed angles range between 0 and 2π, whereas the constraints C_4 and C_5 confine the Tx and Rx variable gains within the continuous range from 0 to 1. The optimization problem defined in (5.44) is non-convex and intractable due to the non-linearity constraints.

5.4.3 Proposed Non-constant Modulus RF Beamforming-Based SI Suppression Scheme

We propose a particle swarm optimization (PSO)-based SI minimization scheme, which optimizes the Tx and Rx variable gain controllers coefficients jointly with the optimal uplink and downlink beam directions $\hat{\theta}_D, \hat{\theta}_U$ while satisfying the constraints of directivity degradation (C_1 and C_2), uplink and downlink perturbed beam search space (C_3), and Tx/Rx gain controller values (C_4 and C_5). The algorithm starts with a swarm of total P

particles, each with its own position, velocity, and fitness value, which are randomly placed in optimization search space of perturbation coefficients. During a total of T iterations, the particle p communicates with others, and move for the exploration of the optimization space to find the optimal solution. We define the perturbation vector $\mathbf{X}_z^{(t)}$ as:

$$\mathbf{X}_z^{(t)} = [\hat{\theta}_D^z, \hat{\theta}_U^z, \hat{\phi}_D^z, \hat{\phi}_U^z, g_1^z, \cdots, g_{N_{ds}}^p, g_1^z, \cdots, g_{N_{us}}^z], \tag{5.45}$$

where $z = 1, \ldots, Z$ and $t = 0, 1, \ldots, T$. For each z^{th} particle, by substituting (5.45) in (5.40) and (5.41), the downlink and uplink RF beamformers $\mathbf{f}_D(\mathbf{X}_z^{(t)})$ and $\mathbf{f}_U(\mathbf{X}_z^{(t)})$ can be obtained as function of perturbation angles ($\hat{\theta}_D^z$, $\hat{\phi}_D^z$) and ($\hat{\theta}_U^z$, $\hat{\phi}_U^z$), and gain controller coefficients ($g_1^z, \cdots, g_{N_{ds}}^z, g_1^z, \cdots, g_{N_{us}}^z$) respectively. By using (5.42), we can write the total achieved SI suppression as follows:

$$\mathrm{A}_{\mathrm{SI}}(\mathbf{X}_z^{(t)}) = -10\log_{10}\left(\frac{1}{N}\sum_n \left|\mathbf{f}_U^T(\mathbf{X}_z^{(t)})\mathbf{H}_{SI}^{(sub)}(:,:,n)\mathbf{f}_D(\mathbf{X}_z^{(t)})\right|^2\right). \tag{5.46}$$

At the t^{th} iteration, the individual best for the z^{th} particle as well as the current best among all particles within the swarm are respectively found as follows:

$$\mathbf{X}_{\text{best},z}^{(t)} = \underset{\mathbf{X}_z^{(t^*)}, \forall t^*=0,1,\cdots,t}{\arg\min} \mathrm{A}_{\mathrm{SI}}(\mathbf{X}_z^{(t^*)}), \tag{5.47}$$

$$\mathbf{X}_{\text{best}}^{(t)} = \underset{\mathbf{X}_{\text{best},z}^{(t)}, \forall z=0,1,\cdots,Z}{\arg\min} \mathrm{A}_{\mathrm{SI}}(\mathbf{X}_{\text{best},z}^{(t)}). \tag{5.48}$$

The convergence of the proposed PSO-based joint optimization scheme for enhanced SI suppression depends on the velocity vector $\mathbf{w}_z$ for both personal best $\mathbf{X}_{\text{best},z}$ and global best $\mathbf{X}_{\text{best}}$ solutions, which is defined as:

$$\mathbf{w}_z^{(t+1)} = \mathbf{\Omega}_1(\mathbf{X}_{\text{best}}^{(t)} - \mathbf{X}_z^{(t)}) + \mathbf{\Omega}_2(\mathbf{X}_{\text{best},z}^{(t)} - \mathbf{X}_z^{(t)}) + \mathbf{\Omega}_3^{(t)}\mathbf{w}_z^{(t)}, \tag{5.49}$$

where $\mathbf{w}_z^{(t)}$ is the velocity of the z^{th} particle at the t^{th} iteration, $\mathbf{\Omega}_1, \mathbf{\Omega}_2$ are the random diagonal matrices with the uniformly distributed entries over $[0, 2]$, and represent the inter-particle relationships and the tendency of each particle to move toward its personal best, respectively. Additionally, we introduce $\mathbf{\Omega}_3 = \left(\frac{T-1}{T}\right)\mathbf{I}_{\left(2N_{RF_D}+2N_{RF_U}\right)}$, a diagonal inertia weight matrix, which helps find the balance between exploration and exploitation for optimal solution in search space. By using (6.19), the position of each particle is updated as:

$$\mathbf{X}_z^{(t+1)} = \mathrm{clip}\left(\mathbf{X}_z^{(t)} + \mathbf{w}_z^{(t+1)}, \mathbf{X}_{\text{Low}}, \mathbf{X}_{\text{Upp}}\right). \tag{5.50}$$

Algorithm 5.2 Proposed NCM-BF-SIS Algorithm

```
Input: $Z, T, \mathbf{H}_{SI}^{(sub)}, (\theta_D, \phi_D), (\theta_U, \phi_U)$.
Output: $\hat{\theta}_D, \hat{\theta}_U, \hat{\phi}_D, \hat{\phi}_U, g_1, \cdots, g_{M_{ds}}, g_1, \cdots, g_{M_{us}}$.
for $t = 0 : T$ do
    for $z = 1 : Z$ do
        if $t = 0$ then
            Initialize the velocity as $\mathbf{w}_z^{(0)} = \mathbf{0}$.
            Initialize $\mathbf{X}_z^{(t)}$ uniformly distributed in $[\mathbf{X}_{\text{Low}}, \mathbf{X}_{\text{Upp}}]$.
        else
            Update the velocity $\mathbf{w}_z^{(t)}$ via (5.49).
            Update the vector $\mathbf{X}_z^{(t)}$ via (5.50).
        end if
        Find the personal best $\mathbf{X}_{z,\text{best},n}^{(t)}$ via (5.47).
    end for
    Find the global best $\mathbf{X}_{\text{best}}^{(t)}$ as in (5.48).
end for
```

Here, we have $\mathbf{X}_{\text{Upp}} \in \mathbb{R}^{\left(2N_{RF_D}+2N_{RF_U}\right)}$ and $\mathbf{X}_{\text{Low}} \in \mathbb{R}^{\left(2N_{RF_D}+2N_{RF_U}\right)}$, which represent the upper and lower boundaries for the perturbation coefficients, respectively and they are determined based on the predefined limits for each perturbation coefficient specified in C_1-C_5. To ensure that the coefficients stay within these boundaries, we employ the clipping function, defined as $\text{clip}(y, i, j) = \min(\max(y, i), j)$. Also, unlike sub-optimal approach, we here consider each perturbation coefficient as a continuous variable inside its boundary. The proposed joint optimization scheme for enhanced SI suppression using PSO is summarized in Algorithm 5.2.

5.5 Illustrative Results and Discussions

In this section, we present the Monte Carlo simulation results to illustrate the performance of the proposed HBF with NOBF RF beamformers and SAS scheme in FD mMIMO systems. In particular, we consider the measured SI channel in an anechoic chamber to provide realistic SI suppression capability and capacity gain of a practical FD mMIMO system over HD mMIMO system. We consider $N_D = N_U = 1$ RF chain to serve a single UL and DL UE with 1×4 and 1×8 sub-array configurations for the results presented hereafter. It is important to mention that the proposed HBF scheme requires only 1 RF chain as compared to FDBF, which need 4 or 8 RF chains to support single UL and single DL UE. Thus, the proposed HBF scheme significantly reduces the number of RF chains, especially when the number of served users increases. For PSO, we use the following

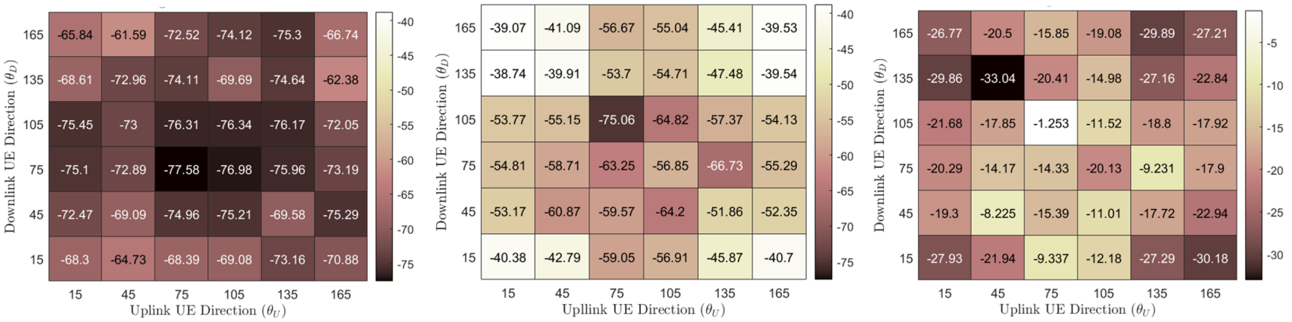

(a) **(b)** **(c)**

Figure 5.5. Achieved SI suppression using 1×4 sub-array with 20 MHz BW. (a) Proposed PBF with SAS. (b) MBF. (c) SI suppression gain values: $Z = 20, \Omega_1 = \Omega_2 = 2$, and $\Omega_3 = 1.1$.

5.5.1 Self-Interference Suppression

In this subsection, we first present the results of achieved SI using the proposed HBF scheme for NOBF RF beamformers with SAS, and compare it to HBF scheme with OBF RF beamformer. In Fig. 5.5, we consider six different angular UE locations (i.e., $\{\theta_D, \theta_U\} \in \{15° : 30° : 180°\}$) and generate the results using 1×4 sub-arrays for Tx and Rx antenna elements with a maximum directivity degradation ϵ =1 dB and a bandwidth of 20 MHz. In MBF scheme, the beams generated by the UL and DL RF beamformers are steered at exact UE locations (i.e., both $\mathbf{f}_D(\theta_D)$ and $\mathbf{f}_U(\theta_U)$ steer the beams at θ_D and θ_U, respectively). It can be seen that the design of RF beamformers $\mathbf{f}_D(\theta_D)$ and $\mathbf{f}_U(\theta_U)$ using MBF can achieve SI suppression ranging from -38.74 dB to -75.05 dB for different UL/DL UE angle pairs. On the other hand, the proposed PBF scheme with SAS can achieve SI suppression ranging from -61.59 dB to -77.57 dB. This shows that the design of RF beamformers $\mathbf{f}_D(\hat{\theta}_D)$, $\mathbf{f}_U(\hat{\theta}_U)$ using the proposed PBF RF beamformers with SAS can provide an additional SI suppression gain of 19 dB on average when compared to MBF, and can further reduce SI by a maximum of 33.04 dB (e.g., for $\theta_D = 135°, \theta_U = 45°$, SI suppression improves from -39.91 dB to -72.96 dB). In other words, by introducing beam perturbation in both UL and DL directions and the selection of the best Tx-Rx sub-array pair can improve SI suppression capability by more than 82% using the proposed PBF with SAS HBF scheme.

The use of a larger sub-array at Tx and Rx can generate narrower beams and can serve large number of users. In Fig. 5.6, we compare the achieved SI suppression results using 1×8 sub-array for six different UL and DL UE angular locations and compare the performance

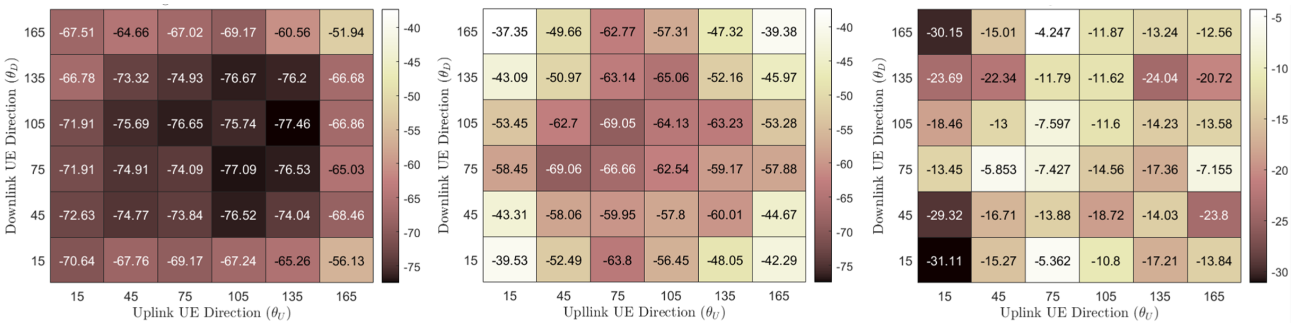

(a)

θ_D \ θ_U	15	45	75	105	135	165
165	-67.51	-64.66	-67.02	-69.17	-60.56	-51.94
135	-66.78	-73.32	-74.93	-76.67	-76.2	-66.68
105	-71.91	-75.69	-76.65	-75.74	-77.46	-66.86
75	-71.91	-74.91	-74.09	-77.09	-76.53	-65.03
45	-72.63	-74.77	-73.84	-76.52	-74.04	-68.46
15	-70.64	-67.76	-69.17	-67.24	-65.26	-56.13

(b)

θ_D \ θ_U	15	45	75	105	135	165
165	-37.35	-49.66	-62.77	-57.31	-47.32	-39.38
135	-43.09	-50.97	-63.14	-65.06	-52.16	-45.97
105	-53.45	-62.7	-69.05	-64.13	-63.23	-53.28
75	-58.45	-69.06	-66.66	-62.54	-59.17	-57.88
45	-43.31	-58.06	-59.95	-57.8	-60.01	-44.67
15	-39.53	-52.49	-63.8	-56.45	-48.05	-42.29

(c)

θ_D \ θ_U	15	45	75	105	135	165
165	-30.15	-15.01	-4.247	-11.87	-13.24	-12.56
135	-23.69	-22.34	-11.79	-11.62	-24.04	-20.72
105	-18.46	-13	-7.597	-11.6	-14.23	-13.58
75	-13.45	-5.853	-7.427	-14.56	-17.36	-7.155
45	-29.32	-16.71	-13.88	-18.72	-14.03	-23.8
15	-31.11	-15.27	-5.362	-10.8	-17.21	-13.84

Figure 5.6. Achieved SI suppression using 1×8 sub-array with 20 MHz BW. (a) Proposed PBF with SAS. (b) MBF. (c) SI suppression gain.

of HBF scheme with PBF and SAS versus HBF scheme with MBF RF beamformers. It is noteworthy to mention that, even though using a larger array structure can narrow the mainbeam width, however, due to the orthogonality, there is still a limitation on the number of orthogonal UL/DL beams that can be generated with such large array structures. As a result, using MBF restricts the maximum number of UL and DL users that can be served simultaneously in FD mMIMO systems. The proposed HBF with PBF RF beamformers and SAS can achieve SI suppression ranging between -51.93 dB and -77.45 dB, where the achieved SI suppression for MBF RF beamformers varies between -37.35 dB to -69.05 dB. Thus, the proposed HBF scheme with PBF RF stages and SAS can provide an additional SI suppression gain of around 15.43 dB (on average) with a maximum SI suppression improvement of around -31.11 dB, which represents an enhanced SI suppression capability of 78.69%.

5.5.2 FD-to-HD Achievable Rate Ratio

In this subsection, we compare the achievable rate of FD mMIMO system versus the HD mMIMO system for UL and DL transmission. In particular, the UL and DL transmissions are operated separately in the case of HD communications, where the received DL signal given in (5.6) does not include IUI by UL UE. Similarly, the received UL signal given in (5.8) does not experience the strong SI. As a benchmark scheme, we consider the angular-based HBF technique in [90], which considers the DL transmission via applying OBF at the RF-stage and RZF at the BB-stage. Similarly, for the UL transmission, we develop the angular-based HC technique using [90] to compare both HD UL and DL rate with FD rate of the proposed HBF scheme. Since the HD DL and UL transmissions are carried out

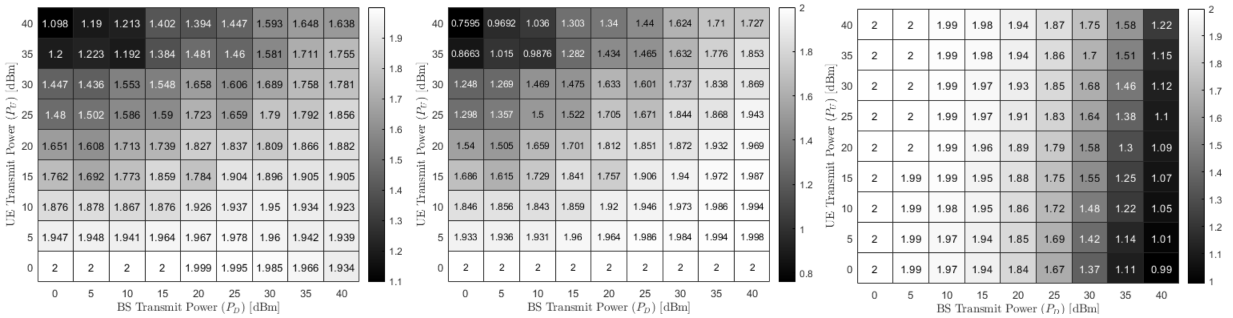

(a) **(b)** **(c)**

Figure 5.7. FD-to-HD rate ratio versus BS/UE transmit power using MBF with 1×4 sub-array at 20 MHz. (a) Total. (b) DL. (c) UL

over either different time-slots or different frequency bands, therefore, the DL, UL and total achievable rate in the HD transmission are normalized as: $R_{D,\text{HD}} = \frac{1}{2}R_D$, $R_{U,\text{HD}} = \frac{1}{2}R_U$, and $R_{\text{Total, HD}} = R_{D,\text{HD}} + R_{U,\text{HD}}$ respectively. To better compare the achievable rate of FD and HD transmission, we use the FD-to-HD rate ratio, which is defined as $\text{Ratio}_D = \frac{R_{D,\text{FD}}}{R_{D,\text{HD}}}$, $\text{Ratio}_U = \frac{R_{U,\text{FD}}}{R_{U,\text{HD}}}$, and $\text{Ratio}_T = \frac{R_{T,\text{FD}}}{R_{T,\text{HD}}}$, where $R_{D,\text{FD}}$, $R_{U,\text{FD}}$ and $R_{T,\text{FD}}$ are the DL, UL and total achievable rates in FD communications and can be calculated using (5.18). In Fig. 5.7, we compare the DL, UL and total FD-to-HD rate ratio versus BS transmit power P_D and UL UE transmit power P_U using the measured SI channel. Given the maximum BS transmit power as 44 dBm at sub-6 GHz band [128], the BS transmit power range is considered as $P_D \in [0, 40]$ dBm. For simplicity, we consider the same range for the UL UE transmit power (i.e., $P_U \in [0, 40]$ dBm) though BS and UE have different hardware constraints. Here, we depict the results for the proposed HBF scheme using OBF RF beamformers to compare the FD-to-HD performance at different BS and UE power levels and to provide understanding of how different power levels can impact the FD achievable rate at a fixed angular location (i.e., $\theta_D = 135°, \theta_U = 15°$).

In Fig. 5.7(a), the total rate ratio is analyzed, which shows that FD transmission can double the capacity with respect to the conventional HD transmission at low power levels of BS and UL UE. Though the FD-to-HD total rate ratio (Ratio_T) decays for very high UL UE transmit power, the proposed HBF scheme can still provide higher capacity ($\geq R_{T,\text{HD}}$) even for the extreme case of very high UL UE power (i.e., at $P_U = 40$ dBm, $\text{Ratio}_T > 1.0$). As shown in Fig. 5.7(b), the DL rate ratio improves when P_D increases and only drops below the unity ratio for $P_U \geq 35$ dBm and low P_D values (i.e., for $P_D \in [0, 10]$ dBm, $\text{Ratio}_T \in [0.8, 1]$. This means HD transmissions can provide higher capacity than FD communications in such cases), where the large UL power boosts the IUI power in comparison to the low DL intended

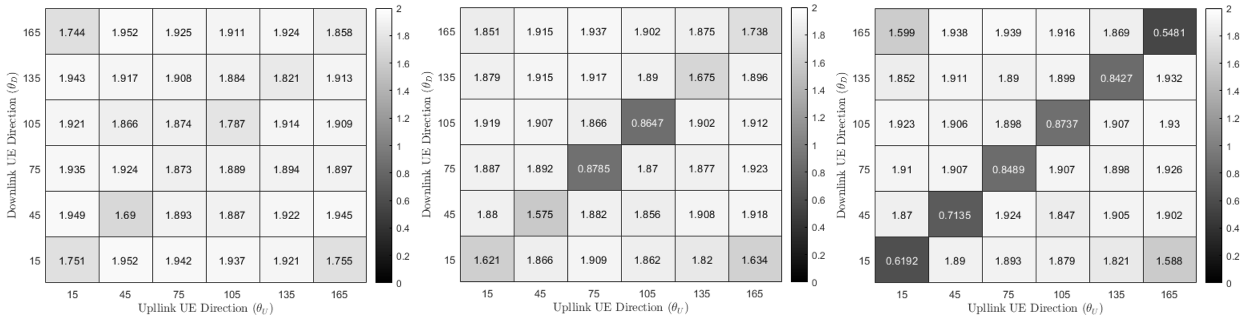

(a) **(b)** **(c)**

Figure 5.8. FD-to-HD total rate ratio at different UL/DL UE angular locations with 1×8 sub-array at 20 MHz. (a) PBF with SAS. (b) PBF. (c) MBF.

signal power (please see (5.6)). Similarly, the UL rate ratio as depicted in Fig. 5.7(c) shows that the increased SI power due to the high BS transmit power negatively affect the UL transmission. For instance, at $P_U = 30$ dBm, the FD-to-HD uplink rate ratio (Ratio_U) is exactly 2.00 and 1.12 for $P_D = 0$ dBm and $P_D = 40$ dBm, respectively.

Fig. 5.8 depicts the FD-to-HD total rate ratio (Ratio_T) for a fixed BS and UL UE transmit power (i.e., $P_D = 30$ dBm and $P_U = 20$ dBm)[5]. Here, we consider six different angular locations for the DL and UL UE (i.e., $\{\theta_D^{\text{ALL}}, \theta_U^{\text{ALL}}\} \in \{15° : 30° : 180°\}$) and compares Ratio_T using 1×8 sub-arrays with 20 MHz BW and maximum directivity degradation $\epsilon = 1$ dB for the following three cases: 1) Proposed HBF with PBF RF beamformers with SAS (MOOP); 2) Proposed HBF with PBF RF beamformers (SOOP)[6]; and 3) Proposed HBF with MBF RF beamformers. Fig. 5.8 shows that HBF with MBF scheme results in poor FD-to-HD rate ratio when both UL and DL UE have same angular locations (on average the total rate ratio is around 0.74). By using the HBF with PBF RF stages (SOOP) can significantly increase the rate ratio at most angular locations, however, due to SI channel characteristics and the use of a fixed Tx-Rx sub-array pair, we can see that SOOP can still result in low FD total rate at few angular locations (e.g., $\{\theta_D, \theta_U\} = \{75°, 105°\}$, and HD transmissions can provide better total rate than FD communications at these angular locations). Moreover, the use of a larger sub-array can still suffer from low FD-to-HD total ratio at certain angular locations, and the number of such angle pairs with low FD-to-HD

---

[5] From Fig. 5.7, we can see that high values of BS and UL UE transmit power can significantly reduce Ratio_T for MBF scheme. Our motivation is to show that using the proposed HBF with PBF with SAS scheme, we can enhance the total rate in FD communications even for the extreme case of very high power UL UE values, thus achieving Ratio_T close to 2.

[6] In this approach, we design PBF RF beamformers for single objective optimization problem (i.e., to minimizing SI). We consider fixed Tx-Rx sub-arrays (without SAS) and find the optimal beam perturbations only.

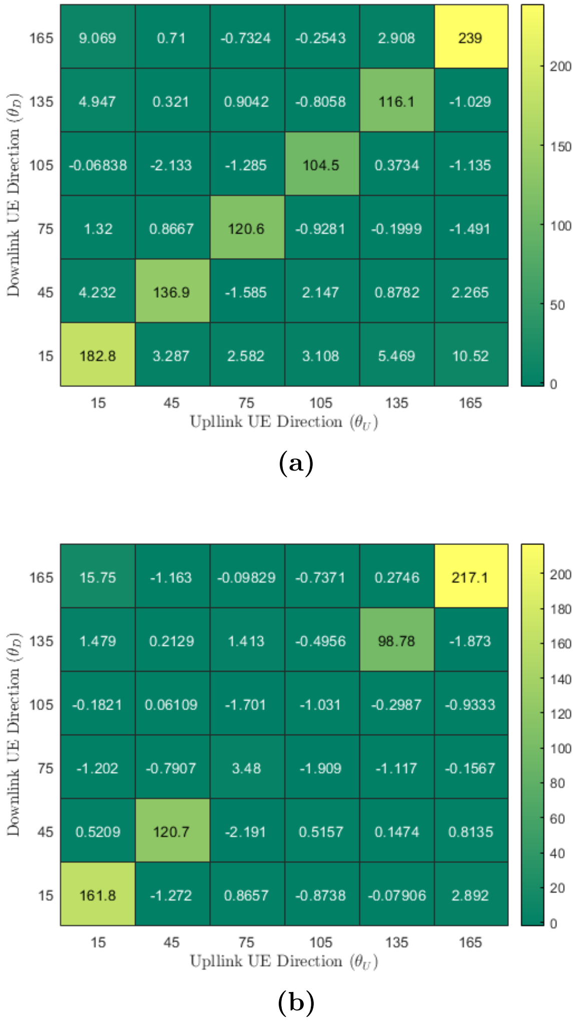

Figure 5.9. FD-to-HD total rate ratio improvement with 1 × 8 sub-array at 20 MHz. (a) PBF with SAS. (b) PBF.

rate ratio can increase for even larger array structures. This issue can be resolved by using HBF with PBF RF beamformer jointly with SAS, which can provide spatial DoF to improve FD rate at all UL/DL UE angular locations. In Fig. 5.8(a), we can see the mean total FD-to-HD rate ratio is around 1.88 $\{\theta_D^{\text{ALL}}, \theta_U^{\text{ALL}}\}$ and 1.79 $\{\theta_D^{\text{SAME}}, \theta_U^{\text{SAME}}\}$, which represents an increase of around 11.6% and 142.3%, respectively when compared to MBF total rate ratio.

Fig. 5.9 plots the FD-to-HD total rate ratio improvement using 1×8 sub-array. Fig. 5.9(b) shows the percentage gain in FD-to-HD total rate ratio for the proposed HBF with PBF RF stages (SOOP) over MBF. We define the percentage improvement in FD-to-HD

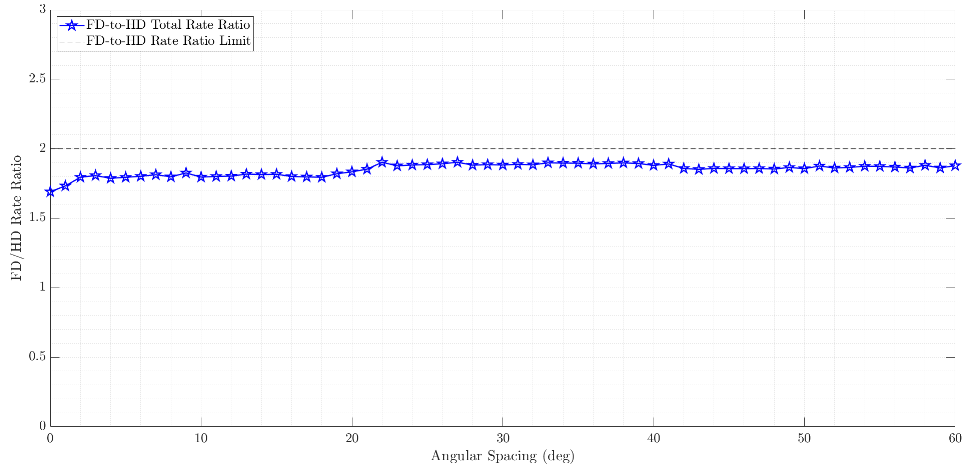

(a)

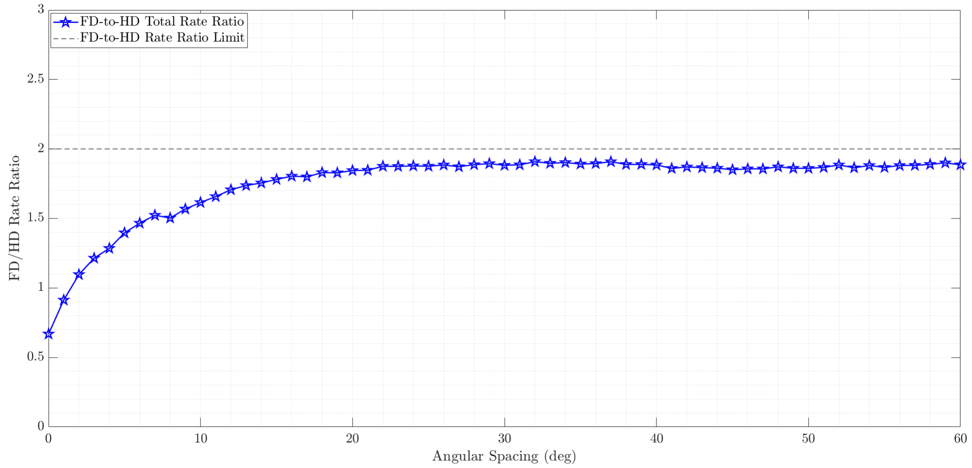

(b)

Figure 5.10. FD-to-HD total rate ratio versus angular separation with 1×4 sub-array at 20 MHz. (a) PBF with SAS. (b) MBF.

total rate ratio as follows:

$$\text{Ratio Gain}(\%) = \left(\frac{\text{Ratio}_{T,s} - \text{Ratio}_{MBF}}{\text{Ratio}_{MBF}}\right) \times 100, \tag{5.51}$$

where $s = \{\text{PBF (SOOP)}, \text{PBF with SAS (MOOP)}\}$. We can see from Fig. 5.9 that compared to the mean gains of 6.57% for $\{\theta_D^{\text{ALL}}, \theta_U^{\text{ALL}}\}$ and 87.8% for $\{\theta_D^{\text{SAME}}, \theta_U^{\text{SAME}}\}$ with SOOP, MOOP can provide the mean gains of 11.6% for $\{\theta_D^{\text{ALL}}, \theta_U^{\text{ALL}}\}$ and 142.3% for $\{\theta_D^{\text{SAME}}, \theta_U^{\text{SAME}}\}$.

In Fig. 5.10, we present the FD-to-HD total rate ratio versus the angular spacing between both UL and DL UE for a fixed power levels usig 1×4 sub-array. Here, we consider the DL

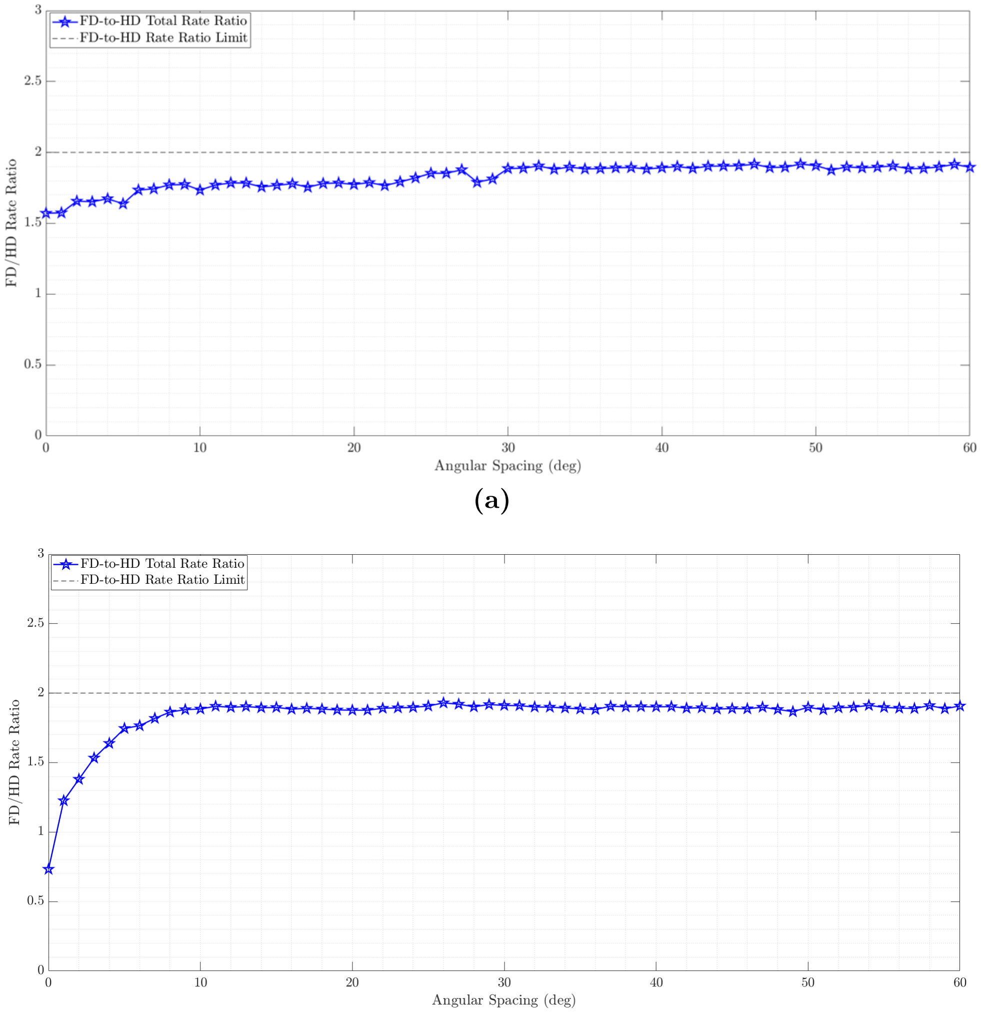

(a)

(b)

Figure 5.11. FD-to-HD total rate ratio versus angular separation with 1 × 8 sub-array at 20 MHz. (a) PBF with SAS. (b) MBF.

UE is located at fixed $\theta_D = 75°$ and the UL UE varies its angular location (i.e., $\theta_U \in \{75° : 1° : 135°\}$). Thus, the angle separation between UL/DL UE can vary from 0° to 60°. It can be seen that by using the proposed HBF with PBF RF stages jointly with SAS (MOOP) can achieve FD-to-HD total rate ratio ≥ 1.5 with minimum angle separation of 0°. In other words, the proposed PBF with SAS (MOOP) can give atleast 1.5 times the total achievable rate of HD transmissions irrespective of UL and DL UE locations in FD mMIMO systems, whereas, with MBF scheme, a minimum angle separation of 7° is required to achieve the rate ratio of at least 1.5. For $\text{Ratio}_T \geq 1.8$, we need angle separation of at least 14° with MBF scheme. However, with the proposed PBF scheme, we require a minimum

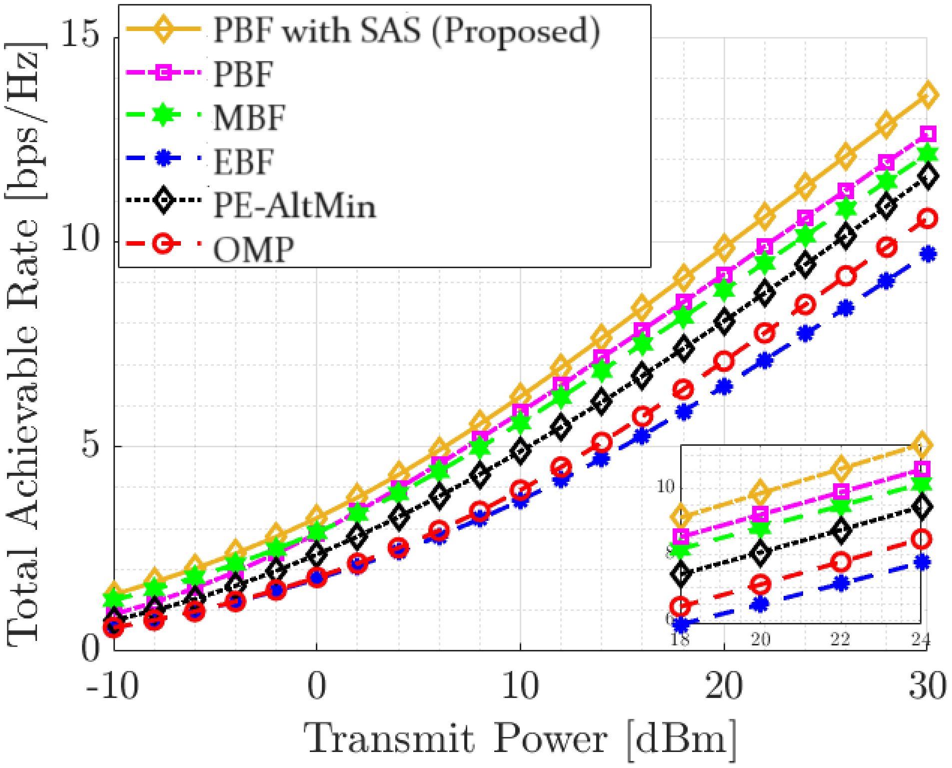

Figure 5.12. Total achievable rate versus transmit power with 1 × 4 sub-array.

angle separation of 3°. Similarly, Fig. 5.11 compares the minimum angle separation for the case when both Tx and Rx are equipped with 1×8 sub-array for DL UE located at fixed $\theta_D = 15°$ and the UL UE varies its angular location (i.e., $\theta_U \in \{15° : 1° : 75°\}$). Compared to the minimum angle separation of 3° and 6° for MBF scheme to achieve ratio ≥ 1.5 and 1.8, respectively, the proposed HBF scheme with PBF RF beamformers and SAS (MOOP) scheme only requires 0° and 5° of UL/DL UE angular separation. It must be noted that the use of larger sub-array can generate narrow beams for UL and DL UE, which can reduce IUI, and thus reducing minimum angle separation. In Fig. 5.12, we compare the total achievable rate versus transmit power of our proposed schemes (i.e., PBF with SAS (MOOP) and PBF (SOOP)) with MBF as well as the HBF solutions presented in [115, 129, 130]. We consider $K_D = K_U = 1$, which are located at azimuth angle $\theta_D = 75°, \theta_U = 135°$. By using 1 × 4 Tx and Rx sub-arrays, it can be seen that compared to MBF and HBF solutions in [115,129,130], the proposed PBF schemes can significantly increase the total achievable rate by suppressing the strong SI. For example, PBF can provide an increase of 1-2 bps/Hz when compared to MBF, however, by using the proposed PBF with SAS, we can achieve a gain of around 3-4 bps/Hz. It is noteworthy to mention that our proposed PBF with SAS can significantly

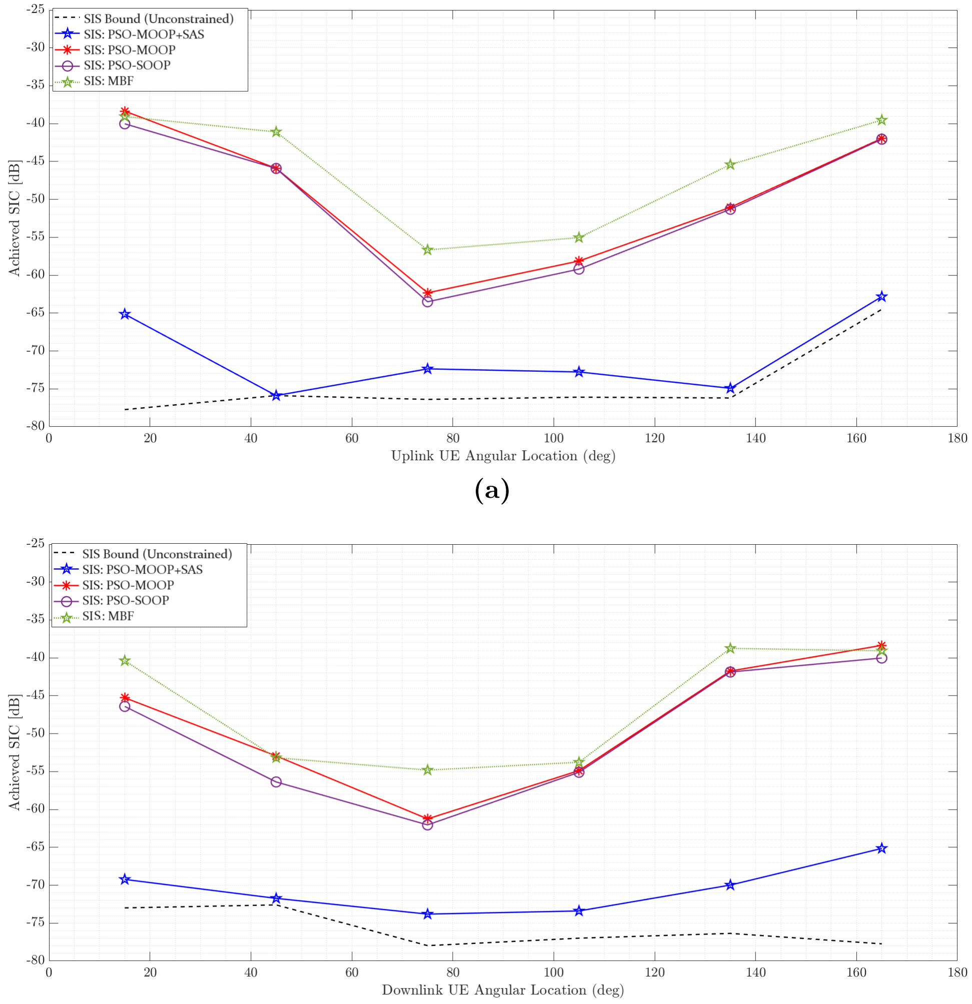

(a)

(b)

Figure 5.13. SI suppression bound comparison using 1×8 sub-array. (a) Achieved SI versus θ_U. (b) Achieved SI versus θ_D.

increase the total achievable rate, especially when operating under the following conditions: 1) harnessing a larger sub-array (i.e., 1×8); and 2) accommodating a greater number of users. This highlights the scalability and adaptability of our approach, offering promising performance enhancements in FD mMIMO systems.

5.5.3 Constrained Versus Unconstrained SI Suppression Comparison

In this section, we compare the achieved SI using 1×8 sub-array for the following schemes: 1) HBF with MBF RF beamformers; 2) HBF with PBF RF beamformers (PBF-SOOP); 3)

HBF with PBF RF beamformers (PBF-MOOP); and 4) HBF with PBF RF beamformers jointly with SAS (PBF-MOOP-SAS). For the NOBF schemes, we compare the results for directivity degradation of $\epsilon = 1$ dB. In Fig. 5.13(a), we plot the achieved SI versus different UL UE angular locations (i.e., $\theta_U \in \{15^\circ : 30^\circ : 180^\circ\}$) for a fixed DL UE location ($\theta_D = 165^\circ$). The results show that MBF scheme can provide very low SI suppression with a minimum value of around -55 dB. In comparison, both PBF schemes (PBF-SOOP and PBF-MOOP) can achieve better SI suppression levels at all UL-DL UE angle pairs with a minimum SI suppression of around -63 dB. However, the use of SAS jointly with PBF for MOOP (PBF-MOOP-SAS) can reduce SI as low as -76 dB, which is very close to lower bound values of SI suppression. Here, the lower bound for SI suppression level can be achieved by considering the loose directivity degradation limits (i.e., $\epsilon = \infty$). In other words, this loose bound can be considered as an unconstrained optimization, which can allow beam perturbations in both UL and DL directions with high directivity degradation. Our objective here is to show that by using the proposed PBF-MOOP-SAS with a tight bound of $\epsilon = 1$ dB, we can closely approach the unbounded SI suppression ($\epsilon = \infty$). Compared to the mean difference of 28.3 dB, 24.1 dB of MBF and PBF-SOOP (PBF-MOOP) schemes from the lower bound, PBF-MOOP-SAS has a mean difference of only around 3.81 dB. Similarly, Fig. 5.13(b) depicts the bounded versus unbounded SI suppression comparisons for different DL UE angular locations (i.e., $\theta_D \in \{15^\circ : 30^\circ : 180^\circ\}$) for a fixed UL UE location ($\theta_U = 15^\circ$). Here, we can see that PBF-MOOP-SAS scheme can achieve SI suppression level close to the bound with an average difference of around 5.2 dB. Thus, we can see that $\mathrm{A}_{\text{SI,PBF-MOOP-SAS}}(\epsilon = \infty) \simeq \mathrm{A}_{\text{SI,PBF-MOOP-SAS}}(\epsilon = 1) \ll \mathrm{A}_{\text{SI,PBF-SOOP}}(\mathrm{A}_{\text{SI,PBF-MOOP}}) \leq \mathrm{A}_{\text{SI,MBF}}$.

5.5.4 Achieved SI and Achievable Rate Ratio Tradeoff

In this section, we compare the achieved SI as well as FD-to-HD total rate ratio for six different UL and DL locations (i.e., $\{\theta_D, \theta_U\} \in \{15^\circ : 30^\circ : 180^\circ\}$), which generates 36 possible UL-DL angle pairs. Fig. 5.14(a) evaluates the frequency (number of occurrences) of UL-DL angle pairs while satisfying certain performance metric. For instance, using MBF scheme, we can achieve SI suppression < -50 dB together with FD-to-HD total rate ratio > 1.5 for a total of $\frac{21}{36}$ UL-DL angle pairs, which represents 58.3% of the total available angle pairs. However, there is $\frac{1}{36}$ UL-DL angle pair to achieve SI < -70 dB jointly with rate ratio > 1.5. On the other hand, the proposed PBF-MOOP-SAS scheme can provide $\frac{34}{36}$ and $\frac{23}{36}$ UL-DL angle pairs for (achieved SI < -50 dB & Ratio > 1.5) and (achieved SI < -70 dB & Ratio > 1.5), respectively. Similarly, Fig. 5.14(b) depicts the performance tradeoff using 1×8 sub-array. The MBF scheme results in $\frac{0}{36}$ UL-DL angle pairs to achieve SI < -70

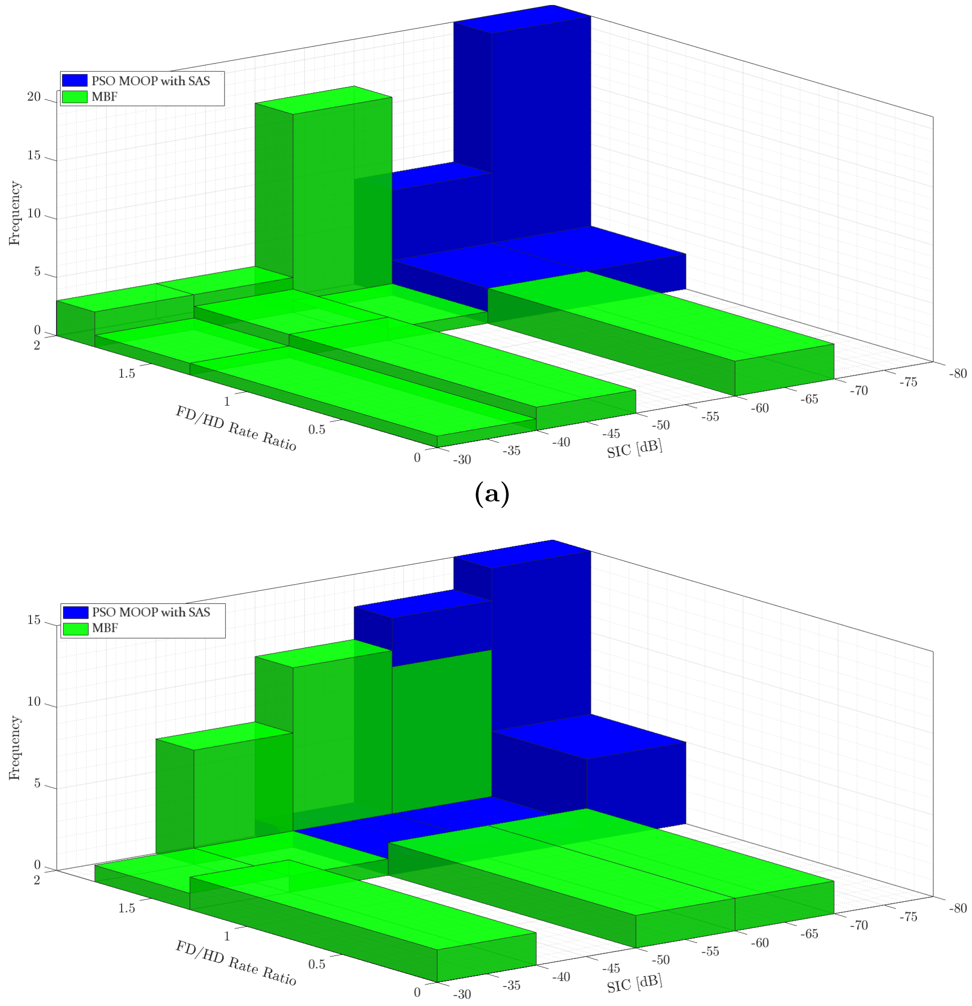

(a)

(b)

Figure 5.14. Achieved SI and FD-to-HD total rate ratio tradeoff using MBF and PBF with SAS schemes. (a) 1×4 sub-array. (b) 1×8 sub-array.

dB & Ratio > 1.5, whereas, the proposed PBF-MOOP-SAS scheme can provide $\frac{20}{36}$ UL-DL angle pairs to achieve SI < -70 dB & Ratio > 1.5. Thus, the proposed PBF-MOOP-SAS scheme can achieve high SI suppression jointly with increased FD-to-HD rate ratio for 55% of the UL-DL angle pairs as compared to 0% in the case of MBF scheme. The detailed performance comparison of the proposed PBF schemes versus MBF for 1 × 4 and 1 × 8 sub-array is summarized in Table 5.1 and Table 5.2, respectively.

Table 5.1. Performance Comparison: PBF with SAS versus MBF (1×4 and 20 MHz BW).

Performance Metrics		HBF Scheme			Improvement using PBF HBF	
		MBF	PBF			
			SOOP	MOOP with SAS	SOOP versus MBF	MOOP + SAS versus MMBF
Achieved SI(dB)	Best[5]	-75.05	-75.9	-77.57	16.25	33.04
	Worst	-38.74	-40.01	-61.59	0.569	1.25
	Avg	-52.6	-59.69	-71.96	7.07	19.33
FD-to-HD Total Rate Ratio (All UL/DL UE locations) [15° : 30° : 165°]	Best	1.930	1.929	1.948	225.8	261.1
	Worst	0.514	0.597	1.598	-6.18	-5.887
	Avg	1.650	1.780	1.886	7.87	14.3
FD-to-HD Total Rate Ratio (Same UL/DL UE locations) [15° : 30° : 165°]	Best	0.879	1.674	1.885	225.8	261.1
	Worst	0.514	0.597	1.598	1.56	83.51
	Avg	0.730	1.371	1.774	87.6	143

Table 5.2. Performance Comparison: PBF with SAS versus MBF (1×8 and 20 MHz BW).

Performance Metrics		HBF Scheme			Improvement using PBF HBF	
		MBF	PBF			
			SOOP	MOOP with SAS	SOOP versus MBF	MOOP + SAS versus MBF
Achieved SI(dB)	Best	-69.0	-77.46	-77.45	17.3	31.11
	Worst	-37.35	-38.9	-51.93	1.16	4.24
	Avg	-55.0	-62.59	-70.43	7.58	15.43
FD-to-HD Total Rate Ratio (All UL/DL UE locations) [15° : 30° : 165°]	Best	1.939	1.936	1.952	217.1	239
	Worst	0.5481	0.864	1.694	-2.19	-2.13
	Avg	1.689	1.80	1.886	6.57	11.6
FD-to-HD Total Rate Ratio (Same UL/DL UE locations) [15° : 30° : 165°]	Best	0.873	1.738	1.872	217.1	239
	Worst	0.548	0.864	1.69	-1.03	104.5
	Avg	0.741	1.392	1.796	87.8	142.3

5.5.5 SI Suppression with NCM URA SC-HBF

In this section, we present the achieved SI suppression results using the proposed NCM-BF-SIS scheme (as discussed in Section 5.4) at different uplink and downlink UE angular locations. In Fig. 5.15, we present the achieved SI using 2×2 URA SC-HBF architecture over a bandwidth of 20 MHz, and compare the performance of NCM-BF-SIS with the following two SI suppression schemes: 1) maximum-directivity-based beamforming scheme (MD-BF-SIS), and 2) constant-modulus RF beamforming scheme (CM-BF-SIS)[7]. In Fig. 5.15(a), we plot the achieved SI suppression for varying uplink and downlink azimuth locations (i.e., $\{\phi_D, \phi_U\} \in \{0^\circ : 30^\circ : 180^\circ\}$) for fixed uplink and downlink elevation angles (i.e., $\theta_D = \theta_U = 90^\circ$). It can be seen that compared to MD-BF-SIS, both NCM-BF-SIS and CM-BF-SIS schemes can provide more uplink-downlink angle-pairs for an enhanced SI suppression. However, the proposed NCM-BF-SIS can achieve the best SI suppression when compared

---

[7] In MD-BF-SIS, $\mathbf{f}_D$ and $\mathbf{f}_U$ steer the beams at exact user locations (i.e., (θ_D, ϕ_D) and (θ_U, ϕ_U) while in CM-BF-SIS, beam angles are optimized (i.e., $\hat{\theta}_D, \hat{\phi}_D, \hat{\theta}_U, \hat{\phi}_U$) to construct the RF stages with fixed gain controllers.

Table 5.3. SI Suppression performance Comparison of NCM-BF-SIS, CM-BF-SIS, MD-BF-SIS scheme.

Sub-Array Configuration		Proposed		MD-BF-SIS
		NCM-BF-SIS	CM-BF-SIS	
2×2 (URA)	Best	-79.6	-77.2	-74.2
	Worst	-36.6	-34.6	-32.2
	Avg	-70.2	-67.3	-49.3
4×4 (URA)	Best	-79.6	-78.2	-74.2
	Worst	-36.7	-35.4	-33.1
	Avg	-72.3	-69.4	-54.4
1×4 (ULA)	Best	-78.69	-76.6	-67.3
	Worst	-34.2	-33.4	-30.2
	Avg	-61.8	-57.4	-49.2

to MD-BF-SIS and CM-BF-SIS schemes, and can bring SI level down to -79.5 dB. The proposed NCM-BF-SIS can further reduce the SI level by around -20 dB and -4 dB versus MD-BF-SIS and CM-BF-SIS schemes, respectively. In Fig. 5.15(b), we compare the achieved SI for varying uplink and downlink elevation angles (i.e., $\{\theta_D, \theta_U\} \in \{0° : 30° : 90°\}$) for fixed $\phi_D = \phi_U = 90°$. The results show that the proposed NCM-BF-SIS scheme can achieve an SI suppression of -75 dB or lower for almost 70 % of the (θ_D, θ_U) angle-pairs. Similarly, Fig. 5.15(c) depicts the SI levels for varying downlink angular locations (i.e., $\theta_D \in \{0° : 30° : 90°\}, \phi_D \in \{0° : 30° : 180°\}$) for fixed uplink angular location $\theta_U = \phi_U = 90°$. The proposed NCM-BF-SIS scheme can achieve SI suppression upto -80 dB. Thus, compared to MD-BF-SIS and CM-BF-SIS schemes, jointly optimizing beam angles with gain controller coefficients in NCM-BF-SIS can significantly enhance SI suppression.

In Fig. 5.16, we present the achieved SI using a 4×4 URA SC-HBF architecture at 20 MHz bandwidth, and compare the performance of NCM-BF-SIS with MD-BF-SIS and CM-BF-SIS schemes. In Fig. 5.16(a), the achieved SI suppression for varying uplink and downlink azimuth locations for fixed uplink and downlink elevation angle $\theta_D = \theta_U = 90°$ is presented, which shows the proposed NCM-BF-SIS can achieve the best SI suppression at all $\phi_D - \phi_U$ angle-pairs. Moreover, compared to 2×2 URA, a 4×4 URA sub-array can provide better performance as the 4×4 array can generate narrower beams than 2×2 sub-array, which results in enhanced SI suppression. Similarly, Fig. 5.16(b) compares the achieved SI suppression for different uplink/downlink angle-pairs. The results show that NCM-BF-SIS diminishes the strong SI for any uplink and downlink angle-pair. For instance, the SI can be reduced by -70 dB or lower for any uplink-downlink angle-pair (θ_D, θ_U) for a fixed

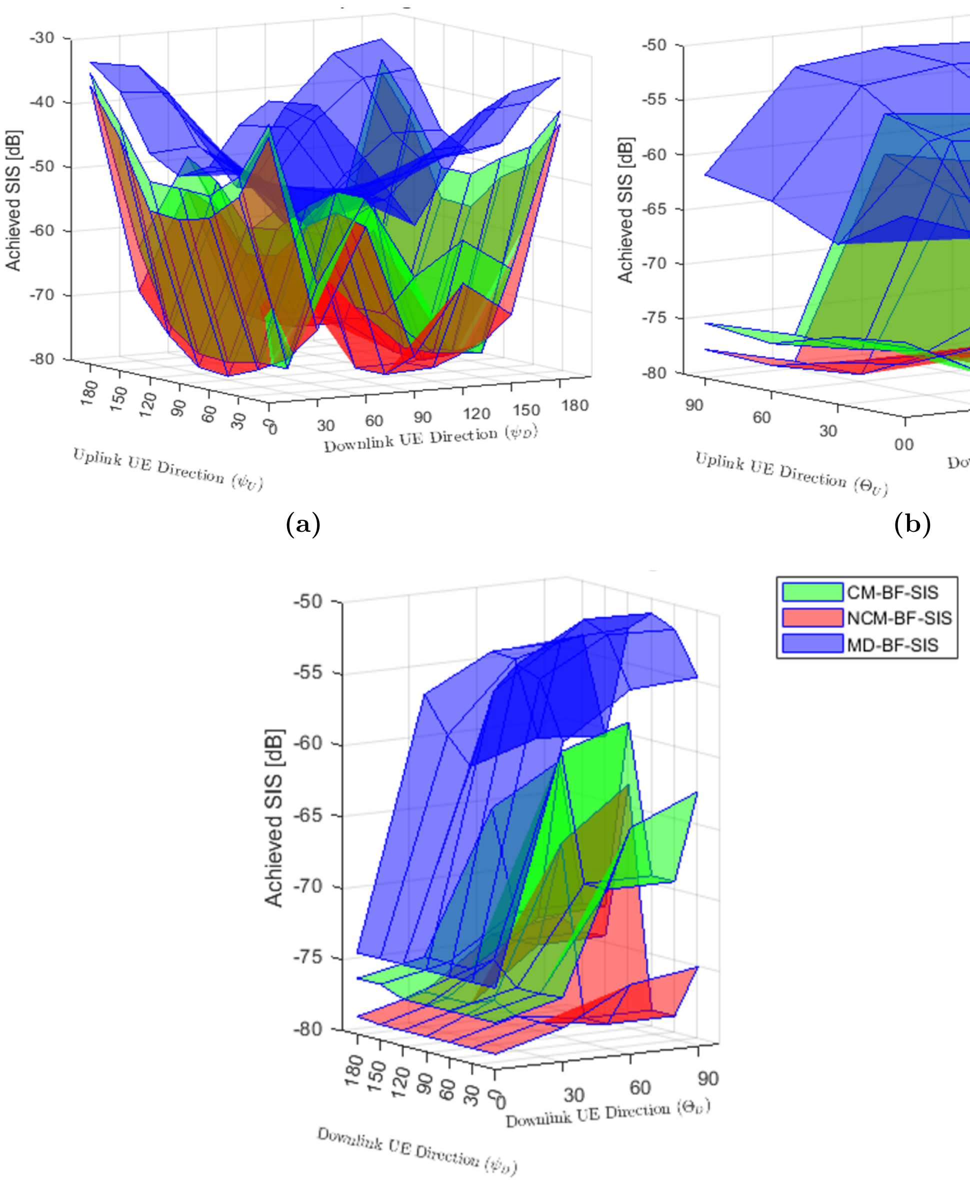

(a) **(b)**

(c)

Figure 5.15. Achieved SI suppression of proposed NCM-BF-SIS with 2×2 sub-array at 20 MHz bandwidth. (a) versus ϕ_D and ϕ_U for fixed ($\theta_D = \theta_U = 90°$). (b) versus θ_D and θ_U for fixed ($\phi_D = \phi_U = 90°$). (c) versus ϕ_D and θ_D for fixed ($\theta_U = \phi_U = 90°$).

$\phi_U = \phi_D = 90°$. In Fig. 5.16(c), we show the achieved SI levels for different downlink user locations (i.e., $\{\theta_D, \phi_D\} \in \{0° : 30° : 180°\}$) for fixed uplink user location $\theta_U = \phi_U = 90°$. It can be seen that the proposed NCM-BF-SIS scheme can attain the SI suppression of -75 dB or lower at all (θ_D, ϕ_D) angle-pairs, whereas MD-BF-SIS scheme can bring the SI level

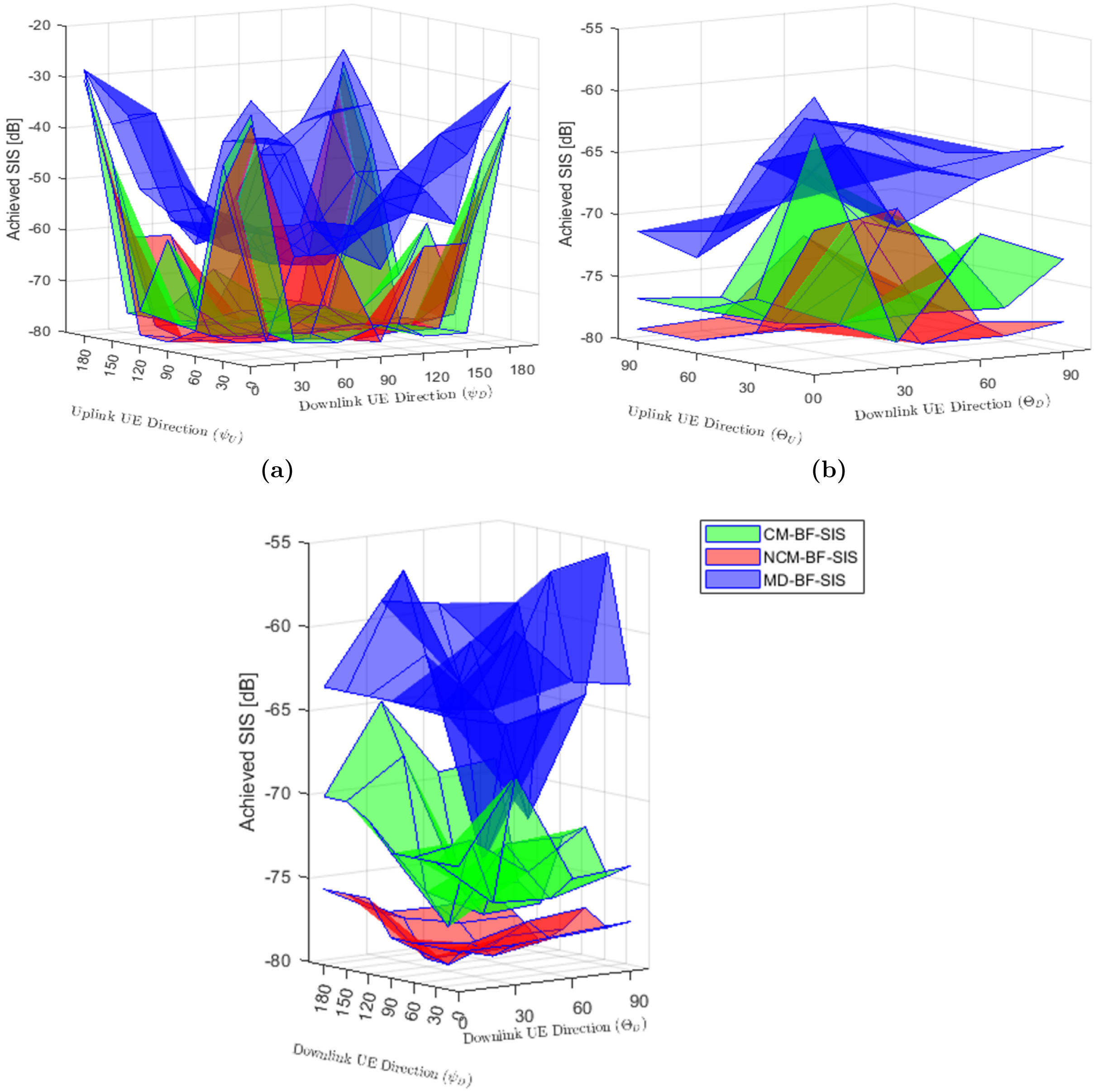

(a) **(b)**

(c)

Figure 5.16. Achieved SI suppression of proposed NCM-BF-SIS with 4×4 sub-array at 20 MHz bandwidth. (a) versus ϕ_D and ϕ_U for fixed ($\theta_D = \theta_U = 90°$). (b) versus θ_D and θ_U for fixed ($\phi_D = \phi_U = 90°$). (c) versus ϕ_D and θ_D for fixed ($\theta_U = \phi_U = 90°$).

down to -75 dB or lower for only a single (θ_D, ϕ_D) angle-pair. Thus, the proposed NCM-BF-SIS significantly alleviate SI for any uplink-downlink user location (for instance, out of 28 possible (θ_D, ϕ_D) angle-pairs, NCM-BF-SIS achieve SI suppression of $\leq$ -75 dB for all 28 pairs, whereas MD-BF-SIS can provide SI suppression of $\leq$ -75 dB for only a single angle-pair). As a result, NCM-BF-SIS can provide more DoF in enhancing FD communications performance irrespective of uplink and downlink user locations.

Finally, Table 5.3 presents the detailed comparison of achieved SI suppression using different URA SC-HBF sizes (2×2 and 4×4) for NCM-BF-SIS, CM-BF-SIS, and MD-BF-SIS schemes over a bandwidth of 20 MHz. Here, we consider varying uplink and downlink azimuth locations (i.e., $\{\phi_D, \phi_U\} \in \{0° : 30° : 180°\}$) for fixed uplink and downlink elevation angles (i.e., $\theta_D = \theta_U = 90°$), and provide the results for best, worst, and average SI suppression. The analysis can be summarized as follows: 1) we can achieve the best SI suppression of around -80 dB by using the proposed NCM-BF-SIS scheme when using either 2×2 or 4×4 URA sub-array; 2) increasing the number of antennas can provide an enhanced SI suppression (for instance, 4×4 URA sub-array can provide more uplink-downlink UE angle-pairs for increased SI suppression than a 2×2 URA sub-array); 3) the proposed NCM-BF-SIS can provide an average SI suppression gain of around -20 dB and -4 dB when compared to MD-BF-SIS and CM-BF-SIS schemes, respectively; and 4) the URA sub-array configuration can minimize SI more effectively than ULA sub-array (for example, an average SI suppression of 2×2 is around -9 dB lower than 1×4 ULA sub-array).

5.6 Concluding Remarks

This chapter considers a FD mMIMO system using a sub-array-based HBF architecture and investigates the capacity gains of FD communications over HD transmissions in a real-time implementation. In particular, the strong SI is suppressed by designing the RF beamformers jointly with SAS to utilize the spatial DoF in large array structures, thus avoiding the use of costly analog SI-cancellation circuits. To achieve capacity gains in FD communications, a multi-objective design framework is considered to minimize SI and maximize the total achievable rate. Based on OTA measured SI channel, we have proposed a novel HBF scheme that applies perturbations to the orthogonal beams in UL and DL beam directions and jointly finds the best Tx-Rx sub-array pair. To solve this challenging non-convex problem, we have proposed a swarm intelligence-based algorithmic solution to find the optimal perturbations and Tx-Rx indices while satisfying the directivity degradation constraints for the UL and DL beams. Illustrative results show that the proposed HBF scheme with PBF RF stages jointly with SAS can achieve high SI suppression compared to MBF for both 1×4 and 1×8 sub-array configurations and can mitigate SI to -78 dB in real life implementations for FD mMIMO systems. Moreover, the proposed HBF scheme can achieve an average capacity gain of around 1.8 for any angular location of UL-DL UE.

5.7 Appendix: Proof of Lemma 5.1

Let $\mathbf{f}_U$ and $\mathbf{f}_D$ be the UL and DL RF beamformers for i^{th} DL UE and j^{th} UL UE, respectively. Then, we can express the RF beamformers as:

$$\mathbf{f}_D(\theta_{D_i}) = \frac{1}{\sqrt{N_D}}[1, e^{j2\pi\Delta\cos(\theta_{D_i})}, \cdots, e^{j2\pi\Delta(N_D-1)\cos(\theta_{D_i})}]^T, \tag{5.52}$$

$$\mathbf{f}_U(\theta_{U_j}) = \frac{1}{\sqrt{N_U}}[1, e^{-j2\pi\Delta\cos(\theta_{U_j})}, \cdots, e^{-j2\pi\Delta(N_U-1)\cos(\theta_{U_j})}]^T. \tag{5.53}$$

Then, we can rewrite the expression for $\mathbf{f}_U^T\mathbf{H}_{SI}\mathbf{f}_D$ as:

$$\begin{aligned}
&\mathbf{f}_U^T\mathbf{H}_{SI}\mathbf{f}_D \\
&= \frac{1}{\sqrt{N_D}}\mathbf{f}_U^T\mathbf{H}_{SI}[1, e^{j2\pi d\cos(\theta_{D_i})}, \cdots, e^{j2\pi d(N_D-1)\cos(\theta_{D_i})}]^T \\
&= \frac{1}{\sqrt{N_U}}[1, e^{-j2\pi d\cos(\theta_{U_j})}, \cdots, e^{-j2\pi d(N_U-1)\cos(\theta_{U_j})}]\mathbf{H}_{SI} \\
&\quad \frac{1}{\sqrt{N_D}}[1, e^{j2\pi d\cos(\theta_{D_i})}, \cdots, e^{j2\pi d(N_D-1)\cos(\theta_{D_i})}]^T \\
&= \frac{1}{\sqrt{N_D N_U}}\sum_{n_u=1}^{N_U}\sum_{n_d=1}^{N_D} h_{n_u,n_d}e^{-j2\pi d(n_u\cos(\theta_{U_j})-n_d\cos(\theta_{D_i}))},
\end{aligned} \tag{5.54}$$

where h_{n_u,n_d} is the (n_u, n_d)-th element of $\mathbf{H}_{SI}$. Since $|\cos(\theta_{U_j})|, |\cos(\theta_{D_i})| \leq 1$, the term inside the exponent of (5.54) is bounded as follows:

$$\begin{aligned}
&|n_u\cos(\theta_{U_j}) - n_d\cos(\theta_{D_i})| \leq n_u|\cos(\theta_{U_j})| + n_d|\cos(\theta_{D_i})| \\
&\leq n_u + n_d \leq N_{us} + N_{ds} - 2,
\end{aligned} \tag{5.55}$$

where the last inequality follows because n_u and n_d both range from 1 to N_U and N_D, respectively. Now, let us consider the term h_{n_u,n_d}. Considering the large array structures, the path loss between the transmit and receive antennas within the same device is generally low due to the short distance between them. Thus, the SI channel, which is the channel from the transmit antenna to the receive antenna in the same device, is expected to be very strong in magnitude. Hence, we can assume that h_{n_u,n_d} has non-negligible values. Next, we analyze the magnitude of the expression $\mathbf{f}_U^T\mathbf{H}_{SI}\mathbf{f}_D$. Applying the triangle inequality, we can write as follows:

$$\begin{aligned}
&|\mathbf{f}_U^T\mathbf{H}_{SI}\mathbf{f}_D| \\
&= \frac{1}{\sqrt{N_D N_U}}\left|\sum_{n_u=1}^{N_U}\sum_{n_d=1}^{N_D} h_{n_u,n_d} e^{-j2\pi d(n_u\cos(\theta_{U_j})-n_d\cos(\theta_{D_i}))}\right| \\
&\leq \frac{1}{\sqrt{N_D N_U}}\sum_{n_u=1}^{N_U}\sum_{n_d=1}^{N_D}|h_{n_u,n_d}| \\
&\leq \frac{1}{\sqrt{N_D N_U}}(N_U+N_D-2)\max_{n_u,n_d}|h_{n_u,n_d}|, \qquad (5.56)
\end{aligned}$$

where the last inequality holds due to the bounds on the indices n_u and n_d. Based on the assumption that the path loss is significant and the SI channel is strong, we can infer that the maximum absolute value of the SI channel coefficients $\max_{n_u,n_d}|h_{n_u,n_d}|$ is very small. Consequently, we can approximate the expression as follows:

$$|\mathbf{f}_U^T\mathbf{H}_{SI}\mathbf{f}_D| \approx \mathbf{0}. \qquad (5.57)$$

This approximation is valid when SI channel is strong, the path loss is significant, and the array dimensions N_U and N_D are sufficiently large. It suggests that the design of DL and UL RF beamforming stages, represented by $\mathbf{F}_D$ and $\mathbf{F}_U$ respectively, can effectively eliminate the interference caused by the SI channel. Hence, we conclude that for a given UL-DL angle-pair $\theta_{D_i}, \theta_{U_j}$ in large array structures, the approximation $\mathbf{F}_U\mathbf{H}_{SI}\mathbf{F}_D \approx \mathbf{0}$ holds, indicating the suppression of SI interference.

Chapter 6

UAV-Assisted Terrestrial Massive MIMO Systems for Enhanced Coverage and Capacity[1]

6.1 Introduction

In the previous chapters, different HBF solutions have been proposed for both half-duplex (HD) and full-duplex (FD) communications in mMIMO systems. With the advent of advanced wireless communications and networking technologies, it is expected that billions of low-power consumption devices, such as wireless sensors will be connected to the internet through the IoT framework, which will significantly increase capacity and coverage needs in mMIMO systems [21]. However, deploying IoT effectively and extensively still poses significant challenges, including efficient information transfer between wireless nodes and gateways. Due to the limited coverage and fixed deployment of terrestrial networks, the integration of UAVs offer key advantages of rapid deployment especially in emergency situations. To address this issue, various routing schemes have been proposed, including direct transmission or relay structures. Nonetheless, when the distance between the IoT end node and the gateway is substantial, direct transmission may not be feasible or may consume excessive power. In such cases, communication through relay can be a more power-efficient alternative. Moreover, deploying cellular stations in urban areas can be a

---

[1] Parts of this chapter have been presented at the 2022 IEEE 96th Vehicular Technology Conference (VTC2022-Fall), London/Beijing [131], the 2023 IEEE 97th Vehicular Technology Conference (VTC2023-Spring), Florence, Italy [132], the 2023 IEEE Global Communications Conference (GLOBECOM), KualaLumpur, Malaysia [133] and published in the IEEE Internet of Things Journal [134].

Table 6.1. A brief comparison of the related literature.

Literature	Contents											
	UAV Operation Mode		Propagation Environment		MIMO		Relay Transmission		Radio Resource Management			Deep Learning
	As BS	As Relay	No Fading (LoS)	Fading (LoS + NLoS)	SU-MIMO	MU-MIMO	With Buffer	Without Buffer	UAV Positioning/Trajectory	Power Allocation	Beamforming	
[135, 136]		✓	✓		✓			✓	✓			
[137]		✓	✓		✓			✓	✓	✓		
[139]		✓	✓			✓		✓	✓	✓		
[140]	✓		✓			✓		✓	✓			
[141]		✓		✓		✓		✓		✓		
[142]		✓		✓	✓		✓		✓			
[143]		✓	✓		✓		✓		✓			
[144]	✓			✓		✓	✓		✓			
[148, 152, 154]	✓			✓		✓		✓	✓		✓	
[149–151]	✓		✓			✓		✓	✓	✓	✓	
[153]	✓			✓		✓		✓	✓	✓	✓	
[154]	✓		✓			✓		✓	✓	✓		
This work		✓		✓		✓	✓		✓	✓	✓	✓

costly and challenging task, which can further complicate the communications coverage issue in the IoT framework [22].

The deployment of UAVs as a relay has garnered significant research attention in recent years, with the objective of designing UAV-assisted systems that maximize throughput or minimize transmit power [135–144]. Most existing research studies on the use of UAVs to assist in communications has overlooked the potential benefits of beamforming solutions, as evidenced by studies such as [135–147]. While some studies have explored beamforming solutions, they have been limited to single-hop communications scenarios and have only examined its application in single links, such as in studies [148–155], where UAVs act as flying BSs rather than relays, making the beamforming solutions inapplicable for dual-hop or relaying structures. The joint optimization of UAV location, power allocation (PA), and HBF design for a dual-hop mmWave MU-mMIMO IoT communications networks is an unaddressed problem, presenting a significant opportunity to advance the field of UAV-based wireless communications. To address this gap in literature, this chapter aims to highlight the full potential of beamforming, and its ability to enhance performance in dual-hop UAV communications networks[1] The main contributions of this work are summarized as follows:

- We propose three novel optimization schemes for maximizing total capacity in UAV-assisted MU-mMIMO IoT systems: 1) joint HBF and optimal PA for fixed UAV location (J-HBF-PSOPA-FL); 2) joint HBF and UAV location optimization for equal PA (J-HBF-PSOL-EQPA); and 3) joint HBF, UAV location optimization and PA (J-HBF-PSOLPA). Using swarm intelligence-based particle swarm optimization (PSO), we tackle the challenging non-convex problem with high-dimensional variable matrices and fractional programming variables, while adhering to constraints like UAV deployment span, total transmit power, PA, and CM. In particular, the RF stages are formulated using slow time-varying angle-of-departure

---

[1] It is worth noting that, unlike prior literature that employs a single antenna in UAV-assisted systems, this study considers large antenna arrays deployed in the mmWave band to consider beamforming issues in fading scenarios. In non-fading situations, for instance, LoS channels, the proposed HBF solutions can further improve performance by providing higher directional gain and reducing interference.

(AoD)/angle-of-arrival (AoA) information, while the BB stages use the reduced-dimension effective channel information with RZF. In J-HBF-PSOPA-FL, we allocate optimal power for multiple IoT users with fixed UAV location, and design the RF and BB stages for maximum capacity. In J-HBF-PSOL-EQPA, we optimize UAV location for equal PA, whereas, in J-HBF-PSOLPA, we jointly optimize both UAV location and PA, and design HBF stages for both UAV and BS. The illustrative results show that J-HBF-PSOLPA can achieve higher total rate compared to J-HBF-PSOL-EQPA and J-HBF-PSOPA-FL schemes.

- To overcome the high computational complexity of J-HBF-PSOLPA, we propose a novel low-complexity DL-based joint HBF, UAV location optimization and PA (J-HBF-DLLPA) algorithm for a UAV-assisted MU-mMIMO IoT systems. The proposed J-HBF-DLLPA-based solution can achieve AR of J-HBF-PSOLPA, while reducing the runtime by $98 - 99$ %. In particular, the proposed J-HBF-DLLPA is built via a fully-connected DNN consisting of two phases: 1) offline supervised learning via the optimal allocated powers and UAV locations calculated with J-HBF-PSOLPA; and 2) real-time prediction of optimal power values and UAV location via the trained DNN.
- We analyze the performance of UAV DF relaying with and without buffering. Most existing studies have explored the option of forwarding the received signal without buffering the data, which fails to fully leverage the UAV's mobility [135–141, 148–155]. The proposed solutions incorporate signal buffering at the UAV, enhancing the relaying performance significantly. Particularly, we analyze the average delay of delay-unconstrained and delay-constrained transmissions, which can be significantly reduced by J-HBF-PSOLPA compared to fixed UAV deployment and equal PA (FL-EQPA).

The rest of this chapter is organized as follows. Section 6.2 discuss the channel model of mmWave UAV-assisted mMIMO systems. In Section 6.3, we present the HBF solution for a single-hop UAV-assisted mMIMO system. Section 6.4 discuss the UAV-assisted amplify-and-forward (AF) relaying followed by the decode-and-forward (DF) relaying in Section 6.5 for a point-to-point mMIMO system. Section 6.6 introduces the UAV-assisted DF relaying for a MU-mMIMO system. The illustrative results are provided in Section 6.7. Finally, the chapter is concluded in Section 6.8.

6.2 Channel Model

While LoS channel models can be useful for simple scenarios, they can be limited in their ability to capture the channel complexities (e.g., multi-path fading and shadowing). On the other hand, mmWave channel models can provide a more accurate representation of the channel characteristics, including the impact of non-LoS (NLoS) paths and obstacles on the signal propagation in UAV-assisted communications. Therefore, we consider mmWave channels for both links. The channel between BS and UAV is modeled based on the Saleh-Valenzuela channel model [156], and is given as:

$$\begin{aligned}\mathbf{H}_1 &= \sum_{c=1}^{C}\sum_{l=1}^{L} z_{1_{cl}} \tau_{1_{cl}}^{-\eta} \mathbf{a}_1^{(r)}(\theta_{cl}^{(r)}, \phi_{cl}^{(r)}) \mathbf{a}_1^{(t)T}(\theta_{cl}^{(t)}, \phi_{cl}^{(t)}) \\ &= \mathbf{A}_1^{(r)} \mathbf{Z}_1 \mathbf{A}_1^{(t)},\end{aligned} \tag{6.1}$$

where C is the total number of clusters, L is the total number of paths, η is the path loss exponent, and $z_{1_{cl}}$ is the complex gain of l^{th} path in c^{th} cluster. Here, $\mathbf{a}_1^{(j)}(\cdot,\cdot)$ is the corresponding transmit or receive array steering vector for uniform rectangular array (URA), which is given as [90]:

$$\begin{aligned}\mathbf{a}_1^{(j)}(\theta, \phi) = &\left[1, e^{-j2\pi d \sin(\theta)\cos(\phi)}, \cdots, e^{-j2\pi d(N_x-1)\sin(\theta)\cos(\phi)}\right] \\ &\otimes \left[1, e^{-j2\pi d \sin(\theta)\sin(\phi)}, \cdots, e^{-j2\pi d(N_y-1)\sin(\theta)\sin(\phi)}\right],\end{aligned} \tag{6.2}$$

where $j = \{t, r\}$, d is the inter-element spacing, $N_x(N_y)$ is the horizontal (vertical) size of corresponding antenna array at BS and UAV, $\mathbf{Z}_1 = \mathrm{diag}(z_{1,1}\tau_{1,1}^{-\eta}, \ldots, z_{1,L}\tau_{1,L}^{-\eta}) \in \mathbb{C}^{L\times L}$ is the diagonal gain matrix, $\mathbf{A}_1^{(r)} \in \mathbb{C}^{N_r \times L}$ and $\mathbf{A}_1^{(t)} \in \mathbb{C}^{L\times N_T}$ are the receive and transmit phase response matrices, respectively. Here, the angles $\theta_{cl}^{(t)} \in \left[\theta_c^{(t)} - \delta_c^{\theta(t)}, \theta_c^{(t)} + \delta_c^{\theta(t)}\right]$ and $\phi_{cl}^{(t)} \in \left[\phi_c^{(t)} - \delta_c^{\phi(t)}, \phi_c^{(t)} + \delta_c^{\phi(t)}\right]$ are the azimuth AoD (AAoD) and elevation AoD (EAoD) for l^{th} path in channel $\mathbf{H}_1$, respectively. $\theta_c^{(t)}$ is the mean AAoD and $\delta_c^{\theta(t)}$ represents the AAoD spread, whereas $\phi_c^{(t)}$ is mean EAoD with spread $\delta_c^{\phi(t)}$. Similarly, the angles $\theta_{cl}^{(r)} \in \left[\theta_c^{(r)} - \delta_c^{\theta(r)}, \theta_c^{(r)} + \delta_c^{\theta(r)}\right]$ and $\phi_{cl}^{(r)} \in \left[\phi_c^{(r)} - \delta_c^{\phi(r)}, \phi_c^{(r)} + \delta_c^{\phi(r)}\right]$ are the azimuth AoA (AAoA) and elevation AoA (EAoA), where $\theta_c^{(r)}$ and $\phi_c^{(r)}$ are the mean AAoA and EAoA with angular spread $\delta_c^{\theta(r)}$ and $\delta_c^{\phi(r)}$, respectively. Then, the channel vector between the UAV and the k^{th} IoT user can be written as follows:

$$\begin{aligned}\mathbf{h}_{2,k}^T &= \textstyle\sum_{l=1}^{L} z_{2,k_l}\tau_{2,k_l}^{-\eta}\mathbf{a}(\theta_{k_l}, \phi_{k_l}) \\ &= \mathbf{z}_{2,k}^T \mathbf{A}_{2,k} \in \mathbb{C}^{N_t},\end{aligned} \tag{6.3}$$

where L is the total number of downlink paths from UAV to IoT nodes, $z_{2,k_l} \sim \mathcal{CN}(0, \frac{1}{L})$ is the complex path gain of l^{th} path in second link, $\mathbf{a}(\cdot,\cdot) \in \mathbb{C}^{N_t}$ is the UAV downlink array phase response vector. As expressed in (6.3), the intended downlink channel constitute two parts: 1) fast time-varying path gain vector $\mathbf{z}_{2,k} = [z_{2,k_1}\tau_{2,k_1}^{-\eta}, \cdots, z_{2,k_L}\tau_{2,k_L}^{-\eta}]^T \in \mathbb{C}^L$; and 2) slow time-varying downlink array phase response matrix $\mathbf{A}_{2,k} \in \mathbb{C}^{L\times N_t}$ with the rows of $\mathbf{a}(\theta_{k_l}, \phi_{k_l})$. Then, the channel matrix for second link is written as:

$$\mathbf{H}_2 = [\mathbf{h}_{2,1}, \cdots, \mathbf{h}_{2,K}]^T = \mathbf{Z}_2\mathbf{A}_2 \in \mathbb{C}^{K\times N_t}, \tag{6.4}$$

where $\mathbf{Z}_2 = [\mathbf{z}_{2,1}, \cdots, \mathbf{z}_{2,K}]^T \in \mathbb{C}^{K\times L}$ is the complete path gain matrix for all downlink IoT nodes.

6.3 Joint HBF and UAV Deployment in Single-Hop mMIMO Systems

In this section, we propose a novel SI-based joint HBF and UAV positioning scheme (JHBFP) to maximize the overall system capacity in mmWave MU-mMIMO systems. Based on the 3D geometry-based mmWave channel model, a two-stage architecture is designed for the proposed JHBFP technique: (i) RF beamformer, and (ii) BB precoder. The RF beamformer is designed by using SVD of channel matrix followed by the BB precoder utilizing the reduced-size effective channel matrix seen from the BB-stage. Both RF and BB stages aim to mitigate the multi-user interference (MU-I) among the users, while reducing the number of RF chains. Afterwards, we present a novel PSO-based UAV location (PSO-L) algorithm for the optimal UAV positioning to maximize ASR of the mmWave MU-mMIMO systems. Here, our primary motivation is to address non-convex UAV placement problem via the proposed PSO-L algorithm. We also propose hemi-spherical (HSA) array configuration for the UAV communications as compared to URA, which is a preferred array structure in the existing UAV studies ([149,157–161]). Illustrative results indicate that, the proposed JHBFP of UAV using PSO-L can significantly enhance the system spectral and energy efficiencies.

6.3.1 System Model

We consider a cellular network in an urban environment consisting of a set of non-vehicular cellular users/IoT devices. Due to possible obstructions (e.g., high-rise buildings., etc.), the direct communication between BS and the users located in a certain geographical

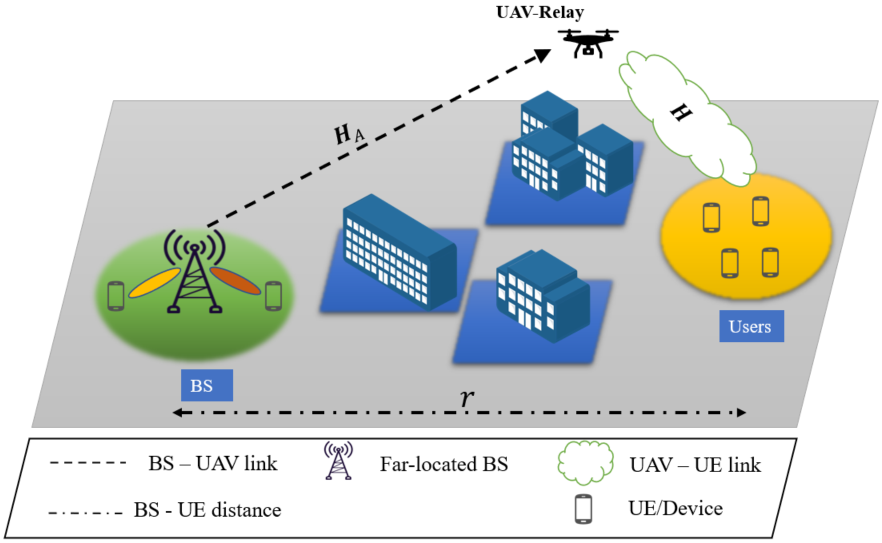

Figure 6.1. UAV-assisted mmWave MU-mMIMO system.

area is not possible as shown in Fig. 6.1. We consider integrating UAV as a flying relay into the existing cellular network that connects the BS with users located at a far distance r. We assume the UAV is placed at a height $D_u > D_b$, where D_b is the height of the BS. Let $\mathcal{K}$ represents the set of users that needs to be served by BS via UAV relay. Let (x_u, y_u, D_u) and (x_k, y_k, z_k) denote the locations of the UAV and k^{th} user, respectively.

We assume the channel $\mathbf{H}_A$ between UAV relay and BS has sufficient capacity for BS-UAV data transfer to serve the users in $\mathcal{K}$. Moreover, the UAV relay is assumed to employ a hybrid precoder/beamformer with an N_T element antenna array and N_{RF} RF chains for simultaneously communicating with K single-antenna users. We consider UAV location optimization jointly with HBF design for UAV-UE link to maximize ASR while the design of BS-UAV link is left for future work. The hybrid beamformer $\mathbf{B} = \mathbf{F}_D\mathbf{B}_D$ consists of the digital baseband precoder $\mathbf{B}_D = [\mathbf{b}_1, \cdots, \mathbf{b}_K] \in \mathbb{C}^{N_{RF}\times K}$ and the analog RF beamformer $\mathbf{F}_D = [\mathbf{f}_1, \cdots, \mathbf{f}_{N_{RF}}] \in \mathbb{C}^{N_T \times N_{RF}}$ that is implemented using phase shifters and thus, imposes a constant-modulus (CM) constraint., i.e., $|\mathbf{F}_D(i,j)| = \frac{1}{\sqrt{N_T}}\ \forall i,j$. The design of HBF reduces the number of RF chains from N_T to N_{RF}, while satisfying $K \leq N_{RF} \ll N_T$. Considering K data streams, the precoded signal at UAV relay is given by:

$$\mathbf{s} = \mathbf{F}_D\mathbf{B}_D\mathbf{d}, \tag{6.5}$$

where $\mathbf{d} \in \mathbb{C}^K$ is the data signal with $\mathbb{E}\{\mathbf{d}\mathbf{d}^{\mathrm{H}}\} = \mathbf{I}_K$. The transmitted signal satisfies the power constraint., i.e., $\mathbb{E}\{\|\mathbf{s}\|_2^2\} \leq P_T$, where P_T is the transmit power at the UAV relay.

Then, the received signal at k^{th} user is given by:

$$\begin{aligned} y_k &= \mathbf{h}_k^{\mathrm{H}} \mathbf{B} \mathbf{s} + n_k, \\ &= \underbrace{\mathbf{h}_k^{\mathrm{H}} \mathbf{F}_D \mathbf{b}_k d_k}_{\text{Desired Signal}} + \underbrace{\sum_{\hat{k} \neq k}^{K} \mathbf{h}_k^{\mathrm{H}} \mathbf{F}_D \mathbf{b}_{d_{\hat{k}}} d_{\hat{k}}}_{\text{IUI}} + \underbrace{n_k}_{\text{Noise}}, \end{aligned} \tag{6.6}$$

where $\mathbf{h}_k \in \mathbb{C}^N$ is the narrowband flat-fading mmWave channel vector between UAV relay and users, $\mathbf{s}_k$ is the data signal for k^{th} user, $\mathbf{b}_k$ is the k^{th} column of $\mathbf{F}_D$, and n_k denotes the additive circular symmetric Gaussian noise such that $n_k \sim \mathcal{CN}(0, \sigma^2)$. By using (6.5) and (6.6), the instantaneous signal-to-interference-plus-noise ratio (SINR) expression at k^{th} user is derived as follows:

$$\mathrm{SINR}_k = \frac{|\mathbf{h}_k^{\mathrm{H}} \mathbf{F}_D \mathbf{b}_k|^2}{\sum_{\hat{k} \neq k}^{K} |\mathbf{h}_k^{\mathrm{H}} \mathbf{F}_D \mathbf{b}_{\hat{k}}|^2 + \sigma^2}. \tag{6.7}$$

By using the instantaneous SINR, the ergodic sum-rate capacity R_{sum} for UAV-assisted mmWave MU-mMIMO systems is given by:

$$R_{\text{sum}}\left(\mathbf{F}_D, \mathbf{B}_D, x_u, y_u\right) = \sum_{k=1}^{K} \mathbb{E}[\log_2(1 + \mathrm{SINR}_k)]. \tag{6.8}$$

For the case where the ground BS is directly serving the users, the ASR can be maximized by designing $\mathbf{F}_D$ and $\mathbf{B}_D$. However, in a UAV-assisted cellular system, where the UAV is deployed at a fixed height z_u and relaying data to the users, the ASR can be maximized by the joint optimization of $\mathbf{F}_D, \mathbf{B}_D$ and $\mathbf{x} = [x_o, y_o] \in \mathbb{R}^2$, where $\mathbf{x}$ represents UAV position to be optimized within the given UAV flying span. By using (6.5) and (6.6), the ASR is written as:

$$\begin{aligned} \max_{\{\mathbf{F}_D, \mathbf{B}_D, x_o, y_o\}} \quad & R_{\text{sum}}\left(\mathbf{F}_D, \mathbf{B}_D, x_u, y_u\right) \\ \text{s.t.} \quad & C_1: |\mathbf{F}_D(i,j)| = \frac{1}{\sqrt{N_T}}, \\ & C_2: \ \mathbb{E}\{\|\mathbf{s}\|_2^2\} \leq P_T, \\ & C_3: x_{\min} \leq x_o \leq x_{\max}, y_{\min} \leq y_o \leq y_{\max}, \end{aligned} \tag{6.9}$$

where C_1 refers to the CM constraint due to the use of phase shifters, C_2 indicates the transmit power constraint at UAV and C_3 implies UAV positioning within the given flying span. Here, $[x_{\min}, x_{\max}]$ and $[y_{\min}, y_{\max}]$ represent the UAV relay deployment range in x-axis and y-axis, respectively. The optimization problem defined in (6.9) is non-convex. To solve this problem, we sequentially develop $\mathbf{F}_D$ and $\mathbf{B}_D$ and apply PSO-L to optimize x_o and y_o.

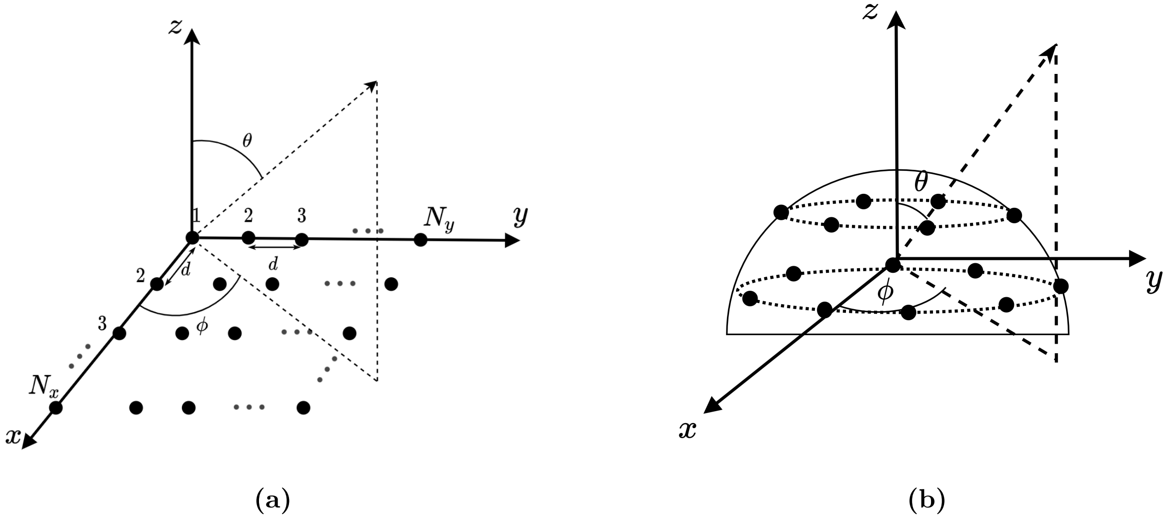

Figure 6.2. UAV-relay array structures: (a) URA (b) HSA.

6.3.2 Low-Complexity Hybrid Beamforming Design

In this section, we first decouple the optimization problem (as given in (6.9)) and present the design of proposed low-complexity hybrid beamformer $\mathbf{B} \in \mathbb{C}^{N_T \times K}$, which maximizes the spectral and energy efficiencies of a UAV-assisted mMIMO system. In particular, the HBF is constructed by concatenating the RF beamformer $\mathbf{F}_D \in \mathbb{C}^{N_T \times N_{RF}}$ and reduced-dimensional MU baseband precoder $\mathbf{B}_D \in \mathbb{C}^{N_{RF} \times K}$. Compared to the existing HBF solutions for UAV-assisted mMIMO systems (e.g., [149, 161]), the proposed HBF design can achieve a high sum-rate and energy efficiency with reduced complexity by using ordered SVD of the MU-mMIMO channel between UAV relay and ground users [98].

6.3.2.1 RF Beamformer Design

We assume K users are clustered into G groups based on their AoD information, where each group contains K_g number of users such that $K = \sum_{g=1}^{G} K_g$. The index $g_k = \sum_{g'=1}^{g-1} K_{g'} + k$ is used to denote the k^{th} user in group g. Then, the channel matrix $\mathbf{H}^{(g)}$ for gth group can be written as:

$$\mathbf{H}^{(g)} = [\mathbf{h}_1, \cdots, \mathbf{h}_{K_g}]^T = \boldsymbol{\mathcal{Q}}^{(g)} \boldsymbol{\Sigma}^{(g)} \boldsymbol{\mathcal{V}}^{H(g)} \in \mathbb{C}^{K_g \times N}, \tag{6.10}$$

where $\boldsymbol{\mathcal{Q}}^{(g)}$ and $\boldsymbol{\mathcal{V}}^{(g)}$ are $K_g \times K_g$ and $N_T \times N_T$ unitary matrices, respectively. $\boldsymbol{\Sigma}^{(g)}$ is a $K_g \times N_T$ rectangular diagonal matrix with non-negative real numbers on the diagonal, and the elements are arranged in decreasing order. For each group g, the low-complexity RF beamformer $\mathbf{F}_g \in \mathbb{C}^{N_T \times N_{RF_g}}$ is constructed by utilizing SVD of the channel matrix $\mathbf{H}^{(g)}$. Then, the complete RF beamformer is given as follows:

$$\mathbf{F}_D = \Big[\mathbf{F}_1, \cdots, \mathbf{F}_G\Big] \in \mathbb{C}^{N_T \times N_{RF}}. \tag{6.11}$$

Let $\boldsymbol{\phi}_n^{(g)} = [e^{jv_{1,n}^{(g)}}, e^{jv_{2,n}^{(g)}}, \ldots, e^{jv_{N,n}^{(g)}}]^T \in \mathbb{C}^{N_T}$ be the phase vector of group g, where $v_{m,n}^{(g)}$ is the phase angle of the $(m,n)-th$ entry of $\mathbf{V}$. Then, we can formulate the phase matrix $\mathbf{\Phi}^{(g)}$ as:

$$\mathbf{\Phi}^{(g)} = [\phi_1^{(g)}, \phi_2^{(g)}, \ldots, \phi_N^{(g)}] \in \mathbb{C}^{N_T \times N_T}. \tag{6.12}$$

Comparing (6.10) and (6.12), we can see that each entry of $\phi_n^{(g)}$ and $\mathbf{V}_g(n)$ have the same phase angle. Then, using N_{RF_g} RF chains for each group, the RF beamformer for g^{th} group can be given as:

$$\mathbf{F}^{(g)} = [\phi_1^{(g)}, \phi_2^{(g)}, \ldots, \phi_{N_{RF_g}}] \in \mathbb{C}^{N_T \times N_{RF_g}}. \tag{6.13}$$

Using $N_{RF} = \sum_{g=1}^{G} N_{RF_g}$, we can then generate the complete RF beamformer as given in (6.11). Then, $\mathbf{H} = [\mathbf{H}_1^T, \cdots, \mathbf{H}_G^T]^T \in \mathbb{C}^{K \times N}$ is the complete channel matrix between UAV relay and K users. Using (6.10), (6.11), the effective channel matrix as seen from the BB-stage is given as:

$$\boldsymbol{\mathcal{H}} = \mathbf{HF} = \begin{bmatrix} \mathbf{H}_1\mathbf{F}_{D,1} & \mathbf{H}_1\mathbf{F}_{D,2} & \ldots & \mathbf{H}_1\mathbf{F}_{D,G} \\ \mathbf{H}_2\mathbf{F}_{D,1} & \mathbf{H}_2\mathbf{F}_{D,2} & \ldots & \mathbf{H}_2\mathbf{F}_{D,G} \\ \vdots & \vdots & \ddots & \vdots \\ \mathbf{H}_G\mathbf{F}_{D,1} & \mathbf{H}_G\mathbf{F}_{D,2} & \ldots & \mathbf{H}_G\mathbf{F}_{D,G} \end{bmatrix} \in \mathbb{C}^{K \times N_{RF}}, \tag{6.14}$$

where the diagonal matrices $\boldsymbol{\mathcal{H}}_g = \mathbf{H}_g\mathbf{F}_g = \mathbf{Z}_g\mathbf{A}_g\mathbf{F}_{D,g} \in \mathbb{C}^{K_g \times N_{RF_g}}$ are the effective channel matrix for group g and the off-diagonal matrices $\boldsymbol{\mathcal{H}}_{\hat{g}} = \mathbf{H}_{\hat{g}}\mathbf{F}_g = \mathbf{Z}_{\hat{g}}\mathbf{A}_{\hat{g}}\mathbf{F}_{D,g} \in \mathbb{C}^{K_{\hat{g}} \times N_{RF_g}}$ represent the effective interference channel matrix between groups g and $\hat{g}$, $\forall \hat{g} \neq g$.

6.3.2.2 BB-Stage Design

After designing the RF-stage, the reduced-size effective CSI $\boldsymbol{\mathcal{H}}$ given in (6.14) is employed for the BB precoder. We consider joint-group-processing (JGP) technique as designed in [90]. The design of BB precoder $\mathbf{W}$ not only reduces the intra-group interference but also mitigate the residual inter-group interference remaining after RF beamformer design. By applying the well-known RZF technique, **W** is defined as:

$$\mathbf{B}_D = \gamma \mathbf{T} \boldsymbol{\mathcal{H}}^H, \tag{6.15}$$

where $\mathbf{T} = \left[\boldsymbol{\mathcal{H}}^H \boldsymbol{\mathcal{H}} + \alpha N_{RF} \mathbf{I}_{N_{RF}}\right]^{-1}$, $\mathbf{I}_{N_{RF}} \in \mathbb{C}^{N_{RF} \times N_{RF}}$, α is the regularization parameter and γ is the normalization factor used to satisfy the power constraint, which can be written as:

$$\gamma = \sqrt{\frac{S}{\mathrm{tr}\{\boldsymbol{\mathcal{H}}^H \mathbf{T}^H \mathbf{F}^H \mathbf{F} \mathbf{T} \boldsymbol{\mathcal{H}}\}}}. \tag{6.16}$$

6.3.3 UAV Deployment with PSO-L

After the design of **F** and **W**, the optimization problem given in (6.9) can be reformulated as:

$$\begin{aligned} \max_{\{x_o, y_o\}} \quad & R_{\text{sum}}\left(\mathbf{F}_D, \mathbf{B}_D, x_u, y_u\right) \\ \text{s.t.} \quad & C_3 : x_{\min} \leq x_o \leq x_{\max}, y_{\min} \leq y_o \leq y_{\max}. \end{aligned} \tag{6.17}$$

Though, the constant modulus constraint for **F** (i.e., C_1 in (6.9)) is satisfied via the solution of RF beamformer design as discussed in Section. 6.3.2.1, however, the resulting problem in (6.17) is still an NP hard [162] because the optimization variables $\{x_o, y_o\}$ are jointly located in both the numerator and denominator of the SINR expression given in (6.7).

We propose a PSO based algorithm for optimization of the UAV relay location (PSO-L) to maximize the capacity of UAV-UE link. PSO is capable of searching the global optimum iteratively for vastly complex spaces and has a faster convergence time. In a UAV-assisted cellular system, the number of feasible UAV positions required to search space is $\left(\frac{x_{max}-x_{min}}{M_x}\right) \times \left(\frac{y_{max}-y_{min}}{M_y}\right)$, where M_x and M_y represents the search space resolution. PSO-L makes use of multiple agents called particles to search the objective function space, which is given in (6.17). PSO-L solves the problem by employing Z particles, which represent the potential solutions for UAV locations. Initially, a swarm of particles, each with its own position, velocity, and fitness value are randomly placed in search space. PSO-L algorithm solves the optimization problem by iteratively updating particle positions; a particle moves to the next position using the best position experienced by the particle and the best position experienced by all the particles. Hence, PSO-L algorithm solves the optimization problem by updating particle positions during T iterations.

In PSO-L, a particle represents the candidate position of UAV and the location is represented by a certain point (x, y) in the search space. Then, the potential position of i^{th}

particle during t^{th} iteration is given as:

$$\mathbf{U}_i^{(t)} = [x_i^{(t)}, y_i^{(t)}], \tag{6.18}$$

where $t = 0, 1, \cdots, T$ represents the iteration index. Thus, each particle calculates the corresponding objective function as given in (6.17), evaluates its personal best solution, communicates with other particles for the global best solution, and moves from $\mathbf{U}^{(t)}$ to $\mathbf{U}^{(t+1)}$ until t approaches T. Let $\mathbf{U}_i^{(t)}$ and $\mathbf{V}_i^{(t)}$ be the position and velocity of i^{th} particle during t^{th} iteration, respectively. The position $\mathbf{U}_i^{(t)}$ is uniformly distributed between $[x_{min}, x_{max}]$ and $[y_{min}, y_{max}]$ while the velocity $\mathbf{V}_i^{(t)}$ is adjusted to $\mathbf{V}_i^{(0)} = \mathbf{0}$. Then, during the iterations, both $\mathbf{U}$ and $\mathbf{V}$ of i^{th} particle are updated as follows:

$$\begin{aligned} \mathbf{V}_i^{(t+1)} &= \omega \mathbf{V}_i^{(t)} + \mu_1 \mathbf{A}_1^{(t)} (\mathbf{U}_{best}^{(t)} - \mathbf{U}_i^{(t)}) + \mu_2 \mathbf{A}_2^{(t)} (\mathbf{U}_{best,i}^{(t)} - \mathbf{U}_i^{(t)}), && (6.19) \\ \mathbf{U}_i^{(t+1)} &= \mathbf{U}_i^{(t)} + \mathbf{V}_i^{(t+1)}, && (6.20) \end{aligned}$$

where ω denotes the inertial weight factor, μ_1 and μ_2 are the learning parameters for the global best $\mathbf{U}_{best}^{(t)}$ and the personal best $\mathbf{U}_{best,i}^{(t)}$, $\mathbf{A}_1^{(t)}$ and $\mathbf{A}_2^{(t)}$ are the matrices with entries uniformly distributed in $[0, 1]$. The function of ω is to control the impact of previous velocity history on current velocity, thus, it is considered vital for convergence as it manages the particle's tradeoff between global and local exploration. By applying (6.8) as the objective function, the personal and global best solutions for i^{th} particle during t^{th} iteration are obtained as:

$$\mathbf{U}_{best,i}^{(t)} = \underset{\mathbf{U}_i^{(t^*)}, \forall t^* = 0,1,\cdots,t}{\arg\max} \quad R_{\text{sum}}(\mathbf{F}, \mathbf{W}, \mathbf{U}_i^{(t^*)}), \tag{6.21}$$

$$\mathbf{U}_{best}^{(t)} = \underset{\mathbf{U}_{best,i}^{(t^*)}, \forall i = 0,1,\cdots,N_p}{\arg\max} \quad R_{\text{sum}}(\mathbf{F}, \mathbf{W}, \mathbf{U}_{best,i}^{(t)}). \tag{6.22}$$

Algorithm 6.1 summarizes the proposed joint hybrid beamformer and UAV positioning (JHBFP) scheme using using PSO-L Algorithm.

Algorithm 6.1 Proposed Joint HBF Design and UAV Positioning (JHBFP) Algorithm Using PSO-L

```
1: Input: $Z, T, G, \mu_1, \mu_2, \omega$, $[\theta_k^{(g)}, \phi_k^{(g)}]$ for $k = 1, \ldots, K$.
2: Output: $x_o, y_o$, $\mathbf{F}_D, \mathbf{B}_D$.
3: for $g = 1 : G$ do
4:     Compute channel matrix $\mathbf{h}_k^{(g)}$ via (6.3).
5:     Using (6.10), form the unitary matrices $\boldsymbol{\mathcal{Q}}^{(g)}$ and $\boldsymbol{\mathcal{V}}^{(g)}$.
6:     for $n = 1 : N$ do
7:         Calculate the phase of each entity of $\boldsymbol{\mathcal{V}}(:, n)^{(g)}$, i.e., $\psi(:, n)^{(g)}$.
8:         Construct the phase vector $\upsilon_n^{(g)}$.
9:     end for
10:    Formulate $\mathbf{\Gamma}^{(g)}$ via (6.12).
11:    Find $\mathbf{F}_D^{(g)}$ using $N_{RF}^{(g)}$ via (6.13).
12:    $\mathbf{F}_D = [\mathbf{F}_D^{(1)}, \mathbf{F}_D^{(2)}, \ldots, \mathbf{F}_D^{(G)}]$.
13:    Compute $\mathbf{B}_D$ using (6.15).
14:    for $i = 1 : Z$ do
15:        Initialize the velocity as $\mathbf{V}_i^{(0)} = \mathbf{0}$.
16:        Diagonal entries of $\mathbf{U}_i^{(0)}$ are uniformly distributed in $[0, 1]$.
17:        Set the personal best $\mathbf{U}_{best,i}^{(0)} = \mathbf{U}_i^{(0)}$.
18:    end for
19:    Find the global best $\mathbf{U}_{best}^{(o)}$ as in (6.22).
20:    for $t = 1 : T$ do
21:        for $i = 1 : Z_p$ do
22:            Update the velocity $\mathbf{V}_i^{(t)}$ as in (6.19).
23:            Update the position $\mathbf{U}_i^{(t)}$ as in (6.20).
24:            Find the personal best $\mathbf{U}_{best,i}^{(t)}$ as in (6.21).
25:        end for
26:        Find the global best $\mathbf{U}_{best}^{(t)}$ as in (6.22).
27:    end for
28: end for
29: Update $\mathbf{F}_D, \mathbf{B}_D$ for $x_o, y_o$ using steps 1-10.
```

6.4 Joint HBF and UAV Deployment in Dual-Hop mMIMO Systems: Amplify-and-Forward (AF) Relaying

In this section, we present a novel joint optimization scheme to maximize the end-to-end throughput in a UAV-assisted mmWave mMIMO communications systems using two different SA configurations, namely spherical array equal-angle (SAEA) and

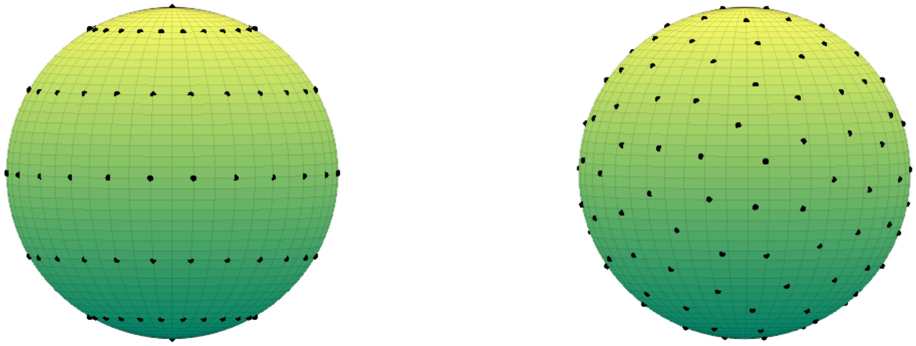
(a)

(b)

Figure 6.3. Spherical array configurations: (a) equal-angle (EA) (b) uniform-space (US).

spherical array uniform-space (SA-US) as shown in Fig. 6.3. In particular, the UAV acts as an amplify-and-forward (AF) relay between a BS and an IoT gateway and the challenging non-convex optimization problem is solved using swarm intelligence (SI)-based particle swarm optimization (PSO) method to find optimal UAV relay positioning within a given deployment region [163]. Then, HBFs for the BS and IoT gateway are designed using an orthogonal matching pursuit (OMP)-based algorithmic solution, whereas, for the UAV relay, both transmit and receive RF beamformers are formulated using singular value decomposition (SVD) of the channel matrices.

6.4.1 System Model

We consider IoT devices and IoT gateway are located in a remote area, which is difficult to access directly by BS (eNodeB) due to obstacles, and UAV is used as AF relay to improve the situation as shown in Fig. 6.4. We assume the UAV relay is placed at a height $h_u > h_1$, where h_1 is the height of the BS. Let (x_u, y_u, h_u), (x_1, y_1, h_1) and (x_2, y_2, h_2) denote the locations of UAV, BS and gateway, respectively.

In the system model as shown in Fig. 6.5, we consider the BS is equipped with N_1 transmit antennas, UAV relay with $N_{u,r}(N_{u,t})$ antennas for receiving (transmitting) signals and gateway with N_2 antennas. Both BS and gateway adopt HBF architecture, where BS consists of a RF beamforming stage $\mathbf{F}_1 \in \mathbb{C}^{N_1 \times N_{RF_1}}$ and BB stage $\mathbf{B}_1$ $\mathbb{C}^{N_{RF_1} \times N_S}$, where N_S represents the data streams from the BS and N_{RF_1} is the RF chains such that $N_S \leq N_{RF_1} \leq N_1$ to guarantee multistream transmission. Considering half-duplex (HD) UAV AF relaying, BS sends N_S data streams through channel $\mathbf{H}_1 \in \mathbb{C}^{N_{u,r} \times N_1}$ in first time slot. Using $N_{u,r}$

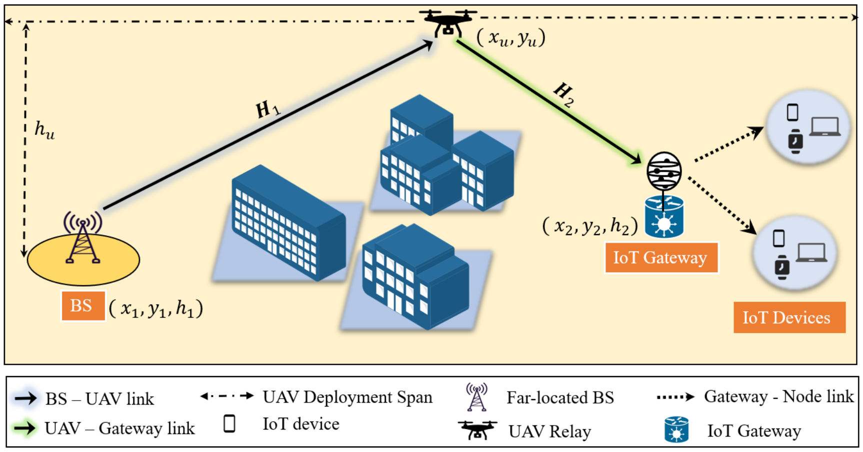

Figure 6.4. UAV-assisted mMIMO IoT communications system.

antennas, the UAV relay receives signals with an RF combiner $\mathbf{F}_{u,r} \in \mathbb{C}^{N_{RF_u} \times N_{u,r}}$. We assume UAV relay transmits the data in the second time slot using RF beamformer $\mathbf{F}_{u,t} \in \mathbb{C}^{N_{u,t} \times N_{RF_u}}$ through channel $\mathbf{H}_2 \in \mathbb{C}^{N_2 \times N_{u,t}}$. The received signal at gateway is processed through RF stage $\mathbf{F}_2 \in \mathbb{C}^{N_{RF_2} \times N_2}$ and BB stage $\mathbf{B}_2\ \mathbb{C}^{N_S \times N_{RF_2}}$. Here, all RF beamforming and combining stages are implemented using phase shifters (PSs) and thus, impose a constant-modulus (CM) constraint, i.e., $|\mathbf{F}_i(j,k)| = \frac{1}{\sqrt{N_i}}$ $(i = 1, 2)$, $|\mathbf{F}_{u,r}(j,k)| = \frac{1}{\sqrt{N_{u,r}}}$, $|\mathbf{F}_{u,t}(j,k)| = \frac{1}{\sqrt{N_{u,t}}}$ $\forall j, k$. The use of RF beamforming and combining stages for BS, UAV relay and gateway greatly reduces the number of RF chains from: 1) N_1 to N_{RF_1}; 2) $N_{u,r}(N_{u,t})$ to N_{RF_u}; and 3) N_2 to N_{RF_2}, respectively. Considering the data signal is $\mathbf{d} = [d_1, d_2, \ldots, d_{N_S}]^T$ with $\mathbb{E}\{\mathbf{d}\mathbf{d}^H\} = \mathbf{I}_{N_S}$ $\in \mathbb{C}^{N_S \times N_S}$, then the signal transmitted by BS can be written as follows:

$$\mathbf{s} = \mathbf{F}_1 \mathbf{B}_1 \mathbf{d}. \tag{6.23}$$

The power constraint at BS can be expressed as $\|\mathbf{F}_1 \mathbf{B}_1\|_F^2 = P_1$, where P_1 denotes the total transmit power of BS. Then, the received signal at UAV relay is given as follows:

$$\begin{aligned} \mathbf{y}_{u,r} &= \mathbf{H}_1 \mathbf{s} + \mathbf{n}_1, \\ &= \mathbf{H}_1 \mathbf{F}_1 \mathbf{B}_1 \mathbf{d} + \mathbf{n}_1, \end{aligned} \tag{6.24}$$

where $\mathbf{n}_1 \in \mathbb{C}^{N_{u,r}}$ denotes the zero-mean complex circularly symmetric Gaussian noise vector at UAV relay with covariance matrix $\mathbb{E}\{\mathbf{n}_1 \mathbf{n}_1^H\} = \sigma_1^2 \mathbf{I}_{N_{u,r}} \in \mathbb{C}^{N_{u,r} \times N_{u,r}}$. Then, the received signal after RF combining at UAV relay is written as follows:

$$\tilde{\mathbf{y}}_{u,r} = \mathbf{F}_{u,r} \mathbf{H}_1 \mathbf{F}_1 \mathbf{B}_1 \mathbf{d} + \mathbf{F}_{u,r} \mathbf{n}_1. \tag{6.25}$$

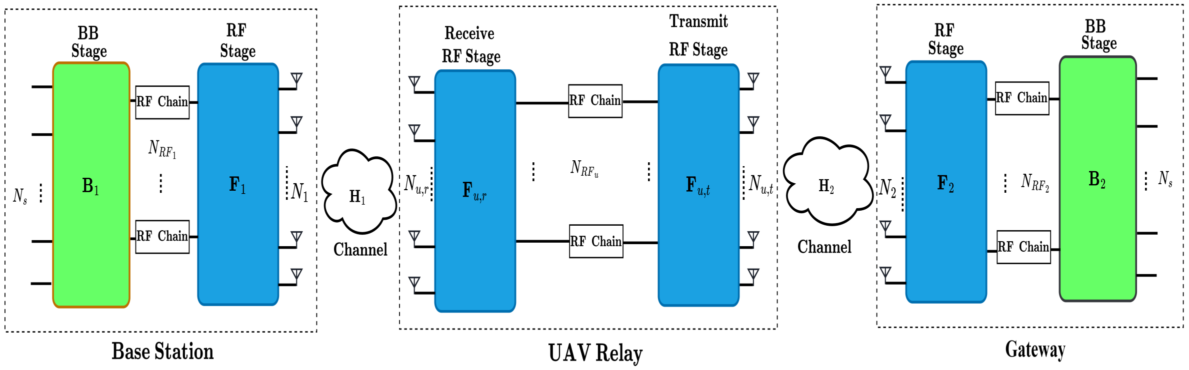

Figure 6.5. UAV-assisted mmWave mMIMO AF relaying architecture.

Ignoring the delay constraints, the transmit signal at UAV relay is given as follows:

$$\mathbf{y}_{u,t} = \mathbf{F}_{u,t}\mathbf{F}_{u,r}\mathbf{H}_1\mathbf{F}_1\mathbf{B}_1\mathbf{d} + \mathbf{F}_{u,t}\mathbf{F}_{u,r}\mathbf{n}_1. \tag{6.26}$$

The power constraint of tranmsitted signal at UAV relay can be expressed as $\|\mathbf{F}_{u,t}\mathbf{F}_{u,r}\|_F^2 = P_u$, where P_u denotes the total transmit power of UAV. The received signal at IoT gateway can be expressed as follows:

$$\mathbf{y}_d = \mathbf{H}_2\mathbf{F}_{u,t}\mathbf{F}_{u,r}\mathbf{H}_1\mathbf{F}_1\mathbf{B}_1\mathbf{d} + \mathbf{H}_2\mathbf{F}_{u,t}\mathbf{F}_{u,r}\mathbf{n}_1 + \mathbf{n}_2, \tag{6.27}$$

where $\mathbf{n}_2$ denotes the additive circular symmetric Gaussian noise such that $\mathbf{n}_2 \sim \mathcal{CN}(\mathbf{0}, \sigma_2^2\mathbf{I}_{N_2})$. After HBF at IoT gateway, the received signal can be written as follows:

$$\tilde{\mathbf{y}}_d = \underbrace{\mathbf{W}_2\mathbf{H}_2\mathbf{F}_{u,t}\mathbf{F}_{u,r}\mathbf{H}_1\mathbf{W}_1\mathbf{d}}_{\text{Desired Signal}} + \underbrace{\mathbf{W}_2\mathbf{H}_2\mathbf{F}_{u,t}\mathbf{F}_{u,r}\mathbf{n}_1}_{\text{UAV Relay Noise}} + \underbrace{\mathbf{W}_2\mathbf{n}_2}_{\text{Gateway Noise}}, \tag{6.28}$$

where $\mathbf{W}_1 = \mathbf{F}_1\mathbf{B}_1$ and $\mathbf{W}_2 = \mathbf{B}_2\mathbf{F}_2$. Then, the spectral efficiency can be calculated as:

$$\mathrm{R} = \frac{1}{2}\log_2\left|\mathbf{I}_{N_S} + \frac{1}{N_S}\mathbf{Q}_n^{-1}\left(\sqrt{P_uP_1}\mathbf{W}_2\mathbf{H}_2\mathbf{F}_{u,t}\mathbf{F}_{u,r}\mathbf{H}_1\mathbf{W}_1\right)\left(\sqrt{P_uP_1}\mathbf{W}_2\mathbf{H}_2\mathbf{F}_{u,t}\mathbf{F}_{u,r}\mathbf{H}_1\mathbf{W}_1\right)^H\right|. \tag{6.29}$$

where $\mathbf{Q}_n^{-1} = \sigma_n^2\Big[(\sqrt{P_u}\mathbf{W}_2\mathbf{H}_2\mathbf{F}_{u,t}\mathbf{F}_{u,r})(\sqrt{P_u}\mathbf{W}_2\mathbf{H}_2\mathbf{F}_{u,t}\mathbf{F}_{u,r})^H + \mathbf{W}_2\mathbf{W}_2^H\Big]^{-1}$ is the covariance matrix of Gaussian noise at UAV relay. For a UAV-assisted mMIMO IoT system, where the UAV is deployed at a fixed height h_u and relaying data to the gateway, the total achievable rate (AR) can be maximized by the joint optimization of $\mathbf{F}_1$, $\mathbf{B}_1$, $\mathbf{F}_{u,t}$, $\mathbf{F}_{u,r}$, $\mathbf{F}_2$, $\mathbf{B}_2$, and $\mathbf{x} = [x_o, y_o] \in \mathbb{R}^2$, where $\mathbf{x}$ represents UAV relay position, which is to be optimized within the given UAV flying span. Then, we can formulate the joint optimization problem as:

$$\begin{aligned}
&\max_{\{\mathbf{F}_1,\mathbf{B}_1,\mathbf{F}_{u,t},\mathbf{F}_{u,r},\mathbf{F}_2,\mathbf{B}_2,x_o,y_o\}} \mathrm{R}(\mathbf{F}_1,\mathbf{B}_1,\mathbf{F}_{u,t},\mathbf{F}_{u,r},\mathbf{F}_2,\mathbf{B}_2,x_o,y_o)\\
&\text{s.t. } C_1: \ |\mathbf{F}_{u,t}(i,j)| = \frac{1}{\sqrt{N_{u,t}}}, |\mathbf{F}_{u,r}(i,j)| = \frac{1}{\sqrt{N_{u,r}}}, \ \forall i,j,\\
&\quad C_2: \ |\mathbf{F}_1(i,j)| = \frac{1}{\sqrt{N_1}}, |\mathbf{F}_2(i,j)| = \frac{1}{\sqrt{N_2}}, \ \forall i,j,\\
&\quad C_3: \ \mathbb{E}\{\|\mathbf{s}\|_2^2\} \le P_1, \mathbb{E}\{\|\mathbf{y}_{u,t}\|_2^2\} \le P_u,\\
&\quad C_4: \ x_{\min} \le x_o \le x_{\max}, y_{\min} \le y_o \le y_{\max},
\end{aligned} \tag{6.30}$$

where C_1 and C_2 refer to the CM constraints due to the use of PSs for UAV and BS/gateway, respectively. C_3 indicates the transmit power constraint for UAV relay and BS, and C_4 implies UAV positioning within the given deployment region. Here, $[(x_{\min}, y_{\min}), (x_{\max}, y_{\max})]$ represents the UAV flying span in x-y plane. The optimization problem defined in (6.30) is non-convex and intractable. To solve this problem, we sequentially develop beamforming stages for BS, UAV and gateway based on arbitrary fixed UAV location to optimize $\{x_o, y_o\}$ using PSO. Then, based on optimal UAV relay position, we re-formulate RF and BB stages for BS and gateway as well as RF beamformer/combiner for UAV based on instantaneous channel matrices $\mathbf{H}_1$ and $\mathbf{H}_2$.

6.4.2 Joint Beamforming and UAV Positioning

To maximize the spectral efficiency (as given in (6.30)), we consider ABF for UAV relay, where we design both transmit and receive RF beamformer/combiner and optimize UAV location together with HBF (i.e., design of RF beamformer and BB stage) for BS and gateway. Since the optimization problem is intractable, we first design $\mathbf{F}_1, \mathbf{B}_1, \mathbf{F}_{u,t}, \mathbf{F}_{u,r}, \mathbf{F}_2, \mathbf{B}_2$ based on arbitrary fixed UAV location, and then re-formulate RF beamformers and baseband stages for optimal UAV location using PSO. Since SVD-based beamforming design is considered optimal for point-to-point mMIMO systems [164], therefore the design of HBF stages for BS and gateway can be found by minimizing the Frobenius norm of the difference between optimal unconstrained beamformers and the corresponding HBF stages as follows:

$$\begin{aligned}
&\min_{\{\mathbf{F}_i,\mathbf{B}_i\}} \quad \|\mathbf{F}_{\text{opt,i}} - \mathbf{F}_i\mathbf{B}_i\|_F\\
&\text{s.t.} \qquad C_2, C_3,
\end{aligned} \tag{6.31}$$

where $\mathbf{F}_{\text{opt,i}}$ is the unconstrained beamformer (combiner), which is derived from SVD of channel matrix between BS and UAV (between UAV and gateway). Using SVD, $\mathbf{H}_1$ can be written as follows:

$$\mathbf{H}_1 = \boldsymbol{\mathcal{Q}}_1 \mathbf{\Sigma_1} \boldsymbol{\mathcal{V}}_\mathbf{1}^\mathbf{H} \in \mathbb{C}^{\mathbf{N_{u,r}} \times \mathbf{N_1}}, \tag{6.32}$$

where $\boldsymbol{\mathcal{Q}}_1$ and $\boldsymbol{\mathcal{V}}_1$ are $N_{u,r} \times N_{u,r}$ and $N_1 \times N_1$ unitary matrices, respectively. $\mathbf{\Sigma}_1$ is a $N_{u,r} \times N_1$ rectangular diagonal matrix with non-negative real numbers on the diagonal. Then, the unconstrained optimal beamformer for BS is formulated as $\mathbf{F}_{\text{opt},1} = \boldsymbol{\mathcal{V}}_{1,1}$, where $\boldsymbol{\mathcal{V}}_1 = [\boldsymbol{\mathcal{V}}_{1,1} \boldsymbol{\mathcal{V}}_{1,2}] \in \mathbb{C}^{N_1 \times N_1}$ [164]. Using SVD, the channel matrix $\mathbf{H}_2$ can be written as follows:

$$\mathbf{H}_2 = \boldsymbol{\mathcal{Q}}_2 \mathbf{\Sigma_2} \boldsymbol{\mathcal{V}}_\mathbf{2}^\mathbf{H} \in \mathbb{C}^{\mathbf{N_2} \times \mathbf{N_{u,t}}}. \tag{6.33}$$

Then, the optimal uncostrained combiner for gateway can be formulated as $\mathbf{F}_{\text{opt},2} = \boldsymbol{\mathcal{V}}_{2,1}$, i.e., right singular vectors of $\mathbf{H}_2$. The HBF stages $\mathbf{F}_1, \mathbf{B}_1, \mathbf{F}_2, \mathbf{B}_2$ are designed using an OMP-based algorithmic solution, which is outlined in Algorithm 6.1. For UAV relay, we design transmit and receive RF beamformer and combiner based on angular location of UAV and gateway, respectively. Let $\boldsymbol{\psi}_n = [e^{j\upsilon_{1,n}}, e^{j\upsilon_{2,n}}, \ldots, e^{j\upsilon_{N_{u,r},n}}]^T \in \mathbb{C}^{N_{u,r}}$ is the receive phase vector, where $\upsilon_{m,n}$ is the phase angle of the $(m,n)-th$ entry of $\boldsymbol{\mathcal{Q}}_1$. Then, we can formulate the receive phase matrix $\mathbf{\Psi}_u^r$ as follows:

$$\mathbf{\Psi}_u^r = [\boldsymbol{\psi}_1, \boldsymbol{\psi}_2, \ldots, \boldsymbol{\psi}_{N_{u,r}}] \in \mathbb{C}^{N_{u,r} \times N_{u,r}}. \tag{6.34}$$

Comparing (6.32) and (6.34), we can see that each entry of ψ_n and $\mathbf{Q}_1(n)$ have the same phase angle. Using N_{RF_u} RF chains at UAV relay, the receive RF combiner can be formulated as:

$$\mathbf{F}_{u,r} = [\boldsymbol{\psi}_1, \boldsymbol{\psi}_2, \ldots, \boldsymbol{\psi}_{N_{RF_u}}]^T \in \mathbb{C}^{N_{RF_u} \times N_{u,r}}. \tag{6.35}$$

Following a similar approach, the transmit RF beamformer at UAV can be formulated by using SVD of $\mathbf{H}_2$. Then, the transmit phase matrix $\mathbf{\Psi}_u^t$ can be written as follows:

$$\mathbf{\Psi}_u^t = [\boldsymbol{\varphi}_1, \boldsymbol{\varphi}_2, \ldots, \boldsymbol{\varphi}_{N_{u,t}}] \in \mathbb{C}^{N_{u,t} \times N_{u,t}}, \tag{6.36}$$

where $\boldsymbol{\varphi}_n = [e^{j\varphi_{1,n}}, e^{j\varphi_{2,n}}, \ldots, e^{j\varphi_{N_{u,t},n}}]^T \in \mathbb{C}^{N_{u,t}}$ is the transmit phase vector, where $\varphi_{m,n}$ is the phase angle of the $(m,n)-th$ entry of $\boldsymbol{\mathcal{V}}_2$. Then, using N_{RF_u} RF chains at UAV relay, the transmit RF beamformer can be formulated as:

$$\mathbf{F}_{u,t} = [\boldsymbol{\varphi}_1, \boldsymbol{\varphi}_2, \ldots, \boldsymbol{\varphi}_{N_{RF_u}}] \in \mathbb{C}^{N_{u,t} \times N_{RF_u}}. \tag{6.37}$$

After the design of RF and BB stages, the optimization problem given in (6.30) can be reformulated as follows:

$$\begin{aligned} \max_{\{x_o, y_o\}} \quad & \mathrm{R}(x_o, y_o) \\ \text{s.t.} \quad & C_4 : x_{\min} \leq x_o \leq x_{\max}, y_{\min} \leq y_o \leq y_{\max}. \end{aligned} \tag{6.38}$$

The resulting optimization problem in (6.38) is still an NP hard and remains a computationally challenging task. Therefore, we propose a PSO-based algorithmic solution to optimize UAV position and sequentially update the RF and BB stages for BS, UAV, and gateway. Initially, Z particles are randomly placed in search space, each with its own position, velocity, and fitness value. Then, during t^{th} iteration, the position $\mathbf{X}_z^{(t)}$ and velocity $\mathbf{Y}_z^{(t)}$ of each z^{th} particle are updated as follows [163]:

$$\mathbf{X}_z^{(t+1)} = \mathbf{X}_z^{(t)} + \mathbf{Y}_z^{(t+1)}, \tag{6.39}$$

$$\mathbf{Y}_z^{(t+1)} = \omega \mathbf{Y}_z^{(t)} + \mu_1 \mathbf{C}_1^{(t)} (\mathbf{X}_{best}^{(t)} - \mathbf{X}_z^{(t)}) + \mu_2 \mathbf{C}_2^{(t)} (\mathbf{X}_{best,z}^{(t)} - \mathbf{X}_z^{(t)}), \tag{6.40}$$

where ω, μ_1, μ_2 are tuning parameters and $\mathbf{C}_1^{(t)}$ and $\mathbf{C}_2^{(t)}$ are the matrices with entries uniformly distributed in $[0, 1]$. Here, each z^{th} particle represents the candidate position of UAV and it iteratively updates its personal best $\mathbf{X}_{best,z}^{(t)}$ and global best $\mathbf{X}_{best}^{(t)}$ solution during a total of T iterations as follows:

$$\mathbf{X}_{best,z}^{(t)} = \underset{\mathbf{X}_z^{(t^*)}, \forall t^* = 0,1,\cdots,t}{\arg\max} \mathrm{R}(\mathbf{F}_1, \mathbf{B}_1, \mathbf{F}_{u,t}, \mathbf{F}_{u,r}, \mathbf{F}_2, \mathbf{B}_2, X_z^{(t^*)}), \tag{6.41}$$

$$\mathbf{X}_{best}^{(t)} = \underset{\mathbf{X}_{best,z}^{(t^*)}, \forall i = 0,1,\cdots,Z_p}{\arg\max} \mathrm{R}(\mathbf{F}_1, \mathbf{B}_1, \mathbf{F}_{u,t}, \mathbf{F}_{u,r}, \mathbf{F}_2, \mathbf{B}_2, X_{best,z}^{(t)}). \tag{6.42}$$

After T iterations, we assign $\mathbf{x} = \mathbf{X}_{best}^{(T)}$. Algorithm 6.2 summarizes the proposed beamforming and UAV deployment scheme.

6.5 Joint HBF and UAV Deployment in SU-mMIMO Systems: Decode-and-Forward (DF) Relaying

In this section, we propose a novel approach to optimize the performance of UAV relay systems in a dual-hop mMIMO communications network. By jointly optimizing the UAV location and HBF design, our approach maximizes the end-to-end throughput of a UAV-assisted mMIMO IoT communications system.

Algorithm 6.2 Joint Beamforming and UAV Positioning

```
1: **Input**: $Z, T$, $(\theta, \phi)$, $(x_1, y_1, z_1)$, $(x_2, y_2, z_2)$, $(x_u, y_u, z_u)$.
2: **Output**: $\mathbf{x}$, $\mathbf{F}_1, \mathbf{B}_1$, $\mathbf{F}_{u,t}$, $\mathbf{F}_{u,r}, \mathbf{F}_2, \mathbf{B}_2$.
3: **for** $i = 1:2$ **do**
4:     Compute $\mathbf{H}_i$ using (6.1).
5:     Find the unitary matrices $\boldsymbol{\mathcal{Q}}_i$ and $\boldsymbol{\mathcal{V}}_i$ using SVD.
6:     $\mathbf{F}_i = [\,]$, $\mathbf{F}_{res,i} = \mathbf{F}_{opt,i}$.
7:     **for** $j = 1 : N_{\text{RF}_i}$ **do**
8:         $\Upsilon_i = (\mathbf{A}_i)^T \mathbf{F}_{res,i}$.
9:         Find the index $k$ which maximizes $(\Upsilon_i \Upsilon_i^*)$.
10:        $\mathbf{F}_i = \left[\mathbf{F}_i \mid (\mathbf{A}_i^T)^{(k)}\right]$.
11:        $\mathbf{B}_i = \left(\mathbf{F}_i^H \mathbf{F}_i\right)^{-1} \mathbf{F}_i^H \mathbf{F}_{opt,i}$.
12:        $\mathbf{F}_{res,i} = \frac{\mathbf{F}_{opt,i} - \mathbf{F}_i \mathbf{B}_i}{\|\mathbf{F}_{opt,i} - \mathbf{F}_i \mathbf{B}_i\|_F}$.
13:    **end for**
14:    $\mathbf{B}_i = \sqrt{P_i} \frac{\mathbf{B}_i}{\|\mathbf{F}_i \mathbf{B}_i\|_F}$.
15: **end for**
16: **for** $n = 1 : N_{\text{RF}_u}$ **do**
17:     Calculate the phase of each entity of $\boldsymbol{\mathcal{Q}}_1$, $\boldsymbol{\mathcal{V}}_2$.
18:     Construct the phase vectors $\boldsymbol{\psi}_n$, $\boldsymbol{\varphi}_n$.
19: **end for**
20: Formulate $\boldsymbol{\Psi}_u^r$, $\boldsymbol{\Psi}_u^t$ via (6.34), (6.36).
21: Construct $\mathbf{F}_{u,r}$, $\mathbf{F}_{u,t}$ using $N_{\text{RF}_u}$ via (6.35), (6.37).
22: **for** $z = 1 : Z$ **do**
23:     Initialize the velocity as $\mathbf{Y}_z^{(0)} = \mathbf{0}$.
24:     Each entry of $\mathbf{X}_z^{(0)}$ is uniformly distributed in $[0, 1]$.
25:     Set the personal best $\mathbf{X}_{best,z}^{(0)} = \mathbf{X}_z^{(0)}$.
26: **end for**
27: Find the global best $\mathbf{X}_{best}^{(0)}$ as in (6.42).
28: **for** $t = 1 : T$ **do**
29:     **for** $z = 1 : Z$ **do**
30:         Update the velocity $\mathbf{Y}_z^{(t)}$ as in (6.40).
31:         Update the position $\mathbf{X}_z^{(t)}$ as in (6.39).
32:         Find the personal best $\mathbf{X}_{best,z}^{(t)}$ as in (6.41).
33:     **end for**
34:     Find the global best $\mathbf{X}_{best}^{(t)}$ as in (6.42).
35: **end for**
36: Update $\mathbf{F}_1, \mathbf{F}_2, \mathbf{B}_1, \mathbf{B}_2, \mathbf{F}_{u,t}, \mathbf{F}_{u,r}$ for $\mathbf{x}$ using steps 1-19.
```

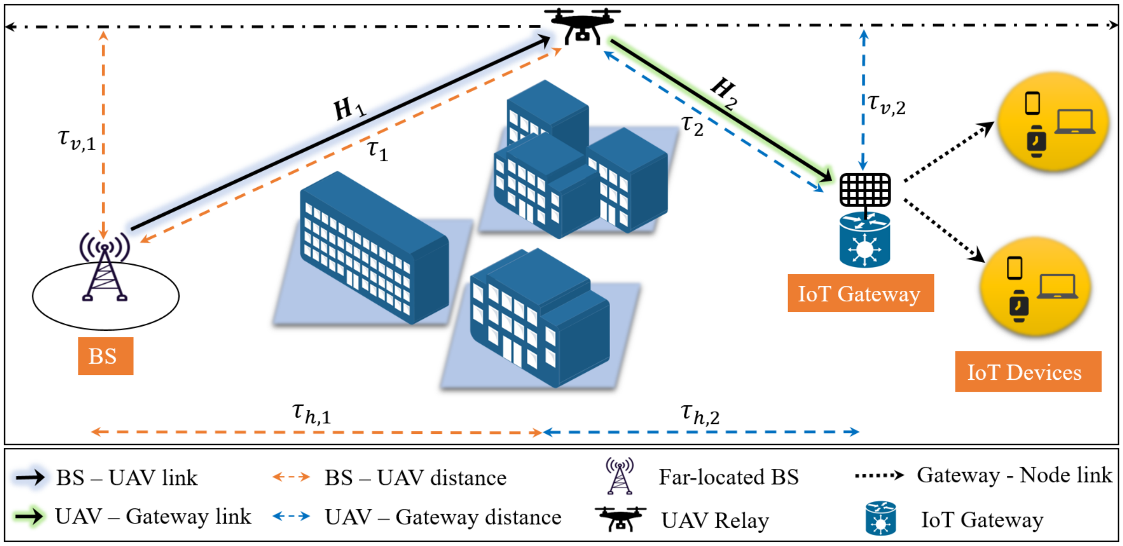

Figure 6.6. UAV-assisted mMIMO DF relaying.

6.5.1 System Model

We consider the case in which an IoT gateway is connected to various IoT devices via wire or wireless links. IoT devices and IoT gateway are located in a remote area, which is difficult to access directly by BS (eNodeB) due to obstacles (e.g., buildings, mountains., etc.), and UAV is used as a dual-hop DF relay to improve the situation as shown in Fig. 6.6. Unlike traditional static relaying, which uses fixed relay locations, we presumptively use a UAV as DF relay. In this chapter, we underline the potential of UAV relays in future mMIMO-enabled IoT systems with no direct link possible between BS and gateway. Let (x_1, y_1, z_1), (x_u, y_u, z_u) and (x_2, y_2, z_2) denote the locations of BS, UAV relay and gateway, respectively. Then, $\tau_{h,i} = \sqrt{(x_u - x_i)^2 + (y_u - y_i)^2}$ and $\tau_{v,i} = |z_u - z_i|$ are the horizontal and vertical distance between UAV & BS ($i = 1$) or UAV & gateway ($i = 2$), and $\tau_h = \sqrt{(x_1 - x_2)^2 + (y_1 - y_2)^2}$ is the horizontal distance between BS and gateway.

In the system model shown in Fig. 6.7, we consider BS is equipped with N_1 antennas, UAV relay with $N_{u,r}(N_{u,t})$ antennas for receiving (transmitting) signals and gateway with N_2 antennas. We consider HBF for all nodes (i.e., BS, UAV and gateway), where BS consists of a RF beamforming stage $\mathbf{F}_1 \in \mathbb{C}^{N_1 \times N_{RF_1}}$ and BB stage $\mathbf{B}_1$ $\mathbb{C}^{N_{RF_1} \times N_S}$. Here, N_S represents the data streams from BS and N_{RF_1} is the RF chains such that $N_S \leq N_{RF_1} \leq N_1$ to guarantee multi-stream transmission. We consider half-duplex (HD) DF relaying, whereas the use of full-duplex (FD) UAV relaying is left as our future work. During the first time slot, N_S data streams are transmitted through channel $\mathbf{H}_1 \in \mathbb{C}^{N_{u,r} \times N_1}$. Using $N_{u,r}$ antennas,

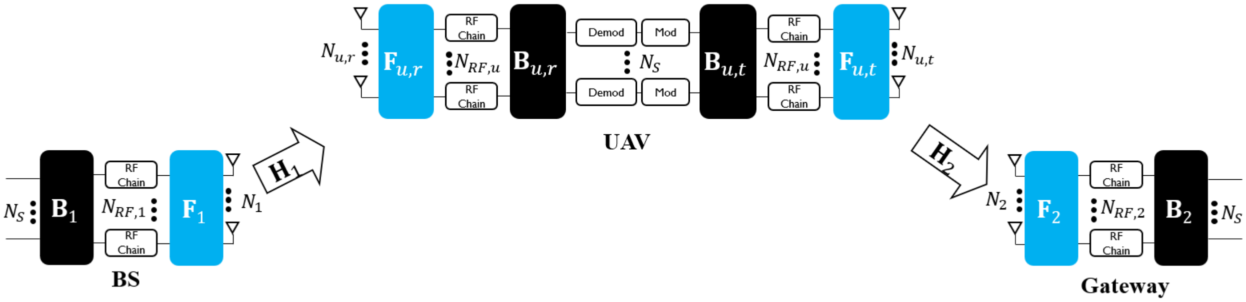

Figure 6.7. UAV-assisted mMIMO HBF system model.

UAV receives signals with RF stage $\mathbf{F}_{u,r} \in \mathbb{C}^{N_{RF_u} \times N_{u,r}}$ and BB stage $\mathbf{B}_{u,r} \in \mathbb{C}^{N_S \times N_{RF_u}}$. We assume UAV transmits the data in the second time slot using RF beamformer $\mathbf{F}_{u,t} \in \mathbb{C}^{N_{u,t} \times N_{RF_u}}$ and BB stage $\mathbf{B}_{u,t} \in \mathbb{C}^{N_{RF_u} \times N_S}$ through channel $\mathbf{H}_2 \in \mathbb{C}^{N_2 \times N_{u,t}}$. The received signal at gateway is processed through RF stage $\mathbf{F}_2 \in \mathbb{C}^{N_{RF_2} \times N_2}$ and BB stage $\mathbf{B}_2$ $\mathbb{C}^{N_S \times N_{RF_2}}$. Here, all RF beamforming/combining stages are implemented using phase shifters and thus, impose a constant-modulus (CM) constraint, i.e., $|\mathbf{F}_1(i,j)| = \frac{1}{\sqrt{N_1}}$, $|\mathbf{F}_{u,r}(i,j)| = \frac{1}{\sqrt{N_{u,r}}}$, $|\mathbf{F}_{u,t}(i,j)| = \frac{1}{\sqrt{N_{u,t}}}$, $|\mathbf{F}_2(i,j)| = \frac{1}{\sqrt{N_2}}$ $\forall i,j$. The design of HBF for UAV DF relaying reduces the number of RF chains from $N_{u,r}(N_{u,t})$ to N_{RF_u}, N_1 to N_{RF_1} and N_2 to N_{RF_2} while satisfying: 1) $N_S \leq N_{RF_1} \ll N_1$; 2) $N_S \leq N_{RF_u} \ll N_{u,r}(N_{u,t})$; and 3) $N_S \leq N_{RF_2} \ll N_2$. Considering the transmitted signal is $\mathbf{d} = [d_1, d_2, \ldots, d_{N_S}]^T$ with $\mathbb{E}\{\mathbf{d}\mathbf{d}^H\} = \mathbf{I}_{N_S} \in \mathbb{C}^{N_S \times N_S}$, then the signal transmitted by BS is given as follows:

$$\mathbf{s}_1 = \mathbf{F}_1 \mathbf{B}_1 \mathbf{d}. \tag{6.43}$$

The power constraint of the beamforming matrices can be expressed as $\|\mathbf{F}_1 \mathbf{B}_1\|_F^2 = P_T$, where P_T denotes the total transmit power of BS. Then, the received signal at UAV is given as follows:

$$\begin{aligned} \mathbf{y}_1 &= \mathbf{H}_1 \mathbf{s}_1 + \mathbf{n}_1, \\ &= \mathbf{H}_1 \mathbf{F}_1 \mathbf{B}_1 \mathbf{d} + \mathbf{n}_1, \end{aligned} \tag{6.44}$$

where $n_1 \in \mathbb{C}^{N_{u,r}}$ denotes the zero-mean complex circularly symmetric Gaussian noise vector at UAV relay with covariance matrix $\mathbb{E}\{\mathbf{n}_1 \mathbf{n}_1^H\} = \sigma_n^2 \mathbf{I}_{N_{u,r}} \in \mathbb{C}^{N_{u,r} \times N_{u,r}}$. Then, the received signal after baseband processing at UAV relay is written as:

$$\tilde{\mathbf{y}}_1 = \mathbf{B}_{u,r} \mathbf{F}_{u,r} \mathbf{H}_1 \mathbf{F}_1 \mathbf{B}_1 \mathbf{d} + \mathbf{B}_{u,r} \mathbf{F}_{u,r} \mathbf{n}_1. \tag{6.45}$$

UAV as DF relay uses $\tilde{\mathbf{y}}_1$ to decode the information and encodes it again for transmission in second time slot. Then, the signal transmitted by UAV is given as:

$$\mathbf{s}_2 = \mathbf{F}_{u,t}\mathbf{B}_{u,t}\hat{\mathbf{d}}, \tag{6.46}$$

where $\hat{\mathbf{d}}$ is the re-encoded signal at UAV relay. After transmitting via channel $\mathbf{H}_2$, the received signal at gateway can be written as follows:

$$\tilde{\mathbf{y}_2} = \mathbf{B}_2\mathbf{F}_2\mathbf{H}_2\mathbf{F}_{u,t}\mathbf{B}_{u,t}\hat{\mathbf{d}} + \mathbf{B}_2\mathbf{F}_2\mathbf{n}_2, \tag{6.47}$$

where $\mathbf{n}_2$ denotes the additive circular symmetric Gaussian noise such that $\mathbf{n}_2 \sim \mathcal{CN}(\mathbf{0}, \sigma_n^2\mathbf{I}_{N_2})$. Then, the achievable rate of first link (i.e., BS → UAV) is given as follows:

$$\mathrm{R}_1 = \log_2\left|\mathbf{I}_{N_S} + \mathbf{Q}_1^{-1}\mathbf{B}_{u,r}\boldsymbol{\mathcal{H}}_1\mathbf{B}_1\mathbf{B}_1^H\boldsymbol{\mathcal{H}}_1^H\mathbf{B}_{u,r}^H\right|, \tag{6.48}$$

where $\mathbf{Q}_1^{-1} = (\sigma_n^2\mathbf{B}_{u,r}\mathbf{F}_{u,r})^{-1}\mathbf{F}_{u,r}^H\mathbf{B}_{u,r}^H$ and $\boldsymbol{\mathcal{H}}_1 = \mathbf{F}_{u,r}\mathbf{H}_1\mathbf{F}_1$. Similarly, the achievable rate for the second link (i.e., UAV → gateway) is given as follows:

$$\mathrm{R}_2 = \log_2\left|\mathbf{I}_{N_S} + \mathbf{Q}_2^{-1}\mathbf{B}_2\boldsymbol{\mathcal{H}}_2\mathbf{B}_{u,t}\mathbf{B}_{u,t}^H\boldsymbol{\mathcal{H}}_2^H\mathbf{B}_2^H\right|, \tag{6.49}$$

where $\mathbf{Q}_2^{-1} = (\sigma_n^2\mathbf{B}_2\mathbf{F}_2)^{-1}\mathbf{F}_2{}^H\mathbf{B}_2^H$ and $\boldsymbol{\mathcal{H}}_2 = \mathbf{F}_2\mathbf{H}_2\mathbf{F}_{u,t}$. For a dual-hop mMIMO IoT system, where the UAV DF relay is deployed at a fixed height z_u and relaying data to gateway, the achievable rate can be maximized by the joint optimization of $\mathbf{F}_1$, $\mathbf{B}_1$, $\mathbf{F}_{u,t}$, $\mathbf{F}_{u,r}$, $\mathbf{B}_{u,t}$, $\mathbf{B}_{u,r}$, $\mathbf{F}_2$, $\mathbf{B}_2$ and $\tau_{h,1}$, where $\tau_{h,1}$ represents the horizontal distance between UAV and BS, which is to be optimized within the given UAV flying span. Then, we can formulate the optimization problem as:

$$\begin{aligned}
&\max_{\{\mathbf{F}_1,\mathbf{B}_1,\mathbf{F}_{u,t},\mathbf{B}_{u,t},\mathbf{F}_{u,r},\mathbf{B}_{u,r},\mathbf{F}_2,\mathbf{B}_2,\tau_{h,1}\}} \quad \frac{1}{2}\min(\mathrm{R}_1,\mathrm{R}_2)\\
&\text{s.t.} \quad C_1: \ |\mathbf{F}_{u,t}(i,j)| = \frac{1}{\sqrt{N_{u,t}}}, |\mathbf{F}_{u,r}(i,j)| = \frac{1}{\sqrt{N_{u,r}}}, \ \forall i,j,\\
&\qquad C_2: \ |\mathbf{F}_1(i,j)| = \frac{1}{\sqrt{N_1}}, |\mathbf{F}_2(i,j)| = \frac{1}{\sqrt{N_2}} \ \forall i,j,\\
&\qquad C_3: \ \mathbb{E}\{\|\mathbf{s}_1\|_2^2\} \le P_T, \mathbb{E}\{\|\mathbf{s}_2\|_2^2\} \le P_T,\\
&\qquad C_4: \ \tau_{h,\min} \le \tau_{h,1} \le \tau_{h,\max},
\end{aligned} \tag{6.50}$$

where C_1 and C_2 refers to the CM constraint due to the use of phase shifters for UAV, BS and gateway, respectively, C_3 indicates the transmit power constraint for UAV and BS, and C_4 implies UAV positioning within the given flying span. Here, $[\tau_{h,\min}, \tau_{h,\max}]$ represents the UAV DF relay deployment range in x-axis and y-axis. The optimization problem defined in (6.50) is non-convex and intractable. To solve this problem, we first develop HBF stages for BS, UAV and gateway based on arbitrary UAV location to optimize $\tau_{h,1}$ using PSO. Then, based on optimal UAV relay location, we re-design RF and BB beamforming stages.

6.5.2 Joint UAV Relay Positioning & Hybrid Beamforming

In this section, our objective is to jointly optimize the UAV relay location and hybrid beamforming to reduce the channel state information (CSI) overhead size while maximizing the throughput of a dual-hop UAV-assisted mMIMO IoT system. First, we design the RF stages $\mathbf{F}_1, \mathbf{F}_{u,r}, \mathbf{F}_{u,t}, \mathbf{F}_2$ based on the slow time-varying AoD and AoA. Then, the BB stages $\mathbf{B}_1, \mathbf{B}_{u,r}, \mathbf{B}_{u,t}, \mathbf{B}_2$ are developed by using SVD.

6.5.2.1 RF-Beamformers Design

We first define AoD and AoA supports as:

$$\text{AoD} = \Big\{\sin(\theta)\left[\cos(\phi), \sin(\phi)\right]\Big|\theta \in \boldsymbol{\theta}_t, \phi \in \boldsymbol{\phi}_t\Big\}, \tag{6.51}$$

$$\text{AoA} = \Big\{\sin(\theta)\left[\cos(\phi), \sin(\phi)\right]\Big|\theta \in \boldsymbol{\theta}_r, \phi \in \boldsymbol{\phi}_r\Big\}, \tag{6.52}$$

where $\boldsymbol{\theta}_i = \left[\theta_i - \delta_i^{\theta}, \theta_i + \delta_i^{\theta}\right]$ and $\boldsymbol{\phi}_i = \left[\phi_i - \delta_i^{\phi}, \phi_i + \delta_i^{\phi}\right]$ denote the azimuth and elevation angle supports, respectively. To exploit all degrees of freedom provided by the channel to maximize the transmit (receive) beamforming gain in either channel link, we consider selecting the columns of $\mathbf{F}_1(\mathbf{F}_{u,r})$ and $\mathbf{F}_{u,t}(\mathbf{F}_2)$ from the subspace spanned by $\mathbf{a}_t(\mathbf{a}_r)$ in first and second link, respectively $\Big($i.e., Span $\{\mathbf{F}_1, \mathbf{F}_{u,t}\} \subset$ Span $(\mathbf{a}_t)$ and Span $\{\mathbf{F}_{u,r}, \mathbf{F}_2\} \subset$ Span $(\mathbf{a}_r)\Big)$. Then, the transmit RF beamformers are constructed via transmit steering vector $\mathbf{e}_t(\theta, \phi) = \frac{1}{\mathcal{M}_t}\left[1, e^{j2\pi d \sin(\theta)\cos(\phi)}, \cdots, e^{j2\pi d(\mathcal{M}_{x,t}-1)\sin(\theta)\cos(\phi)}\right]^T \otimes \left[1, e^{j2\pi d \sin(\theta)\sin(\phi)}, \cdots, e^{j2\pi d(\mathcal{M}_{y,t}-1)\sin(\theta)\sin(\phi)}\right]^T$, where $\mathcal{M}_t = \{N_1, N_{u,t}\}$. We define N orthogonal steering vectors via generating the quantized angle-pairs as $\lambda_{x,t}^{u} = -1 + \frac{2u-1}{\mathcal{M}_{x,t}}$ for $u = 1, \cdots, \mathcal{M}_{x,t}$ and $\lambda_{y,t}^{k} = -1 + \frac{2k-1}{\mathcal{M}_{y,t}}$ for $k = 1, \cdots, \mathcal{M}_{y,t}$. The use of quantized angle-pairs minimizes the RF chain utilization while covering the complete AoD and AoA supports. Then, the quantized angle-pairs inside the AoD support satisfying (7.14) are obtained as:

$$(\lambda_{x,t}^{u}, \lambda_{y,t}^{k}) \;\Big|\; \sin(\theta)\cos(\phi) \in \boldsymbol{\lambda}_{x,t}^{u}, \sin(\theta)\sin(\phi) \in \boldsymbol{\lambda}_{y,t}^{k}, \tag{6.53}$$

where $\boldsymbol{\lambda}^u_{x,t} = \left[\lambda^u_{x,t} - \frac{1}{\mathcal{M}_{x,t}}, \lambda^u_{x,t} + \frac{1}{\mathcal{M}_{x,t}}\right]$ is the boundary of $\lambda^u_{x,t}$, and $\boldsymbol{\lambda}^k_{y,t} = \left[\lambda^k_{y,t} - \frac{1}{\mathcal{M}_{y,t}}, \lambda^k_{y,t} + \frac{1}{\mathcal{M}_{y,t}}\right]$ is the boundary of $\lambda^k_{y,t}$. By using (7.14) and (6.53), the transmit RF beamformers for BS and UAV are found as:

$$\mathbf{F}_1 = \left[\mathbf{e}_{\mathbf{t}}\left(\lambda^{u_1}_{x,t}, \lambda^{k_1}_{y,t}\right), \dots, \mathbf{e}_t\left(\lambda^{u_{N_{RF,1}}}_{x,t}, \lambda^{k_{N_{RF,1}}}_{y,t}\right)\right] \in \mathbb{C}^{N_1 \times N_{RF,1}} \tag{6.54}$$

$$\mathbf{F}_{u,t} = \left[\mathbf{e}_{\mathbf{t}}\left(\lambda^{u_1}_{x,t}, \lambda^{k_1}_{y,t}\right), \dots, \mathbf{e}_t\left(\lambda^{u_{N_{RF,u}}}_{x,t}, \lambda^{k_{N_{RF,u}}}_{y,t}\right)\right] \in \mathbb{C}^{N_{u,t} \times N_{RF,u}} \tag{6.55}$$

Following similar approach, the receive RF beamformers can be designed via receive steering vector $\mathbf{e}_r(\theta, \phi) = \frac{1}{\mathcal{M}_r}\left[1, e^{-j2\pi d \sin(\theta)\cos(\phi)}, \cdots, e^{-j2\pi d(\mathcal{M}_{x,r}-1)\sin(\theta)\cos(\phi)}\right]^T$ $\otimes \left[1, e^{-j2\pi d \sin(\theta)\sin(\phi)}, \cdots, e^{-j2\pi d(\mathcal{M}_{y,r}-1)\sin(\theta)\sin(\phi)}\right]^T$, where $\mathcal{M}_r = \{N_2, N_{u,r}\}$. Using quantized angle-pairs as $\lambda^u_{x,r} = -1 + \frac{2u-1}{\mathcal{M}_{x,r}}$ for $u = 1, \cdots, \mathcal{M}_{x,r}$ and $\lambda^k_{y,r} = -1 + \frac{2k-1}{\mathcal{M}_{y,r}}$ for $k = 1, \cdots, \mathcal{M}_{y,r}$, we can formulate the receive RF beamformers for U and D as:

$$\mathbf{F}_{u,r} = \left[\mathbf{e}_{\mathbf{r}}\left(\lambda^{u_1}_{x,r}, \lambda^{k_1}_{y,r}\right), \dots, \mathbf{e}_r\left(\lambda^{u_{N_{RF,u}}}_{x,r}, \lambda^{k_{N_{RF,u}}}_{y,r}\right)\right]^T \in \mathbb{C}^{N_{RF,u} \times N_{u,r}} \tag{6.56}$$

$$\mathbf{F}_2 = \left[\mathbf{e}_{\mathbf{r}}\left(\lambda^{u_1}_{x,r}, \lambda^{k_1}_{y,r}\right), \dots, \mathbf{e}_r\left(\lambda^{u_{N_{RF,1}}}_{x,r}, \lambda^{k_{N_{RF,1}}}_{y,r}\right)\right]^T \in \mathbb{C}^{N_2 \times N_{RF,2}}, \tag{6.57}$$

where the quantized angle-pairs inside the AoA support satisfying (7.15) are obtained as:

$$(\lambda^u_{x,r}, \lambda^k_{y,r}) \;\Big|\; \sin(\theta)\cos(\phi) \in \boldsymbol{\lambda}^u_{x,r}, \sin(\theta)\sin(\phi) \in \boldsymbol{\lambda}^k_{y,r}, \tag{6.58}$$

where $\boldsymbol{\lambda}^u_{x,r} = [\lambda^u_{x,r} - \frac{1}{\mathcal{M}_{x,r}}, \lambda^u_{x,r} + \frac{1}{\mathcal{M}_{x,r}}]$ is the boundary of $\lambda^u_{x,r}$, and $\boldsymbol{\lambda}^k_{y,r} = [\lambda^k_{y,r} - \frac{1}{\mathcal{M}_{y,r}}, \lambda^k_{y,r} + \frac{1}{\mathcal{M}_{y,r}}]$ is the boundary of $\lambda^k_{y,r}$.

6.5.2.2 BB-Stage Design and UAV Deployment

After designing the transmit and receive RF beamformers for BS, UAV and gateway, the effective channel matrices for first and second link as seen from the BB-stages are given as:

$$\boldsymbol{\mathcal{H}}_1 = \mathbf{F}_{u,r}\mathbf{H}_1\mathbf{F}_1 \tag{6.59}$$

$$\boldsymbol{\mathcal{H}}_2 = \mathbf{F}_2\mathbf{H}_2\mathbf{F}_{u,t} \tag{6.60}$$

By using SVD of effective channel matrix as $\boldsymbol{\mathcal{H}}_i = \mathbf{U}_i\boldsymbol{\Sigma}_i\mathbf{V}_i^H$, where $\mathbf{U}_i \in \mathbb{C}^{\mathcal{N}_{\mathcal{RF},\mathcal{R}} \times rank(\boldsymbol{\mathcal{H}}_i)}$ and $\mathbf{V}_i \in \mathbb{C}^{\mathcal{N}_{\mathcal{RF},\mathcal{T}} \times rank(\boldsymbol{\mathcal{H}}_i)}$ are tall unitary matrices and $\boldsymbol{\Sigma}_i$ is the diagonal matrix with singular values in the decreasing order. Here, $\mathcal{N}_{\mathcal{RF},\mathcal{T}} = \{N_{RF,1}, N_{RF,u}\}$ and $\mathcal{N}_{\mathcal{RF},\mathcal{R}} = \{N_{RF,2}, N_{RF,u}\}$ represents the transmit and receive RF chains, respectively. Assuming rank$(\boldsymbol{\mathcal{H}}_i) \geq N_S$, $\mathbf{V}_i$

can be partitioned as $\mathbf{V}_i = [\mathbf{V}_{i,1}, \mathbf{V}_{i,2}]$ with $\mathbf{V}_{i,1} \in \mathbb{C}^{\mathcal{N}_{\mathcal{RF},\mathcal{T}} \times N_S}$. Then, the optimal $\mathbf{B}_1$ and $\mathbf{B}_{u,r}$ in first link can be obtained as [165]:

$$\mathbf{B}_1 = \sqrt{\frac{P_T}{N_S}}\mathbf{V}_1, \qquad \mathbf{B}_{u,r} = \mathbf{U}_1^H. \tag{6.61}$$

Similarly, the optimal $\mathbf{B}_2$ and $\mathbf{B}_{u,t}$ in second link can be obtained as:

$$\mathbf{B}_{u,t} = \mathbf{U}_2^H, \qquad \mathbf{B}_2 = \sqrt{\frac{P_T}{N_S}}\mathbf{V}_2. \tag{6.62}$$

The design of RF and BB stages reduces the optimization problem given in (6.50) by satisfying the constraints $C_1 - C_3$. Then, the optimization problem can be reformulated as:

$$\begin{aligned} \max_{\tau_{h,1}} \quad & \frac{1}{2}\min\Big(\mathrm{R}_1, \mathrm{R}_2\Big) \\ \text{s.t.} \quad & C_4 : \tau_{h,\min} \leq \tau_{h,1} \leq \tau_{h,\max}. \end{aligned} \tag{6.63}$$

This resulting problem in (6.63) is still NP hard as the UAV location affects the channel state information, which, in turn, affects the beamforming design of the RF and BB stages. Therefore, the problem is combinatorial and involves a large search space, making it difficult to find the optimal solution within a reasonable time frame. Hence, we propose a PSO-based algorithmic solution for jointly optimizing UAV location and sequentially updating both RF and BB stages for BS, UAV, and gateway. The algorithm starts with a swarm of Z particles, each with its own position, velocity, and fitness value, which are randomly placed in search space. Let $\tau_i^{(t)}$ and $W_i^{(t)}$ be the position and velocity of i^{th} particle during t^{th} iteration, respectively. Then, during the iterations, both $\tau_i^{(t)}$ and $W_i^{(t)}$ of i^{th} particle are updated as follows:

$$W_i^{(t+1)} = \omega W_i^{(t)} + \mu_1 z_1(\tau_{best}^{(t)} - \tau_i^{(t)}) + \mu_2 z_2(\tau_{best,i}^{(t)} - \tau_i^{(t)}), \tag{6.64}$$

$$\tau_i^{(t+1)} = \tau_i^{(t)} + W_i^{(t+1)}, \tag{6.65}$$

where ω, μ_1, μ_2 are tuning parameters and z_1 and z_2 are random numbers between 0 and 1. Each i^{th} particle represents the candidate position of UAV and it iteratively updates its

Algorithm 6.3 Proposed Joint HBF and UAV Positioning and HBF Algorithm

```
1: Input: $Z_p, T$, $(\theta, \phi)$, $(x_1, y_1, z_1)$, $(x_2, y_2, z_2)$, $(x_u, y_u, z_u)$.
2: Output: $\tau_{h,1}$, $\mathbf{F}_1$, $\mathbf{B}_1$, $\mathbf{F}_{u,t}$, $\mathbf{B}_{u,t}$, $\mathbf{F}_{u,r}$, $\mathbf{B}_{u,r}$, $\mathbf{F}_2$, $\mathbf{B}_2$.
3: Formulate transmit RF beamformers using (6.54), (6.55).
4: Formulate receive RF beamformers using (6.56), (6.57).
5: Using (6.59), (6.60), form the unitary matrices $\mathbf{U}_i$ and $\mathbf{V}_i$.
6: Construct BB stages via (6.61), (6.62).
7: for $i = 1 : Z_p$ do
8:     Initialize the velocity as $W_i^{(0)} = 0$.
9:     Each entry of $\tau_i^{(0)}$ is uniformly distributed in $[0, 1]$.
10:    Set the personal best $\tau_{best,i}^{(0)} = \tau_i^{(0)}$.
11: end for
12: Find the global best $\tau_{best}^{(0)}$ as in (6.67).
13: for $t = 1 : T$ do
14:     for $i = 1 : Z_p$ do
15:         Update the velocity $W_i^{(t)}$ as in (6.64).
16:         Update the position $\tau_i^{(t)}$ as in (6.65).
17:         Find the personal best $\tau_{best,i}^{(t)}$ as in (6.66).
18:     end for
19:     Find the global best $\tau_{best}^{(t)}$ as in (6.67).
20: end for
21: Update $\mathbf{B}_1, \mathbf{B}_2, \mathbf{B}_{u,t}, \mathbf{B}_{u,r}$ for $\tau_{h,1}$ using steps 1-4.
```

personal best and global best solution during a total of T iterations as:

$$\tau_{best,i}^{(t)} = \underset{\tau_i^{(t^*)}, \forall t^*=0,1,\cdots,t}{\arg\max} \frac{1}{2} \min\left(\mathrm{R}_1(\tau_i^{(t^*)}), \mathrm{R}_2(\tau_i^{(t^*)})\right), \tag{6.66}$$

$$\tau_{best}^{(t)} = \underset{\tau_{best,i}^{(t^*)}, \forall i=0,1,\cdots,Z_p}{\arg\max} \frac{1}{2} \min\left(\mathrm{R}_1(\tau_{best,i}^{(t)}), \mathrm{R}_2(\tau_{best,i}^{(t)})\right). \tag{6.67}$$

After T iterations, we assign $\tau_{h,1} = \tau_{h,1,best}^{(T)}$. Algorithm 6.3 summarizes the proposed joint HBF and UAV relay deployment scheme. The developed algorithm is applicable to both fixed and movable nodes.

6.6 Joint HBF and UAV Deployment in MU-mMIMO Systems: Decode-and-Forward (DF) Relaying

In this section, we consider a UAV-assisted MU-mMIMO systems, where a DF relay in the form of a UAV facilitates the transmission of multiple data streams from BS to multiple IoT users. A joint optimization problem of HBF, UAV relay positioning, and power allocation (PA) to multiple IoT users to maximize the total achievable rate (AR) is investigated. The study adopts a geometry-based mmWave channel model for both links and proposes three different swarm intelligence-based algorithmic solutions to optimize: 1) UAV location with equal PA; 2) PA with fixed UAV location; and 3) joint PA with UAV deployment. The radio frequency (RF) stages are designed to reduce the number of RF chains based on the slow time-varying angular information, while the BB stages are designed using the reduced-dimension effective channel matrices. Then, a novel DL-based low-complexity joint hybrid beamforming, UAV location and power allocation optimization scheme (J-HBF-DLLPA) is proposed via fully-connected DNN, consisting of an offline training phase, and an online prediction of UAV location and optimal power values for maximizing the AR.

6.6.1 System Model

The present study delves into a challenging scenario where multiple IoT devices are connected to an IoT gateway through either wired or wireless links. This setup is situated in a remote area that is difficult to access directly by BS/eNodeB due to various obstacles such as buildings, mountains, etc. Then, a UAV is introduced as a dual-hop DF relay to access the IoT users, as depicted in Fig. 6.8. We assume that there is no direct link between BS and IoT devices due to severe blockage. In contrast to traditional static relaying, which relies on fixed relay locations, we investigate the potential of using UAVs as DF relays for future mMIMO-enabled IoT systems where direct link communication between BS and IoT node ends is not feasible. It is important to note that the algorithms proposed in Sections III and IV are not only limited to fixed/static node locations but can be applicable to movable nodes (i.e., dynamic environment). Let (x_b, y_b, z_b), (x_u, y_u, z_u) and (x_k, y_k, z_k) denote the locations of BS, UAV relay and k^{th} IoT node, respectively. We define the 3D distances for a

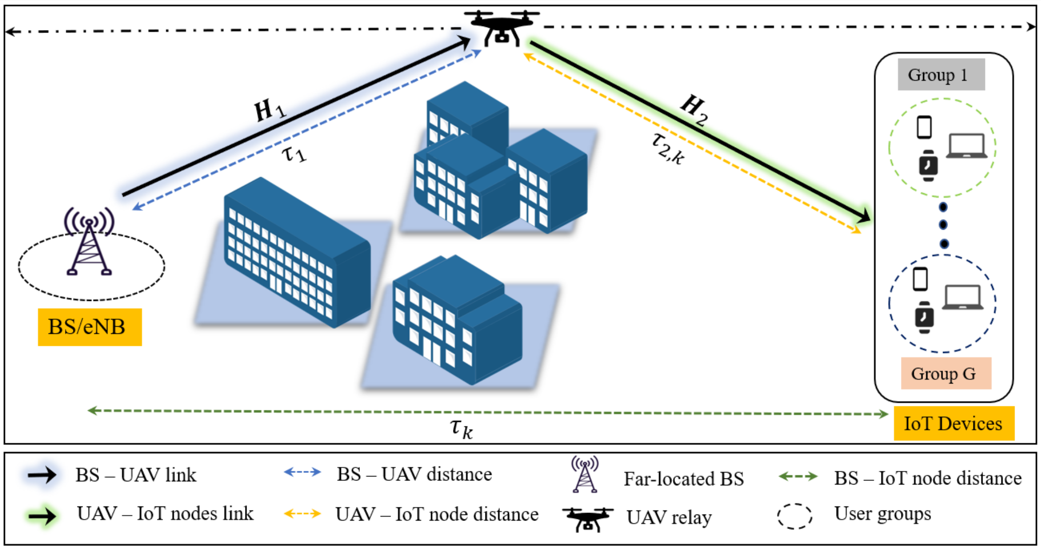

Figure 6.8. Network model of UAV-assisted relaying in MU-mMIMO IoT systems.

UAV-assisted mmWave MU-mMIMO IoT system as follows:

$$\begin{aligned}\tau_1 &= \sqrt{(x_u - x_b)^2 + (y_u - y_b)^2 + (z_u - z_b)^2} \\ \tau_{2,k} &= \sqrt{(x_u - x_k)^2 + (y_u - y_k)^2 + (z_u - z_k)^2} \\ \tau_k &= \sqrt{(x_b - x_k)^2 + (y_b - y_k)^2 + (z_b - z_k)^2}\end{aligned} \tag{6.68}$$

where τ_1, $\tau_{2,k}$ and τ_k are the 3D distance between UAV & BS, between UAV and k^{th} IoT node, and between BS and k^{th} IoT node, respectively.

In the system model shown in Fig. 6.9, we consider BS equipped with N_T antennas, UAV relay with N_r antennas for receiving and N_t antennas to serve K single-antenna IoT nodes clustered in G groups, where g^{th} group has K_g IoT nodes such that $K = \sum_{g=1}^{G} K_g$. For the downlink transmission of $N_S = K$ data streams, we consider HBF for BS and UAV, where BS consists of a RF beamforming stage $\mathbf{F}_b \in \mathbb{C}^{N_T \times N_{RF_b}}$ and BB stage $\mathbf{B}_b \in \mathbb{C}^{N_{RF_b} \times K}$. Here, N_{RF_b} is the RF chains such that $N_S \leq N_{RF_b} \leq N_T$ to guarantee multi-stream transmission. We consider half-duplex (HD) DF relaying, whereas the use of full-duplex (FD) UAV relaying is left as our future work. During the first time slot, K data streams are transmitted through channel $\mathbf{H}_1 \in \mathbb{C}^{N_r \times N_T}$. Using N_r antennas, UAV receives signals with RF stage $\mathbf{F}_{u,r} \in \mathbb{C}^{N_{RF_u} \times N_r}$ and BB stage $\mathbf{B}_{u,r} \in \mathbb{C}^{K \times N_{RF_u}}$. We assume UAV transmits the data in the second time slot using RF beamformer $\mathbf{F}_{u,t} = \left[\mathbf{f}_{u,t,1}, \cdots, \mathbf{f}_{u,t,N_{RF_u}}\right] \in \mathbb{C}^{N_t \times N_{RF_u}}$, BB stage $\mathbf{B}_{u,t} = [\mathbf{b}_{u,t,1}, \cdots, \mathbf{b}_{u,t,K}] \in \mathbb{C}^{N_{RF_u} \times K}$, and MU PA matrix $\mathbf{P} = \text{diag}(\sqrt{p_1}, \ldots, \sqrt{p_K}) \in \mathbb{C}^{K \times K}$ through channel $\mathbf{H}_2 \in \mathbb{C}^{K \times N_t}$, where p_k reflects the allocated power to k^{th} user. The

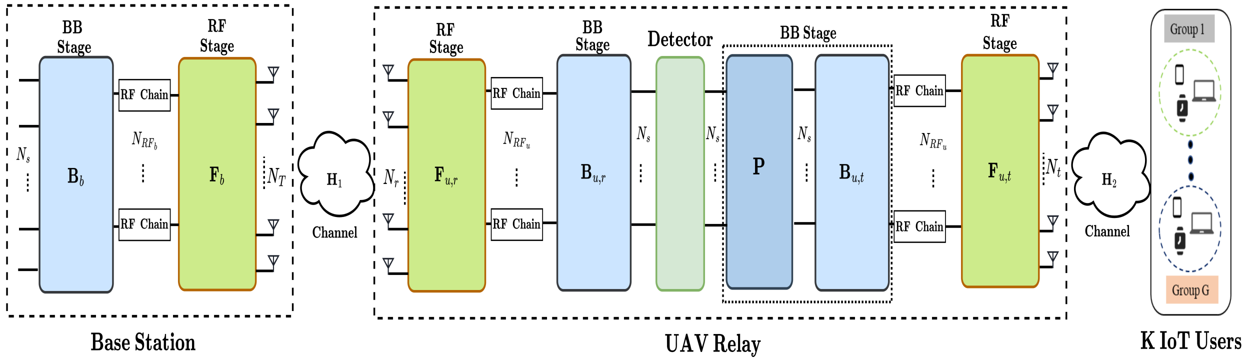

Figure 6.9. System model of UAV-assisted DF relaying in MU-mMIMO IoT networks.

implementation of all RF beamforming/combining stages involves the use of PSs and thus, impose a CM constraint, i.e., $|\mathbf{F}_b(i,j)| = \frac{1}{\sqrt{N_T}}$, $|\mathbf{F}_{u,r}(i,j)| = \frac{1}{\sqrt{N_r}}$, $|\mathbf{F}_{u,t}(i,j)| = \frac{1}{\sqrt{N_t}}$ $\forall i,j$. The design of HBF greatly reduces the number of RF chains, for instance, from N_T RF chains to N_{RF_b} for BS, from $N_t(N_r)$ RF chains to N_{RF_u} for UAV whilst satisfying: 1) $K \leq N_{RF_b} \ll N_T$; and 2) $K \leq N_{RF_u} \ll N_r(N_t)$. For the data signal $\mathbf{d} = [d_1, d_2, \ldots, d_K]^T$ with $\mathbb{E}\{\mathbf{d}\mathbf{d}^H\} = \mathbf{I}_K$ $\in \mathbb{C}^{K \times K}$, the signal transmitted by BS is given as follows:

$$\mathbf{s}_1 = \mathbf{F}_b \mathbf{B}_b \mathbf{d}. \tag{6.69}$$

Let P_T be the total transmit power of BS. The design of $\mathbf{F}_b$ and $\mathbf{B}_b$ satisfies the power constraint $\|\mathbf{F}_b \mathbf{B}_b\|_F^2 = P_T$. Then, the received signal at UAV is:

$$\begin{aligned} \mathbf{y}_1 &= \mathbf{H}_1 \mathbf{s}_1 + \mathbf{n}_1, \\ &= \mathbf{H}_1 \mathbf{F}_b \mathbf{B}_b \mathbf{d} + \mathbf{n}_1, \end{aligned} \tag{6.70}$$

where $n_1 \in \mathbb{C}^{N_r}$ denotes the zero-mean complex circularly symmetric Gaussian noise vector at UAV relay with covariance matrix $\mathbb{E}\{\mathbf{n}_1 \mathbf{n}_1^H\} = \sigma_n^2 \mathbf{I}_{N_r} \in \mathbb{C}^{N_r \times N_r}$. Subsequently, the received signal after baseband processing at UAV relay is written as follows:

$$\tilde{\mathbf{y}}_1 = \mathbf{B}_{u,r} \mathbf{F}_{u,r} \mathbf{H}_1 \mathbf{F}_b \mathbf{B}_b \mathbf{d} + \mathbf{B}_{u,r} \mathbf{F}_{u,r} \mathbf{n}_1. \tag{6.71}$$

UAV as DF relay uses $\tilde{\mathbf{y}}_1$ to decode the information and re-encodes it for transmission in second time slot. Then, the signal transmitted by UAV is:

$$\mathbf{s}_2 = \mathbf{F}_{u,t} \mathbf{B}_{u,t} \mathbf{P} \hat{\mathbf{d}}, \tag{6.72}$$

where $\hat{\mathbf{d}}$ is the re-encoded signal at UAV relay. After transmitting via channel $\mathbf{H}_2$, the received signal at k^{th} IoT node in g^{th} group can be written as:

$$\begin{aligned} y_{g_k} &= \mathbf{h}_{2,g_k}^T \mathbf{s}_2 + n_{2,g_k} = \mathbf{h}_{2,g_k}^T \mathbf{F}_{u,t} \mathbf{B}_{u,t} \mathbf{P} \hat{\mathbf{d}} + n_{g_k}, \\ &= \underbrace{\sqrt{p_{g_k}} \mathbf{h}_{2,g_k}^T \mathbf{F}_{u,t} \mathbf{b}_{u,t,g_k} \hat{d}_{g_k}}_{\text{Desired Signal}} + \underbrace{\sum_{\hat{k} \neq k}^{K_g} \sqrt{p_{g_{\hat{k}}}} \mathbf{h}_{2,g_k}^T \mathbf{F}_{u,t} \mathbf{b}_{u,t,g_{\hat{k}}} \hat{d}_{g_{\hat{k}}}}_{\text{Intra-group interference}} \\ &+ \underbrace{\sum_{q \neq g}^{G} \sum_{\hat{k}=1}^{K_g} \sqrt{p_{q_{\hat{k}}}} \mathbf{h}_{2,g_k}^T \mathbf{F}_{u,t} \mathbf{b}_{u,t,q_{\hat{k}}} \hat{d}_{q_{\hat{k}}}}_{\text{Inter-group interference}} + \underbrace{n_{g_k}}_{\text{Noise}}, \end{aligned} \tag{6.73}$$

where $g_k = k + \sum_{g'=1}^{g-1} K_{g'}$ is the IoT node index, $\mathbf{h}_{2,g_k} \in \mathbb{C}^{N_t}$ is the channel vector between UAV and corresponding IoT node, and $\mathbf{n}_{g_k}$ denotes the complex circular symmetric Gaussian noise distributed as $\mathcal{CN}(\mathbf{0}, \sigma^2)$. Then, the achievable rate of first link (between BS and UAV) is:

$$\mathrm{R}_1 \left(\mathbf{F}_b, \mathbf{B}_b, \mathbf{F}_{u,r}, \mathbf{B}_{u,r} \right) = \log_2 \left| \mathbf{I}_K + \mathbf{Q}_1^{-1} \mathbf{B}_{u,r} \boldsymbol{\mathcal{H}}_1 \mathbf{B}_b \mathbf{B}_b^H \boldsymbol{\mathcal{H}}_1^H \mathbf{B}_{u,r}^H \right|, \tag{6.74}$$

where $\mathbf{Q}_1^{-1} = (\sigma_n^2 \mathbf{B}_{u,r} \mathbf{F}_{u,r})^{-1} \mathbf{F}_{u,r}^H \mathbf{B}_{u,r}^H$ and $\boldsymbol{\mathcal{H}}_1 = \mathbf{F}_{u,r} \mathbf{H}_1 \mathbf{F}_b$. Similarly, the total AR for the second link (between UAV and multiple IoT nodes) is based on the instantaneous SINR, which is given as:

$$\mathrm{SINR}_{g_k} = \frac{p_{g_k} |\mathbf{h}_{2,k}^H \mathbf{F}_{u,t} \mathbf{b}_{u,t,g_k}|^2}{\sum_{\hat{k} \neq k}^{K_g} p_{g_{\hat{k}}} |\mathbf{h}_{2,k}^H \mathbf{F}_{u,t} \mathbf{b}_{u,t,g_{\hat{k}}}|^2 + \sum_{q \neq g}^{G} \sum_{\hat{k} \neq k}^{K_g} p_{q_{\hat{k}}} |\mathbf{h}_{2,k}^H \mathbf{F}_{u,t} \mathbf{b}_{u,t,q_{\hat{k}}}|^2 + \sigma^2}. \tag{6.75}$$

By using the instantaneous SINR, the ergodic sum-rate capacity of the second link R_2 for the UAV-assisted mmWave MU-mMIMO IoT systems can be written as:

$$\mathrm{R}_2 \left(\mathbf{F}_{u,t}, \mathbf{B}_{u,t}, \mathbf{P}, x_u, y_u \right) = \mathbb{E} \left\{ \sum_{g=1}^{G} \sum_{k=1}^{K_g} \mathbb{E}[\log_2(1 + \mathrm{SINR}_{g_k})] \right\}. \tag{6.76}$$

6.6.2 Problem Formulation

Considering the UAV is positioned at a fixed height z_u, and operates as DF relay, the total AR can be maximized by the joint optimization of the beamforming stages $\mathbf{F}_b$, $\mathbf{B}_b$, $\mathbf{F}_{u,t}$, $\mathbf{F}_{u,r}$, $\mathbf{B}_{u,t}$ and $\mathbf{B}_{u,r}$ with optimal PA matrix $\mathbf{P}$ and UAV positioning $\mathbf{x}_o = [x_o, y_o]^T \in \mathbb{R}^2$. Here, $\mathbf{x}_o$ represents the 2-D UAV deployment in a given flying span. Then, we can formulate the optimization problem as follows:

$$\begin{aligned}
&\max_{\{\mathbf{F}_b,\mathbf{B}_b,\mathbf{F}_{u,t},\mathbf{B}_{u,t},\mathbf{F}_{u,r},\mathbf{B}_{u,r},\mathbf{P},\mathbf{x}_o\}} \quad \mathrm{R}_T\\
&\text{s.t.} \quad C_1: \ |\mathbf{F}_{u,t}(i,j)| = \frac{1}{\sqrt{N_t}}, |\mathbf{F}_{u,r}(i,j)| = \frac{1}{\sqrt{N_r}}, \ \forall i,j,\\
&\qquad C_2: \ |\mathbf{F}_b(i,j)| = \frac{1}{\sqrt{N_T}}, \ \forall i,j,\\
&\qquad C_3: \ \mathbb{E}\{\|\mathbf{s}_1\|_2^2\} \leq P_T,\\
&\qquad C_4: \ \mathbb{E}\{\|\mathbf{s}_2\|_2^2\} = \textstyle\sum_{k=1}^{K} p_k \mathbf{b}_{u,t,k}^H \mathbf{F}_{u,t}^H \mathbf{F}_{u,t} \mathbf{b}_{u,t,k} \leq P_T,\\
&\qquad C_5: \ p_k \geq 0, \ \forall k,\\
&\qquad C_6: \ \mathbf{x}_{\min} \leq \mathbf{x}_o \leq \mathbf{x}_{\max},
\end{aligned} \tag{6.77}$$

where $\mathrm{R}_T = \frac{1}{2}\min(\mathrm{R}_1, \mathrm{R}_2)$ is the total transmission rate from BS to multiple IoT devices under DF protocol, C_1 and C_2 refers to the CM constraint due to the use of PSs for UAV and BS, respectively, C_3 and C_4 represents the transmit power constraint for BS and UAV, respectively, C_5 is the non-negative allocated power to each IoT node, and C_6 implies UAV deployment within the given flying span. Here, $[\mathbf{x}_{\min}, \mathbf{x}_{\max}] = [(x_{\min}, y_{\min}), (x_{\max}, y_{\max})]$ represents the UAV deployment range in 2-D space. The optimization problem defined in (6.77) is non-convex and intractable due to the following reason: 1) the CM constraint at each RF stage; and 2) fractional programming variables are entangled with each other. To solve this challenging problem, we propose three different PSO-based algorithmic solutions in Section 6.6.3, which can achieve a near-optimal solution in finding optimal PA $\mathbf{P}$ and UAV deployment $\mathbf{x}_o$. Then, in Section IV, we introduce a novel low-complexity DL-based solution, which can reduce the runtime while providing similar performance to proposed PSO-based solutions.

6.6.3 Joint HBF, PA and UAV Location Optimization

In this section, our objectives are to reduce the CSI overhead and the number of RF chains, while mitigating the inter-user interference to maximize the total achievable rate of a dual-hop UAV-assisted MU-mMIMO IoT systems. In this regard, we consider the joint optimization of the UAV location, PA to multiple IoT users, and HBF design for BS and UAV. Since the optimization problem is intractable, we first design $\mathbf{F}_b, \mathbf{B}_b, \mathbf{F}_{u,t}, \mathbf{F}_{u,r}, \mathbf{B}_{u,t}, \mathbf{B}_{u,r}$ based on some fixed UAV location, and then re-formulate RF and BB stages for the optimal UAV location as well as adjusting the allocated power in the

MU PA block $\mathbf{P}$ by using three different algorithmic schemes: 1) optimal PA for fixed UAV location; 2) UAV location optimization for equal PA; and 3) joint UAV location optimization and optimal PA.

6.6.3.1 RF-Beamformer Design

The design of RF stages $\mathbf{F}_b, \mathbf{F}_{u,r}, \mathbf{F}_{u,t}$ intends to maximize the beamforming gain for the desired signals expressed in (6.71) and (6.73). We design the RF stages $\mathbf{F}_b, \mathbf{F}_{u,r}, \mathbf{F}_{u,t}$ based on the slow time-varying AoD and AoA. By using (6.1), the effective channel for first link can be written as follows:

$$\boldsymbol{\mathcal{H}}_1 = \mathbf{F}_{u,r}\mathbf{H}_1\mathbf{F}_b = \mathbf{F}_{u,r}\boldsymbol{A}_1^{(r)}\mathbf{Z}_1\boldsymbol{A}_1^{(t)}\mathbf{F}_b \tag{6.78}$$

To maximize the transmit (receive) beamforming gain and exploit all degrees of freedom (DoF) provided by the first channel, the columns of $\mathbf{F}_b(\mathbf{F}_{u,r})$ should belong to the subspace spanned by $\mathbf{A}_1^{(t)}(\mathbf{A}_1^{(r)})$. Thus, we should satisfy $\text{Span}\left(\mathbf{F}_b\right) \subset \text{Span}(\mathbf{A}_1^{(t)})$ and $\text{Span}\left(\mathbf{F}_{\text{u,r}}\right) \subset \text{Span}(\mathbf{A}_1^{(r)})$. Here, it is worthwhile to mention that the transmit (receive) phase response matrix $\mathbf{A}_1^{(t)}(\mathbf{A}_1^{(r)})$ is a function of slow time-varying AoD(AOA) information. Thus, the AoD and AoA supports for first channel are defined as follows:

$$\text{AoD} = \Big\{\sin(\theta)[\cos(\phi), \sin(\phi)]\Big|\theta \in \boldsymbol{\theta}_1^{(t)}, \phi \in \boldsymbol{\phi}_1^{(t)}\Big\}, \tag{6.79}$$

$$\text{AoA} = \Big\{\sin(\theta)[\cos(\phi), \sin(\phi)]\Big|\theta \in \boldsymbol{\theta}_1^{(r)}, \phi \in \boldsymbol{\phi}_1^{(r)}\Big\}, \tag{6.80}$$

where $\boldsymbol{\theta}_1^{(t)} = \cup_{c=1}^{C}[\theta_{1,c}^{(t)} - \delta_{1,c}^{(t)\theta}, \theta_{1,c}^{(t)} + \delta_{1,c}^{(t)\theta}]$ and $\boldsymbol{\phi}_1^{(t)} = \cup_{c=1}^{C}[\phi_{1,c}^{(t)} - \delta_{1,c}^{(t)\phi}, \phi_{1,c}^{(t)} + \delta_{1,c}^{(t)\phi}]$ denote the azimuth and elevation AOD supports of first channel, respectively. Similarly, $\boldsymbol{\theta}_1^{(r)} = \cup_{c=1}^{C}\left[\theta_{1,c}^{(r)} - \delta_{1,c}^{(r)\theta}, \theta_{1,c}^{(r)} + \delta_{1,c}^{(r)\theta}\right]$ and $\boldsymbol{\phi}_1^{(r)} = \cup_{c=1}^{C}\left[\phi_{1,c}^{(r)} - \delta_{1,c}^{(r)\phi}, \phi_{1,c}^{(r)} + \delta_{1,c}^{(r)\phi}\right]$ represent the azimuth and elevation AoA supports of the channel between BS and UAV, respectively. Then, the transmit RF beamformer $\mathbf{F}_b$ is constructed via transmit steering vector as follows:

$$\begin{aligned}\mathbf{e}_b^{(t)}\left(\theta, \phi\right) = \frac{1}{\sqrt{N_{x,T}}}\Big[1, e^{j2\pi d\sin(\theta)\cos(\phi)}, \cdots, e^{j2\pi d\left(N_{x,T}-1\right)\sin(\theta)\cos(\phi)}\Big]^T \otimes \\ \frac{1}{\sqrt{N_{y,T}}}\Big[1, e^{j2\pi d\sin(\theta)\sin(\phi)}, \cdots, e^{j2\pi d\left(N_{y,T}-1\right)\sin(\theta)\sin(\phi)}\Big]^T.\end{aligned} \tag{6.81}$$

To reduce the RF chains utilization while covering the complete AoD and AoA supports, we define the quantized angle-pairs as: $\lambda_{x,b}^{n(t)} = -1 + \frac{2n-1}{N_{x,T}}$ for $n = 1, \cdots, N_{x,T}$ and $\lambda_{y,b}^{k(t)} = -1 + \frac{2k-1}{N_{y,T}}$ for $k = 1, \cdots, N_{y,T}$. Here, $N_{x,T}$ and $N_{y,T}$ are the antenna elements along x and y axis, respectively. Then, the quantized angle-pairs inside the AoD support satisfying (6.79) are obtained as:

$$(\lambda_{x,b}^{n(t)}, \lambda_{y,b}^{k(t)}) \,\Big|\, \sin(\theta)\cos(\phi) \in \boldsymbol{\lambda}_{x,b}^{n(t)}, \sin(\theta)\sin(\phi) \in \boldsymbol{\lambda}_{y,b}^{k(t)}, \tag{6.82}$$

where $\boldsymbol{\lambda}_{x,b}^{n(t)} = \Big[\lambda_{x,b}^{n(t)} - \frac{1}{N_{x,T}}, \lambda_{x,b}^{n(t)} + \frac{1}{N_{y,T}}\Big]$ is the boundary of $\lambda_{x,b}^{n(t)}$, and $\boldsymbol{\lambda}_{y,b}^{k(t)} = \Big[\lambda_{y,b}^{k(t)} - \frac{1}{N_{y,T}}, \lambda_{y,b}^{k(t)} + \frac{1}{N_{y,T}}\Big]$ is the boundary of $\lambda_{y,b}^{k(t)}$. By using (6.79) and (6.82), $\mathbf{F}_b$ can be written in the form of transmit steering vector as:

$$\mathbf{F}_b = \Big[\mathbf{e}_b^{(t)}\Big(\lambda_{x,b}^{n_1(t)}, \lambda_{y,b}^{k_1(t)}\Big), \cdots, \mathbf{e}_b^{(t)}\Big(\lambda_{x,b}^{n_{N_{RF_b}}(t)}, \lambda_{y,b}^{k_{N_{RF_b}}(t)}\Big)\Big] \in \mathbb{C}^{N_T \times N_{RF_b}}. \tag{6.83}$$

Following similar approach, we can design the UAV receive RF stage via receive steering vector as follows:

$$\begin{aligned}\mathbf{e}_u^{(r)}(\theta, \phi) = \frac{1}{\sqrt{N_{x,r}}}&[1, e^{-j2\pi d \sin(\theta)\cos(\phi)}, \cdots, e^{-j2\pi d(N_{x,r}-1)\sin(\theta)\cos(\phi)}]^T \otimes \\ &\frac{1}{\sqrt{N_{y,r}}}[1, e^{-j2\pi d \sin(\theta)\sin(\phi)}, \cdots, e^{-j2\pi d(N_{y,r}-1)\sin(\theta)\sin(\phi)}]^T.\end{aligned} \tag{6.84}$$

Using quantized angle-pairs as $\lambda_{x,u}^{n(r)} = -1 + \frac{2n-1}{N_{x,r}}$ for $n = 1, \cdots, N_{x,r}$ and $\lambda_{y,u}^{k(r)} = -1 + \frac{2k-1}{N_{y,r}}$ for $k = 1, \cdots, N_{y,r}$, the UAV receive RF stage can be formulated as:

$$\mathbf{F}_{u,r} = \Big[\mathbf{e}_u^{(r)}\Big(\lambda_{x,u}^{n_1(r)}, \lambda_{y,u}^{k_1(r)}\Big), \cdots, \mathbf{e}_u^{(r)}\Big(\lambda_{x,u}^{n_{N_{RF_u}}(r)}, \lambda_{y,u}^{k_{N_{RF_u}}(r)}\Big)\Big]^T \in \mathbb{C}^{N_{RF_u} \times N_r}, \tag{6.85}$$

where the quantized angle-pairs to provide AoA support while satisfying (7.15) are obtained as:

$$(\lambda_{x,u}^{n(r)}, \lambda_{y,u}^{k(r)}) \,\Big|\, \sin(\theta)\cos(\phi) \in \boldsymbol{\lambda}_{x,u}^{n(r)}, \sin(\theta)\sin(\phi) \in \boldsymbol{\lambda}_{y,u}^{k(r)}, \tag{6.86}$$

where $\boldsymbol{\lambda}_{x,u}^{n(r)} = \Big[\lambda_{x,u}^{n(r)} - \frac{1}{N_{x,r}}, \lambda_{x,u}^{n(r)} + \frac{1}{N_{x,r}}\Big]$ is the boundary of $\lambda_{x,u}^{n(r)}$, and $\boldsymbol{\lambda}_{y,u}^{k(r)} = \Big[\lambda_{y,u}^{k(r)} - \frac{1}{N_{y,r}}, \lambda_{y,u}^{k(r)} + \frac{1}{N_{y,r}}\Big]$ is the boundary of $\lambda_{y,u}^{k(r)}$. After the design of $\mathbf{F}_b, \mathbf{F}_{u,r}$ RF stages, the UAV transmit RF stage is designed to support K IoT users, which are clustered into G groups based on their AoD information. Here, each group g contains K_g number of IoT users such that $K = \sum_{g=1}^{G} K_g$. The index $g_k = \sum_{g'=1}^{g-1} K_{g'} + k$ is used to denote the k^{th} IoT user in group g. According to the user groups, we design G different sub-blocks for the UAV transmit RF stage as $\mathbf{F}_{u,t} = [\mathbf{F}_{u,t,1}, \mathbf{F}_{u,t,2}, \cdots, \mathbf{F}_{u,t,G}] \in \mathbb{C}^{N_t \times N_{RF_u}}$, where $\mathbf{F}_{u,t,g} \in \mathbb{C}^{N_t \times N_{RF_{u,g}}}$ denotes the RF beamfomer for group g such that $N_{RF_u} = \sum_{g=1}^{G} N_{RF_{u,g}}$. Then, $\boldsymbol{\mathcal{H}}_2 = \mathbf{H}_2\mathbf{F}_{u,t} \in \mathbb{C}^{K \times N_{RF_u}}$ is the reduced-size effective channel matrix seen from UAV transmit baseband stage $\mathbf{B}_{u,t}$. By defining $\mathbf{H}_2 = \left[\mathbf{H}_{2,1}^T, \cdots, \mathbf{H}_{2,G}^T\right]^T \in \mathbb{C}^{K \times N_t}$, the effective channel matrix for second link can be expressed as:

$$\boldsymbol{\mathcal{H}}_2 = \begin{bmatrix} \mathbf{H}_{2,1}\mathbf{F}_{u,t,1} & \mathbf{H}_{2,1}\mathbf{F}_{u,t,2} & \dots & \mathbf{H}_{2,1}\mathbf{F}_{u,t,G} \\ \mathbf{H}_{2,2}\mathbf{F}_{u,t,1} & \mathbf{H}_{2,2}\mathbf{F}_{u,t,2} & \dots & \mathbf{H}_{2,2}\mathbf{F}_{u,t,G} \\ \vdots & \vdots & \ddots & \vdots \\ \mathbf{H}_{2,G}\mathbf{F}_{u,t,1} & \mathbf{H}_{2,G}\mathbf{F}_{u,t,2} & \dots & \mathbf{H}_{2,G}\mathbf{F}_{u,t,G} \end{bmatrix}, \tag{6.87}$$

where the diagonal block-matrix $\boldsymbol{\mathcal{H}}_{2,g} = \mathbf{H}_{2,g}\mathbf{F}_{u,t,g} = \mathbf{Z}_{2,g}\mathbf{A}_{2,g}\mathbf{F}_{u,t}$ is the effective channel matrix for group g and the off-diagonal block-matrix $\boldsymbol{\mathcal{H}}_{2,\hat{g}} = \mathbf{H}_{2,g}\mathbf{F}_{u,t,g} = \mathbf{Z}_{2,\hat{g}}\mathbf{A}_{2,\hat{g}}\mathbf{F}_{u,t}$ is the effective interference channel matrix between groups g and $\hat{g}, \forall \hat{g} \neq g$. The RF beamformer matrices are designed to eliminate inter-group interference as:

$$\mathbf{A}_{2,\hat{g}}\mathbf{F}_{u,t,g} \approx 0, \ \forall \hat{g} \neq g \ \text{ and } \ \hat{g}, g = 1, \cdots, G. \tag{6.88}$$

To design $\mathbf{F}_{u,t}$, which can satisfy the above zero condition, the columns of $\mathbf{F}_{u,t,g}$ should belong to the intersection of the null spaces of $\mathbf{A}_{2,\hat{g}}$, i.e., Span $(\mathbf{F}_{u,t,g}) \subset \cap_{\hat{g} \neq g} \mathrm{Null}\,(\mathbf{A}_{2,\hat{g}})$. Moreover, in order to maximize the beamforming gain, the columns of $\mathbf{F}_{u,t,g}$ should belong to the subspace spanned by $\mathbf{A}_{2,g}$, i.e., $\mathrm{Span}\,(\mathbf{F}_{u,t,g}) \subset \mathrm{Span}\,(\mathbf{A}_{2,g})$. Thus, the intersection of $\mathrm{Span}\,(\mathbf{A}_{2,g})$ and $\mathrm{Null}\,(\mathbf{A}_{2,\hat{g}})\,, \forall \hat{g} \neq g$, should not be empty to obtain the RF beamformer matrix satisfying the above conditions. Similar to the design $\mathbf{F}_b$, the AoD support of the group g can be expressed as the union of AoD supports for all IoT user in the corresponding group as:

$$\mathrm{AoD}_g = \left\{\sin(\theta)[\cos(\phi), \sin(\phi)] \middle| \theta \in \boldsymbol{\theta}_{2,g}, \phi \in \boldsymbol{\phi}_{2.g}\right\}, \tag{6.89}$$

where $\boldsymbol{\theta}_{2,g} = \left[\theta_{2,g}^{\min}, \theta_{2,g}^{\max}\right] = \left[\min_{2,g_k,\hat{g}} \theta_{2,g_k,\hat{g}}, \max_{2,g_k,\hat{g}} \theta_{2,g_k,\hat{g}}\right]$ is the elevation angle support for group g and $\boldsymbol{\phi}_{2.g} = \left[\phi_{2,g}^{\min}, \phi_{2,g}^{\max}\right] = \left[\min_{2,g_k,\hat{g}} \phi_{2,g_k,\hat{g}}, \max_{2,g_k,\hat{g}} \phi_{2,g_k,\hat{g}}\right]$ is the azimuth angle support for group g. To achieve Span $(\mathbf{F}_{u,t,g}) \subset \mathrm{Span}\,(\mathbf{A}_{2,g})$, the columns of the UAV transmit RF beamformer for the group g can be constructed as:

$$\mathbf{F}_{u,t,g} = \{\mathbf{e}_u^{(t)}\,(\varphi, \vartheta) \,\big|\, (\varphi, \vartheta) \in \mathrm{AoD}_g\}, \tag{6.90}$$

where $\varphi = \sin\theta\cos\phi$ and $\vartheta = \sin\theta\sin\phi$ represent the beam directions for the UAV transmit steering vector for uniform rectangular array (URA), which is defined as follows:

$$\mathbf{e}_u^{(t)}(\varphi, \vartheta) = \mathbf{e}_{x,u}^{(t)}(\varphi) \otimes \mathbf{e}_{y,u}^{(t)}(\vartheta). \tag{6.91}$$

Then, we can construct the UAV transmit RF beamformer for each group g based on the quantized angle-pairs as:

$$\begin{aligned}\mathbf{F}_{u,t,g} = \Big[&\mathbf{e}_u^{(t)}(\lambda_{x,u}^{n_1(t)}, \lambda_{y,u}^{k_1(t)}), \cdots, \\ &\cdots, \mathbf{e}_u^{(t)}(\lambda_{x,u}^{n_{N_{RF_{u,g}}}(t)}, \lambda_{y,u}^{k_{N_{RF_{u,g}}}(t)})\Big] \in \mathbb{C}^{N_t \times N_{RF_{u,g}}},\end{aligned} \tag{6.92}$$

where $\boldsymbol{\lambda}_{x,u}^{n_i(t)} = \left[\lambda_{x,u}^{n_i(t)} - \frac{1}{N_{x,t}}, \lambda_{x,u}^{n_i(t)} + \frac{1}{N_{x,t}}\right]$ is the boundary of $\lambda_{x,u}^{n_i(t)}$, and $\boldsymbol{\lambda}_{y,u}^{k_i(t)} = \left[\lambda_{y,u}^{k_i(t)} - \frac{1}{N_{y,t}}, \lambda_{y,u}^{k_i(t)} + \frac{1}{N_{y,t}}\right]$ is the boundary of $\lambda_{y,u}^{k_i(t)}$. The BS and UAV RF-stage designs do not require the fast time-varying instantaneous CSI and it is only based on the slow time-varying AoD/AoA information. Particularly, the design of BS and UAV RF beamformers require only four angular parameters, which are the mean of elevation and azimuth AoD (AoA) and their angular spread.

6.6.3.2 BB-Stage Design

After designing the RF beamforming stages, we design the BB stages $\mathbf{B}_b$ and $\mathbf{B}_{u,r}^{(m)}$ based on the effective channel matrix $\boldsymbol{\mathcal{H}}_1$ (as given in (6.78)). By using singular value decomposition (SVD), we can write:

$$\boldsymbol{\mathcal{H}}_1 = \mathbf{U}_1 \boldsymbol{\Sigma}_1 \mathbf{V}_1^H, \tag{6.93}$$

where $\mathbf{U}_1 \in \mathbb{C}^{N_{RF_u} \times rank(\boldsymbol{\mathcal{H}}_1)}$ and $\mathbf{V}_1 \in \mathbb{C}^{N_{RF_b} \times rank(\boldsymbol{\mathcal{H}}_1)}$ are tall unitary matrices and $\boldsymbol{\Sigma}_1$ is the diagonal matrix with singular values in the decreasing order such that $\boldsymbol{\Sigma}_1 = \text{diag}(\sigma_1^2, \cdots, \sigma_{rank(\boldsymbol{\mathcal{H}}_1)}^2) \in \mathbb{C}^{rank(\boldsymbol{\mathcal{H}}_1) \times rank(\boldsymbol{\mathcal{H}}_1)}$. Assuming $\text{rank}(\boldsymbol{\mathcal{H}}_1) \geq K$, $\mathbf{V}_1$ can be partitioned as $\mathbf{V}_1 = [\mathbf{V}_{1,1}, \mathbf{V}_{1,2}]$ with $\mathbf{V}_{1,1} \in \mathbb{C}^{N_{RF_b} \times K}$. Then, the BB stages $\mathbf{B}_b$ and $\mathbf{B}_{u,r}$ for BS and UAV can be obtained as follows [165]:

$$\mathbf{B}_b = \sqrt{\frac{P_T}{K}} \mathbf{V}_1 \in \mathbb{C}^{N_{RF_b} \times K}, \tag{6.94}$$

$$\mathbf{B}_{u,r} = \mathbf{U}_1^H \in \mathbb{C}^{K \times N_{RF_u}}. \tag{6.95}$$

Similarly, the reduced-size effective CSI $\boldsymbol{\mathcal{H}}_2$ given in (6.87) is employed for the UAV transmit BB stage design. We consider joint-group-processing (JGP) technique as designed in [90, 98, 166]. The design of BB stage $\mathbf{B}_{u,t}$ not only reduces the intra-group interference but also mitigate the residual inter-group interference remaining after RF beamformer design. By applying the RZF technique, $\mathbf{B}_{u,t}$ is defined as follows:

$$\mathbf{B}_{u,t} = (\boldsymbol{\mathcal{H}}_2^H \boldsymbol{\mathcal{H}}_2 + \beta N_{RF_u} \mathbf{I}_{N_{RF_u}})^{-1} \boldsymbol{\mathcal{H}}_2^H \in \mathbb{C}^{N_{RF_u} \times K}, \tag{6.96}$$

where $\beta = \frac{\sigma^2}{P_T}$ is the regularization parameter and $\mathbf{I}_{N_{RF_u}} \in \mathbb{C}^{N_{RF_u} \times N_{RF_u}}$. The power constraint (i.e., C_4 in (6.77)) will be adjusted by designing multi-user PA block $\mathbf{P}$ in Section 6.6.3.3.

6.6.3.3 UAV Deployment and Multi-User Power Allocation

After the formulation of RF beamformers $\mathbf{F}_b$, $\mathbf{F}_{u,r}$, $\mathbf{F}_{u,t}$ and BB stages $\mathbf{B}_b$, $\mathbf{B}_{u,t}$, $\mathbf{B}_{u,r}$, the optimization problem for maximum achievable rate can be formulated as follows:

$$\begin{aligned} \max_{\{\mathbf{P}, \mathbf{x}_o\}} \quad & \mathrm{R}_T(\mathbf{F}_b, \mathbf{B}_b, \mathbf{F}_{u,t}, \mathbf{B}_{u,t}, \mathbf{F}_{u,r}, \mathbf{B}_{u,r}, \mathbf{P}, \mathbf{x}_u) \\ \text{s.t.} \quad & C_4: \ \mathbb{E}\{\|\mathbf{s}_2\|_2^2\} = \textstyle\sum_{k=1}^K p_k \mathbf{b}_{u,t,k}^H \mathbf{F}_{u,t}^H \mathbf{F}_{u,t} \mathbf{b}_{u,t,k} \leq P_T, \\ & C_5: \ p_k \geq 0, \ \forall k, \\ & C_6: \ \mathbf{x}_{\min} \leq \mathbf{x}_o \leq \mathbf{x}_{\max}, \end{aligned} \tag{6.97}$$

where R_T is defined in (6.77). Even though the CM constraints for the RF beamformers and transmit power constraint for BS (i.e., C_1, C_2 and C_3 given in (6.77)) are satisfied via the RF and BB stages developed in Section 6.6.3.1 and 6.6.3.2, the updated optimization problem in (6.97) is still non-convex due to the joint dependence of both the allocated powers p_k, and the UAV location $\mathbf{x}_o = [x_o, y_o]^T$ on the SINR expression in (6.75), which is used in the sum-rate R_2 calculation as given in (6.76). To overcome this challenge, we propose different PSO-based algorithmic solutions, which employ multiple agents, called particles, to explore the search space of objective function given in (6.97). Initially, Z_p particles are randomly placed in search space, where each particle communicates with other particles to share their personal best solution and update the current global best solution for the objective function. The particles then move iteratively for T iterations to reach the global optimum solution. Our PSO-based algorithms rely on two components, deterministic and stochastic, to guide the motion of the particles. The deterministic component utilizes knowledge from global and personal best solutions, while the stochastic component involves random movements. The proposed PSO-based algorithmic schemes are as follows: 1) optimal PA for fixed UAV location; 2) UAV positioning for equal PA; and 3) joint UAV positioning and optimal PA.

6.6.3.3.1 Optimal PA for Fixed UAV Location In this problem, we allocate optimal MU power values $\mathbf{P}$ for a fixed UAV location $\mathbf{x}_u$. Then, the i^{th} particle at the t^{th} iteration represents an instance of the PA matrix as follows:

$$\mathbf{P}_i^{(t)} = \operatorname{diag}(\sqrt{p_{1,i}^{(t)}}, \cdots, \sqrt{p_{K,i}^{(t)}}) \in \mathbb{R}^{K \times K}, \tag{6.98}$$

where, $i = 1, \cdots, Z_p$ and $t = 0, 1, \cdots, T$ are the particle index and iteration index, respectively. The objective function $R_T(\mathbf{F}_b, \mathbf{B}_b, \mathbf{F}_{u,t}, \mathbf{B}_{u,t}, \mathbf{F}_{u,r}, \mathbf{B}_{u,r}, \mathbf{P}_i^{(t)}, \mathbf{x}_u)$ is calculated after evaluating the personal best and communicating for the global best solutions for each i^{th} particle. The particles move from $\mathbf{P}_i^{(t)}$ to $\mathbf{P}_i^{(t+1)}$ until the maximum number of iterations is reached. To satisfy the transmit power constraints C_4 and C_5 given in (6.97), we define the following:

$$\kappa_i^{(t)} = \sqrt{\frac{P_T}{\mathbb{E}\left\{ \left\| \mathbf{F}_{u,t}\mathbf{B}_{u,t}\hat{\mathbf{P}}_i^{(t)}\hat{\mathbf{d}} \right\|_2^2 \right\}}} \overset{(a)}{=} \sqrt{\frac{P_T}{\sum_{k=1}^{K} \hat{p}_{k,i}^{(t)} \mathbf{b}_{u,t,k}^H \mathbf{b}_{u,t,k}}}, \tag{6.99}$$

where (a) follows the unitary property of UAV transmit beamformer (i.e., $\mathbf{F}_{u,t}^H \mathbf{F}_{u,t} = \mathbf{I}_{N_{RF_u}}$). The normalized PA matrix is given as: $\hat{\mathbf{P}}_i^{(t)} = \operatorname{diag}(\sqrt{\hat{p}_{1,i}^{(t)}}, \cdots, \sqrt{\hat{p}_{K,i}^{(t)}}) \in \mathbb{R}^{K \times K}$ with $\hat{p}_{k,i}^{(t)} \in [0, 1]$. Here, $\mathbf{P}_i^{(t)}$ satisfies the transmit power constraints for any $\hat{\mathbf{P}}_i^{(t)}$ by defining $\mathbf{P}_i^{(t)} = \kappa_i^{(t)} \hat{\mathbf{P}}_i^{(t)}$. The PSO-based optimal PA solution is defined by two variables: the position $\hat{\mathbf{P}}_i^{(t)} \in \mathbb{R}^{K \times K}$ and velocity $\mathbf{W}_i^{(t)} \in \mathbb{R}^{K \times K}$. Initially, the diagonal entries of $\hat{\mathbf{P}}_i^{(0)}$ are uniformly distributed over the range $[0, 1]$, while the velocity is set as $\mathbf{W}_i^{(0)} = 0$. During the iterations, the velocity and position matrices of i^{th} particle are updated as follows:

$$\mathbf{W}_i^{(t+1)} = \gamma_1 \mathbf{Y}_1^{(t)} (\hat{\mathbf{P}}_{\text{best}}^{(t)} - \hat{\mathbf{P}}_i^{(t)}) + \gamma_2 \mathbf{Y}_2^{(t)} (\hat{\mathbf{P}}_{\text{best},i}^{(t)} - \hat{\mathbf{P}}_i^{(t)}) + \gamma_3^{(t)} \mathbf{W}_i^{(t)}, \tag{6.100}$$

$$\hat{\mathbf{P}}_i^{(t+1)} = \operatorname{clip}(\hat{\mathbf{P}}_i^{(t)} + \operatorname{clip}(\mathbf{W}_i^{(t+1)}, [w_{\min}, w_{\max}]), [0, 1]), \tag{6.101}$$

where γ_1 and γ_2 are the learning parameters for the global best $\mathbf{P}_{best}^{(t)}$ and the personal best $\mathbf{P}_{\text{best},i}^{(t)}, \gamma_3^{(t)} = \mu - \frac{t}{T}(\mu_u - \mu_l)$ is the inertia parameters with the upper bound μ_u and lower bound μ_l for decreasing the velocity as the number of iterations increases, $\mathbf{Y}_1^{(t)}$ and $\mathbf{Y}_2^{(t)}$ are the random diagonal matrices with the uniformly distributed entries over $[0, 1]$, $w_{\min}$ and $w_{\max}$ denote the minimum and maximum acceptable velocity for the particles, respectively. Here, clip $(x, [a, b]) = \max(a, \min(x, b))$ is used to prevent exceeding the maximum/minimum acceptable velocity and normalized power. Then, at t^{th} iteration, the personal best of the

Algorithm 6.4 Proposed Joint HBF and Optimal PA for Fixed UAV Location (J-HBF-PSOPA-FL) Algorithm

```
Input: $Z, T$, $(\theta, \phi)$, $(x_1, y_1, z_1)$, $(x_u, y_u, z_u)$.
Output: $\mathbf{P}$, $\mathbf{F}_b$, $\mathbf{B}_b$, $\mathbf{F}_{u,t}$, $\mathbf{B}_{u,t}$, $\mathbf{F}_{u,r}$, $\mathbf{B}_{u,r}$.
Formulate BS RF and BB stages using (6.54), (6.94).
Formulate UAV receive HBF stages using (6.56), (6.95).
Construct UAV transmit HBF stages via (6.92), (6.96).
for $i = 1 : Z$ do
    Initialize the velocity as $\mathbf{W}_i^{(0)} = \mathbf{0}$.
    Each entry of $\hat{\mathbf{P}}_i^{(0)}$ is uniformly distributed in $[0, 1]$.
    Set the personal best $\hat{\mathbf{P}}_{\text{best},i}^{(0)} = \hat{\mathbf{P}}_i^{(0)}$.
end for
Find the global best $\hat{\mathbf{P}}_{\text{best}}^{(0)}$ as in (6.103).
for $t = 1 : T$ do
    for $i = 1 : Z$ do
        Update the velocity $\mathbf{W}_i^{(t)}$ as in (6.100).
        Update the position $\hat{\mathbf{P}}_i^{(t)}$ as in (6.101).
        Find the personal best $\hat{\mathbf{P}}_{\text{best},i}^{(t)}$ as in (6.102).
    end for
    Find the global best $\hat{\mathbf{P}}_{\text{best}}^{(t)}$ as in (6.103).
end for
$\mathbf{P} = \kappa_{\text{best}}^{(T)} \hat{\mathbf{P}}_{\text{best}}^{(T)}$
```

i^{th} particle and the global best over Z_p particles are respectively obtained as follows:

$$\hat{\mathbf{P}}_{\text{best},i}^{(t)} = \underset{\hat{\mathbf{P}}_i^{(t^*)}, \forall t^*=0,1,\cdots,t}{\arg\max} \; R_T(\mathbf{F}_b, \mathbf{B}_b, \mathbf{F}_{u,t}, \mathbf{B}_{u,t}, \mathbf{F}_{u,r}, \mathbf{B}_{u,r}, \kappa_i^{(t^*)} \hat{\mathbf{P}}_i^{(t^*)}, \mathbf{x}_u), \tag{6.102}$$

$$\hat{\mathbf{P}}_{best}^{(t)} = \underset{\hat{\mathbf{P}}_{\text{best},i}^{(t)}, \forall i=0,1,\cdots,Z_p}{\arg\max} \; R_T(\mathbf{F}_b, \mathbf{B}_b, \mathbf{F}_{u,t}, \mathbf{B}_{u,t}, \mathbf{F}_{u,r}, \mathbf{B}_{u,r}, \kappa_{\text{best},i}^{(t)} \hat{\mathbf{P}}_{\text{best},i}^{(t)}, \mathbf{x}_u), \tag{6.103}$$

Finally, the multi-user PA matrix can be derived as follows:

$$\mathbf{P} = \kappa_{\text{best}}^{(T)} \hat{\mathbf{P}}_{\text{best}}^{(T)}, \tag{6.104}$$

where $\kappa_{\text{best}}^{(t)}$ can be calculated by substituting $\hat{\mathbf{P}}_{\text{best}}^{(T)}$ into (6.99). The summary of the proposed PSO-based optimal PA for fixed UAV location with HBF is outlined in Algorithm 6.4.

6.6.3.3.2 UAV Positioning for Equal PA In this problem, we optimize UAV location $\mathbf{x}_u = [x_u, y_u]^T$ in a given deployment span for fixed MU PA matrix $\mathbf{P}$, which is defined as:

$$\mathbf{P} = \varepsilon \mathbf{I}_K \in \mathbb{C}^{K \times K}, \tag{6.105}$$

where ε is the normalization factor used to satisfy the power constraints C_4, C_5, and can be written as follows:

$$\varepsilon = \sqrt{\frac{P_T}{\mathrm{tr}\, \mathbb{E}\{\hat{\mathbf{d}} \boldsymbol{\mathcal{H}}_2^H \mathbf{T}^H \mathbf{F}_{u,t}^H \mathbf{F}_{u,t} \mathbf{T} \boldsymbol{\mathcal{H}}_2\}}}, \tag{6.106}$$

where $\mathbf{T} = (\boldsymbol{\mathcal{H}}_2^H \boldsymbol{\mathcal{H}}_2 + \alpha N_{RF_u} \mathbf{I}_{N_{RF_u}})^{-1}$. Since the number of feasible UAV positions required to search space is $\left(\frac{x_{\max} - x_{\min}}{\Delta_x}\right) \times \left(\frac{y_{\max} - y_{\min}}{\Delta_y}\right)$, where Δ_x and Δ_y represents the search space resolution, hence, we propose a PSO-based algorithmic solution to find optimal UAV position while maximizing R_T. Following a similar approach as in Section 6.6.3.3, the i^{th} particle at the t^{th} iteration now represents an instance of the UAV location as:

$$\mathbf{X}_i^{(t)} = [x_i^{(t)}, y_i^{(t)}]^T \in \mathbb{R}^2. \tag{6.107}$$

Here, the corresponding particle i represents the candidate UAV position and calculates the objective function as $R_T(\mathbf{F}_b, \mathbf{B}_b, \mathbf{F}_{u,t}, \mathbf{B}_{u,t}, \mathbf{F}_{u,r}, \mathbf{B}_{u,r}, \mathbf{P}, \mathbf{X}_i^{(t)})$. Then, the position $\mathbf{X}_i^{(t)}$ and velocity $\mathbf{V}_i^{(t)}$ are updated as follows:

$$\mathbf{X}_i^{(t+1)} = \mathbf{X}_i^{(t)} + \mathbf{V}_i^{(t+1)}, \tag{6.108}$$

$$\mathbf{V}_i^{(t+1)} = \gamma_1 \mathbf{Y}_1^{(t)} (\hat{\mathbf{X}}_{\text{best}}^{(t)} - \hat{\mathbf{X}}_i^{(t)}) + \gamma_2 \mathbf{Y}_2^{(t)} (\hat{\mathbf{X}}_{\text{best},i}^{(t)} - \hat{\mathbf{X}}_i^{(t)}) + \gamma_3^{(t)} \mathbf{V}_i^{(t)} \tag{6.109}$$

Then, the personal and global best solutions for i^{th} particle during t^{th} iteration are obtained as follows:

$$\mathbf{X}_{\text{best},i}^{(t)} = \underset{\mathbf{X}_i^{(t^*)}, \forall t^* = 0,1,\cdots,t}{\arg\max} \; R_T(\mathbf{F}_b, \mathbf{B}_b, \mathbf{F}_{u,t}, \mathbf{B}_{u,t}, \mathbf{F}_{u,r}, \mathbf{B}_{u,r}, \mathbf{P}, \mathbf{X}_i^{(t^*)}), \tag{6.110}$$

$$\mathbf{X}_{best}^{(t)} = \underset{\mathbf{X}_{\text{best},i}^{(t)}, \forall i = 0,1,\cdots,Z_p}{\arg\max} \; R_T(\mathbf{F}_b, \mathbf{B}_b, \mathbf{F}_{u,t}, \mathbf{B}_{u,t}, \mathbf{F}_{u,r}, \mathbf{B}_{u,r}, \mathbf{P}, \mathbf{X}_{\text{best},i}^{(t)}), \tag{6.111}$$

After T iterations, we update $\mathbf{x}_o = \mathbf{X}_{\text{best}}^{(T)}$. The pseudo-code is given in Algorithm 6.5, which summarizes the proposed PSO-based UAV positioning for equal PA with HBF.

Algorithm 6.5 Proposed Joint HBF and UAV Deployment for Equal PA (J-HBF-PSOL-EQPA) Algorithm

```
Input: $Z_p, T$, $(\theta, \phi)$, $(x_1, y_1, z_1)$, $(x_u, y_u, z_u)$.
Output: $\mathbf{x}_o$, $\mathbf{P}$, $\mathbf{F}_b$, $\mathbf{B}_b$, $\mathbf{F}_{u,t}$, $\mathbf{B}_{u,t}$, $\mathbf{F}_{u,r}$, $\mathbf{B}_{u,r}$.
Formulate BS RF and BB stages using (6.54), (6.94).
Formulate UAV receive HBF stages using (6.56), (6.95).
Construct UAV transmit HBF stages via (6.92), (6.96).
for $i = 1 : Z_p$ do
    Initialize the velocity as $\mathbf{V}_i^{(0)} = \mathbf{0}$.
    Each entry of $\mathbf{X}_i^{(0)}$ is uniformly distributed in $[0, 1]$.
    Set the personal best $\mathbf{X}_{\text{best},i}^{(0)} = \mathbf{X}_i^{(0)}$.
end for
Find the global best $\mathbf{X}_{\text{best}}^{(0)}$ as in (6.111).
for $t = 1 : T$ do
    for $i = 1 : Z_p$ do
        Update the velocity $\mathbf{V}_i^{(t)}$ as in (6.109).
        Update the position $\mathbf{X}_i^{(t)}$ as in (6.108).
        Find the personal best $\mathbf{X}_{\text{best},i}^{(t)}$ as in (6.110).
    end for
    Find the global best $\mathbf{X}_{\text{best}}^{(t)}$ as in (6.111).
end for
$\mathbf{x}_o = \mathbf{X}_{\text{best}}^{(T)}$
Update $\mathbf{B}_b$, $\mathbf{B}_{u,t}$, $\mathbf{B}_{u,r}$ for $\mathbf{x}_o$.
```

6.6.3.3.3 Joint UAV Positioning and Optimal PA

In this problem, we jointly optimize UAV location $\mathbf{x}_u = [x_u, y_u]^T$ and $\mathbf{P}$, which are given by (6.98) and (6.107), respectively. To solve this non-convex optimization problem, we propose a PSO-based algorithmic solution to optimize $\mathbf{x}_u$ and $\mathbf{P}$ whilst maximizing the total achievable rate R_T. Here, the i^{th} particle at the t^{th} iteration now represents an instance of the UAV location and multi-user PA matrix, which is given as follows:

$$\mathbf{J}_{p,i}^{(t)} = [\mathbf{X}_i^{(t)}, \hat{\mathbf{P}}_i^{(t)}]^T = [x_i^{(t)}, y_i^{(t)}, \sqrt{\hat{p}_{1,i}^{(t)}}, \cdots, \sqrt{\hat{p}_{K,i}^{(t)}}]^T \in \mathbb{R}^{K+2}, \tag{6.112}$$

where each particle i represents the candidate UAV position and PA to K IoT users, and calculates the objective function as $R_T(\mathbf{F}_b, \mathbf{B}_b, \mathbf{F}_{u,t}, \mathbf{B}_{u,t}, \mathbf{F}_{u,r}, \mathbf{B}_{u,r}, \kappa_i^{(t)} \hat{\mathbf{P}}_i^{(t)}, \mathbf{X}_i^{(t)})$. Here, $\hat{\mathbf{P}}_i^{(t)} = \text{diag}(\sqrt{\hat{p}_{1,i}^{(t)}}, \cdots, \sqrt{\hat{p}_{K,i}^{(t)}}) \in \mathbb{R}^{K \times K}$ is the normalized PA matrix with $\hat{p}_{k,i}^{(t)} \in [0, 1]$ and similar to Section III-C1, the transmit power constraints for any $\hat{\mathbf{P}}_i^{(t)}$ are satisfied by defining $\mathbf{P}_i^{(t)} = \kappa_i^{(t)} \hat{\mathbf{P}}_i^{(t)}$. Then, the position $\mathbf{J}_{p,i}^{(t)}$ and velocity $\mathbf{J}_{v,i}^{(t)}$ for i^{th} particle during t^{th}

Algorithm 6.6 Proposed Joint HBF, UAV Location Optimization and PA (J-HBF-PSOLPA) Algorithm

```
Input: $Z, T$, $(\theta, \phi)$, $(x_1, y_1, z_1)$, $(x_u, y_u, z_u)$.
Output: $\mathbf{x}_o$, $\mathbf{P}$, $\mathbf{F}_b$, $\mathbf{B}_b$, $\mathbf{F}_{u,t}$, $\mathbf{B}_{u,t}$, $\mathbf{F}_{u,r}$, $\mathbf{B}_{u,r}$.
Formulate BS RF and BB stages using (6.54), (6.94).
Formulate UAV receive HBF stages using (6.56), (6.95).
Construct UAV transmit HBF stages via (6.92), (6.96).
for $i = 1 : Z$ do
    Initialize the velocity as $\mathbf{J}_{v,i}^{(0)} = \mathbf{0}$.
    Each entry of $\mathbf{J}_{p,i}^{(0)}$ is uniformly distributed in $[0, 1]$.
    Set the personal best $\mathbf{J}_{p,\text{best},i}^{(0)} = \mathbf{J}_{p,i}^{(0)}$.
end for
Find the global best $\mathbf{J}_{p,\text{best}}^{(0)}$ as in (6.116).
for $t = 1 : T$ do
    for $i = 1 : Z$ do
        Update the velocity $\mathbf{J}_{v,i}^{(t)}$ as in (6.114).
        Update the position $\mathbf{J}_{p,i}^{(t)}$ as in (6.113).
        Find the personal best $\mathbf{J}_{p,\text{best},i}^{(t)}$ as in (6.115).
    end for
    Find the global best $\mathbf{J}_{p,\text{best}}^{(t)}$ as in (6.116).
end for
$\mathbf{x}_o = \mathbf{J}_{p,\text{best}}^{(T)}$, $\mathbf{P} = \kappa_{\text{best}}^{(T)} \hat{\mathbf{P}}_{\text{best}}^{(T)}$
Update $\mathbf{B}_b$, $\mathbf{B}_{u,t}$, $\mathbf{B}_{u,r}$ for $\mathbf{x}_o$.
```

iteration are updated as follows:

$$\mathbf{J}_{p,i}^{(t+1)} = \mathbf{J}_{p,i}^{(t)} + \mathbf{J}_{v,i}^{(t+1)}, \tag{6.113}$$

$$\mathbf{J}_{v,i}^{(t+1)} = \gamma_1 \mathbf{Y}_1^{(t)} (\mathbf{J}_{p,\text{best}}^{(t)} - \mathbf{J}_{p,i}^{(t)}) + \gamma_2 \mathbf{Y}_2^{(t)} (\mathbf{J}_{p,\text{best},i}^{(t)} - \mathbf{J}_{p,i}^{(t)}) + \gamma_3^{(t)} \mathbf{J}_{v,i}^{(t)}, \tag{6.114}$$

Finally, the personal and global best solutions for i^{th} particle during t^{th} iteration are obtained as follows:

$$\mathbf{J}_{p,\text{best},i}^{(t)} = \underset{\mathbf{J}_{p,i}^{(t^*)}, \forall t^*=0,1,\cdots,t}{\arg\max} \; R_T(\mathbf{F}_b, \mathbf{B}_b, \mathbf{F}_{u,t}, \mathbf{B}_{u,t}, \mathbf{F}_{u,r}, \mathbf{B}_{u,r}, \kappa_i^{(t^*)} \hat{\mathbf{P}}_i^{(t^*)}, \mathbf{X}_i^{(t^*)}), \tag{6.115}$$

$$\mathbf{J}_{p,\text{best}}^{(t)} = \underset{\mathbf{J}_{p,\text{best},i}^{(t)}, \forall i=0,1,\cdots,Z_p}{\arg\max} \; R_T(\mathbf{F}_b, \mathbf{B}_b, \mathbf{F}_{u,t}, \mathbf{B}_{u,t}, \mathbf{F}_{u,r}, \mathbf{B}_{u,r}, \kappa_{\text{best},i}^{(t)} \hat{\mathbf{P}}_{\text{best,i}}^{(t)}, \mathbf{X}_i^{(t)}), \tag{6.116}$$

After T iterations, we update $\mathbf{x}_o = \mathbf{X}_{\text{best}}^{(T)}$ and $\mathbf{P} = \kappa_{\text{best}}^{(T)} \hat{\mathbf{P}}_{\text{best}}^{(T)}$. Algorithm 6.6 gives the pseudo-code of the proposed PSO-based joint UAV positioning and optimal PA with HBF.

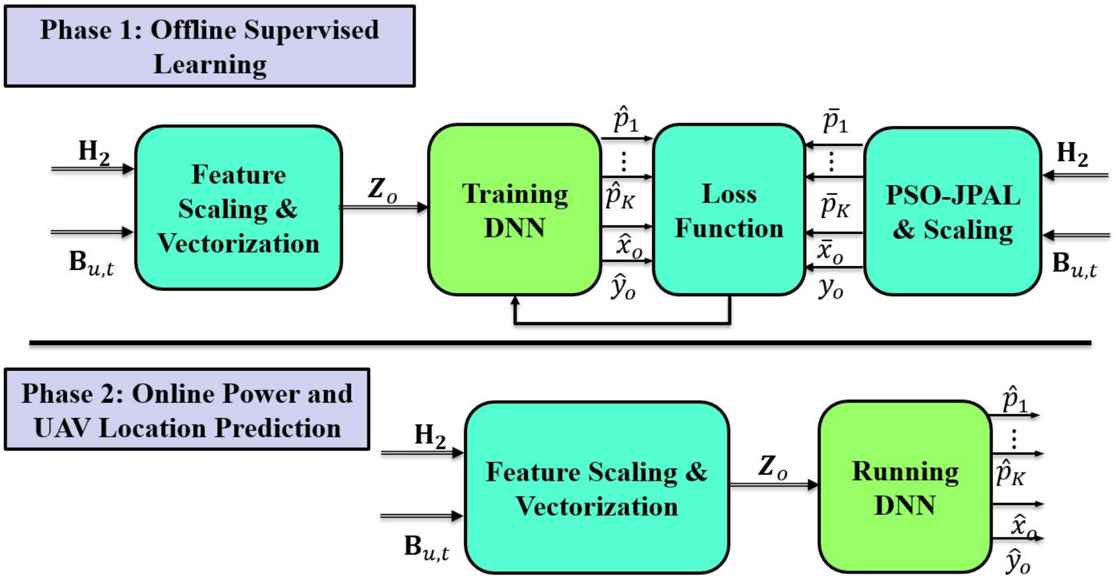

Figure 6.10. Block diagram of offline supervised learning and real-time prediction in J-HBF-DLLPA algorithm.

6.6.3.4 Low-Complexity DL-Based Joint Power Allocation and UAV Positioning

The proposed joint HBF, PA and UAV location schemes can achieve near-optimal capacity for a UAV-assisted MU-mMIMO IoT systems. Additionally, compared to the computationally expensive exhaustive search method, the proposed solutions offer higher computational efficiency. However, as the number of IoT users increases, the proposed PSO-based solutions require more iterations and longer run time, which may render them impractical for real-time online applications of UAV-assisted MU-MIMO IoT systems. To address this challenge, we propose a low-complexity DL-based algorithm, called J-HBF-DLLPA, which can achieve a near-optimal AR while maintaining a reasonable run time. The proposed algorithm has two phases, as illustrated in Fig. 6.10: 1) Phase 1 applies the offline supervised learning via the optimal allocated power and UAV location values calculated by J-HBF-PSOLPA; and 2) Phase 2 runs the trained J-HBF-DLLPA algorithm for predicting the allocated powers and UAV location in the real-time online applications. Therefore, the remaining part of this section focuses on the deep neural network (DNN) architecture, loss functions, dataset preparation, and training process for the proposed low-complexity J-HBF-DLLPA algorithm.

6.6.3.4.1 Proposed Deep Neural Network Architecture We employ a fully-connected DNN architecture with four hidden layers as depicted in Fig. 6.11, which aims to predict the optimal allocated powers for K IoT users as well as UAV optimal location in a given deployment span. We consider L_i neurons in each i^{th} hidden layer (HL) with $i = 1, \cdots, 4$. As shown in Fig. 6.10, the proposed J-HBF-DLLPA algorithm uses the effective channel matrix between UAV and K IoT users $\boldsymbol{\mathcal{H}}_2 \in \mathrm{C}^{K \times N_{RF_u}}$ given in (6.4), and the UAV transmit BB stage $\mathbf{B}_{u,t} \in \mathbb{C}^{N_{RF_u} \times K}$ given in (6.96) as inputs, which are first subject to feature scaling and vectorization operations. Subsequently, the input layer feature vector is derived as:

$$\mathbf{z}_0 = \begin{bmatrix} \omega_1 \mathbf{z}_{\tilde{\mathbf{h}}_{2,1}} \\ \vdots \\ \omega_1 \mathbf{z}_{\tilde{\mathbf{h}}_{2,K}} \\ \omega_2 \mathbf{z}_{\mathbf{b}_{u,t,1}} \\ \vdots \\ \omega_2 \mathbf{z}_{\mathbf{b}_{u,t,K}} \\ \omega_3 \mathbf{z}_{\mathbf{BB}_{u,t}} \\ \omega_4 \mathbf{z}_{\mathbf{BB,inv,u,t}} \end{bmatrix} \in \mathbb{R}^{L_0}, \tag{6.117}$$

where $L_0 = (2N_t + 2N_{RF_u} + 2)K$ is the input feature size, $\mathbf{z}_{\tilde{\mathbf{h}}_{2,k}} = [\mathrm{Re}(\tilde{\mathbf{h}}_{2,k}^T), \mathrm{Im}(\tilde{\mathbf{h}}_{2,k}^T)]^T \in \mathbb{R}^{2N_t}$, $\mathbf{z}_{\mathbf{b}_{u,t,k}} = [\mathrm{Re}(\mathbf{b}_{u,t,k}^T), \mathrm{Im}(\mathbf{b}_{u,t,k}^T)]^T \in \mathbb{R}^{2N_{RF_u}}$, $\mathbf{z}_{\mathbf{BB}_{u,t}^T} = [\mathbf{b}_{u,t,1}^H \mathbf{b}_{u,t,1}, \cdots, \mathbf{b}_{u,t,K}^H \mathbf{b}_{u,t,K}]^T \in \mathbb{R}^K$ and $\mathbf{x}_{\mathbf{BB,inv,u,t}^T} = [\frac{1}{\mathbf{b}_{u,t,1}^H \mathbf{b}_{u,t,1}}, \cdots, \frac{1}{\mathbf{b}_{u,t,K}^H \mathbf{b}_{u,t,K}}]^T \in \mathbb{R}^K$ are respectively the non-scaled input feature vectors for the effective channel, UAV transmit BB stage, the gain of each BB precoder vector and its inverse. By implementing the maximum absolute scaling [167], the corresponding scaling coefficients are calculated as:

$$\omega_1 = \max\left(|\mathbf{z}_{\tilde{\mathbf{h}}_{2,1}}^T|, \cdots, |\mathbf{z}_{\tilde{\mathbf{h}}_{2,K}}^T|\right)^{-1} \tag{6.118}$$

$$\omega_2 = \max\left(|\mathbf{z}_{\tilde{\mathbf{b}}_{u,t,1}}^T|, \cdots, |\mathbf{z}_{\tilde{\mathbf{b}}_{u,t,K}}^T|\right)^{-1} \tag{6.119}$$

$$\omega_3 = \max\left(\mathbf{b}_{u,t,1}^H \mathbf{b}_{u,t,1}^H, \cdots, \mathbf{b}_{u,t,K}^H \mathbf{b}_{u,t,K}^H\right)^{-1} \tag{6.120}$$

$$\omega_4 = \max\left(\mathbf{b}_{u,t,1}^H \mathbf{b}_{u,t,1}^H, \cdots, \mathbf{b}_{u,t,K}^H \mathbf{b}_{u,t,K}^H\right). \tag{6.121}$$

The proposed algorithm utilizes the maximum absolute scaling technique to scale the input feature vector between -1 and 1 (i.e., $\mathbf{z}_0 \in (-1, 1]$), which prevents certain features from dominating the learning process. In the offline supervised learning process, the optimal power allocation and UAV location values are calculated as the output labels via the computationally expensive J-HBF-PSOLPA algorithm. Similar to the input features, we also apply the maximum absolute scaling to the optimal allocated powers and UAV

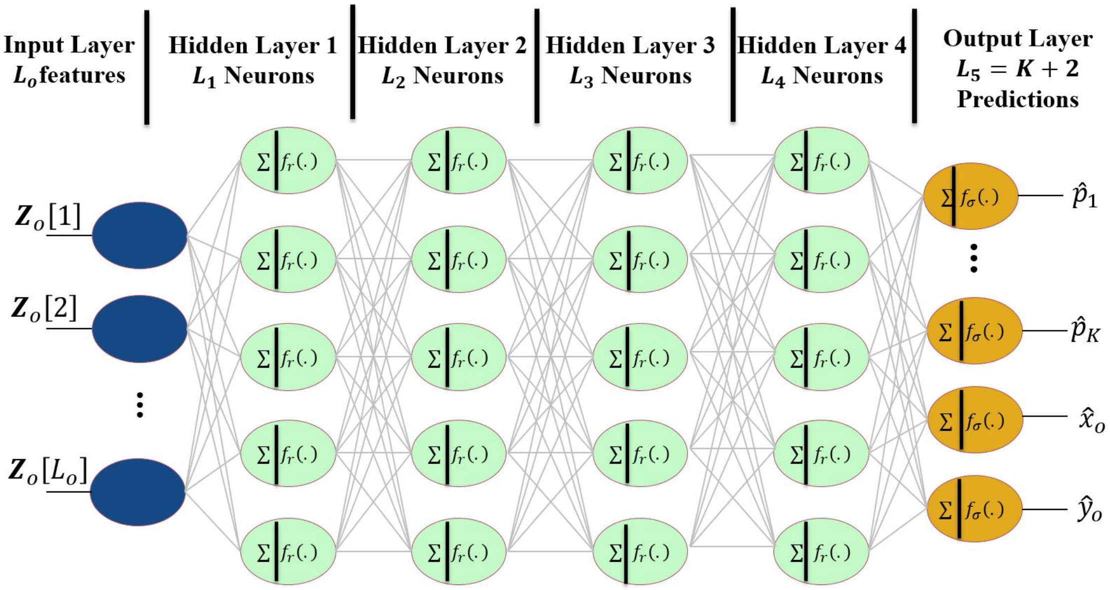

Figure 6.11. Deep neural network architecture for J-HBF-DLLPA algorithm.

location as follows:

$$\bar{x}_o = \frac{x_o}{\max(x_o, y_o)} \in [0, 1] \tag{6.122}$$

$$\bar{y}_o = \frac{y_o}{\max(x_o, y_o)} \in [0, 1] \tag{6.123}$$

$$\bar{p}_k = \frac{p_k^{\text{opt}}}{\max(p_1^{\text{opt}}, \cdots, p_K^{\text{opt}})} \in [0, 1]. \tag{6.124}$$

To perform non-linear operations, we adopt the rectified linear unit (ReLU) as the activation function in the hidden layers (i.e., $f_r(z) = \max(0, z)$. Therefore, using the input feature vector of $\mathbf{z}_0$ given in (6.117), the output of i^{th} hidden layer is computed as $\mathbf{z}_i = f_r(\mathbf{U}_{i-1}\mathbf{z}_{i-1} + \mathbf{b}_{i-1}) \in \mathbb{R}^{L_i}$, where $\mathbf{U}_{i-1} \in \mathbb{R}^{L_i \times L_{i-1}}$ and $\mathbf{b}_{i-1} \in \mathbb{R}^{L_i}$ are the weight matrix and bias vector, respectively. To ensure that the predicted output values are between 0 and 1, we apply the sigmoid function at the output layer (i.e., $f_\sigma(z) = \frac{1}{1+e^{-\infty}}$). Thus, the predicted power and UAV location values via the DNN architecture are written as follows:

$$\begin{aligned}[\hat{p}_1, \hat{p}_2, \cdots, \hat{p}_K, \hat{x}_o, \hat{y}_o] &= f_\sigma(\mathbf{U}_4\mathbf{z}_4 + \mathbf{b}_4) \\ &= f_\sigma(\mathbf{U}_4 f_r(\mathbf{U}_3 f_r(\mathbf{U}_2 f_r(\mathbf{U}_1 f_r(\mathbf{U}_0\mathbf{x}_0 + \mathbf{b}_0) + \mathbf{b}_1) + \mathbf{b}_2) + \mathbf{b}_3) + \mathbf{b}_4).\end{aligned} \tag{6.125}$$

6.6.3.4.2 Loss Functions We here consider two loss functions by using the predicted and optimal power values: 1) mean square error (MSE); and 2) mean absolute error (MAE). When there are S_r network realizations in the dataset, the MSE loss function is given by:

$$\mathcal{L}_{\text{MSE}} = \frac{1}{S_r K} \sum_{i=1}^{S_r} \sum_{k=1}^{K} (\bar{p}_{k,i} - \hat{p}_{k,i})^2 + \frac{1}{S_r} \sum_{i=1}^{S_r} (\bar{x}_o - \hat{x}_o)^2 + \frac{1}{S_r} \sum_{i=1}^{S_r} (\bar{y}_o - \hat{y}_o)^2. \tag{6.126}$$

Similarly, the MAE loss function is written as:

$$\mathcal{L}_{\text{MAE}} = \frac{1}{S_r K} \sum_{i=1}^{S_r} \sum_{k=1}^{K} |\bar{p}_{k,i} - \hat{p}_{k,i}| + \frac{1}{S_r} \sum_{i=1}^{S_r} |\bar{x}_o - \hat{x}_o| + \frac{1}{S_r} \sum_{i=1}^{S_r} |\bar{y}_o - \hat{y}_o|. \tag{6.127}$$

The weight matrices $\mathbf{U}_i$ and bias vectors $\mathbf{b}_i$ of the DNN architecture are updated by back-propagating the gradients of the loss function from the output layer to the input layer. This helps in reducing the loss and accurately predicting the optimal allocated power and UAV location values, and thus, maximizing the total AR as expressed in (6.97).

6.6.3.4.3 Data Generation & Training Process We generated a dataset of $S_r = 100.000 = 10^5$ network realizations to train the proposed DNN architecture, as shown in Fig. 6.10. For each realization, we randomly varied the path gains, AoD parameters, and UE location to generate the channel vector for each UE as given in (6.3). The corresponding optimal allocated powers and UAV location are calculated via the J-HBF-PSOLPA algorithm 6.6 (Section 6.6.3.3.3) and stored in the dataset. The total available dataset was split into 80% for training and 20% for validation for the offline supervised learning process (i.e., Phase 1). After completing the offline supervised learning process, the online power allocation and UAV location (i.e., Phase 2) is tested with a purely new test dataset. The DNN architecture for the proposed J-HBF-DLLPA algorithm is implemented using the open-source DL libraries in TensorFlow [168].

6.7 Illustrative Results

In this section, we present the Monte-Carlo simulation results based on the proposed algorithmic solutions. Table 6.2 outlines the simulation setup based on the 3D micro-cell scenario [90] for the results discussed hereafter. Moreover, for PSO-based results, we use $Z_p = 20$, $\gamma_1 = \gamma_2 = 2$ and $\gamma_3 = 1.1$.

Table 6.2. Simulation Parameters

Number of antennas		$(N_T, N_t, N_r) = 144$	
Number of paths	Path loss exponent	$L = 10$	3.6
Frequency	Channel Bandwidth	28 GHz	100 MHz
Noise PSD	Reference Path Loss α	-174 dBm/Hz	61.34 dB
BS/Gateway height	UAV height	10 m	20 m
User groups	# of users per group	$G = 1$ or 2	$K_g = \frac{K}{G}$
UAV x-axis range	UAV y-axis range	$[x_{min}, x_{max}] = [0, 100]\, m$	$[y_{min}, y_{max}] = [0, 100]\, m$
Mean AAoD/AAoA (1^{st} link)	Mean AAoD (2^{nd} link)	120°	$\phi_g = 21^\circ + 120^\circ(g-1)$
Mean EAoD/EAoA (1^{st} link)	Mean EAoD (2^{nd} link)	60°	$\theta_g = 60^\circ$
Azimuth/Elevation Angle Spread	# of network realizations	±10°	2000
Minimum horizontal distance $\tau_{h,\min}$	Maximum horizontal distance $\tau_{h,\min}$	0	100 [m]

6.7.1 Spectral Efficiency

In this section, we compare the spectral efficiency of the proposed PSO-based algorithmic solutions for a UAV-assisted MU-mMIMO IoT systems. To achieve this, we first analyze the rate of each link individually for a fixed UAV location and transmit power $P_T = 20$ dBm. Specifically, we consider that the BS is located at $(x_b, y_b, z_b) = (0, 0, 10)$, the UAV is deployed at fixed location $(x_u, y_u, z_u) = (50, 50, 20)$ and the IoT users are randomly distributed and located at a far distance from BS $(x_k, y_k) \in [50, 100]$. We then compare the optimal UAV location for maximizing the capacity of the first link using two schemes: 1) exhaustive search; and 2) the proposed PSO-based UAV deployment and equal PA (J-HBF-PSOL-EQPA) over a given deployment span of $[(x_{\min}, y_{\min}), (x_{\max}, y_{\max})] = [0, 100]$. The results show that the optimal location for the UAV to maximize the capacity of the first link is close to the BS, as demonstrated in Fig. 6.12(b). Furthermore, the proposed J-HBF-PSOL-EQPA can find the global optimal solution for almost 95% of the realizations, as shown in 6.12(a). Fig. 6.13 plots the rate of first link R_1 using J-HBF-PSOL-EQPA versus different 2-D UAV locations, which shows similar performance to exhaustive search solution presented in Fig. 6.12(b).

Fig. 6.14 analyzes the total rate of second link R_2 for exhaustive search and J-HBF-PSOL-EQPA. Due to the randomness in the placement of the IoT users, finding a single optimal UAV location that covers all IoT users while minimizing interference is a challenging task. However, the proposed J-HBF-PSOL-EQPA can find optimal UAV placement close to global solution as depicted in Fig. 6.14(a). Fig. 6.15 plots the AR of second link versus different UAV 2-D locations for $P_T = 20$ dBm, which shows that UAV placement by the proposed J-HBF-PSOL-EQPA can give higher AR when compared to UAV deployed at some fixed location. Fig. 6.16 compares the AR versus transmit power P_T of the proposed HBF solution for four cases: 1) PSO-based UAV location and PSO-based PA (J-HBF-PSOLPA); 2) PSO-based UAV location and equal PA (J-HBF-PSOL-EQPA); 3) fixed UAV location and PSO-based PA (J-HBF-PSOPA-FL); and 4) fixed UAV location and equal PA (FL-EQPA).

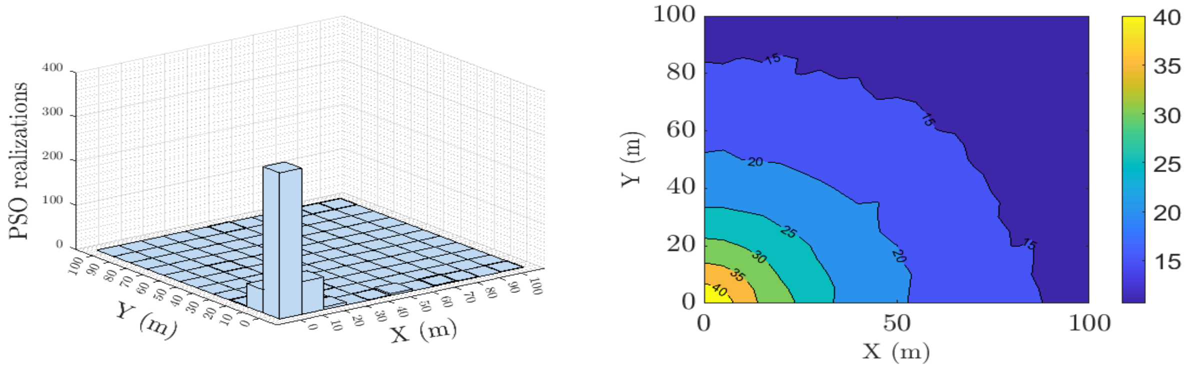

(a) **(b)**

Figure 6.12. Comparison of AR R_1. (a) Number of realizations for best UAV location using J-HBF-PSOL-EQPA. (b) Contour plot using exhaustive search.

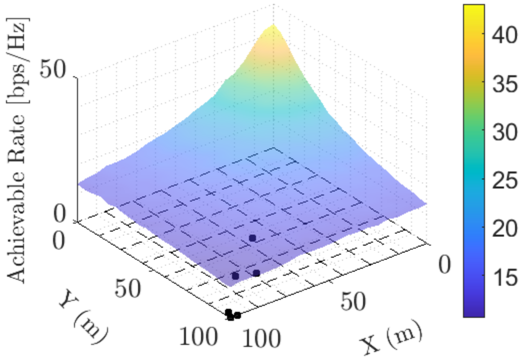

Figure 6.13. Achievable rate R_1 versus $(x-y)$-coordinates at $P_T = 40$ dBm.

The results show that all proposed algorithmic schemes can increase the total capacity of a UAV-assisted MU-mMIMO IoT systems when compared to the FL-EQPA case. Comparing the single optimizations (i.e., PSO location-EQ PA and fixed location-PSO PA), we can see that optimizing UAV location only can provide a higher AR than allocating optimal power to multiple IoT users. However, in a highly dynamic environment, where the IoT users are far located and randomly distributed, the joint optimization of UAV location and power allocation can achieve higher spectral efficiency (i.e., $\mathrm{R}_{\mathrm{PSOL-PSOPA}} \geq \mathrm{R}_{\mathrm{PSOL-EQPA}} \gg \mathrm{R}_{\mathrm{FL-PSOPA}}$). Moreover, compared to FL-EQPA case at $P_T = 40$ dBm, the proposed J-HBF-PSOPA-FL, J-HBF-PSOL-EQPA, and J-HBF-PSOLPA schemes can increase the total AR by 77%, 155%, and 200%, respectively. We also compare the performance with the existing

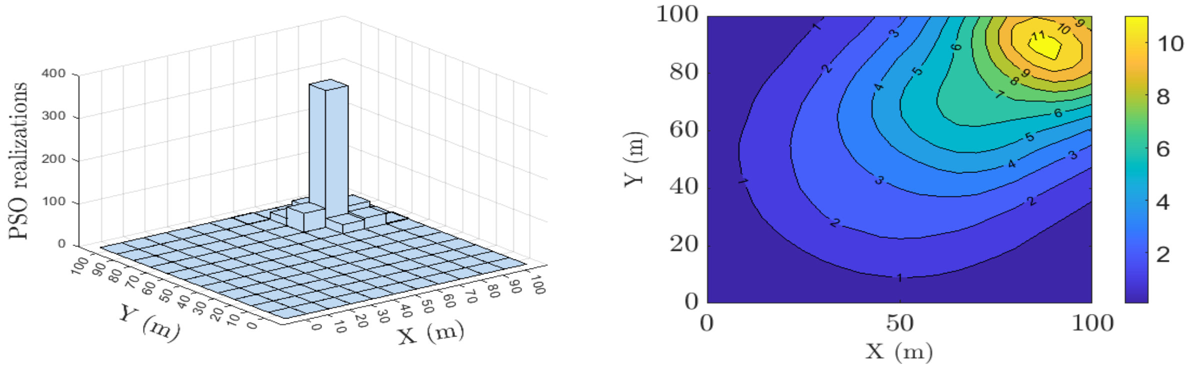

(a) **(b)**

Figure 6.14. Comparison of AR R_2. (a) Number of realizations for best UAV location using J-HBF-PSOL-EQPA. (b) Contour plot using exhaustive search.

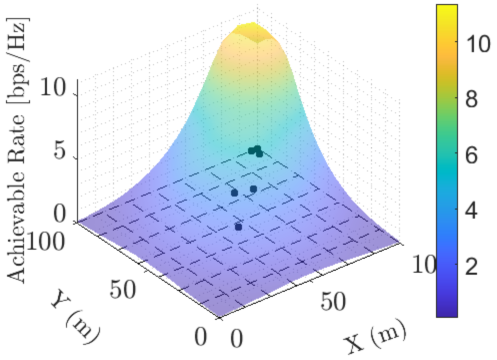

Figure 6.15. Achievable rate R_2 versus $(x - y)$-coordinates at $P_T = 40$ dBm.

HBF solutions. For instance, compared to HBF schemes presented in [70,130], the proposed J-HBF-PSOLPA can provide a higher AR. Similarly, compared to the iterative successive approximation (ISA) algorithmic solution in [169], which requires full CSI, the proposed J-HBF-PSOLPA can provide better performance with reduced CSI overhead size.

6.7.2 Buffer-Aided Transmission

Section 6.7.1 of this study presents a comparison of different proposed PSO-based algorithms for conventional relaying in UAV-assisted wireless systems, i.e., UAV receives the data transmitted by BS in first time slot, decode the data, and then forwards it to

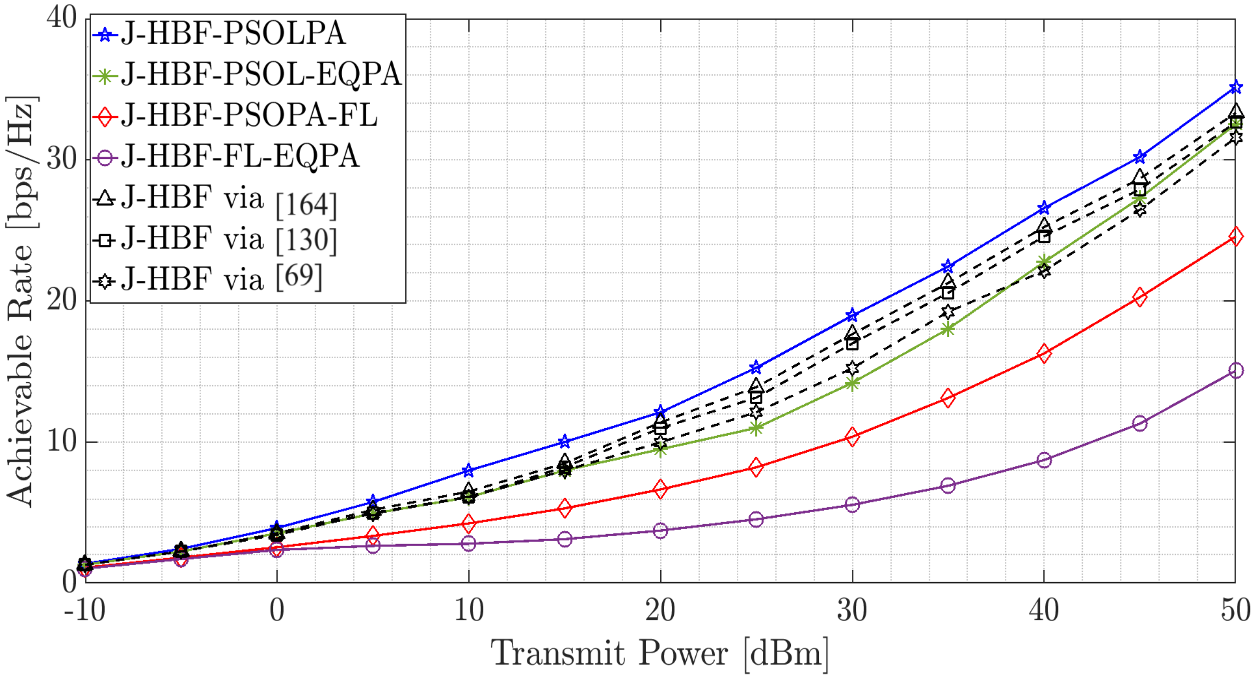

Figure 6.16. Total AR R_T versus P_T for different proposed algorithmic schemes.

multiple IoT users in the second time slot. This pre-scheduled approach may not perform well in UAV-assisted wireless systems because the channel qualities (i.e., $\mathbf{H}_1$ and $\mathbf{H}_2$) can vary significantly with time, preventing the UAV relay from exploiting the best transmitting and receiving channels. In addition, unlike static relays, UAVs can fly close to BS, store the data in a buffer, and then fly close to multiple IoT users. The results in Section 6.7.1 are based on a fixed optimized location for the UAV relay, which can increase the rate of one link but may degrade the rate for other link [2]. To fully exploit the potential of a mobile relay and to further maximize the capacity of a UAV-assisted MU-mMIMO IoT systems, we propose a buffer-aided UAV relay that can store the data in a buffer while transitioning from one optimal location for link 1 to an optimal location for link 2. By considering two possible locations for UAV, we can maximize the SINR for each link, leading to a higher total rate.

In Fig. 6.17, we compare AR versus transmit power for UAVs with buffer and without buffer. For the buffer-aided UAV, we consider two scenarios for delay-unconstrained applications. In FL-EQPA, we consider UAV is deployed at fixed location ($x_u, y_u = 50, 50$) and multiple IoT users have equal PA. However, the UAV does not transmit in consecutive

---

[2] Since R_2 is the minimum of (R_1, R_2), therefore UAV is deployed close to multiple users to maximize R_2, however, it increases the pathloss for first link, which results in slight rate degradation for R_1 (Fig. 6.12 - 6.15).

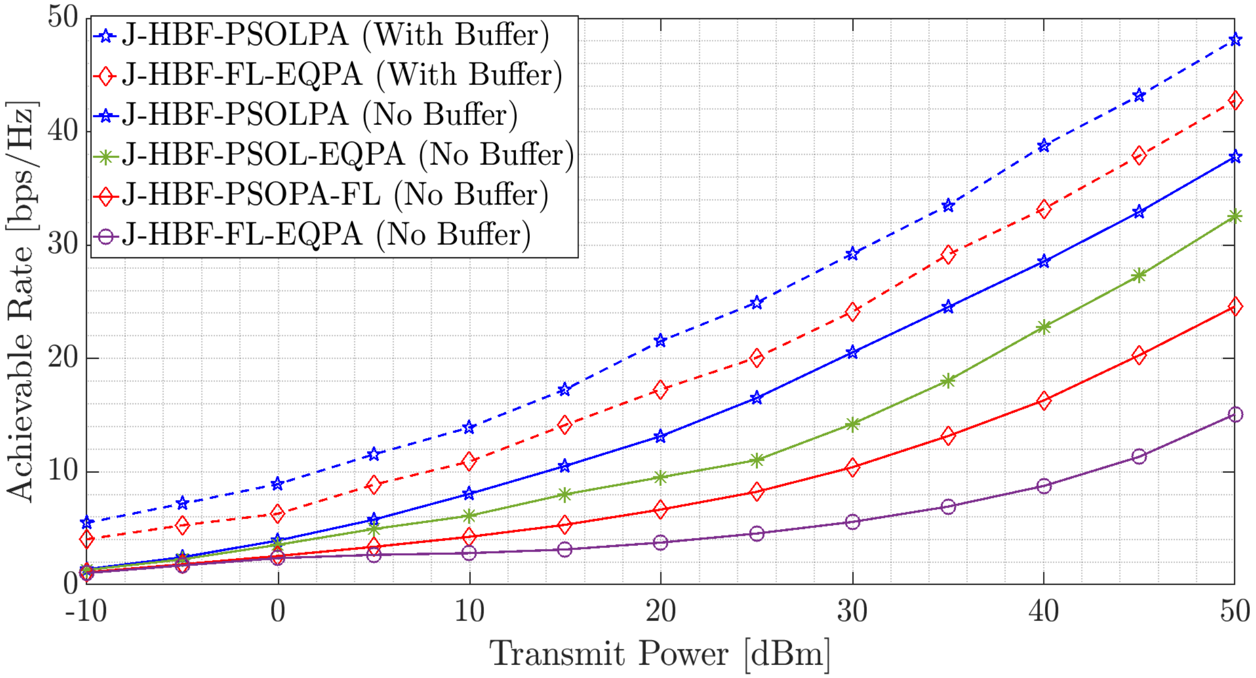

Figure 6.17. Total AR R_T versus P_T for buffer-aided transmissions.

time slots. In the second scenario, J-HBF-PSOLPA, we consider two different UAV locations (close to BS for link 1 and close to multiple IoT users for link 2) and do not use pre-scheduled transmissions. The results show that using buffers at UAV can significantly increase the capacity (e.g., from 10 bps/Hz for FL-EQPA (without buffer) to 62 bps/Hz for J-HBF-PSOLPA (with buffer) at $P_T = 40$ dBm, which represents more than five fold increase in capacity). It is important to note that we assume a buffer size as $B = \infty$, and thus, it represents a performance upper bound for a UAV-assisted MU-mMIMO IoT system in a delay-constrained transmissions. For delay-unconstrained transmissions, the average delay tends to ∞ as $B \rightarrow \infty$. However, with the simple heuristic modifications proposed in this subsection, the proposed algorithmic solutions for delay-unconstrained transmission can also be employed for delay-constrained transmission at the expense of a small performance degradation due to the delay constraint. Let D denote the waiting time (delay) experienced for a bit transmitted from the BS to the multiple IoT users via UAV relay equipped with buffer and having queuing size Q bits. Then, for the HD UAV-assisted MU-mMIMO IoT systems, we use Little's Law to relate D to Q. Let $\lambda = \min(\mathrm{R}_1, \mathrm{R}_2)$ be the arrival rate, then we can express D as [170]:

$$D = \frac{Q}{\min(\mathrm{R}_1, \mathrm{R}_2)}. \tag{6.128}$$

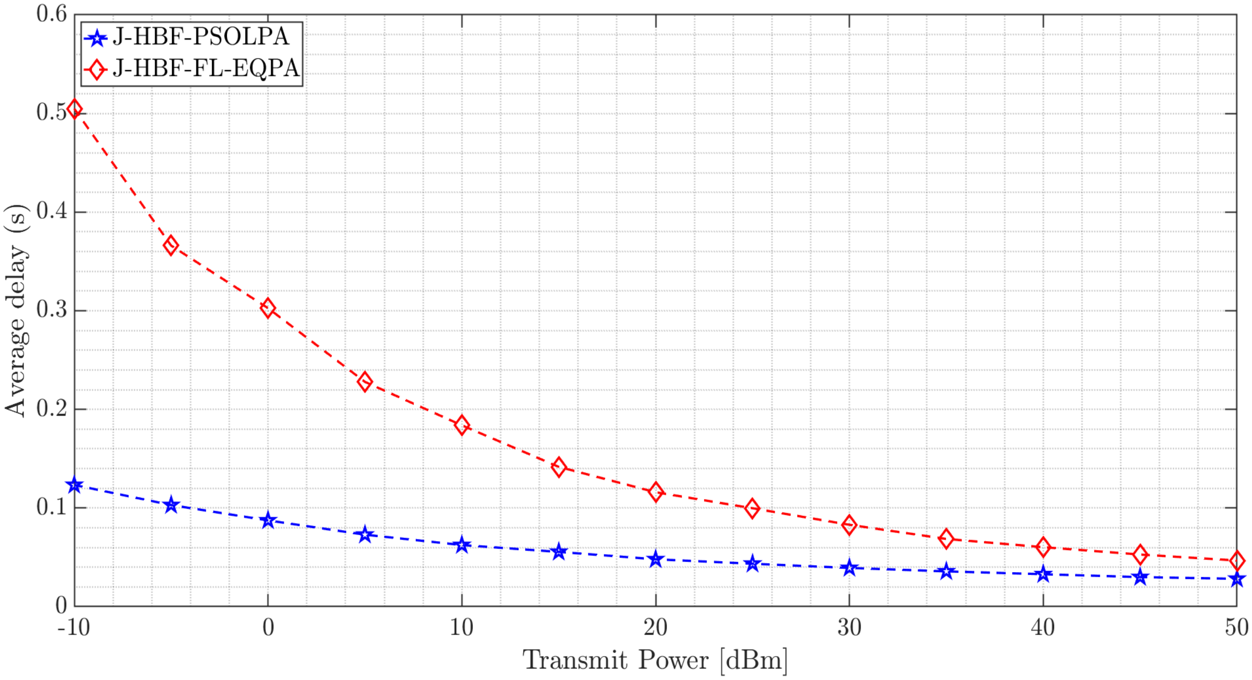

Figure 6.18. Average delay D versus transmit power P_T.

We assume a first-in-first-out (FIFO) queuing mechanism for the UAV buffer, where the UAV receives data from the BS at a rate of R_1, and transmits it to the IoT users at rate of R_2 incurring a delay D due to queuing bits Q of buffer [3]. Fig. 6.18 plots the average delay versus transmit power P_T for the cases of: 1) FL-EQPA; and 2) J-HBF-PSOLPA. It can be seen that for a fixed queuing size of $Q = 2$ bits, increasing P_T can result in reduced average delay due to an increased AR for both cases. However, the proposed J-HBF-PSOLPA can reduce the average delay by approximately 50% when compared to FL-EQPA. In Fig. 6.19, we plot average delay versus queuing size Q for a fixed transmit power $P_T = 20$ dBm. As expected, higher queuing size results in increased delay. However, by utilizing the proposed J-HBF-PSOLPA, we can decrease D by more than 140% (e.g., at $Q = 8$ bits, D can be reduced from 0.48s to 0.2s). Finally, we compare the average delay versus P_T and Q for FL-EQPA and J-HBF-PSOLPA in Fig. 6.20. Our results show that the proposed J-HBF-PSOLPA can significantly reduce the average delay for any combination of P_T and Q. Thus, it can be applied to both delay-unconstrained and delay-constrained applications in UAV-assisted MU-mMIMO IoT systems.

---

[3] It is important to note that the arrival rate R_1 is greater than the departure rate R_2 for the given system (i.e., $\mathrm{R}_1 > \mathrm{R}_2$), the stability of the system is still guaranteed due to the assumption of $\min(\mathrm{R}_1, \mathrm{R}_2)$ being used as the arrival rate. This ensures that the overall arrival rate is always less than or equal to the departure rate, which is necessary for the stability of the system.

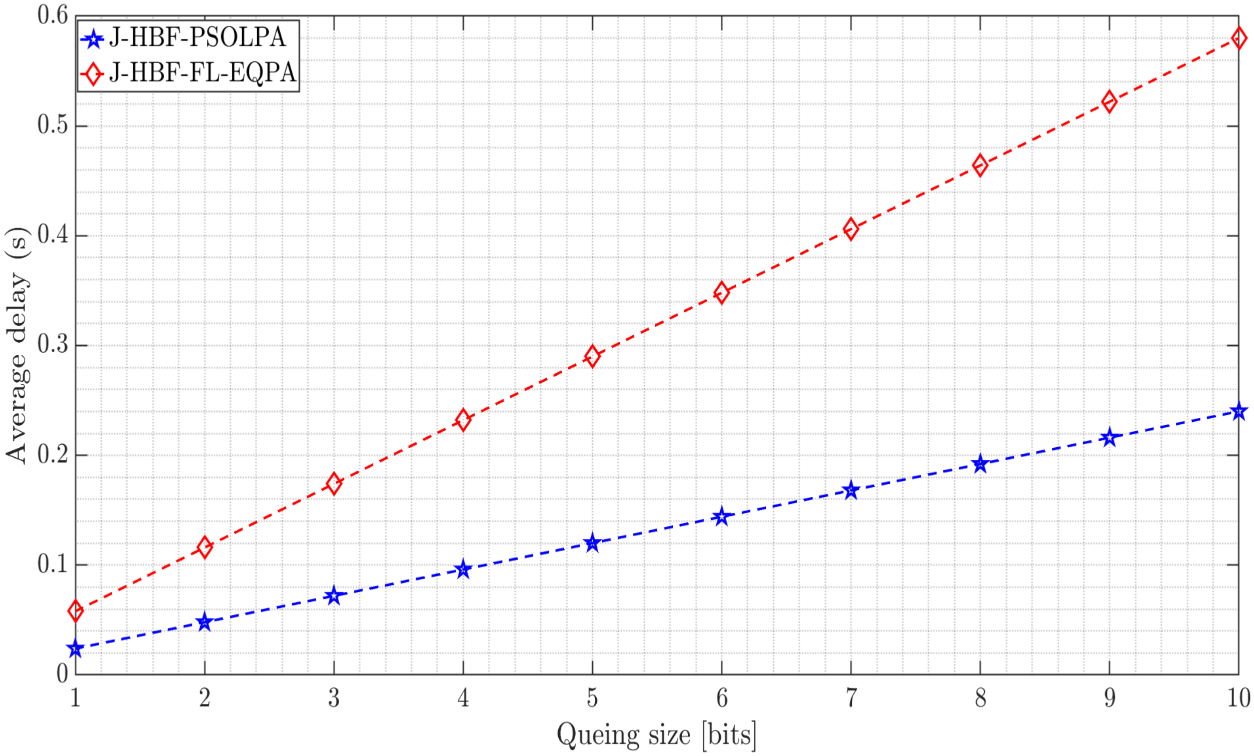

Figure 6.19. Average delay D versus queuing size Q.

6.7.3 Low-Complexity DL-Based Performance

In this section, we present the results obtained using the proposed low-complexity J-HBF-DLLPA algorithm and compare its performance with that of J-HBF-PSOLPA. Table 6.3 outlines the hyper-parameters for the proposed DNN architecture, which is given in Fig. 6.11. Fig. 6.21 exhibits the MSE performance for training and validation datasets under varying learning rates $\alpha = \{0.001, 0.01, 0.03, 0.1\}$ over a total of 15 epochs. The larger values of α, such as 0.1 and 0.03 result in higher validation error, which requires a significant number of iterations to converge. In contrast, smaller values of $\alpha = 0.01$ and 0.001 can provide lower MSE for validation dataset, even with a few epochs. Notably, $\text{MSE}_{\alpha=0.001} < \text{MSE}_{\alpha=0.01} < \text{MSE}_{\alpha=0.03} \ll \text{MSE}_{\alpha=0.1}$, which emphasizes the importance of appropriately choosing the learning rate. Similarly, Fig. 6.22 compares the MSE performance for training and validation datasets with different number of hidden layers (HL) in DNN architecture. We evaluate the error for 15 epoch for HL $= \{2, 3, 4\}$. It can be seen that DNN with 2 or 3 HL can achieve low MSE. However, it may require a large number of epochs to converge. By using HL $= 4$, we can achieve a better MSE performance for validation dataset ($\text{MSE}_{\text{HL}=4} < \text{MSE}_{\text{HL}=3} < \text{MSE}_{\text{HL}=2}$).

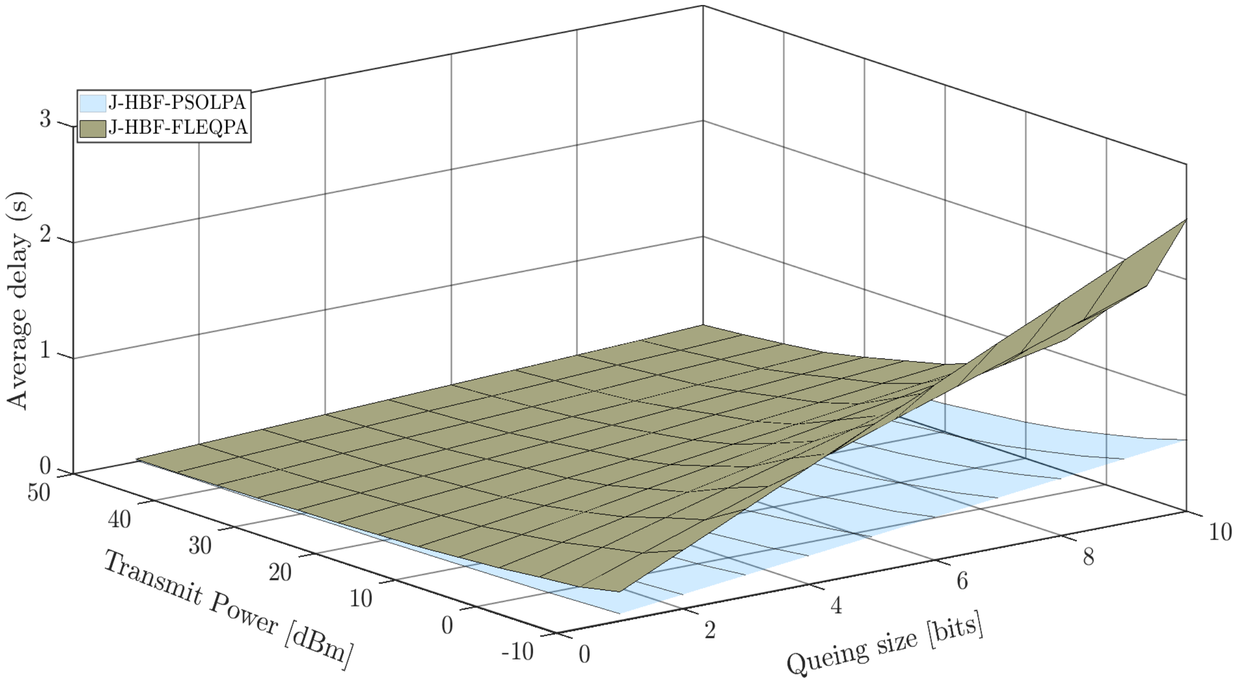

Figure 6.20. Average delay D versus transmit power P_T and queuing size Q.

Table 6.3. DNN Parameters

Regularizer		L2	
1^{st} hidden layer size	2^{nd} hidden layer size	$L_1 = 1024$	$L_2 = 512$
3^{rd} hidden layer size	4^{th} hidden layer size	$L_3 = 256$	$L_4 = 128$
Optimizer	Learning Rate	ADAM	0.001
Dataset Size	Test Data	$S_r = 100,000$	$S_t = 1,000$
Batch Size	Epoch Size	32	15

To avoid over-fitting of the training data, our proposed DNN architecture incorporates regularization techniques. In Fig. 6.23, we compare the MSE performance of the training and validation datasets for the following cases: 1) no regularization; 2) L1 regularization; and 3) L2 regularization. The use of either L1 or L2 regularization techniques prevent over-fitting, and can predict the power and location values close to optimal solution on test data [4]. Another important factor in optimizing the DNN architecture is selecting an appropriate batch size (B_S), which can have a significant impact on memory usage, convergence speed, training stability, and model generalization. In Fig. 6.24(a), we compare the MSE performance of the validation dataset for $B_S = \{2, 4, 16, 32, 64\}$. Our

---

[4] When there is no regularization, then the DNN architecture gives very low MSE for training dataset but its performance on validation dataset degrades after a few epochs.

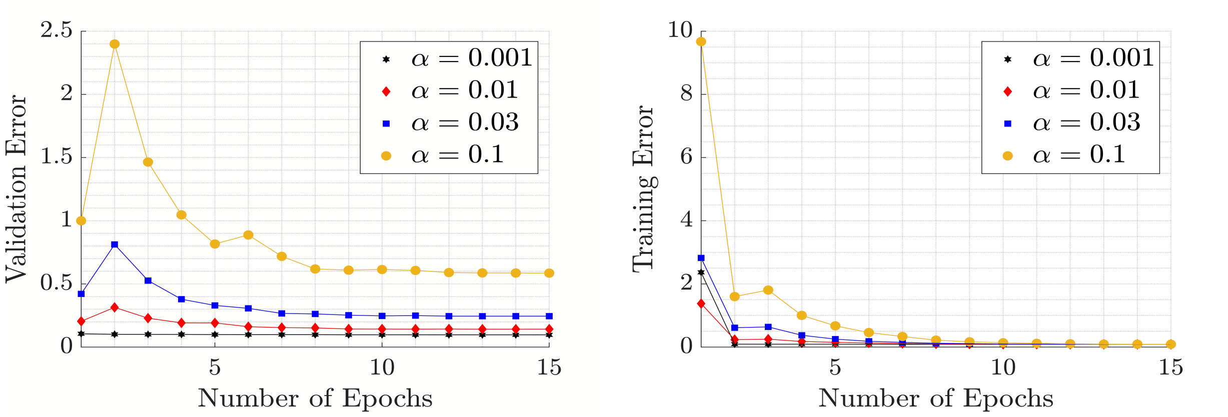

(a) **(b)**

Figure 6.21. MSE loss versus epoch for different learning rates. (a) Validation error. (b) Training error.

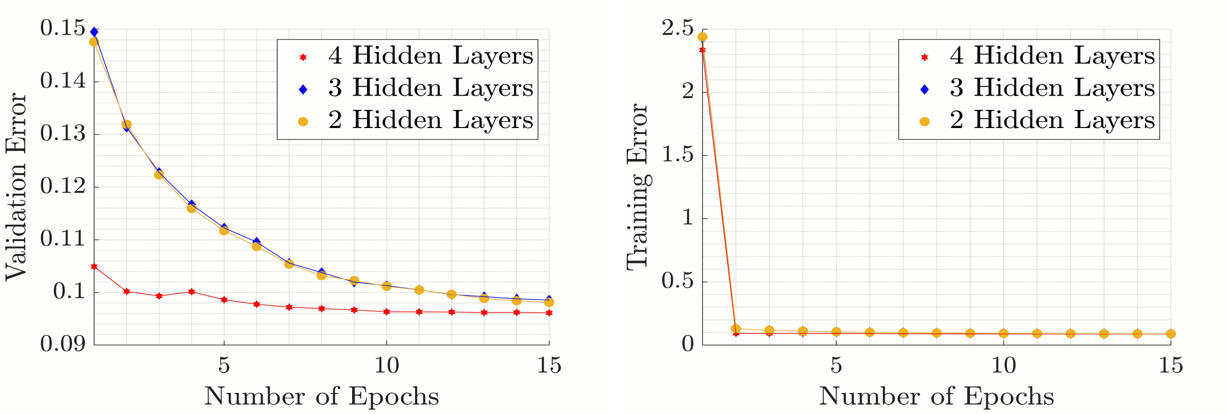

(a) **(b)**

Figure 6.22. MSE loss versus epoch for different hidden layers. (a) Validation error. (b) Training error.

results indicate that $B_S = 4, 16$, or 32 can provide lower MSE, but the runtime for $B_S = 4$ and 16 can be significantly longer than BS= 32, especially for larger datasets with $100,000$ realizations. Therefore, we use $B_S = 32$, which can provide a lower MSE with low computational complexity.

Fig. 6.25 compares the total AR of J-HBF-PSOLPA with low-complexity DL solutions, namely, J-HBF-DLLPA with MSE, and J-HBF-DLLPA with MAE, for $G = 1$, $K = 3$ at $P_T = 20$ dBm. We provide the AR performance evaluations for training, validation, and test datasets. For benchmark comparison, we compare the proposed DL-based solutions with

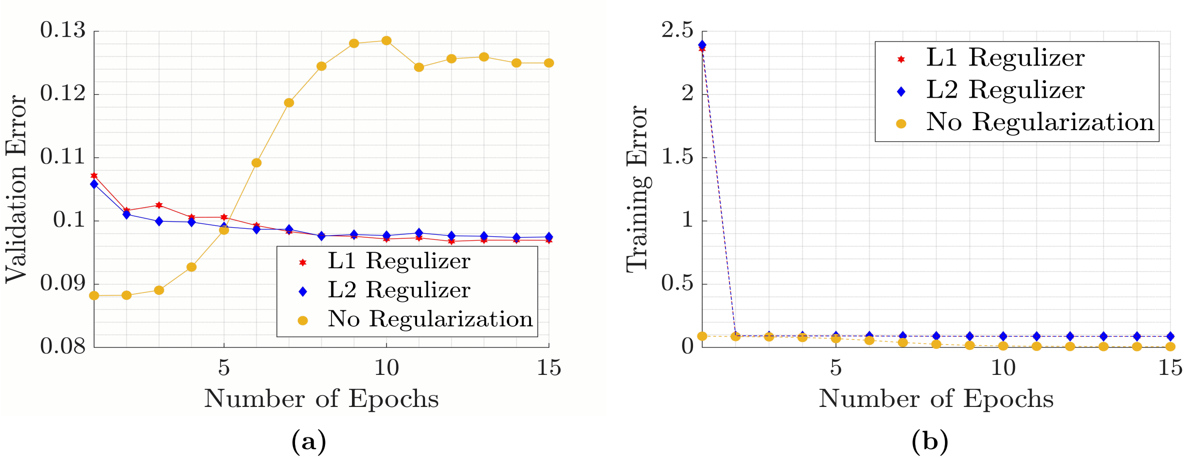

Figure 6.23. MSE loss versus epoch for regularization. (a) Validation error. (b) Training error.

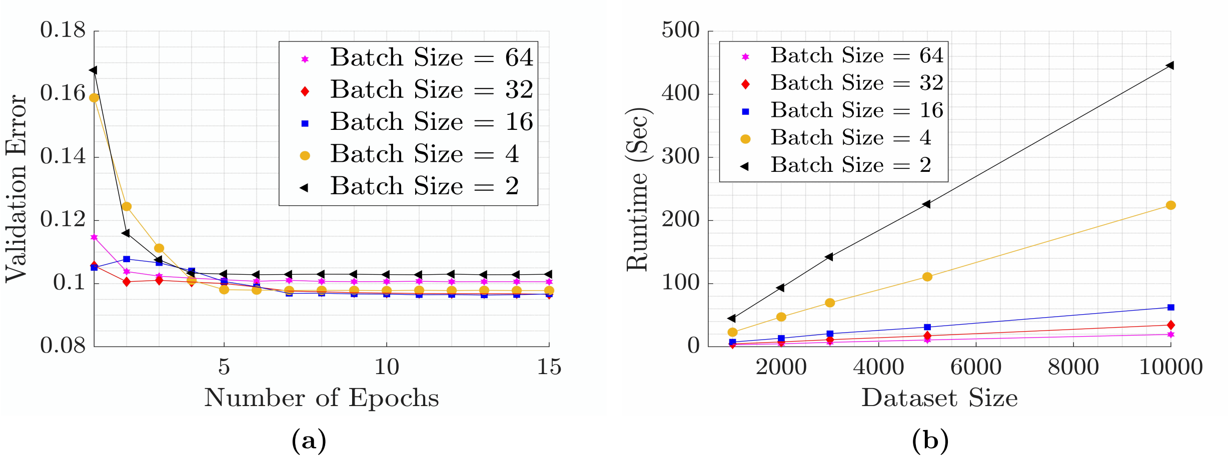

Figure 6.24. MSE loss versus epoch for different batch sizes. (a) Validation error. (b) Runtime.

J-HBF-PSOLPA and FL-EQPA. The numerical results show that both DL-based solutions can achieve AR close to PSO-based solution for all datasets and outperform FL-EQPA. For instance, J-HBF-DLLPA with MSE and MAE can provide the total AR of 14.3 and 14.2 bps/Hz, which is 98.6% and 97.4% of the total capacity achieved by J-HBF-PSOLPA, indicating a performance difference of only 1.3% and 2.06%, respectively. Furthermore, compared to FL-EQPA, both DL-based solutions show more than two-fold increase in AR.

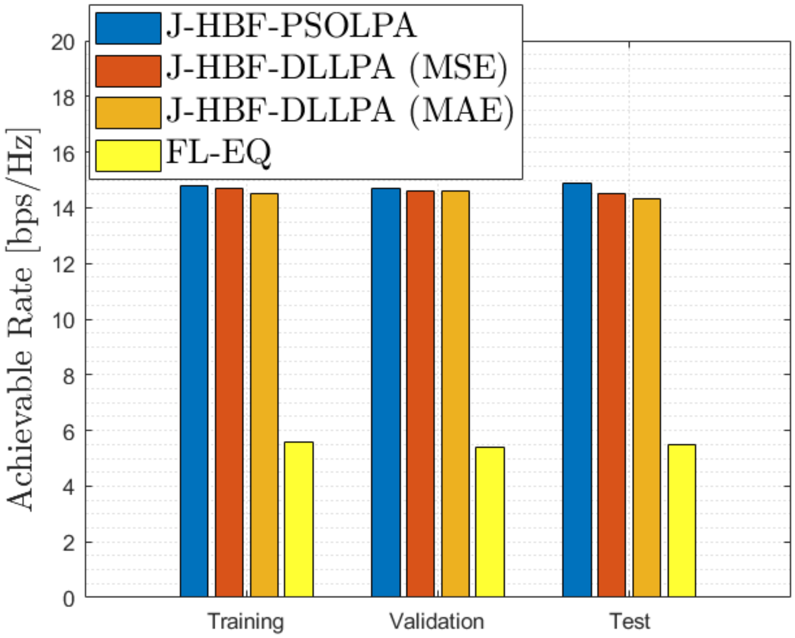

Figure 6.25. Total AR evaluation on training, validation and test dataset for J-HBF-PSOLPA and J-HBF-DLLPA.

6.7.4 Complexity Analysis

In this section, we compare the computational complexity of several proposed solutions for UAV-assisted MU-mMIMO IoT systems. Specifically, we compare: 1) J-HBF-PSOPA-FL; 2) J-HBF-PSOL-EQPA; 3) J-HBF-PSOLPA; and 4) J-HBF-DLLPA. In Fig. 6.26, we present the runtime results for different numbers of IoT users for $G = 2$, where $K = \{2, 4, 6, 8\}$. We provide the runtime for 1000 network realizations for test data. It is noteworthy to mention that the offline trained DNN architecture for J-HBF-DLLPA algorithm run on MATLAB[5]. The proposed J-HBF-DLLPA outperforms the computational complex J-HBF-PSOLPA, J-HBF-PSOL-EQPA, and J-HBF-PSOPA-FL algorithms by significantly reducing the runtime. For example, for a small number of IoT users ($K = 2$), J-HBF-PSOLPA, J-HBF-PSOL-EQPA, and J-HBF-PSOPA-FL take approximately 489, 234, and 376 sec to predict $K + 2$ values, whereas with J-HBF-DLLPA, only about 2 sec are enough to predict the optimal UAV location and power allocation values. This means that the proposed J-HBF-DLLPA with MSE requires only about $0.4\% - 0.8\%$ of the runtime of different PSO-based algorithmic solutions without impacting the total AR

---

[5] For the MATLAB runtime results, we implement both PSO-based J-HBF-PSOLPA and DL-based J-HBF-DLLPA via a PC with Intel Core(TM) i7-4770 CPU @ 3.4 GHz and 32 GB RAM.

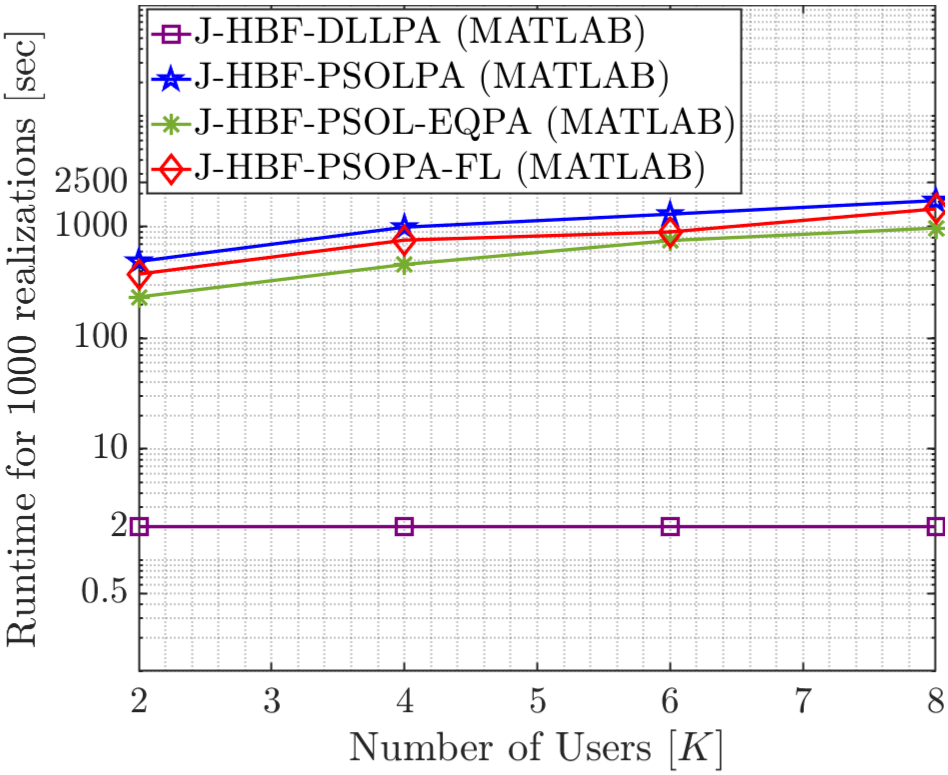

Figure 6.26. Runtime comparison of proposed HBF solutions for different numbers of users.

performance. When the number of IoT users are increased to $K = 8$, then J-HBF-PSOLPA, J-HBF-PSOL-EQPA, and J-HBF-PSOPA-FL can take around 1725, 976, and 1453 sec, representing an increase of approximately 252%, 317%, and 287%, respectively, whereas with the proposed J-HBF-DLLPA, the predictions take only about 2.2 sec, which is $\approx$ 0.127% of runtime of J-HBF-PSOLPA. Then, we consider the computational complexity of the proposed angular-based HBF design. For the RF beamformers $\mathbf{F}_b$ and $\mathbf{F}_{u,r}$ require $\mathcal{O}(N_T)$ and $\mathcal{O}(N_r)$ operations, respectively. Meanwhile, for $\mathbf{F}_{u,t}$, the complexity is $\mathcal{O}(GN_t)$ to serve G different IoT user groups. For BB stages $\mathbf{B}_b$ and $\mathbf{B}_{u,r}$, we require $\mathcal{O}(N^3_{RF_b})$ and $\mathcal{O}(N^3_{RF_u})$ operations, respectively. For $\mathbf{B}_{u,t}$, the complexity is $\mathcal{O}(N^3_{RF_u} + KN^2_{RF_u})$, where $\mathcal{O}(KN^2_{RF_u})$ is for computation of $\boldsymbol{\mathcal{H}}_2^H\boldsymbol{\mathcal{H}}$ and $\mathcal{O}(N^3_{RF_u})$ is for matrix inversion. Overall, the HBF design for BS and UAV requires $\mathcal{O}(N_T + N_r + GN_t + N^3_{RF_b} + N^3_{RF_u} + KN^2_{RF_u})$ operations. Let us consider the J-HBF-PSOPA-FL algorithm, which requires $\mathcal{O}(Z_p)$ to initialize particles and $\mathcal{O}(K^2Z_p)$ operations to find K global solutions. Then, for a total of T PSO iterations, we need $\mathcal{O}(TZ_p(N^3_{RF_u} + KN^2_{RF_u}))$. Ignoring the small computational terms (for instance, matrix multiplication, matrix inversion), the overall computational complexity of J-HBF-PSOPA-FL is $\mathcal{O}(TZ_p(N_{RF_u}^3 + KN_{RF_u}^2))$. Similarly, the complexities of J-HBF-PSOL-EQPA and J-HBF-PSOLPA are computed as $\mathcal{O}(TZ_p(N_T + N_r + GN_t + N_{RF_b}^3 + N_{RF_u}^3 + KN_{RF_u}^2)$ and $\mathcal{O}(TZ_p(N_T + N_r + GN_t + N_{RF_b}^3 + (N_{RF_u}^3 + KN_{RF_u}^2)^2)$, respectively. Now, let us discuss the proposed DNN architecture with the hyper-parameters provided in Table 6.3. The complexity of the training phase can be calculated as follows:

- Forward Pass: 1) the *input layer* has $(2N_t + 2N_{RFu} + 2)K$ neurons, and computing the output of the input layer requires $\mathcal{O}((2N_t + 2NRF_u + 2)K)$ operations; 2) there are four HL with $1024, 512, 256$ and 128 neurons, respectively, and the total complexity of computing the output of each HL can be computed as follows: $\mathcal{O}(1024)$ (layer 1), $\mathcal{O}(512)$ (layer 2), $\mathcal{O}(256)$ (layer 3), $\mathcal{O}(128)$ (Layer 4). Therefore, the total complexity of computing the output of all HL is $\mathcal{O}(1024 + 512 + 256 + 128) = \mathcal{O}(1920)$; 3) the *output layer* has $K + 2$ neurons, so the complexity of final layer is $\mathcal{O}(K + 2)$. The overall complexity of the forward pass is $\mathcal{O}((2N_t + 2N_{RFu} + 2)K + 3840 + K + 2) = \mathcal{O}((2N_t + 2NRF_u + 2)K)$.

- Backward Pass: The backward propagation involves computing gradients of the loss function with respect to the weights and biases of the DNN. The overall complexity of the backward pass is $\mathcal{O}(N_{\text{params}})$, where N_{params} is the total number of parameters in the DNN [6].

- Assuming a batch size of 32 and 15 epochs, the total number of forward and backward passes would be $N_{\text{batch}} \cdot N_{\text{epochs}} = 480$. Therefore, the total computational complexity of the DNN during training phase can be approximated as $\mathcal{O}(N_{\text{params}} N_{\text{batch}} N_{\text{epochs}}) \approx \mathcal{O}(3.42 \cdot 10^{11})$.

Compared to different proposed solutions using PSO, the DNN architecture has a higher computational complexity during training phase, however, once fully trained, the proposed DNN architecture requires only $\mathcal{O}(1)$ operations for predicting $K+2$ output values for a input feature vector of size $(2N_t + 2N_{RF_u} + 2)K$. This is because the complexity is proportional to the number of layers and neurons in each layer, which is a constant value for a trained DNN. Thus, the proposed J-HBF-DLLPA offers a low-complexity solution for real-time applications in UAV-assisted MU-mMIMO IoT systems.

---

[6] The total number of parameters in the DNN can be calculated as follows: (i) input layer to HL 1 : $(2N_t + 2N_{RF_u} + 2)K \times 1024$, (ii) HL 1 to HL 2 : 1024×512, (iii) HL 2 to HL 3 : 512×256, (iv) HL 3 to HL 4 : 256×128, (v) HL 4 to output layer: 128

6.8 Concluding Remarks

In this chapter, a UAV-assisted MU-mMIMO IoT communications system has been considered, where the UAV operates as a decode-and-forward relay between BS and multiple IoT users. The problem of jointly designing the hybrid beamforming stages for BS and UAV together with UAV deployment and optimal power allocation to multiple users is taken into consideration. For this challenging non-convex problem, we have proposed three different PSO-based algorithmic solutions to optimize the UAV location, and the power allocated to IoT users, which are not directly accessible to BS. Then, based on the optimized UAV location, and power allocation, the hybrid beamforming stages for BS and UAV transmit and receive are sequentially updated for a maximum total achievable rate. In particular, the RF stages are designed using the angular location of nodes, reducing the number of RF chains, while the BB stages are designed using reduced-dimension effective channel, which significantly reduces MU interference among IoT nodes. Then, a deep learning-based low-complexity joint hybrid beamforming, UAV location optimization and power allocation scheme (J-HBF-DLLPA) has been proposed for maximizing the achievable rate. The results illustrate that the proposed PSO-based solutions can significantly enhance the capacity of a UAV-assisted MU-mMIMO IoT system as well as reduce the average delay for delay-constrained transmissions. Additionally, the proposed J-HBF-DLLPA can closely approach the capacity of PSO-based solutions and greatly reducing the runtime by 99%, which makes the implementation suitable for real-time online applications in UAV-assisted MU-mMIMO IoT systems.

Chapter 7

Multiple UAV-Assisted Cooperative DF Relaying for Enhanced Coverage and Capacity[1]

7.1 Introduction

In the previous chapter, we consider a single UAV operating as a relay between BS and obscured users, which can provide only limited user coverage and access. On the other hand, a network of multiple UAVs can efficiently enlarge the coverage region and increase the number of served users [172–174]. The authors in [172] propose a multi-UAV relaying system, and compared the performance of a single multi-hop link and multiple dual-hop links. In [173], the position of multiple UAV-mounted BS is optimized to enhance the coverage area, while satisfying quality-of-service (QoS) requirements. Similarly, the placement and the number of UAVs are optimized in [174], while adhering to network capacity and coverage constraints. Research works such as [131, 132, 137, 149, 172–174] have ignored the direct link between the BS and IoT users. However, it is well known that when direct link is non-negligible or not too weak, the spatial diversity can be enhanced via direct and cooperative multiple path (through UAV relays). In practice, assuming no direct link simplifies the design of the joint source-relay beamforming.

In this chapter, we consider a more practical cooperative transmission approach, integrating both the direct link from BS to IoT devices and the indirect links via multiple UAV relays to IoT users in MU-mMIMO IoT systems to enhance the capacity and

---

[1] Parts of this chapter have been presented at the 2024 IEEE International Conference on Communications, Denver, USA [171].

overcome the coverage issues. Our objectives here are twofold: first, to show that the use of multiple UAVs as relays can significantly increase the sum-rate capacity; and second, the optimization of UAV location, user association, and power allocation (PA) at BS and UAVs combined with HBF design can provide better performance than fixed UAV locations with equal PA.

The main contributions of this work are summarized as follows:

- We consider multiple UAVs-assisted cooperative DF relaying mMIMO system, where the users received the signals from both BS and via UAVs. When the direct link is involved, the received signals via source-to-destination link and multiple UAV relay-to-destination links are combined at the destination (user terminal) to enhance the overall signal strength. As such, the beamforming vector design at the BS needs to take into account both of these links. Furthermore, the optimization problem becomes more complex, which is solved using nature-inspired optimization solutions.

- The joint optimization of multiple UAV placements, PA at the BS, and the design of HBF for both the BS and UAVs is considered in this work. To solve the challenging non-convex problem, we utilize structured sequential optimization to address the multi-faceted optimization problem by splitting it into two subproblems. First, K-means-based user clustering is used for UAV-users association based on the 3D geometry-based millimeter-wave (mmWave) channel model. Then, the location of each UAV is optimized jointly with PA using swarm intelligence. The RF beamforming stages for BS and UAVs are designed based on the slow time-varying angle-of-departure (AoD)/angle-of-arrival (AoA) information, and BB stages are formulated using the reduced-dimensional effective channel matrices.

- The illustrative results show that multiple UAV-assisted cooperative relaying systems outperform a single UAV system in practical user distributions. Moreover, compared to fixed positions and equal PA of UAVs and BS, the joint optimization of UAV location and PA substantially enhances the total achievable rate.

The rest of this chapter is organized as follows. Section 7.2 presents the system and channel model of multiple UAV-assisted mMIMO system. In Section 7.3, we present the HBF design jointly with PA and UAV deployment. The illustrative results are provided in Section 7.4. Finally, the chapter is concluded in Section 7.5.

7.2 System and Channel Model

In this section, we introduce the system and channel models of the proposed multi-UAV-assisted relaying and the HBF design for a multiple dual-hop MU-mMIMO IoT system.

7.2.1 System Model

We consider a downlink MU-mMIMO IoT network, where a large number of non-overlapping IoT devices are connected to an IoT gateway via wire or wireless links. Due to severe shadowing and blocking effect, many ground IoT devices experience low signal-quality from the BS/eNodeB that is equipped with a large array having N_b antenna elements. To address this challenging scenario, we consider a cooperative relaying system model as shown in Fig. 7.1(a), to serve $\mathbb{K} = \{1, \cdots, K\}$ single-antenna IoT nodes, which are clustered in G groups, where g^{th} group has K_g IoT nodes such that $K = \sum_{g=1}^{G} K_g$. Then, M_u different UAVs, indexed by the set $\mathbb{U} = \{u_1, u_2, \cdots, u_{M_u}\}$, are deployed to serve $K = M_u K_m$ IoT users, where K_m is number of users served by m^{th} UAV, which operates as DF relay between BS/eNodeB and IoT node[1]. Let (x_b, y_b, z_b), $(x_u^{(m)}, y_u^{(m)}, z_u^{(m)})$ and (x_k, y_k, z_k) denote the locations of BS, m^{th} UAV relay, and k^{th} IoT user, respectively. Then, we define the 3D distances for multiple UAV-assisted MU-mMIMO IoT system as follows:

- $\tau_1^{(m)} = \sqrt{(x_u^{(m)} - x_b)^2 + (y_u^{(m)} - y_b)^2 + (z_u^{(m)} - z_b)^2}$,
- $\tau_{2,k}^{(m)} = \sqrt{(x_u^{(m)} - x_k)^2 + (y_u^{(m)} - y_k)^2 + (z_u^{(m)} - z_k)^2}$,
- $\tau_k = \sqrt{(x_b - x_k)^2 + (y_b - y_k)^2 + (z_b - z_k)^2}$,

where $\tau_1^{(m)}$, $\tau_{2_k}^{(m)}$ and τ_k are the 3D distance between m^{th} UAV & BS, between m^{th} UAV and k^{th} IoT node, and between BS and k^{th} IoT node, respectively. Each UAV is equipped with $N_r (N_t)$ antennas for receiving (transmitting) signals from (to) BS (IoT users). For simplicity, we assume a homogeneous fleet of UAVs with consistent specifications and functionality. Unlike traditional static relaying, which uses fixed relay locations, we presumptively use multiple UAVs as a movable relays.

For the downlink transmission of $N_S = K$ data streams, we consider HBF for BS and all UAV relays as shown in Fig. 7.2. The BS consists of RF beamforming stage $\mathbf{F}_b \in \mathbb{C}^{N_b \times N_{RF_b}}$, BB stage $\mathbf{B}_b \in \mathbb{C}^{N_{RF_b} \times K}$, and MU PA matrix $\mathbf{P}_b = \text{diag}(\sqrt{p_{b_1}}, \cdots, \sqrt{p_{b_K}}) \in \mathbb{C}^{K \times K}$. Here, N_{RF_b} is the RF chains such that $N_S \leq N_{RF_b} \leq N_b$ to guarantee multi-stream

---

[1] We assume equal UAV-user clustering for simplicity. However, it can be applicable for unequal user clustering, which is left as our future work.

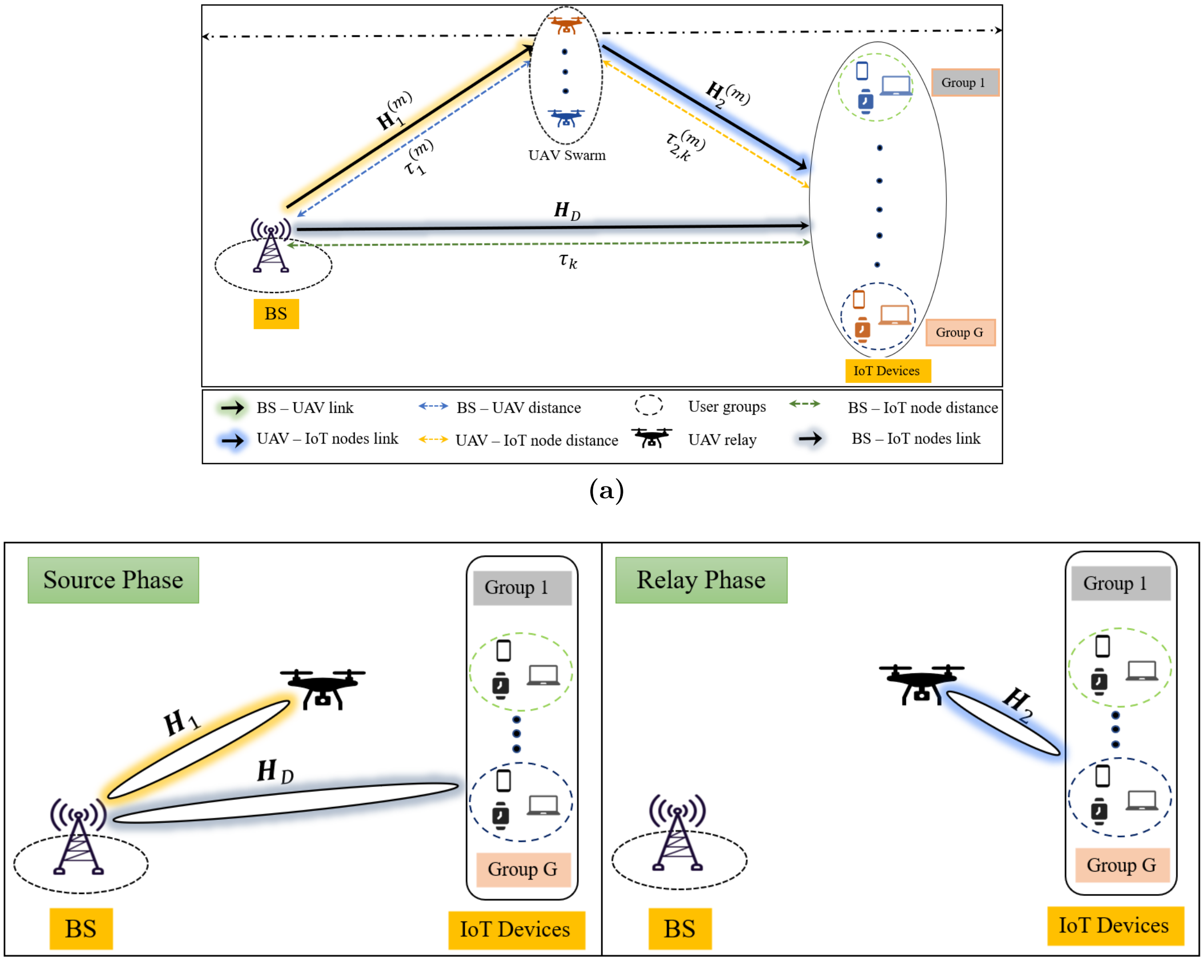

(a)

(b)

Figure 7.1. Multiple UAV-assisted MU-mMIMO IoT communications. (a) network model. (b) UAV as DF relay transmission phases.

transmission. We consider half-duplex (HD) DF relaying for each UAV. Therefore, each round of information transmission from BS to IoT nodes can be divided into two phases: 1) source phase (SP); and 2) relay phase (RP) as illustrated in Fig. 7.1(b). In SP, BS transmits K data streams to the following: 1) K IoT users through channel $\mathbf{H}_D \in \mathbb{C}^{K \times N_b}$; and 2) each m^{th} UAV via channel $\mathbf{H}_1^{(m)} \in \mathbb{C}^{N_r \times N_b}$. Using N_r antennas, each UAV receives signals with RF stage $\mathbf{F}_{u,r}^{(m)} \in \mathbb{C}^{N_{RF_u} \times N_r}$ and BB stage $\mathbf{B}_{u,r}^{(m)} \in \mathbb{C}^{K \times N_{RF_u}}$. In RP, each UAV decodes the received information and then forwards the decoded information to K IoT nodes using RF beamformer $\mathbf{F}_{u,t}^{(m)} \in \mathbb{C}^{N_t \times N_{RF_u}}$, BB stage $\mathbf{B}_{u,t}^{(m)} \in \mathbb{C}^{N_{RF_u} \times K}$, and MU PA matrix $\mathbf{P}_u^{(m)} = \text{diag}(\sqrt{p_{u_1}^{(m)}}, \cdots, \sqrt{p_{u_K}^{(m)}}) \in \mathbb{C}^{K \times K}$ through channel $\mathbf{H}_2^{(m)} \in \mathbb{C}^{K \times N_t}$, where $p_{u_k}^{(m)}$ reflects the allocated power to k^{th} user from m^{th} UAV. The implementation of all RF

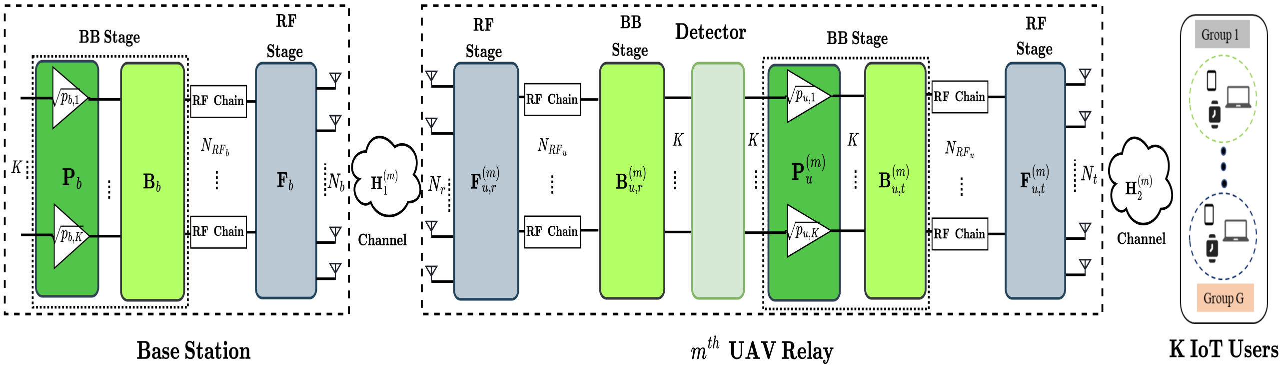

Figure 7.2. Multiple UAV-assisted MU-mMIMO HBF system model.

beamforming/combining stages involves the use of phase-shifters (PSs) and thus, impose a constant-modulus (CM) constraint, i.e., $|\mathbf{F}_b(i,j)| = \frac{1}{\sqrt{N_b}}$, $|\mathbf{F}_{u,r}^{(m)}(i,j)| = \frac{1}{\sqrt{N_r}}$, $|\mathbf{F}_{u,t}^{(m)}(i,j)| = \frac{1}{\sqrt{N_t}}$ $\forall i,j,m$. For the data signal $\mathbf{d} = [d_1, d_2, \cdots, d_K]^T$ with $\mathbb{E}\{\mathbf{d}\mathbf{d}^H\} = \mathbf{I}_K \in \mathbb{C}^{K\times K}$, the signal received at m^{th} UAV (after BB processing) during SP is given as follows:

$$\tilde{\mathbf{y}}_u^{(m)} = \mathbf{B}_{u,r}^{(m)}\mathbf{F}_{u,r}^{(m)}\mathbf{H}_1^{(m)}\mathbf{F}_b\mathbf{B}_b\mathbf{P}_b\mathbf{d} + \mathbf{B}_{u,r}^{(m)}\mathbf{F}_{u,r}^{(m)}\mathbf{n}_u^{(m)}, \tag{7.1}$$

where $n_u^{(m)} \in \mathbb{C}^{N_{u,r}}$ denotes the zero-mean complex circularly symmetric Gaussian noise vector at m^{th} UAV relay with covariance matrix $\mathbb{E}\{\mathbf{n}_u\mathbf{n}_u^H\} = \sigma_{n_u}^2\mathbf{I}_{N_{u,r}} \in \mathbb{C}^{N_{u,r}\times N_{u,r}}$. Then, the signal transmitted by m^{th} UAV during RP is given as:

$$\hat{\mathbf{s}}^{(m)} = \mathbf{F}_{u,t}^{(m)}\mathbf{B}_{u,t}^{(m)}\mathbf{P}_u^{(m)}\hat{\mathbf{d}}^{(m)}, \tag{7.2}$$

where $\hat{\mathbf{d}}^{(m)}$ is the re-encoded signal at m^{th} UAV relay. Each IoT node receives signal from BS and each m^{th} UAV during SP and RP, respectively. Then, the received signal at k^{th} IoT node from BS and m^{th} UAV can be written as:

$$\begin{aligned} y_k^{(m)} &= y_{k,SP} + y_{k,RP}^{(m)}, \\ &= \mathbf{h}_{D,k}^T\mathbf{F}_b\mathbf{B}_b\mathbf{P}_b\hat{d}_k + n_{D_k} + \mathbf{h}_{2,k}^{T(m)}\mathbf{F}_{u,t}^{(m)}\mathbf{B}_{u,t}^{(m)}\mathbf{P}_u^{(m)}\hat{d}_k^{(m)} + n_{2_k}^{(m)}, \\ &= \underbrace{\sqrt{p_{b_k}}\mathbf{h}_{D,k}^T\mathbf{F}_b\mathbf{B}_b\mathbf{P}_b\hat{d}_k + \sqrt{p_{u_k^{(m)}}}\mathbf{h}_{2,k}^{T(m)}\mathbf{F}_{u,t}^{(m)}\mathbf{B}_{u,t}^{(m)}\mathbf{P}_u^{(m)}\hat{d}_k^{(m)}}_{\text{Desired Signal}} + \\ &\underbrace{\sum_{\hat{k}=1}^{K}\sqrt{p_{b_{\hat{k}}}}\mathbf{h}_{D,k}^T\mathbf{F}_b\mathbf{B}_b\mathbf{P}_b\hat{d}_{\hat{k}} + \sum_{\hat{k}=1}^{K}\sqrt{p_{u_k^{(m)}}}\mathbf{h}_{2,k}^{T(m)}\mathbf{F}_{u,t}^{(m)}\mathbf{B}_{u,t}^{(m)}\mathbf{P}_u^{(m)}\hat{d}_{\hat{k}}^{(m)}}_{\text{Total MU-interference}} \\ &+ \underbrace{n_{D_k} + n_{2_k}^{(m)}}_{\text{Total Noise}}, \end{aligned} \tag{7.3}$$

where $n_{D_k} \sim \mathcal{CN}(\mathbf{0}, \sigma_{n_D}^2)$ and $n_{2_k}^{(m)} \sim \mathcal{CN}(\mathbf{0}, \sigma_{n_2}^2)$ are the additive circular symmetric Gaussian noise at k^{th} IoT node. The power constraint of the beamforming matrices can be expressed as $\|\mathbf{F}_b \mathbf{B}_b \mathbf{P}_b\|_F^2 = P_T$ and $\|\mathbf{F}_{u,t}^{(m)} \mathbf{B}_{u,t}^{(m)} \mathbf{P}_u^{(m)}\|_F^2 = P_u^{(m)}$, where P_T and $P_u^{(m)}$ denote the total transmit power of BS and m^{th} UAV, respectively. Then, the achievable rate of first link (i.e., BS → m^{th} UAV) is given as follows:

$$\mathrm{R}_1^{(m)} = \log_2 \left| \mathbf{I}_K + \mathbf{Q}_1^{-1(m)} \mathbf{B}_{u,r}^{(m)} \boldsymbol{\mathcal{H}}_1^{(m)} \mathbf{B}_b \mathbf{B}_b^H \boldsymbol{\mathcal{H}}_1^{H(m)} \mathbf{B}_{u,r}^{H(m)} \right|, \tag{7.4}$$

where $\mathbf{Q}_1^{-1(m)} = (\sigma_{n_u}^2 \mathbf{B}_{u,r}^{(m)} \mathbf{F}_{u,r}^{(m)})^{-1} \mathbf{F}_{u,r}^{H(m)} \mathbf{B}_{u,r}^{H(m)}$ and $\boldsymbol{\mathcal{H}}_1^{(m)} = \mathbf{F}_{u,r}^{(m)} \mathbf{H}_1^{(m)} \mathbf{F}_b$. The signal-to-interference-plus-noise ratio (SINR) of k^{th} IoT node via m^{th} UAV is given as [175]:

$$\gamma_k^{(m)} = \frac{p_{b_k} |\mathbf{h}_{D_k}^H \mathbf{F}_b \mathbf{b}_{b_k}|^2}{\sum\limits_{\hat{k} \neq k} p_{b_{\hat{k}}} |\mathbf{h}_{D_k}^H \mathbf{F}_b \mathbf{b}_{b_{\hat{k}}}|^2 + \sigma_{n_D}^2} + \frac{p_{u_k}^{(m)} |\mathbf{h}_{2_k}^{H(m)} \mathbf{F}_{u,t}^{(m)} \mathbf{b}_{u,t_k}^{(m)}|^2}{\sum\limits_{\hat{k} \neq k} p_{u_{\hat{k}}}^{(m)} |\mathbf{h}_{2_k}^{H(m)} \mathbf{F}_{u,t}^{(m)} \mathbf{b}_{u,t_{\hat{k}}}^{(m)}|^2 + \sigma_{n2}^{2(m)}}. \tag{7.5}$$

The achievable rate for the m^{th} second link (i.e., from m^{th} UAV to K_m users) can be written as:

$$\mathrm{R}_2^{(m)} = \mathbb{E}\Big\{ \sum_{i=1}^{K_m} \log_2 (1 + \gamma_i^{(m)}) \Big\}. \tag{7.6}$$

For multiple dual-hop MU-mMIMO IoT system, where each m^{th} UAV is deployed at a fixed height z_u^m, and relaying data to K_m IoT nodes, the total achievable rate can be maximized by the joint optimization of $\mathbf{F}_b$, $\mathbf{B}_b$, $\mathbf{F}_{u,t}^{(m)}$, $\mathbf{F}_{u,r}^{(m)}$, $\mathbf{B}_{u,t}^{(m)}$, $\mathbf{B}_{u,r}^{(m)}$, $\mathbf{P}_b$, $\mathbf{P}_u^{(m)}$ and the UAV location $\mathbf{x}^{(m)} = [x_o^{(m)}, y_o^{(m)}]^T \in \mathbb{R}^2$, which is to be optimized within the given deployment area. Then, we can formulate the optimization problem as:

$$\begin{aligned}
&\max_{\left\{\mathbf{F}_b, \mathbf{B}_b, \mathbf{F}_{u,t}^{(m)}, \mathbf{B}_{u,t}^{(m)}, \mathbf{F}_{u,r}^{(m)}, \mathbf{B}_{u,r}^{(m)}, \mathbf{P}_b, \mathbf{P}_u^{(m)}, \mathbf{x}^{(m)}\right\}} \quad \mathrm{R}_T \\
&\text{s.t.} \quad C_1 : |\mathbf{F}_{u,t}^{(m)}(i,j)| = \frac{1}{\sqrt{N_t}}, |\mathbf{F}_{u,r}^{(m)}(i,j)| = \frac{1}{\sqrt{N_r}}, \ \forall i, j, m, \\
&\qquad C_2 : |\mathbf{F}_b(i,j)| = \frac{1}{\sqrt{N_b}}, \forall i, j, \\
&\qquad C_3 : \bigcup_{m \in M_u} K_m = K, \quad \forall m, \\
&\qquad C_4 : \mathbb{E}\{\|\mathbf{s}_1\|_2^2\} \leq P_T, \mathbb{E}\{||\hat{\mathbf{s}}^{(m)}||_2^2\} \leq P_T, \forall m, \\
&\qquad C_5 : p_{b_k} \geq 0, p_{u_k}^{(m)} \geq 0, \quad \forall k, m, \\
&\qquad C_6 : \mathbf{x}_{\min} \leq \mathbf{x}_o^{(m)} \leq \mathbf{x}_{\max}, \quad \forall m,
\end{aligned} \tag{7.7}$$

where $\mathrm{R}_T = \sum_{m=1}^{M_u}(1/2)\min(\mathrm{R}_1^{(m)}, \mathrm{R}_2^{(m)})$ is the total achievable rate, C_1 and C_2 refers to the CM constraint due to the use of PSs for UAV and BS, respectively, C_3 ensures that the total user count is consistent with the counts for each UAV, C_4 indicates the total transmit power constraint for UAV and BS, C_5 represents the non-negative allocated power to each IoT node from BS and each UAV, and C_6 implies UAV deployment within the given flying span. Here, $[\mathbf{x}_{\min}, \mathbf{x}_{\max}] = [(x_{\min}, y_{\min}), (x_{\max}, y_{\max})]$ represents the deployment range for each UAV in 2-D space. The optimization problem defined in (7.7) is non-convex and intractable. Thus, we develop a sub-optimal solution for (7.7) in Section III.

7.2.2 Channel Model

We consider mmWave channels for both links. The channel between BS and m^{th} UAV is modeled based on the Saleh-Valenzuela channel model, and is given as:

$$\mathbf{H}_1^{(m)} = \sum_{c=1}^{N_C}\sum_{l=1}^{L} z_{1_{cl}}^{(m)} \tau_{1_{cl}}^{-\eta_o(m)} \mathbf{a}_{1,r}^{(m)}(\theta_{r_{cl}}^{(m)}, \phi_{r_{cl}}^{(m)}) \mathbf{a}_{1,t}^{T(m)}(\theta_{t_{cl}}^{(m)}, \phi_{t_{cl}}^{(m)}), \tag{7.8}$$

where N_C is the total number of clusters, L is the total number of paths, η_o is the path loss exponent, $z_{1_{cl}}^{(m)}$ is the complex gain of l^{th} path in c^{th} cluster for m^{th} UAV, and $\mathbf{a}_{1,j}^{(m)}(\cdot,\cdot)$ is the corresponding transmit or receive array steering vector for uniform rectangular array (URA), which is given as [134]:

$$\mathbf{a}_{1,j}^{(m)}(\theta^{(m)}, \phi^{(m)}) = \Big[1, \cdots, e^{-j2\pi d(N_x-1)\sin(\theta^{(m)})\cos(\phi^{(m)})}\Big] \otimes \Big[1, \cdots, e^{-j2\pi d(N_y-1)\sin(\theta^{(m)})\sin(\phi^{(m)})}\Big], \tag{7.9}$$

where $j = \{t, r\}$, d is the inter-element spacing, and $N_x(N_y)$ is the horizontal (vertical) size of corresponding antenna array at BS and UAV. Here, the angles $\theta_{j_{cl}}^{(m)} \in \Big[\theta_{j_c}^{(m)} - \delta_{j_c}^{\theta(m)}, \theta_{j_c}^{(m)} + \delta_{j_c}^{\theta(m)}\Big]$ and $\phi_{j_{cl}}^{(m)} \in \Big[\phi_{j_c}^{(m)} - \delta_{j_c}^{\phi(m)}, \phi_{j_c}^{(m)} + \delta_{j_c}^{\phi(m)}\Big]$ are the azimuth and elevation AoD($j = t$) or AoA ($j = r$) for l^{th} path in channel $\mathbf{H}_1^{(m)}$, respectively. Here, $\theta_{j_c}^{(m)}$ and $\phi_{j_c}^{(m)}$ are the mean azimuth and elevation angles, respectively with $\delta_{j_c}^{\theta(m)}$ ($\delta_{j_c}^{\phi(m)}$) represents the azimuth(elevation) angle spread. The channel vector between the UAV(or BS) and the k^{th} IoT node can be written as:

$$\mathbf{h}_{i,k}^T = \textstyle\sum_{q=1}^{Q} z_{i,k_q}\tau_{i,k_q}^{-\eta}\mathbf{a}(\theta_{k_q}, \phi_{k_q}) = \mathbf{z}_{i,k}^T\mathbf{A}_{i,k} \in \mathbb{C}^N, \tag{7.10}$$

where $i = \{D, 2\}$, Q is the total number of downlink paths from UAV(or BS) to IoT nodes, $z_{i,k_l} \sim \mathcal{CN}(0, \frac{1}{L})$ is the complex path gain of l^{th} path, $\mathbf{a}(\cdot,\cdot) \in \mathbb{C}^N$ is the downlink array phase response vector. Then, the complete channel matrix for K IoT nodes can be written as:

$$\mathbf{H}_i = [\mathbf{h}_{i,1}, \cdots, \mathbf{h}_{i,K}]^T = \mathbf{Z}_i \mathbf{A}_i \in \mathbb{C}^{K \times N_t}, \tag{7.11}$$

where $\mathbf{Z}_i = [\mathbf{z}_{i,1}, \cdots, \mathbf{z}_{i,K}]^T \in \mathbb{C}^{K \times L}$ is the complete path gain matrix for all downlink IoT nodes and $\mathbf{A}_{i,k} \in \mathbb{C}^{L \times N}$ is the slow time-varying array phase response matrix.

7.3 Proposed Joint User Association, Multiple UAV Positioning, PA & Hybrid Beamforming

In this section, our objective is to optimize each UAV location jointly with PA from BS and UAV, and sequentially design HBF stages for BS and each UAV to reduce the channel state information (CSI) overhead size while maximizing the throughput of a multiple UAV-assisted MU-mMIMO IoT system. First, we discuss the UAV-user association using K-means-based user clustering.

7.3.1 UAV-User Association

The proposed scheme leverages K-means-based user association to assign K_m users to nearest m^{th} UAV while maintaining exclusive user-UAV associations. The objective is to minimize the sum of squared distances between users and their assigned m^{th} UAV (i.e., $\min \sum_{m=1}^{M} \sum_{k=1}^{K} z_{km} ||\mathbf{x}_k - \mathbf{x}_u^{(m)}||^2$). Here, z_{km} is the assignment variable, which is defined as:

$$z_{km} = \begin{cases} 1, & \text{if user } k \text{ is assigned to UAV } m, \\ 0, & \text{otherwise.} \end{cases} \tag{7.12}$$

7.3.2 Joint UAV Deployment, Optimal PA and HBF Design

In this section, our objective is to design the HBF stages for BS and M UAVs by using sequential optimization. Initially, both RF and BB stages are constructed using some fixed UAV locations. Then, we employ swarm intelligence to optimize each UAV location as well as PA from BS and each UAV for maximum total achievable rate. Finally, the RF and BB stages are re-formulated for the optimal UAV location as well as the allocated power in the MU PA blocks $\mathbf{P}_b$ and $\mathbf{P}_u^{(m)}$.

7.3.2.1 RF & BB Stage Design

The RF beamforming stage for BS and each UAV (both transmit and receive) are designed as:

$$\mathbf{F} = \left[\mathbf{e}_j\left(\lambda_x^{u_1}, \lambda_y^{k_1}\right), \cdots, \mathbf{e}_j\left(\lambda_x^{u_{N_{RF}}}, \lambda_y^{k_{N_{RF}}}\right)\right] \in \mathbb{C}^{N_T \times N_{RF}}, \tag{7.13}$$

where $j = \{t, r\}$ and $\mathbf{e}(\cdot,\cdot)$ is the corresponding transmit or receive steering vector, which is defined as $\mathbf{e}\left(\theta, \phi\right) = \frac{1}{\mathcal{N}_t}\left[1, e^{j2\pi d \sin(\theta)\cos(\phi)}, \cdots, e^{j2\pi d(\mathcal{N}_{x,t}-1)\sin(\theta)\cos(\phi)}\right]^T \otimes \left[1, e^{j2\pi d \sin(\theta)\sin(\phi)}, \cdots, e^{j2\pi d(\mathcal{N}_{y,t}-1)\sin(\theta)\sin(\phi)}\right]^T$, where $\mathcal{N}_T = \{N_b, N_t, N_r\}$. Here, the RF beamformers are constructed via quantized angle-pairs, which are defined as $\lambda_x^u = -1 + \frac{2u-1}{\mathcal{N}_{x,t}}$ for $u = 1, \cdots, \mathcal{N}_{x,t}$ and $\lambda_y^k = -1 + \frac{2k-1}{\mathcal{N}_{y,t}}$ for $k = 1, \cdots, \mathcal{N}_{y,t}$. The quantized angle-pairs reduces the number of RF chains at BS and each UAV while providing complete AoD/AoA supports, which are defined as:

$$\text{AoD} = \left\{\sin\left(\theta\right)\left[\cos\left(\phi\right), \sin\left(\phi\right)\right]\Big|\theta \in \boldsymbol{\theta}_t, \phi \in \boldsymbol{\phi}_t\right\}, \tag{7.14}$$

$$\text{AoA} = \left\{\sin\left(\theta\right)\left[\cos\left(\phi\right), \sin\left(\phi\right)\right]\Big|\theta \in \boldsymbol{\theta}_r, \phi \in \boldsymbol{\phi}_r\right\}, \tag{7.15}$$

where $\boldsymbol{\theta}_i = \left[\theta_i - \delta_i^\theta, \theta_i + \delta_i^\theta\right]$ and $\boldsymbol{\phi}_i = \left[\phi_i - \delta_i^\phi, \phi_i + \delta_i^\phi\right]$ denote the azimuth and elevation angle supports, respectively. After designing the transmit and receive RF beamformers for BS, and each UAV, the effective channel matrices $\boldsymbol{\mathcal{H}}_1^{(m)}$ and $\boldsymbol{\mathcal{H}}_2^{(m)}$ as seen from the BB-stages are given as follows:

$$\boldsymbol{\mathcal{H}}_1^{(m)} = \mathbf{F}_{u,r}^{(m)}\mathbf{H}_1^{(m)}\mathbf{F}_b = \mathbf{U}_1^{(m)}\boldsymbol{\Sigma}_1^{(m)}\mathbf{V}_1^{H(m)}, \tag{7.16}$$

$$\boldsymbol{\mathcal{H}}_2^{(m)} = \begin{bmatrix} \mathbf{H}_{2,1}^{(m)}\mathbf{F}_{u,t,1}^{(m)} & \dots & \mathbf{H}_{2,1}^{(m)}\mathbf{F}_{u,t,G}^{(m)} \\ \vdots & \ddots & \vdots \\ \mathbf{H}_{2,G}^{(m)}\mathbf{F}_{u,t,1}^{(m)} & \dots & \mathbf{H}_{2,G}^{(m)}\mathbf{F}_{u,t,G}^{(m)} \end{bmatrix}, \tag{7.17}$$

where $\mathbf{U}_i^{(m)} \in \mathbb{C}^{N_{RF_u} \times rank(\boldsymbol{\mathcal{H}}_1^{(m)})}$ and $\mathbf{V}_i^{(m)} \in \mathbb{C}^{N_{RF_b} \times rank(\boldsymbol{\mathcal{H}}_1^{(m)})}$ are tall unitary matrices and $\boldsymbol{\Sigma}_1^{(m)}$ is the diagonal matrix with singular values in the decreasing order for m^{th} UAV. Then, $\mathbf{B}_{u,r}^{(m)}$ for m^{th} UAV is defined as:

$$\mathbf{B}_{u,r}^{(m)} = \mathbf{U}_1^{H(m)}. \tag{7.18}$$

The reduced-size effective CSI $\boldsymbol{\mathcal{H}}_2^{(m)}$ given in (7.17) is employed for designing $\mathbf{B}_{u,t}^{(m)}$ by using regularized zero-forcing (RZF) technique, and is defined as follows:

$$\mathbf{B}_{u,t}^{(m)} = (\boldsymbol{\mathcal{H}}_2^{H(m)}\boldsymbol{\mathcal{H}}_2^{(m)} + \alpha^{(m)} N_{RF_u}\mathbf{I}_{N_{RF_u}})^{-1}\boldsymbol{\mathcal{H}}_2^{H(m)}, \tag{7.19}$$

where $\alpha^{(m)} = \frac{\sigma^{2(m)}}{P_T^{(m)}}$ is the regularization parameter and $\mathbf{I}_{N_{RF_u}} \in \mathbb{C}^{N_{RF_u} \times N_{RF_u}}$. The optimal design of $\mathbf{B}_b$ is formulated using an effective channel $\boldsymbol{\mathcal{H}}_{1D}$, which constitutes all channel components from BS (i.e., $\mathbf{H}_D$ and $\mathbf{H}_2^{(m)}, \forall m = 1, \cdots, M$). Then, the total effective channel can be written as:

$$\boldsymbol{\mathcal{H}}_{1D} = [\mathbf{H}_D, \mathbf{H}_1^{(1)}, \mathbf{H}_1^{(2)}, \cdots, \mathbf{H}_1^{(M)}] \in \mathbb{C}^{(MN_r+K) \times K}. \tag{7.20}$$

By using SVD of effective channel $\boldsymbol{\mathcal{H}}_{1D}$, we can design $\mathbf{B}_b$ by using tall unitary matrix $\mathbf{V}_{1D} \in \mathbb{C}^{N_{RF_b} \times rank(\boldsymbol{\mathcal{H}}_{1D})}$ as [134]:

$$\mathbf{B}_b = \sqrt{\frac{P_T}{K}} \mathbf{V}_{1D} \in \mathbb{C}^{N_{RF_b} \times K}. \tag{7.21}$$

7.3.2.2 Joint Multiple UAV Positioning and Optimal PA

After the design of RF and BB stages for BS and UAVs, the optimization problem given in (7.7) can be reformulated as:

$$\begin{aligned} \max_{\left\{\mathbf{P}_b, \mathbf{P}_u^{(m)}, \mathbf{x}^{(m)}\right\}} \quad & \mathrm{R}_T \\ \text{s.t.} \quad & C_4 - C_6. \end{aligned} \tag{7.22}$$

This resulting problem in (7.22) is still non-convex due to the joint dependence of both the allocated powers p_{b_k}, $p_{u_k}^{(m)}$ and the UAV location $\mathbf{x}^{(m)} = [x_o^{(m)}, y_o^{(m)}]^T$ on the SINR expression in (7.5), which is used in the sum-rate $\mathrm{R}_2^{(m)}$ calculation as given in (7.6). To overcome this challenge, we propose sequential optimization using swarm intelligence, which employs multiple agents, called particles, to explore the search space of objective function given in (7.22). Initially, Z particles are randomly placed in search space, where each particle communicates with other particles to share their personal best and update the current global best solution for the objective function. The particles then move iteratively for T iterations to reach the global optimum solution. In particular, each UAV location $\mathbf{x}_u^{(m)} = [x_u^{(m)}, y_u^{(m)}]^T$ and $\mathbf{P}_b$, $\mathbf{P}_u^{(m)}$ are optimized by using particle swarm optimization (PSO)-based algorithmic solution while maximizing the total achievable rate. Here, the z^{th} particle at the t^{th} iteration now represents an instance of the each UAV location and multi-user PA matrices, which is given as follows:

$$\begin{aligned}\mathbf{J}^{(t)}_{p_z} = [\mathbf{X}^{(t)}_z, \hat{\mathbf{P}}^{(t)}_{b_z}, \hat{\mathbf{P}}^{(t)}_{u_z}]^T = [&x^{(t)}_{1_z}, y^{(t)}_{1_z}, \cdots, x^{(t)}_{M_z}, y^{(t)}_{M_z}, \sqrt{\hat{p}^{(t)}_{b,1_z}}, \cdots, \sqrt{\hat{p}^{(t)}_{b,K_z}}, \cdots, \\ &\cdots, \sqrt{\hat{p}^{(t)}_{u_1,1_z}}, \cdots, \sqrt{\hat{p}^{(t)}_{u_1,K_z}}, \cdots, \sqrt{\hat{p}^{(t)}_{u_M,1_z}}, \cdots, \sqrt{\hat{p}^{(t)}_{u_M,K_z}}]^T \in \mathbb{R}^{2K+2M},\end{aligned} \tag{7.23}$$

where each particle z represents the M_u UAV positions and PA to K IoT users from BS and each m^{th} UAV, and calculates the objective function as $R_T(\mathbf{F}_b, \mathbf{B}_b, \mathbf{F}^{(m)}_{u,t}, \mathbf{B}^{(m)}_{u,t}, \mathbf{F}^{(m)}_{u,r}, \mathbf{B}^{(m)}_{u,r}, \kappa^{(t)}_{b_z}\hat{\mathbf{P}}^{(t)}_{b_z}, \kappa^{(t)}_{u_z}\hat{\mathbf{P}}^{(t)}_{u_z}, \mathbf{X}^{(t)}_z)$. We define $\hat{\mathbf{P}}^{(t)}_{b_z} = \text{diag}(\sqrt{\hat{p}^{(t)}_{b,1_z}}, \cdots, \sqrt{\hat{p}^{(t)}_{b,K_z}}) \in \mathbb{R}^{K\times K}$ and $\hat{\mathbf{P}}^{(t)}_{u_z} = [\hat{\mathbf{P}}^{(t)}_{u_{1_z}}, \cdots, \hat{\mathbf{P}}^{(t)}_{u_{M_z}}]$, where $\hat{\mathbf{P}}^{(t)}_{u_{m_z}} = \text{diag}(\sqrt{\hat{p}^{(t)}_{u_m,1_z}}, \cdots, \sqrt{\hat{p}^{(t)}_{u_m,K_z}}) \in \mathbb{R}^{K\times K}$ as the normalized PA matrices with $\hat{p}^{(t)}_{b,k_i}$, $\hat{p}^{(t)}_{u_m,k_z} \in [0,1]$. Then, the transmit power constraints for $\hat{\mathbf{P}}^{(t)}_{b_z}$ and $\hat{\mathbf{P}}^{(t)}_{u_z}$ are satisfied by defining $\mathbf{P}^{(t)}_{b_z} = \kappa^{(t)}_{b_z}\hat{\mathbf{P}}^{(t)}_{b_z}$ and $\mathbf{P}^{(t)}_{u_z} = \kappa^{(t)}_{u_z}\hat{\mathbf{P}}^{(t)}_{u_z}$. The position $\mathbf{J}^{(t)}_{p_z}$ and velocity $\mathbf{J}^{(t)}_{v_z}$ for i^{th} particle during t^{th} iteration are updated as follows:

$$\mathbf{J}^{(t+1)}_{p_z} = \mathbf{J}^{(t)}_{p_z} + \mathbf{J}^{(t+1)}_{v_z}, \tag{7.24}$$

$$\mathbf{J}^{(t+1)}_{v_i} = \gamma_1 \mathbf{Y}^{(t)}_1 (\mathbf{J}^{(t)}_{p_{\text{best}}} - \mathbf{J}^{(t)}_{p_i}) + \gamma_2 \mathbf{Y}^{(t)}_2 (\mathbf{J}^{(t)}_{p_{\text{best}_i}} - \mathbf{J}^{(t)}_{p_i}) + \gamma^{(t)}_3 \mathbf{J}^{(t)}_{v_i}. \tag{7.25}$$

Finally, the personal and global best solutions for z^{th} particle during t^{th} iteration are obtained as follows:

$$\begin{aligned}\mathbf{J}^{(t)}_{p_{\text{best}_z}} = \underset{\mathbf{J}^{(t^*)}_{p_z}, \forall t^*=0,1,\cdots,t}{\arg\max} \; & R_T(\mathbf{F}_b, \mathbf{B}_b, \mathbf{F}^{(m)}_{u,t}, \mathbf{B}^{(m)}_{u,t}, \mathbf{F}^{(m)}_{u,r}, \cdots, \\ & \cdots, \mathbf{B}^{(m)}_{u,r}, \kappa^{(t^*)}_{b_z}\hat{\mathbf{P}}^{(t^*)}_{b_z}, \kappa^{(t^*)}_{u_z}\hat{\mathbf{P}}^{(t^*)}_{u_z}, \mathbf{X}^{(t^*)}_z),\end{aligned} \tag{7.26}$$

$$\begin{aligned}\mathbf{J}^{(t)}_{p_{\text{best}}} = \underset{\mathbf{J}^{(t)}_{p_{\text{best}_z}}, \forall z=0,1,\cdots,Z}{\arg\max} \; & R_T(\mathbf{F}_b, \mathbf{B}_b, \mathbf{F}^{(m)}_{u,t}, \mathbf{B}^{(m)}_{u,t}, \mathbf{F}^{(m)}_{u,r}, \cdots, \\ & \cdots, \mathbf{B}^{(m)}_{u,r}, \kappa^{(t)}_{\text{best},b_z}\hat{\mathbf{P}}^{(t)}_{\text{best,b}_z}, \kappa^{(t)}_{\text{best},u_z}\hat{\mathbf{P}}^{(t)}_{\text{best,u}_z}, \mathbf{X}^{(t)}_z).\end{aligned} \tag{7.27}$$

After T iterations, we update $\mathbf{x}^{(m)} = \mathbf{X}^{(T)}_{\text{best}}$, $\mathbf{P}_b = \kappa^{(T)}_{\text{best},b}\hat{\mathbf{P}}^{(T)}_{\text{best},b}$ and $\mathbf{P}^{(m)}_u = \kappa^{(T)}_{\text{best},u}\hat{\mathbf{P}}^{(T)}_{\text{best},u}$.

7.4 Illustrative Results

In this section, the Monte-Carlo simulation results are presented based on the proposed scheme. Table I outlines the simulation setup based on the 3D micro-cell scenario [134] for the results discussed hereafter. The PSO parameters are chosen as: N_p=20, γ_1=γ_2= 2 and γ_3=

Table 7.1. Simulation Parameters

Number of antennas		$(N_b, N_r, N_t) = 64$	
Number of paths	Path loss exponent	$L = 10$	3.6
Frequency	Channel Bandwidth	28 GHz	100 MHz
Noise PSD	Number of UAVs M	−174 dBm/Hz	2 or 3
BS	UAV height	10 m	20 m
UAV x-axis range	UAV y-axis range	$[x_{min}, x_{max}] = [0, 100]\,m$	$[y_{min}, y_{max}] = [0, 100]\,m$
Azimuth AoD/AoA (1^{st} link)	Azimuth AoD/AoA (2^{nd} link)	120°	150°
Elevation AoD/AoA (1^{st} link)	Elevation AoD/AoA (2^{nd} link)	60°	30°
Azimuth/Elevation Angle Spread	# of network realizations	±10°	2000

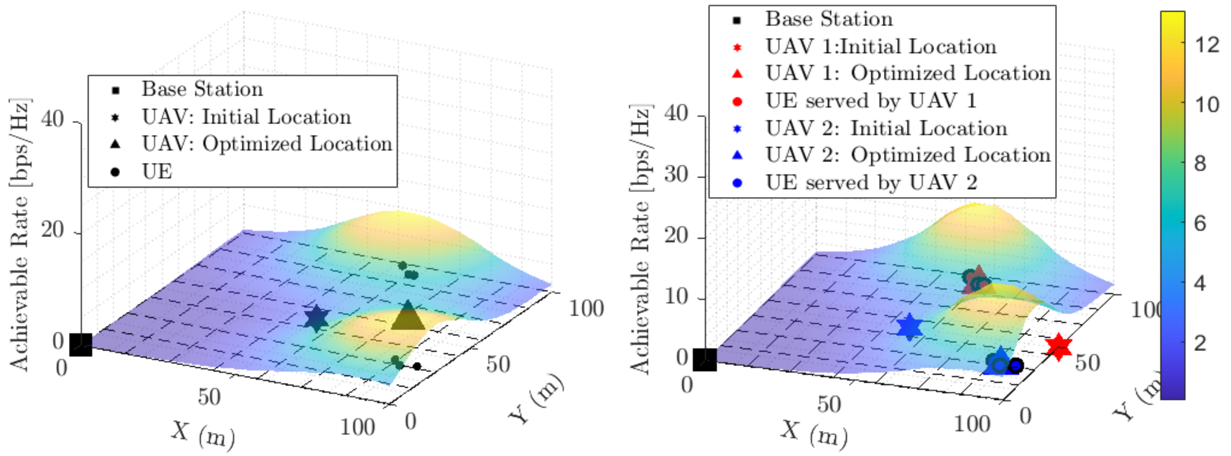

(a) **(b)**

Figure 7.3. Achievable rate R_2 versus $(x-y)$-coordinates at $P_T^{(m)} = 20$ dBm. (a) Single UAV deployment ($M_u = 1$). (b) Multiple UAV deployment ($M_u = 2$).

1.1. In Fig. 7.3(a), we compare the achievable rate R_2 versus transmit power for the following two cases: 1) a single UAV ($M = 1$) deployed at initial fixed location $(x_u, y_u) = (50, 50)$; and 2) multiple UAVs ($M = 2$) deployed at initial fixed locations $(x_u^{(1)}, y_u^{(1)}) = (50, 50)$, $(x_u^{(2)}, y_u^{(2)}) = (100, 50)$. We consider a practical user distribution scenario where the users are located at multiple locations (i.e., $(x_k, y_k) \in$ [50,100]) from BS, which is located at $(x_b, y_b) = (0, 0)$. It can be seen from Fig. 7.3(a) that the proposed scheme can optimize the UAV location, however, it can only achieve a sub-optimal solution as a single UAV can not be positioned optimally to support a large number of users. Moreover, each k^{th} user experience interference from $K-1$ users, which leads to low achievable rate. To improve the performance, a multiple UAV-assisted system (i.e., $M = 2$) is used in Fig. 7.3(b), where each UAV can support $K_m = K/M$ users based on the proposed scheme and find the optimal deployments close to its associated K_m users. It can be seen that using the proposed PSO-

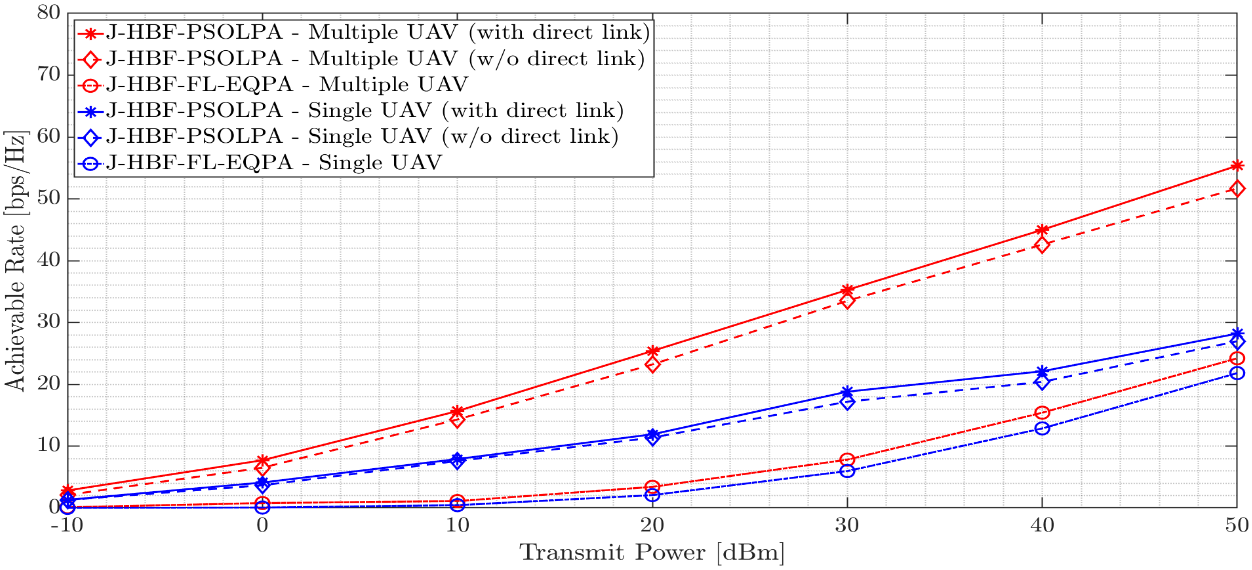

Figure 7.4. Total AR R_T versus P_T for single and multiple UAV system.

based UAV location and PA (J-HBF-PSOLPA) scheme, each UAV can optimally cluster its users, and then find the optimal deployment while achieving the maximum achievable rate. Thus, a multiple UAV-assisted MU-mMIMO system can overcome the coverage and capacity limitation of a single UAV in more practical scenarios.

Fig. 7.4 compares the achievable rate of a multiple UAV system versus a single UAV system for the following cases: 1) J-HBF-PSOLPA with direct link from BS (we consider optimal PA at each UAV while considering equal PA from BS); 2) J-HBF-PSOLPA without direct link from BS; and 3) fixed UAV location and equal PA (FL-EQPA). It can be seen that by using $M = 2$ UAV can provide approximately 2.5 times the achievable rate when compared to a single UAV case ($M = 1$). For instance, the achievable rate at $P_T = 50$ dBm is increased from 27 bps/Hz to 58 bps/Hz, which indicates around 250% increase in total achievable rate. Moreover, compared to FL-EQPA, the proposed scheme can significantly enhance the performance by optimizing the UAV locations and the allocated powers. The inclusion of direct link from BS to users (i.e., cooperative relaying) can provide an additional 4 to 5 bps/Hz rate improvement for all cases. Fig. 7.5 compares the achievable rate for different number of UAVs (i.e., for $M = 2$ or $M = 3$) for the following four cases: 1) J-HBF-PSOLPA with direct link and optimal PA at BS and each UAV; and 2) J-HBF-PSOLPA with direct link and optimal PA at each UAV only; 3) J-HBF-PSOLPA without direct link; and 4) J-HBF-FL-EQPA. The analysis can be summarized as follows: 1) the optimal PA from BS and each UAV can provide an improved performance (e.g., an increase of $\approx 10\%$ rate) when compared to only optimal PA at each UAV; 2) by increasing the number of UAVs,

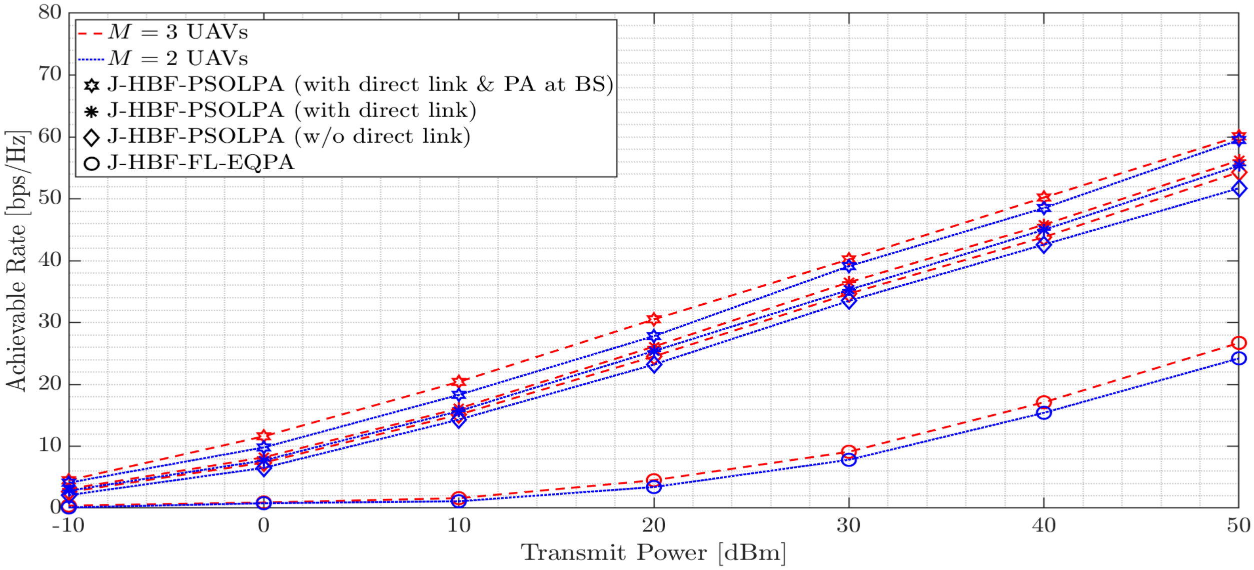

Figure 7.5. Total AR R_T versus P_T for 2 and 3 UAV system.

we can achieve a higher achievable rate (e.g., the rate can be increased by 5-7% when M is increased from 2 to 3). Moreover, by increasing the number of UAVs, we can further improve the performance as each UAV cluster less number of users, which leads to reduced MU interference, and thus, an increased achievable rate. However, it must be noted that optimizing the number of UAVs is beyond the scope of this research, and is left as our future work.

7.5 Concluding Remarks

In this chapter, we considered a MU-mMIMO IoT cooperative relaying system, where multiple UAV DF relays connect the BS to a large number of users. We have proposed a sequential optimization scheme that employed swarm intelligence to assign users to UAVs through K-means clustering, and optimized the UAV locations and power allocation from BS and each UAV, followed by the design of RF and BB stages for maximum achievable rates. The RF stages are designed using the angular information of UAVs and users, while BB stages are designed using reduced-dimension effective channel matrices. Our findings show that multiple UAV-assisted cooperative relaying system works better than single UAV, especially when taking into account the practical user distributions. Moreover, compared to fixed positions and equal power distribution of UAV, the optimization of UAV locations and power allocation substantially improves the achievable rate.

Chapter 8

Conclusions

In this chapter, we first present a detailed summary of the main contributions in this thesis, then discuss some potential research directions as future works.

8.1 Summary

Massive MIMO is a pivotal technology for enhancing coverage and capacity in 5G and beyond wireless communications networks. By using large antenna arrays at BS, mMIMO enables 3D beamforming, leading to improved capacity, higher energy efficiency, and reduced interference. However, conventional single-stage fully digital beamforming techniques face challenges such as high hardware cost and substantial channel estimation overhead due to the need for dedicated RF chains per antenna. Two-stage hybrid beamforming (HBF) is proposed as a solution, employing fewer RF chains to interconnect analog RF beamformers and digital baseband precoders/combiners, thereby addressing these issues. However, despite effective HBF solutions, future wireless systems require supporting a large number of users (both terrestrial and aerial) for different IoT applications. Most traditional mMIMO systems often use uniform linear arrays (ULA), which are spatially inefficient and limited in their ability to illuminate both azimuth and elevation angles, thus unable to support aerial communications. This limitation also affects the ability to serve a large number of users, especially in varying angular locations (e.g., to serve ground users as well as aerial users simultaneously). According to ITU's IMT-2030 (6G) framework, which highlights the need for enhanced capabilities (e.g., peak data rate, latency, connection density, mobility, and reliability) and new capabilities (e.g., ubiquitous coverage, sensing, sustainability, resilience, and positioning), the future wireless networks are expected to adopt integrated terrestrial and non-terrestrial network (NTN) architectures, which can provide high data rates with enhanced coverage. In this thesis, we have proposed different HBF techniques for both terrestrial and UAV-assisted terrestrial communications for mMIMO systems to address various objectives, such as interference mitigation, sum-rate maximization, energy efficiency, enhanced SIS, and low channel estimation overhead.

In Chapter 3, we have investigated different 2D array configurations to be used at BS for enhanced capacity in mMIMO systems. We have considered three different HBF architectures, which are as follows: (i) HBF using full-resolution PSs and DACs with a baseband transfer block for constant-modulus RF beamformer, (ii) HBF using b-bit PSs and full-resolution DACs with an orthogonal matching pursuit (OMP) based algorithm that can approach the optimal unconstrained RF beamformer, and (iii) HBF using b-bit PSs and q-bit DACs, which takes into account the DAC quantization noise. In these proposed HBF schemes, our objectives are not only to reduce the hardware cost/complexity by utilizing a limited number of RF chains but also to lower the CSI overhead size by designing RF-stage via slow time-varying CSI (i.e., angular information). Then, we have used the reduced-size effective CSI to design the BB-stage for reduced multi-user interference (MUI). The illustrative results compare the spatial, spectral and energy efficiencies of HBF designs for different antenna-arrays. Specifically, the concentric circular array (CCA) can achieve much higher performance than other 2-D array configurations. Furthermore, we also show that the proposed HBF schemes achieve higher sum-rate and energy efficiency than other HBF benchmarks.

Chapter 4 has extended the comparison to different three-dimensional (3D) array structures in mMIMO systems. Here, we have studied the performance of uniform rectangular array (URA), cylindrical array (CA), hemi-spherical array (HSA), and spherical array (SA). The proposed HBF scheme involves two stages: (i) RF beamforming based on singular value decomposition (SVD) of the channel matrix, and baseband MU precoding based on the instantaneous effective baseband channel to mitigate MU-interference by a regularized zero-forcing (RZF) technique. The illustrative results show that, in comparison to 2D arrays, 3D array structures can provide high spectral and energy efficiencies as well as non-varying achievable rate independent from the user angular location. Thus, 3D structures can be useful in supporting both terrestrial and aerial communications.

In Chapter 5, we have proposed different novel full-duplex hybrid beamforming (FD-HBF) techniques to enhance the overall capacity in mMIMO systems based on over-the-air (OTA) measurements of the self-interference (SI) channel. Here, we leverage the spatial degrees of freedom (DoF) in mMIMO systems to enhance FD capacity without the need for expensive analog SI-cancellation circuitry. For a single uplink, single downlink user setup, we have developed both constant modulus (CM) and non-constant modulus (NCM) RF-stages via slow time-varying angular information to maximize the intended signal power and suppress the strong SI power. Particularly, both CM and NCM RF-stages are constructed to suppress the strong SI power by introducing beam perturbations within an allowed directivity degradation. Additionally, we also utilized the sub-array configurations at BS to select the best Tx/Rx indices jointly with beam perturbation for enhanced SI suppression. Afterwards, the BB-stages have been built via the reduced-size effective intended channel. It is shown that FD-HBF significantly suppresses the strong SI power by achieving upto 80 dB SI suppression capability, which remarkably improves the achievable rate capacity when compared to its half-duplex (HD) counterpart.

In Chapter 6, we have introduced a UAV-assisted terrestrial system to enhance both coverage and capacity in mMIMO systems. Here, the UAVs operate as relaying structures to extend the coverage area of BS for obscured users. We considered UAV as amplify-and-forward (AF) relay as well as decode-and-forward (DF) relay in both SU-mMIMO and MU-mMIMO systems, where the overall capacity is maximized by jointly optimizing the UAV placement, power allocation (PA) to users and by utilizing angular-based HBF solutions for both BS and UAV. We have introduced two AI/ML-based algorithms for the joint UAV deployment and PA. Firstly, we develop a particle swarm optimization based joint UAV location and PA (PSOLPA) algorithm, which achieved near-optimal sum-rate capacity at the expense of longer runtime for the larger number of users. Secondly, we have introduced a novel deep learning based UAV location and PA (DLLPA) algorithm for faster and more robust prediction of UAV deployment and PA. The illustrative results depict that DLLPA closely approaches the optimal sum-rate capacity with remarkably reduced runtime.

Chapter 7 has extended the UAV-assisted communications to the multiple UAVs-assisted terrestrial networks to support a large number of users, enhancing both coverage and capacity. We have considered multiple UAVs operating as DF relays, which connect the BS to a large number of IoT devices and utilized structured sequential optimization to address the multi-faceted optimization problem by splitting it into two sub-problems. Here, first we have used K-means-based user clustering for UAV-users association. Then, the location of each UAV is optimized jointly with PA using swarm intelligence. The RF stages are designed based on the slow time-varying angular information, while BB stages are designed utilizing the reduced-dimension effective channel matrices. In the results, we have shown that multiple UAV-assisted cooperative relaying systems outperform a single UAV system in practical user distributions, thus supporting a large number of users for future IoT applications.

8.2 Potential Future Works

This thesis has presented various HBF solutions to overcome the technical challenges towards the practical implementation of mMIMO systems in the terrestrial and UAV-assisted terrestrial communications networks. While concluding this thesis, we would like to point out possible avenues for the future research directions:

- **Integrated Wireless Information and Power Transfer (IWIPT):** It is expected that the number of smart devices will surpass 25.4 billion by 2030 . With billions of low-power consumption devices, such as wireless sensors, connecting to the internet through the IoT framework, there is a significant increase in both energy demand and data traffic. RF transmissions have long been utilized as a means of wireless information transfer (WIT). Recent advancements in energy harvesting (EH) circuit design have made RF signals a feasible source of power for wireless devices [176–178]. In contrast to traditional wireless networks, where nodes are powered by fixed energy sources, such as batteries, which must be replaced or replenished manually when they run out, RF-enabled wireless power transfer (WPT) eliminates the problem of battery replacement by ensuring a constant supply of energy. As a result, WPT is particularly appealing for applications in which replacing batteries is inconvenient (e.g., for IoT applications) or even impractical (e.g., for implanted devices in human body). In the context of this thesis, the proposed HBF solutions for mMIMO systems can be further extended to optimize both power and information transfer. This includes designing adaptive EH mechanisms, managing interference effectively, and creating resource allocation algorithms that dynamically balance power and data needs. Additionally, conducting real-world experiments to validate these schemes would further solidify IWIPT's practical applications.

- **Near-Field Communications (NFC):** Recently, NFC has gained significant attention as it possess the potential for high-capacity, low-latency communication over short distances. This is particularly important in densely populated environments, IoT networks, and UAV-assisted communication systems, where efficient and secure data transfer is crucial [179–181]. The research work of this thesis can be extended to focus on developing HBF techniques tailored for NFC, optimizing signal focusing and spatial efficiency. This includes exploring NFC applications in UAV-assisted systems, developing methods to mitigate interference, designing energy-efficient solutions, and integrating NFC in IoT devices for improved communication between sensors and actuators.

- **Joint Sensing and Communications (JSAC):** JSAC is a promising area that merges data transmission with environmental sensing, providing a unified platform for both communication and situational awareness. This convergence is crucial for applications such as autonomous vehicles, smart cities, and advanced surveillance systems, where real-time data and environmental context are essential [182, 183]. The HBF solutions presented in this thesis can be extended to simultaneously optimize communication and sensing tasks. This includes designing beamforming strategies that adapt based on real-time sensing data, integrating multiple sensing modalities, and exploring UAV-assisted sensing to enhance coverage and accuracy. Additionally, implementing these techniques in practical hardware and ensuring real-time adaptability in dynamic environments would significantly advance JCAS applications.

- **Reconfigurable Intelligent Surface aided HBF design:** The recent emergence of reconfigurable intelligent surfaces (RIS) has significantly enhanced propagation environments in wireless communications [184, 185]. RIS utilizes numerous passive, low-cost reflective elements to alter the phase of incoming signals, thereby improving the limited scattering typically encountered in mmWave and terahertz frequency bands. The proposed HBF solutions in this thesis can be further extended to RIS-assisted mMIMO systems. Furthermore, most of the existing RIS studies in the literature considers a fixed deployment. In a dynamic environment, single or multiple movable RIS can be used to serve a large number of users. Additionally, together with UAV-assisted DF relay, a hybrid reflector-relay structure can be used to achieve high spectral-energy efficiency tradeoff when compared to either RIS or relay structure operating alone.

Bibliography

[1] Ericsson, “5G systems - enabling the transformation of industry and society.” White Paper, Jan 2017.

[2] 5G Americas, “LTE to 5G: Cellular and broadband innovation.” White Paper, Aug 2017.

[3] Ericsson, “5G advanced: Evolution towards 6G.” White Paper, June 2023.

[4] I. T. U. (ITU), “IMT traffic estimates for the years 2020 to 2030.” Tech. Rep. ITU-R M.2370-0, July 2015.

[5] “Internet of things statistics for 2022 - taking things apart.” https://dataprot.net/statistics/iot-statistics/, Mar 2022.

[6] Ericsson, “Ericsson mobility report.” Tech. Rep., Nov 2023.

[7] F. Tariq, M. R. A. Khandaker, K.-K. Wong, M. A. Imran, M. Bennis, and M. Debbah, “A speculative study on 6G,” *IEEE Wirel. Commun.*, vol. 27, no. 4, pp. 118–125, 2020.

[8] 3GPP TR 38.913, “Study on scenarios and requirements for next generation access technologies (version 14.2.0).” 3GPP, Tech. Rep., May 2017.

[9] I. T. U. (ITU), “Minimum requirements related to technical performance for IMT-2020 radio interface(s).” Tech. Rep. ITU-R M.2410-0, Nov 2017.

[10] 3GPP TS 38.211, “NR; physical channels and modulation (version 16.7.0).” 3GPP, Tech. Rep., Oct 2021.

[11] I. T. U. (ITU), “Guidelines for evaluation of radio interface technologies for IMT-2020.” Tech. Rep. ITU-R M.2412-0, Oct 2017.

[12] Ericsson, “Ericsson mobility report.” Tech. Rep., June 2020.

[13] G. Americas, "New services and applications with 5G ultra-reliable low latency communications." White Paper, Nov 2018.

[14] L. Lu, G. Y. Li, A. L. Swindlehurst, A. Ashikhmin, and R. Zhang, "An overview of massive mimo," *IEEE J. Sel. Topics Signal Process.*

[15] E. G. Larsson, O. Edfors, F. Tufvesson, and T. L. Marzetta, "Massive MIMO for next generation wireless systems," *IEEE Commun. Mag.*, vol. 52, no. 2, pp. 186–195, 2014.

[16] E. Bjornson, L. Van der Perre, S. Buzzi, and E. G. Larsson, "Massive MIMO in Sub-6 GHz and mmWave: Physical, practical, and use-case differences," *IEEE Wireless Commun.*, vol. 26, no. 2, pp. 100–108, 2019.

[17] J. Lee, J.-K. Han, and J. Zhang, "MIMO technologies in 3GPP LTE and LTE-advanced," *EURASIP J Wirel Commun Netw*, vol. 2009, pp. 1–10, 2009.

[18] T. L. Marzetta, "Noncooperative cellular wireless with unlimited numbers of base station antennas," *IEEE Trans. Wireless Commun.*, vol. 9, no. 11, pp. 3590–3600, 2010.

[19] W. Feng, J. Wang, Y. Chen, X. Wang, N. Ge, and J. Lu, "UAV-aided MIMO communications for 5G Internet of Things," *IEEE Internet Things J.*, vol. 6, no. 2, pp. 1731–1740, 2018.

[20] A. F. Molisch, V. V. Ratnam, S. Han, Z. Li, S. L. H. Nguyen, L. Li, and K. Haneda, "Hybrid beamforming for massive MIMO: A survey," *IEEE Commun. Mag.*, vol. 55, no. 9, pp. 134–141, 2017.

[21] L. Chettri and R. Bera, "A comprehensive survey on Internet of Things (IoT) toward 5G wireless systems," *IEEE Internet Things J.*, vol. 7, no. 1, pp. 16–32, 2020.

[22] L. Bai, L. Zhu, X. Zhang, W. Zhang, and Q. Yu, "Multi-satellite relay transmission in 5G: Concepts, techniques, and challenges," *IEEE Netw.*, vol. 32, no. 5, pp. 38–44, 2018.

[23] M. Mozaffari, W. Saad, M. Bennis, Y.-H. Nam, and M. Debbah, "A tutorial on UAVs for wireless networks: Applications, challenges, and open problems," *IEEE communications surveys & tutorials*, vol. 21, no. 3, pp. 2334–2360, 2019.

[24] Q. Wu and R. Zhang, "Common throughput maximization in UAV-enabled OFDMA systems with delay consideration," *IEEE Trans. Commun.*, vol. 66, no. 12, pp. 6614–6627, 2018.

[25] K. Meng, D. Li, X. He, and M. Liu, "Space pruning based time minimization in delay constrained multi-task UAV-based sensing," *IEEE Trans. Veh. Technol.*, vol. 70, no. 3, pp. 2836–2849, 2021.

[26] J. Lyu, Y. Zeng, and R. Zhang, "Cyclical multiple access in UAV-aided communications: A throughput-delay tradeoff," *IEEE Wireless Commun. Lett.*, vol. 5, no. 6, pp. 600–603, 2016.

[27] W. Roh, J.-Y. Seol, J. Park, B. Lee, J. Lee, Y. Kim, J. Cho, K. Cheun, and F. Aryanfar, "Millimeter-wave beamforming as an enabling technology for 5G cellular communications: theoretical feasibility and prototype results," *IEEE Commun. Mag.*, vol. 52, no. 2, pp. 106–113, 2014.

[28] C. A. Balanis, *Antenna theory: analysis and design.* John wiley & sons, 2016.

[29] N. Fatema, G. Hua, Y. Xiang, D. Peng, and I. Natgunanathan, "Massive MIMO linear precoding: A survey," *IEEE Syst. J.*, vol. 12, no. 4, pp. 3920–3931, 2017.

[30] B. Yang, Z. Yu, J. Lan, R. Zhang, J. Zhou, and W. Hong, "Digital beamforming-based massive MIMO transceiver for 5G millimeter-wave communications," *IEEE Trans. Microw. Theory Techn.*, vol. 66, no. 7, pp. 3403–3418, 2018.

[31] E. Ali, M. Ismail, R. Nordin, and N. F. Abdulah, "Beamforming techniques for massive MIMO systems in 5G: overview, classification, and trends for future research," *Front. Inf. Technol. Electron. Eng*, vol. 18, pp. 753–772, 2017.

[32] "5G; study on scenarios and requirements for next generation access technologies," 3GPP, TR 38.913 Ver. 17.0.0, May 2022.

[33] S. S. Ioushua and Y. C. Eldar, "A family of hybrid analog–digital beamforming methods for massive MIMO systems," *IEEE Trans. Signal Process.*, vol. 67, no. 12, pp. 3243–3257, 2019.

[34] Y. Wang, W. Zou, and Y. Tao, "Analog precoding designs for millimeter wave communication systems," *IEEE Trans. Veh. Technol.*, vol. 67, no. 12, pp. 11733–11745, 2018.

[35] X. Gao, L. Dai, S. Han, I. Chih-Lin, and R. W. Heath, “Energy-efficient hybrid analog and digital precoding for mmWave MIMO systems with large antenna arrays,” *IEEE J. Sel. Areas Commun.*, vol. 34, no. 4, pp. 998–1009, 2016.

[36] L. Liang, W. Xu, and X. Dong, “Low-complexity hybrid precoding in massive multiuser MIMO systems,” *IEEE Wireless Commun. Lett.*, vol. 3, no. 6, pp. 653–656, 2014.

[37] T. E. Bogale, L. B. Le, A. Haghighat, and L. Vandendorpe, “On the number of RF chains and phase shifters, and scheduling design with hybrid analog–digital beamforming,” *IEEE Trans. Wireless Commun.*, vol. 15, no. 5, pp. 3311–3326, 2016.

[38] W. Ni, X. Dong, and W. Lu, “Near-optimal hybrid processing for massive MIMO systems via matrix decomposition,” *IEEE Trans. Signal Process.*, vol. 65, no. 15, pp. 3922–3933, 2017.

[39] S. He, C. Qi, Y. Wu, and Y. Huang, “Energy-efficient transceiver design for hybrid sub-array architecture MIMO systems,” *IEEE Access*, vol. 4, pp. 9895–9905, 2016.

[40] W. Ni and X. Dong, “Hybrid block diagonalization for massive multiuser MIMO systems,” *IEEE Trans. Commun.*, vol. 64, no. 1, pp. 201–211, 2016.

[41] A. Li and C. Masouros, “Hybrid analog-digital Millimeter-Wave MU-MIMO transmission with virtual path selection,” *IEEE Commun. Lett.*, vol. 21, no. 2, pp. 438–441, 2017.

[42] X. Yu, J.-C. Shen, J. Zhang, and K. B. Letaief, “Alternating minimization algorithms for hybrid precoding in millimeter wave MIMO systems,” *IEEE J. Sel. Topics Signal Process.*, vol. 10, no. 3, pp. 485–500, 2016.

[43] E. Everett, A. Sahai, and A. Sabharwal, “Passive self-interference suppression for full-duplex infrastructure nodes,” *IEEE Trans. Wireless Commun.*, vol. 13, no. 2, pp. 680–694, 2014.

[44] M. S. Sim, M. Chung, D. Kim, J. Chung, D. K. Kim, and C.-B. Chae, “Nonlinear self-interference cancellation for full-duplex radios: From link-level and system-level performance perspectives,” *IEEE Commun. Mag.*, vol. 55, no. 9, pp. 158–167, 2017.

[45] Z. Zhang, X. Chai, K. Long, A. V. Vasilakos, and L. Hanzo, “Full duplex techniques for 5G networks: self-interference cancellation, protocol design, and relay selection,” *IEEE Commun. Mag.*, vol. 53, no. 5, pp. 128–137, 2015.

[46] B. Debaillie, D.-J. van den Broek, C. Lavín, B. van Liempd, E. A. M. Klumperink, C. Palacios, J. Craninckx, B. Nauta, and A. Pärssinen, "Analog/RF solutions enabling compact full-duplex radios," *IEEE J. Sel. Areas Commun.*, vol. 32, no. 9, pp. 1662–1673, 2014.

[47] H. Nawaz and I. Tekin, "Dual-polarized, differential fed microstrip patch antennas with very high interport isolation for full-duplex communication," *IEEE Trans. Antennas Propag.*, vol. 65, no. 12, pp. 7355–7360, 2017.

[48] C. X. Mao, Y. Zhou, Y. Wu, H. Soewardiman, D. H. Werner, and J. S. Jur, "Low-profile strip-loaded textile antenna with enhanced bandwidth and isolation for full-duplex wearable applications," *IEEE Trans. Antennas Propag.*, vol. 68, no. 9, pp. 6527–6537, 2020.

[49] D. Korpi, M. Heino, C. Icheln, K. Haneda, and M. Valkama, "Compact inband full-duplex relays with beyond 100 db self-interference suppression: Enabling techniques and field measurements," *IEEE Trans. Antennas Propag.*, vol. 65, no. 2, pp. 960–965, 2017.

[50] T. Le-Ngoc, Y. Gong, M. Mahmood, A. Koc, R. Morawski, J. G. Griffiths, P. Guillemette, J. Zaid, and P. Wang, "Full-duplex in massive multiple-input multiple-output," *IEEE Open J. Veh. Technol.*, vol. 5, pp. 560–576, 2024.

[51] Y. Gong, M. Mahmood, R. Morawski, and T. Le-Ngoc, "Dual-layer metamaterial rectangular antenna arrays for in-band full-duplex massive MIMO," *IEEE Access*, 2023.

[52] E. Ahmed and A. M. Eltawil, "All-digital self-interference cancellation technique for full-duplex systems," *IEEE Trans. Wireless Commun.*, vol. 14, no. 7, pp. 3519–3532, 2015.

[53] M. Fozooni, M. Matthaiou, S. Jin, and G. C. Alexandropoulos, "Massive MIMO relaying with hybrid processing," in *Proc. IEEE Int. Conf. Commun. (ICC)*, pp. 1–6, IEEE, 2016.

[54] L. Sanguinetti, A. A. D'Amico, and Y. Rong, "A tutorial on the optimization of amplify-and-forward MIMO relay systems," *IEEE J. Sel. Areas Commun.*, vol. 30, no. 8, pp. 1331–1346, 2012.

[55] K. T. Truong, P. Sartori, and R. W. Heath, "Cooperative algorithms for MIMO amplify-and-forward relay networks," *IEEE Trans. Signal Process.*, vol. 61, no. 5, pp. 1272–1287, 2013.

[56] K. Xiong, P. Fan, Z. Xu, H.-C. Yang, and K. B. Letaief, "Optimal cooperative beamforming design for MIMO decode-and-forward relay channels," *IEEE Trans. Signal Process.*, vol. 62, no. 6, pp. 1476–1489, 2014.

[57] M. Mahmood, A. Koc, and T. Le-Ngoc, "2D antenna array structures for hybrid massive MIMO precoding," in *Proc. IEEE Global Commun. Conf. (GLOBECOM)*, Taipei, Taiwan, Dec. 7-11, 2020.

[58] M. Mahmood, A. Koc, and T. Le-Ngoc, "Massive-MIMO hybrid precoder design using few-bit DACs for 2D antenna array structures," in *Proc. IEEE Int. Conf. Commun. (ICC)*, Montreal, Canada, Jun 14-23, 2021.

[59] M. Mahmood, A. Koc, and T. Le-Ngoc, "Energy-efficient MU-massive-MIMO hybrid precoder design: Low-resolution phase shifters and digital-to-analog converters for 2D antenna array structures," *IEEE Open J. Commun. Soc.*, pp. 1842–1861, 2021.

[60] A. Adhikary, J. Nam, J.-Y. Ahn, and G. Caire, "Joint spatial division and multiplexing—the large-scale array regime," *IEEE Trans. Inf. Theory*, vol. 59, no. 10, pp. 6441–6463, 2013.

[61] J. Nam, A. Adhikary, J. Ahn, and G. Caire, "Joint spatial division and multiplexing: Opportunistic beamforming, user grouping and simplified downlink scheduling," *IEEE J. Sel. Topics Signal Process.*, vol. 8, no. 5, pp. 876–890, 2014.

[62] D. Kim, G. Lee, and Y. Sung, "Two-stage beamformer design for massive MIMO downlink by trace quotient formulation," *IEEE Trans. Commun.*, vol. 63, no. 6, pp. 2200–2211, 2015.

[63] S. Park, A. Alkhateeb, and R. W. Heath, "Dynamic subarrays for hybrid precoding in wideband mmWave MIMO systems," *IEEE Trans. Wireless Commun.*, vol. 16, no. 5, pp. 2907–2920, 2017.

[64] Y. Jeon, C. Song, S. Lee, S. Maeng, J. Jung, and I. Lee, "New beamforming designs for joint spatial division and multiplexing in large-scale MISO multi-user systems," *IEEE Trans. Wireless Commun.*, vol. 16, no. 5, pp. 3029–3041, 2017.

[65] A. Koc, A. Masmoudi, and T. Le-Ngoc, “Hybrid beamforming for uniform circular arrays in multi-user massive MIMO systems,” in *Proc. 32nd IEEE Can. Conf. Electr. Comput. Eng. (CCECE)*, Edmonton, Canada, May. 5-8, 2019.

[66] R. Mai and T. Le-Ngoc, “Nonlinear hybrid precoding for coordinated multi-cell massive MIMO systems,” *IEEE Trans. Veh. Technol.*, vol. 68, no. 3, pp. 2459–2471, 2019.

[67] S. Zarei, W. Gerstacker, and R. Schober, “Low-complexity hybrid Linear/Tomlinson-Harashima precoding for downlink large-scale MU-MIMO systems,” in *IEEE Globecom Workshops (GC Wkshps)*, Washington, DC USA, Dec. 4-8, 2016.

[68] C. Pradhan, A. Li, L. Zhuo, Y. Li, and B. Vucetic, “Hybrid-precoding for mmWave multi-user communications in the presence of beam-misalignment,” *IEEE Trans. Wireless Commun.*, vol. 19, no. 9, pp. 6083–6099, 2020.

[69] F. Sohrabi and W. Yu, “Hybrid beamforming with finite-resolution phase shifters for large-scale MIMO systems,” in *Proc. IEEE 16th Int. Workshop Signal Process. Advances Wireless Commun. (SPAWC)*, Stockholm, Sweden, Jun. 27 - July. 1, 2015.

[70] F. Sohrabi and W. Yu, “Hybrid digital and analog beamforming design for large-scale antenna arrays,” *IEEE J. Sel. Topics Signal Process.*, vol. 10, no. 3, pp. 501–513, 2016.

[71] S. Payami, M. Ghoraishi, and M. Dianati, “Hybrid beamforming for large antenna arrays with phase shifter selection,” *IEEE Trans. Wireless Commun.*, vol. 15, no. 11, pp. 7258–7271, 2016.

[72] Z. Wang, M. Li, Q. Liu, and A. L. Swindlehurst, “Hybrid precoder and combiner design with low-resolution phase shifters in mmWave MIMO systems,” *IEEE J. Sel. Topics Signal Process.*, vol. 12, no. 2, pp. 256–269, 2018.

[73] H. Li, Q. Liu, Z. Wang, and M. Li, “Transmit antenna selection and analog beamforming with low-resolution phase shifters in mmWave MISO systems,” *IEEE Commun. Lett.*, vol. 22, no. 9, pp. 1878–1881, 2018.

[74] H. Li, Q. Liu, Z. Wang, and M. Li, “Joint antenna selection and analog precoder design with low-resolution phase shifters,” *IEEE Trans. Veh. Technol.*, vol. 68, no. 1, pp. 967–971, 2018.

[75] H. Li, M. Li, and Q. Liu, “Hybrid beamforming with dynamic subarrays and low-resolution PSs for mmWave MU-MISO systems,” *IEEE Trans. Commun.*, vol. 68, no. 1, pp. 602–614, 2019.

[76] H. Seleem, A. I. Sulyman, and A. Alsanie, “Hybrid precoding-beamforming design with Hadamard RF codebook for mmWave large-scale MIMO systems,” *IEEE Access*, vol. 5, pp. 6813–6823, 2017.

[77] H. Li, M. Li, Q. Liu, and A. L. Swindlehurst, “Dynamic hybrid beamforming with low-resolution PSs for wideband mmWave MIMO-OFDM systems,” *IEEE J. Sel. Areas Commun.*, vol. 38, no. 9, pp. 2168–2181, 2020.

[78] C. Wang, C. Wen, S. Jin, and S. Tsai, “Finite-alphabet precoding for massive MU-MIMO with low-resolution DACs,” *IEEE Trans. Wireless Commun.*, vol. 17, no. 7, pp. 4706–4720, 2018.

[79] S. Jacobsson, G. Durisi, M. Coldrey, T. Goldstein, and C. Studer, “Quantized precoding for massive MU-MIMO,” *IEEE Trans. Commun.*, vol. 65, pp. 4670–4684, Nov. 2017.

[80] L. N. Ribeiro, S. Schwarz, M. Rupp, and A. L. F. de Almeida, “Energy efficiency of mmWave massive MIMO precoding with low-resolution DACs,” *IEEE J. Sel. Topics Signal Process.*, vol. 12, no. 2, pp. 298–312, 2018.

[81] J. Mo, A. Alkhateeb, S. Abu-Surra, and R. W. Heath, “Hybrid architectures with few-bit ADC receivers: Achievable rates and energy-rate tradeoffs,” *IEEE Trans. Wireless Commun.*, vol. 16, no. 4, pp. 2274–2287, 2017.

[82] K. Roth, H. Pirzadeh, A. L. Swindlehurst, and J. A. Nossek, “A comparison of hybrid beamforming and digital beamforming with low-resolution ADCs for multiple users and imperfect CSI,” *IEEE J. Sel. Topics Signal Process.*, vol. 12, no. 3, pp. 484–498, 2018.

[83] A. Koc and T. Le-Ngoc, “Hybrid millimeter-wave massive MIMO systems with low CSI overhead and Few-Bit DACs/ADCs,” in *Proc. IEEE 92th Veh. Technol. Conf. (VTC-Fall)*, Victoria, Canada, Nov. 18 - Dec. 16, 2020.

[84] J. Hoydis, S. ten Brink, and M. Debbah, “Massive MIMO in the UL/DL of cellular networks: How many antennas do we need?,” *IEEE J. Sel. Areas Commun.*, vol. 31, no. 2, pp. 160–171, 2013.

[85] C. B. Peel, B. M. Hochwald, and A. L. Swindlehurst, “A vector-perturbation technique for near-capacity multiantenna multiuser communication-part I: channel inversion and regularization,” *IEEE Trans. Commun.*, vol. 53, no. 1, pp. 195–202, 2005.

[86] J. D. Krieger, C. Yeang, and G. W. Wornell, "Dense delta-sigma phased arrays," *IEEE Trans. Antennas Propag.*, vol. 61, no. 4, pp. 1825–1837, 2013.

[87] J. A. Tropp and A. C. Gilbert, "Signal recovery from random measurements via orthogonal matching pursuit," *IEEE Trans. Inf. Theory*, vol. 53, no. 12, pp. 4655–4666, 2007.

[88] O. El Ayach, S. Rajagopal, S. Abu-Surra, Z. Pi, and R. W. Heath, "Spatially sparse precoding in millimeter wave MIMO systems," *IEEE Trans. Wireless Commun.*, vol. 13, no. 3, pp. 1499–1513, 2014.

[89] Da-Shan Shiu, G. J. Foschini, M. J. Gans, and J. M. Kahn, "Fading correlation and its effect on the capacity of multielement antenna systems," *IEEE Trans. Commun.*, vol. 48, no. 3, pp. 502–513, 2000.

[90] A. Koc, A. Masmoudi, and T. Le-Ngoc, "3D angular-based hybrid precoding and user grouping for uniform rectangular arrays in massive MU-MIMO systems," *IEEE Access*, vol. 8, pp. 84689–84712, 2020.

[91] Y. Xiong, "Achievable rates for massive MIMO relaying systems with variable-bit ADCs/DACs," *IEEE Commun. Lett.*, vol. 24, no. 5, pp. 991–994, 2020.

[92] C. Kong, C. Zhong, S. Jin, S. Yang, H. Lin, and Z. Zhang, "Full-duplex massive MIMO relaying systems with low-resolution ADCs," *IEEE Trans. Wireless Commun.*, vol. 16, no. 8, pp. 5033–5047, 2017.

[93] W. B. Abbas, F. Gomez-Cuba, and M. Zorzi, "Millimeter wave receiver efficiency: A comprehensive comparison of beamforming schemes with low resolution ADCs," *IEEE Trans. Wireless Commun.*, vol. 16, no. 12, pp. 8131–8146, 2017.

[94] R. L. Haupt, "Optimized element spacing for low sidelobe concentric ring arrays," *IEEE Trans. Antennas Propag.*, vol. 56, no. 1, pp. 266–268, 2008.

[95] E. Vlachos, A. Kaushik, and J. Thompson, "Energy efficient transmitter with low resolution DACs for massive MIMO with partially connected hybrid architecture," in *2018 IEEE 87th Vehicular Technology Conference (VTC Spring)*, pp. 1–5, 2018.

[96] J. C. Chen, "Energy-efficient analog combiner design using low-resolution phase shifters and antenna selection for mmWave D2D communications," *IEEE Trans. Veh. Technol.*, vol. 69, no. 11, pp. 13979–13984, 2020.

[97] R. Méndez-Rial, C. Rusu, N. González-Prelcic, A. Alkhateeb, and R. W. Heath, "Hybrid MIMO architectures for millimeter wave communications: Phase shifters or switches?," *IEEE Access*, vol. 4, pp. 247–267, 2016.

[98] M. Mahmood, A. Koc, and T. Le-Ngoc, "3-D antenna array structures for millimeter wave multi-user massive MIMO hybrid precoder design: A performance comparison," *IEEE Commun. Lett.*, vol. 26, no. 6, pp. 1393–1397, 2022.

[99] W. Ryoo and W. Sung, "Beamforming using uniform spherical arrays: Array construction, beam characteristics, and multi-rank transmission," *IEEE Access*, vol. 9, pp. 38731–38741, 2021.

[100] E. Yaacoub, M. Al-Husseini, A. Chehab, K. Abualsaud, T. Khattab, and M. Guizani, "3D beamforming with massive cylindrical arrays for physical layer secure data transmission," *IEEE Commun. Lett.*, vol. 23, no. 5, pp. 830–833, 2019.

[101] P. Zhao and Z. Wang, "Joint user scheduling and hybrid precoding for multi-user mmWave systems with two-layer PS network," in *Proc. IEEE Global Commun. Conf. (GLOBECOM)*, pp. 1–6, IEEE, Dec. 2018.

[102] D. Zhang, P. Pan, R. You, and H. Wang, "SVD-based low-complexity hybrid precoding for millimeter-wave MIMO systems," *IEEE Commun. Lett.*, vol. 22, no. 10, pp. 2176–2179, 2018.

[103] M. Mahmood, A. Koc, D. T. Nguyen, R. Morawski, and T. Le-Ngoc, "Sub-array selection in full-duplex massive MIMO for enhanced self-interference suppression," in *Proc. IEEE Global Commun. Conf. (GLOBECOM)*, pp. 5835–5840, 2023.

[104] M. Mahmood, Y. Zhang, R. Morawski, and T. Le-Ngoc, "Adaptive modulus RF beamforming for enhanced self-interference suppression in full-duplex massive MIMO systems," in *Proc. IEEE Wireless Commun. Netw. Conf. (WCNC)*, April. 2024, arXiv:2402.08230.

[105] M. Mahmood, A. Koc, R. Morawski, and T. Le-Ngoc, "Achieving capacity gains in practical full-duplex massive MIMO systems: A multi-objective optimization approach using hybrid beamforming," *IEEE Open J. Commun. Soc.*, vol. 5, pp. 2268–2286, 2024.

[106] Y. Liu, P. Roblin, X. Quan, W. Pan, S. Shao, and Y. Tang, "A full-duplex transceiver with two-stage analog cancellations for multipath self-interference," *IEEE Trans. Microw. Theory Techn.*, vol. 65, no. 12, pp. 5263–5273, 2017.

[107] K. E. Kolodziej, J. G. McMichael, and B. T. Perry, "Multitap RF canceller for in-band full-duplex wireless communications," *IEEE Trans. Wireless Commun.*, vol. 15, no. 6, pp. 4321–4334, 2016.

[108] J. W. Kwak, M. S. Sim, I.-W. Kang, J. Park, K.-K. Wong, and C.-B. Chae, "Analog self-interference cancellation with practical RF components for full-duplex radios," *IEEE Trans. Wireless Commun.*, pp. 1–1, 2022.

[109] M. A. Islam, G. C. Alexandropoulos, and B. Smida, "Joint analog and digital transceiver design for wideband full duplex MIMO systems," *IEEE Trans. Wireless Commun.*, vol. 21, no. 11, pp. 9729–9743, 2022.

[110] M. Duarte, C. Dick, and A. Sabharwal, "Experiment-driven characterization of full-duplex wireless systems," *IEEE Trans. Wireless Commun.*, vol. 11, no. 12, pp. 4296–4307, 2012.

[111] T. Dinc, A. Chakrabarti, and H. Krishnaswamy, "A 60 GHz CMOS full-duplex transceiver and link with polarization-based antenna and RF cancellation," *IEEE J. Solid-State Circuits*, vol. 51, no. 5, pp. 1125–1140, 2016.

[112] E. Everett, C. Shepard, L. Zhong, and A. Sabharwal, "Softnull: Many-antenna full-duplex wireless via digital beamforming," *IEEE Trans. Wireless Commun.*, vol. 15, no. 12, pp. 8077–8092, 2016.

[113] A. Koc and T. Le-Ngoc, "Full-duplex mmWave massive MIMO systems: A joint hybrid precoding/combining and self-interference cancellation design," *IEEE Open J. Commun. Soc.*, vol. 2, pp. 754–774, 2021.

[114] S. Huberman and T. Le-Ngoc, "MIMO full-duplex precoding: A joint beamforming and self-interference cancellation structure," *IEEE Trans. Wireless Commun.*, vol. 14, no. 4, pp. 2205–2217, 2015.

[115] Y. Zhang, M. Xiao, S. Han, M. Skoglund, and W. Meng, "On precoding and energy efficiency of full-duplex millimeter-wave relays," *IEEE Trans. Wireless Commun.*, vol. 18, no. 3, pp. 1943–1956, 2019.

[116] Z. Luo, L. Zhao, L. Tonghui, H. Liu, and R. Zhang, "Robust hybrid precoding/combining designs for full-duplex millimeter wave relay systems," *IEEE Trans. Veh. Technol.*, vol. 70, no. 9, pp. 9577–9582, 2021.

[117] A. Koc and T. Le-Ngoc, “Intelligent non-orthogonal beamforming with large self-interference cancellation capability for full-duplex multiuser massive MIMO systems,” *IEEE Access*, vol. 10, pp. 51771–51791, 2022.

[118] K. Satyanarayana, M. El-Hajjar, P.-H. Kuo, A. Mourad, and L. Hanzo, “Hybrid beamforming design for full-duplex millimeter wave communication,” *IEEE Trans. Veh. Technol.*, vol. 68, no. 2, pp. 1394–1404, 2019.

[119] I. P. Roberts, J. G. Andrews, and S. Vishwanath, “Hybrid beamforming for millimeter wave full-duplex under limited receive dynamic range,” *IEEE Trans. Wireless Commun.*, vol. 20, no. 12, pp. 7758–7772, 2021.

[120] Y. Cai, K. Xu, A. Liu, M. Zhao, B. Champagne, and L. Hanzo, “Two-timescale hybrid analog-digital beamforming for mmWave full-duplex MIMO multiple-relay aided systems,” *IEEE J. Sel. Areas Commun.*, vol. 38, no. 9, pp. 2086–2103, 2020.

[121] Y. Chen, D. Chen, T. Jiang, and L. Hanzo, “Millimeter-wave massive MIMO systems relying on generalized sub-array-connected hybrid precoding,” *IEEE Trans. Veh. Technol.*, vol. 68, no. 9, pp. 8940–8950, 2019.

[122] C. Lin, G. Y. Li, and L. Wang, “Subarray-based coordinated beamforming training for mmWave and Sub-THz communications,” *IEEE J. Sel. Areas Commun.*, vol. 35, no. 9, pp. 2115–2126, 2017.

[123] C. Lin and G. Y. Li, “Energy-efficient design of indoor mmWave and Sub-THz systems with antenna arrays,” *IEEE Trans. Wireless Commun.*, vol. 15, no. 7, pp. 4660–4672, 2016.

[124] X. Song, T. Kühne, and G. Caire, “Fully-/partially-connected hybrid beamforming architectures for mmWave MU-MIMO,” *IEEE Trans. Wireless Commun.*, vol. 19, no. 3, pp. 1754–1769, 2020.

[125] X. Cheng, B. Yu, L. Yang, J. Zhang, G. Liu, Y. Wu, and L. Wan, “Communicating in the real world: 3D MIMO,” *IEEE Wireless Commun.*, vol. 21, no. 4, pp. 136–144, 2014.

[126] Y. Gong, R. Morawski, H. H. Lee, and T. Le-Ngoc, “A miniaturized 8x8 dual-layer EBG slotted circularly polarized patch antenna array for mMIMO,” in *Proc. IEEE Global Commun. Conf. (GLOBECOM)*, pp. 6511–6516, 2022.

[127] “5G; NR;. base station (BS) radio transmission and reception,” 3GPP, TS 38.104 Ver. 16.4.0, July 2020.

[128] “5G; study on channel model for frequencies from 0.5 to 100 GHz,” 3GPP, TR 38.901 Ver. 16.1.0, Nov. 2020.

[129] P. Zhao and Z. Wang, “Joint user scheduling and hybrid precoding for multi-user mmWave systems with two-layer PS network,” in *Proc. IEEE Global Commun. Conf. (GLOBECOM)*, pp. 1–6, 2018.

[130] X. Yu, J.-C. Shen, J. Zhang, and K. B. Letaief, “Alternating minimization algorithms for hybrid precoding in millimeter wave MIMO systems,” *IEEE J. Sel. Topics Signal Process.*, vol. 10, no. 3, pp. 485–500, 2016.

[131] M. Mahmood, A. Koc, and T. Le-Ngoc, “PSO-based joint UAV positioning and hybrid precoding in UAV-assisted massive MIMO systems,” in *Proc. IEEE 96th Veh. Technol. Conf. (VTC-Fall)*, pp. 1–6, 2022.

[132] M. Mahmood, A. Koc, and T. Le-Ngoc, “Spherical array-based joint beamforming and UAV positioning in massive MIMO systems,” in *Proc. IEEE 97th Veh. Technol. Conf. (VTC-Spring)*, pp. 1–5, 2023.

[133] A. Koc, M. Mahmood, and T. Le-Ngoc, “Efficient dual-hop massive mimo iot networks with uav df relaying and hybrid beamforming,” in *Proc. IEEE Global Commun. Conf. (GLOBECOM)*, pp. 6414–6419, 2023.

[134] M. Mahmood, M. Ghadaksaz, A. Koc, and T. Le-Ngoc, “Deep learning meets swarm intelligence for UAV-assisted IoT coverage in massive MIMO,” *IEEE Internet Things J.*, vol. 11, no. 5, pp. 7679–7696, 2024.

[135] S. Zhang, H. Zhang, Q. He, K. Bian, and L. Song, “Joint trajectory and power optimization for UAV relay networks,” *IEEE Commun. Lett.*, vol. 22, no. 1, pp. 161–164, 2018.

[136] Y. Chen, W. Feng, and G. Zheng, “Optimum placement of UAV as relays,” *IEEE Commun. Lett.*, vol. 22, no. 2, pp. 248–251, 2017.

[137] X. Jiang, Z. Wu, Z. Yin, and Z. Yang, “Power and trajectory optimization for UAV-enabled Amplify-and-Forward relay networks,” *IEEE Access*, vol. 6, pp. 48688–48696, 2018.

[138] F. Ono, H. Ochiai, and R. Miura, “A wireless relay network based on unmanned aircraft system with rate optimization,” *IEEE Trans. Wireless Commun.*, vol. 15, no. 11, pp. 7699–7708, 2016.

[139] Y. Guo, S. Yin, and J. Hao, “Joint placement and resources optimization for multi-user UAV-relaying systems with underlaid cellular networks,” *IEEE Trans. Veh. Technol.*, vol. 69, no. 10, pp. 12374–12377, 2020.

[140] W. Wang, N. Qi, L. Jia, C. Li, T. A. Tsiftsis, and M. Wang, “Energy-efficient UAV-relaying 5G/6G spectrum sharing networks: Interference coordination with power management and trajectory design,” *IEEE Open J. Commun. Soc.*, vol. 3, pp. 1672–1687, 2022.

[141] L. Sboui, H. Ghazzai, Z. Rezki, and M.-S. Alouini, “Achievable rates of UAV-relayed cooperative cognitive radio MIMO systems,” *IEEE Access*, vol. 5, pp. 5190–5204, 2017.

[142] J.-H. Lee, K.-H. Park, Y.-C. Ko, and M.-S. Alouini, “Throughput maximization of mixed FSO/RF UAV-aided mobile relaying with a buffer,” *IEEE Trans. Wireless Commun.*, vol. 20, no. 1, pp. 683–694, 2021.

[143] X. Lin, W. Mei, and R. Zhang, “A new Store-Then-Amplify-and-Forward protocol for UAV mobile relaying,” *IEEE Wireless Commun. Lett.*, vol. 9, no. 5, pp. 591–595, 2020.

[144] Y. Tang, M. H. Cheung, and T.-M. Lok, “Delay-tolerant UAV-assisted communication: Online trajectory design and user association,” *IEEE Trans. Veh. Technol.*, vol. 71, no. 12, pp. 13137–13151, 2022.

[145] F. Jiang, K. Wang, L. Dong, C. Pan, W. Xu, and K. Yang, “Deep-learning-based joint resource scheduling algorithms for hybrid MEC networks,” *IEEE Internet Things J.*, vol. 7, no. 7, pp. 6252–6265, 2020.

[146] Y. Pan, Y. Yang, and W. Li, “A deep learning trained by genetic algorithm to improve the efficiency of path planning for data collection with multi-UAV,” *IEEE Access*, vol. 9, pp. 7994–8005, 2021.

[147] H. Huang, Y. Yang, H. Wang, Z. Ding, H. Sari, and F. Adachi, “Deep reinforcement learning for UAV navigation through massive MIMO technique,” *IEEE Trans. Veh. Technol.*, vol. 69, no. 1, pp. 1117–1121, 2020.

[148] L. Zhu, J. Zhang, Z. Xiao, X.-G. Xia, and R. Zhang, "Multi-UAV aided millimeter-wave networks: Positioning, clustering, and beamforming," *IEEE Trans. Wireless Commun.*, vol. 21, no. 7, pp. 4637–4653, 2022.

[149] J. Du, W. Xu, Y. Deng, A. Nallanathan, and L. Vandendorpe, "Energy-saving UAV-assisted multiuser communications with massive MIMO hybrid beamforming," *IEEE Commun. Lett.*, vol. 24, no. 5, pp. 1100–1104, 2020.

[150] X. Pang, J. Tang, N. Zhao, X. Zhang, and Y. Qian, "Energy-efficient design for mmWave-enabled NOMA-UAV networks," *Sci. China Inf. Sci.*, vol. 64, pp. 1–14, 2021.

[151] W. Feng, J. Tang, N. Zhao, X. Zhang, X. Wang, K.-K. Wong, and J. A. Chambers, "Hybrid beamforming design and resource allocation for UAV-aided wireless-powered mobile edge computing networks with NOMA," *IEEE J. Sel. Areas Commun.*, vol. 39, no. 11, pp. 3271–3286, 2021.

[152] K. Liu, Y. Liu, P. Yi, Z. Xiao, and X.-G. Xia, "Deployment and robust hybrid beamforming for UAV MmWave communications," *IEEE Trans. Commun.*, pp. 1–1, 2023.

[153] X. Yu, X. Huang, K. Wang, F. Shu, and X. Dang, "Joint design of power allocation, beamforming, and positioning for energy-efficient UAV-aided multiuser millimeter-wave systems," *IEEE J. Sel. Areas Commun.*, vol. 40, no. 10, pp. 2930–2945, 2022.

[154] W. Feng, N. Zhao, S. Ao, J. Tang, X. Zhang, Y. Fu, D. K. C. So, and K.-K. Wong, "Joint 3D trajectory and power optimization for UAV-aided mmWave MIMO-NOMA networks," *IEEE Trans. Commun.*, vol. 69, no. 4, pp. 2346–2358, 2021.

[155] Z. Xiao, H. Dong, L. Bai, D. O. Wu, and X.-G. Xia, "Unmanned aerial vehicle base station (UAV-BS) deployment with millimeter-wave beamforming," *IEEE Internet Things J.*, vol. 7, no. 2, pp. 1336–1349, 2020.

[156] R. Méndez-Rial, C. Rusu, N. González-Prelcic, A. Alkhateeb, and R. W. Heath, "Hybrid MIMO architectures for millimeter wave communications: Phase shifters or switches?," *IEEE Access*, vol. 4, pp. 247–267, 2016.

[157] M. Mozaffari, W. Saad, M. Bennis, and M. Debbah, "Efficient deployment of multiple unmanned aerial vehicles for optimal wireless coverage," *IEEE Commun. Lett.*, vol. 20, no. 8, pp. 1647–1650, 2016.

[158] M. Alzenad, A. El-Keyi, F. Lagum, and H. Yanikomeroglu, “3-D placement of an unmanned aerial vehicle base station (UAV-BS) for energy-efficient maximal coverage,” *IEEE Wireless Commun. Lett.*, vol. 6, no. 4, pp. 434–437, 2017.

[159] Z. Yang, C. Pan, M. Shikh-Bahaei, W. Xu, M. Chen, M. Elkashlan, and A. Nallanathan, “Joint altitude, beamwidth, location, and bandwidth optimization for UAV-enabled communications,” *IEEE Commun. Lett.*, vol. 22, no. 8, pp. 1716–1719, 2018.

[160] X. Xi, X. Cao, P. Yang, J. Chen, T. Quek, and D. Wu, “Joint user association and UAV location optimization for UAV-aided communications,” *IEEE Wireless Commun. Lett.*, vol. 8, no. 6, pp. 1688–1691, 2019.

[161] L. Zhu, J. Zhang, Z. Xiao, and R. Schober, “Optimization of multi-UAV-BS aided millimeter-wave massive MIMO networks,” in *Proc. IEEE Global Commun. Conf. (GLOBECOM)*, pp. 1–6, 2020.

[162] J. Plachy, Z. Becvar, P. Mach, R. Marik, and M. Vondra, “Joint positioning of flying base stations and association of users: Evolutionary-based approach,” *IEEE Access*, vol. 7, pp. 11454–11463, 2019.

[163] A. Koc and T. Le-Ngoc, “Swarm intelligence based power allocation in hybrid millimeter-wave massive MIMO systems,” in *Proc. IEEE IEEE Wirel. Commun. Netw. Conf. (WCNC)*, pp. 1–7, 2021.

[164] Y. Zhang, M. Xiao, S. Han, M. Skoglund, and W. Meng, “On precoding and energy efficiency of full-duplex millimeter-wave relays,” *IEEE Trans. Wireless Commun.*, vol. 18, no. 3, pp. 1943–1956, 2019.

[165] A. Koc and T. Le-Ngoc, “Hybrid millimeter-wave massive MIMO systems with low CSI overhead and few-bit DACs/ADCs,” in *Proc. IEEE 92th Veh. Technol. Conf. (VTC-Fall)*, pp. 1–5, 2020.

[166] M. Mahmood, A. Koc, and T. Le-Ngoc, “Energy-efficient MU-massive-MIMO hybrid precoder design: Low-resolution phase shifters and digital-to-analog converters for 2D antenna array structures,” *IEEE Open J. Commun. Soc.*, vol. 2, pp. 1842–1861, 2021.

[167] A. Koc, M. Wang, and T. Le-Ngoc, “Deep learning based multi-user power allocation and hybrid precoding in massive MIMO systems,” in *Proc. IEEE Int. Conf. Commun. (ICC)*, pp. 5487–5492, 2022.

[168] T. Developers, “Tensorflow,” *Zenodo*, 2021.

[169] X. Xue, Y. Wang, L. Dai, and C. Masouros, “Relay hybrid precoding design in millimeter-wave massive MIMO systems,” *IEEE Trans. Signal Process.*, vol. 66, no. 8, pp. 2011–2026, 2018.

[170] J. D. Little, “A proof for the queuing formula: L= λ w,” *Oper. Res.*, vol. 9, no. 3, pp. 383–387, 1961.

[171] M. Mahmood, Y. Yuan, and T. Le-Ngoc, “Multiple UAV-assisted cooperative DF relaying in multi-user massive MIMO IoT systems,” in *Proc. IEEE Int. Conf. Commun. (ICC)*, June. 2024, arXiv:2404.03068.

[172] Y. Chen, N. Zhao, Z. Ding, and M.-S. Alouini, “Multiple UAVs as relays: Multi-hop single link versus multiple dual-hop links,” *IEEE Trans. Wireless Commun.*, vol. 17, no. 9, pp. 6348–6359, 2018.

[173] C. Zhang, L. Zhang, L. Zhu, T. Zhang, Z. Xiao, and X.-G. Xia, “3D deployment of multiple UAV-mounted base stations for UAV communications,” *IEEE Trans. Commun.*, vol. 69, no. 4, pp. 2473–2488, 2021.

[174] N. Nouri, F. Fazel, J. Abouei, and K. N. Plataniotis, “Multi-UAV placement and user association in uplink MIMO ultra-dense wireless networks,” *IEEE Trans. Mobile Comput.*, vol. 22, no. 3, pp. 1615–1632, 2023.

[175] K. Xiong, P. Fan, Z. Xu, H.-C. Yang, and K. B. Letaief, “Optimal cooperative beamforming design for MIMO decode-and-forward relay channels,” *IEEE Trans. Signal Process.*, vol. 62, no. 6, pp. 1476–1489, 2014.

[176] S. Özyurt, A. F. Coşkun, S. Büyükçorak, G. Karabulut Kurt, and O. Kucur, “A survey on multiuser SWIPT Communications for 5G+,” *IEEE Access*, vol. 10, pp. 109814–109849, 2022.

[177] A. Costanzo, D. Masotti, G. Paolini, and D. Schreurs, “Evolution of SWIPT for the IoT world: Near- and far-field solutions for simultaneous wireless information and power transfer,” *IEEE Microw. Mag.*, vol. 22, no. 12, pp. 48–59, 2021.

[178] W. Feng, J. Tang, Y. Yu, J. Song, N. Zhao, G. Chen, K.-K. Wong, and J. Chambers, “UAV-enabled SWIPT in IoT networks for emergency communications,” *IEEE Wireless Commun.*, vol. 27, no. 5, pp. 140–147, 2020.

[179] M. Cui, Z. Wu, Y. Lu, X. Wei, and L. Dai, "Near-field MIMO communications for 6G: Fundamentals, challenges, potentials, and future directions," *IEEE Commun. Mag.*, vol. 61, no. 1, pp. 40–46, 2023.

[180] Y. Liu, Z. Wang, J. Xu, C. Ouyang, X. Mu, and R. Schober, "Near-field communications: A tutorial review," *IEEE Open J. Commun. Soc.*, vol. 4, pp. 1999–2049, 2023.

[181] H. Zhang, N. Shlezinger, F. Guidi, D. Dardari, M. F. Imani, and Y. C. Eldar, "Beam focusing for near-field multiuser MIMO communications," *IEEE Trans. Wireless Commun.*, vol. 21, no. 9, pp. 7476–7490, 2022.

[182] X. Fang, W. Feng, Y. Chen, N. Ge, and Y. Zhang, "Joint communication and sensing toward 6G: Models and potential of using MIMO," *IEEE Internet Things J.*, vol. 10, no. 5, pp. 4093–4116, 2023.

[183] A. Liu, Z. Huang, M. Li, Y. Wan, W. Li, T. X. Han, C. Liu, R. Du, D. K. P. Tan, J. Lu, Y. Shen, F. Colone, and K. Chetty, "A survey on fundamental limits of integrated sensing and communication," *IEEE Commun. Surv. Tutor.*, vol. 24, no. 2, pp. 994–1034, 2022.

[184] S. H. Hong, J. Park, S.-J. Kim, and J. Choi, "Hybrid beamforming for intelligent reflecting surface aided millimeter wave MIMO systems," *IEEE Trans. Wireless Commun.*, vol. 21, no. 9, pp. 7343–7357, 2022.

[185] M.-H. T. Nguyen, E. Garcia-Palacios, T. Do-Duy, O. A. Dobre, and T. Q. Duong, "UAV-aided aerial reconfigurable intelligent surface communications with massive MIMO system," *IEEE Trans. Cogn. Commun. Netw.*, vol. 8, no. 4, pp. 1828–1838, 2022.